

Techniques for Enhancing Electron Microscopy

by

Akshay Agarwal

B.Tech., M. Tech., Indian Institute of Technology Bombay (2014)

S.M., Massachusetts Institute of Technology (2016)

Submitted to the Department of Electrical Engineering and Computer
Science

in partial fulfillment of the requirements for the degree of

Doctor of Philosophy in Electrical Engineering and Computer Science

at the

MASSACHUSETTS INSTITUTE OF TECHNOLOGY

September 2020

© Massachusetts Institute of Technology 2020. All rights reserved.

Author
Department of Electrical Engineering and Computer Science
August 28, 2020

Certified by
Karl K. Berggren
Professor of Electrical Engineering and Computer Science
Thesis Supervisor

Accepted by
Leslie A. Kolodziejcki
Professor of Electrical Engineering and Computer Science
Chair, Department Committee on Graduate Students

Techniques for Enhancing Electron Microscopy

by

Akshay Agarwal

Submitted to the Department of Electrical Engineering and Computer Science
on August 28, 2020, in partial fulfillment of the
requirements for the degree of
Doctor of Philosophy in Electrical Engineering and Computer Science

Abstract

Electron microscopy is a powerful imaging technique that allows us to push the limits of our understanding of materials at the nanoscale. An important limitation in the application of electron microscopy to organic and biological materials is sample damage induced by the electron beam. Recently, quantum mechanical and adaptive illumination imaging schemes have been devised to use the available electron dose efficiently to get the maximum information about the specimen. The primary requirement for the implementation of these schemes is efficient illumination and detection of electrons in the microscopes, which has limited the applicability of such low-dose imaging techniques.

In this thesis, we have developed and implemented low-dose imaging schemes achievable with current technology on a wide range of electron microscopes. We have also proposed microscopy schemes that combine ideas from quantum mechanical and adaptive illumination imaging to lower the electron dose required for imaging by up to an order of magnitude. Further, we have developed electron count imaging on a scanning electron microscope (SEM) and demonstrated improvement of up to 30% in image quality for the same imaging dose. Finally, we have implemented an adaptive illumination scheme on the SEM and demonstrated that the incident electron dose can be traded off with a tolerable increase in imaging errors. The work in this thesis improves the dose reduction possible with quantum imaging and adaptive illumination schemes and represents a major step towards their implementation in different types of electron microscopes.

Thesis Supervisor: Karl K. Berggren

Title: Professor of Electrical Engineering and Computer Science

Acknowledgments

The work in this thesis would not have been possible without the expertise, support, and advice of several people. I would like to begin by thanking my thesis advisor, Prof. Karl K. Berggren, for supporting my research ideas and giving me the freedom to pursue them. Six years ago, I arrived at MIT as a timid, fresh-off-the-plane grad student, and Karl welcomed me into his group. I will fondly remember our many sessions of debating over aspects of quantum physics on a whiteboard. Karl's commitment to transparent and honest scientific communication has always been inspirational for me, and I hope this thesis lives up to those ideals.

I also want to thank my committee members, Prof. Vivek K. Goyal and Prof. Dirk R. Englund. I have thoroughly enjoyed my collaboration with Vivek over the past three years, and much of the work in this thesis rests on theoretical foundations that Vivek laid out. Dirk's feedback and questions during committee meetings always pushed me to think about aspects of my work I had not considered before, and this thesis is all the better for it. I also owe thanks to Prof. James LeBeau, whose generously lent his expertise on electron microscopy and always made himself available to brainstorm new research ideas.

The scientific content of this thesis was shaped by the many collaborators I had during grad school. I want to thank Dr. Chung-Soo Kim and Prof. Richard Hobbs, who were my first mentors in grad school and taught me a lot about the conduct and communication of research. I also want to thank Prof. Dirk van Dyck, who welcomed me to his group in Belgium as a visiting scientist in 2016 and gave me the belief that I could do interesting work in electron microscopy. My research over the last couple years has also been strengthened by collaborations with John Simonaitis, Navid Abedzadeh, and Yuri van Staaden, and I am grateful for their contributions to this work. I also want to acknowledge the many fruitful and stimulating discussions I had with members of the QEM collaboration over the years.

One of the things no one tells you about a PhD is that almost all the people you meet at the start of your PhD will leave before you do. My colleagues, both past and present, in the Quantum Nanostructure and Nanofabrication group have always supported me through this journey - Faraz, Vitor, Yachin, Sam, Francesco, Chung-Soo, Richie, Sarah, Brian, Andrew, Di, Emily, Yujia, Donnie, Navid, John, Ashley, Marco, and Marco.

I want to thank Vatsal Shah for being an amazing and supportive friend through our times at IIT Bombay and grad school (MIT for me and UT Austin for him). We started together, and I am so glad we are finishing this together too! I also want to thank Atalay Ileri for his patience and understanding. I am so glad we are roommates again! Thank you both for tolerating all my quirks and long periods of silence.

I have met some amazing educators over the last six years who have given me the opportunity to grow as a teacher and think deeply about education. I want to thank Dr. Elizabeth Cavicchi, Lisa Schneier, and Dr. Paula Hooper, for showing me what kindness, generosity, and exceptional teaching can look like.

Thank you so much to my family - my parents, Abhai and Anuradha Agarwal, my brother, Aabhas Agarwal, and my bhabhi, Akshita Agarwal. My parents have always put my needs before theirs and ensured that I had a great learning environment. I promise I will call more often!

Finally, I want to thank my girlfriend/co-presenter/quarantine buddy Dr. Sarah Goodman. I am so lucky that you accepted my final rose and chose to go on this journey with me. Your work ethic and dedication to social justice inspire me, and I am so excited for our lives together! मैं भी तुमसे प्यार करता हूँ ।

Contents

List of Figures	13
List of Tables	17
1 Introduction	19
1.1 Introduction to electron microscopy modalities	20
1.1.1 Transmission and Scanning Transmission Electron Microscopy (TEM/STEM)	21
1.1.2 Scanning Electron Microscopy (SEM)	25
1.1.3 Detectors for SEs	29
1.2 Techniques for reducing incident electron dose	33
1.2.1 IFM-based QEM	36
1.2.2 Adaptive and Structured Illumination	40
1.3 Requirements for implementation of adaptive illumination and quan- tum imaging in electron microscopy	42
1.3.1 History of electron counting in SEM	43

1.3.2	Challenges and requirements	45
1.4	Work in this thesis	47
2	Reduced-dose electron microscopy through conditional sample re-illumination	49
2.1	Error and damage in STEM and IFM imaging	51
2.1.1	Apparatus and Terminology	51
2.1.2	Analysis of STEM and IFM approaches with single-shot illumination and $N = 2$ electrons	53
2.1.3	Analysis of STEM imaging schemes with single-shot illumination and $N \sim \text{Poisson}(\lambda t)$ electrons	57
2.2	Conditional re-illumination	73
2.2.1	Evolution of q_m	77
2.2.2	Error and damage in conditional re-illumination	78
2.3	Conclusions	84
3	Image quality metrics and schemes for conditional re-illumination for grayscale samples in an SEM	87
3.1	Image quality metrics for grayscale images	89
3.1.1	Contrast	89
3.1.2	Mean absolute relative error	91
3.1.3	Signal-to-noise ratio	94

3.2	Schemes for implementation of grayscale conditional re-illumination for grayscale objects	102
3.2.1	M -limited conditional re-illumination	104
3.2.2	N_{SE} -limited conditional re-illumination	104
3.3	Conclusions	105
4	Histogram- and oscilloscope-based secondary electron counting in SEM	107
4.1	SE counting using image histograms	109
4.1.1	Image histograms in SEM	110
4.1.2	SE quantization in SEM image histograms	116
4.1.3	Characterization of in-chamber and in-lens detectors using SE counting	123
4.2	SE counting using oscilloscope outcoupling	128
4.2.1	Introduction to oscilloscope outcoupling	130
4.2.2	Oscilloscope histograms and statistics	131
4.3	Conclusions	136
5	Electron count imaging and conditional re-illumination for reduced-dose SEM	139
5.1	Scan waveforms on the SEM	140
5.1.1	Analysis of SEM scan waveforms	140
5.1.2	Synchronizing SEM scan with oscilloscope frame capture	144

5.2	Analysis of acquisition frames	146
5.2.1	Calculating image resolution from linescan waveforms	147
5.2.2	Aligning acquisition frames and finding linescan period	148
5.2.3	Finding linescan duration and extracting SE signal during scanning	150
5.2.4	Counting SE pulses	151
5.3	Results of SE count imaging	152
5.3.1	SE count imaging with in-chamber detector	153
5.3.2	SE count imaging with in-chamber and in-lens detectors	154
5.3.3	Probability distribution of SEs	159
5.4	Offline conditional re-illumination	162
5.4.1	Images from conditional re-illumination schemes	163
5.4.2	Analysis of image quality and relative incident dose for conditional re-illumination schemes	165
5.5	Schemes for online electron counting and conditional re-illumination	168
5.5.1	Scheme for online SE count imaging	170
5.5.2	Scheme for online conditional re-illumination	173
5.6	Conclusions	174
6	Summary and future outlook	179
6.1	Summary of work	179
6.2	Future outlook	181

6.2.1	Combination of conditional re-illumination with quantum mechanical imaging schemes	181
6.2.2	Extensions of SE counting	185
Appendix A Example calculation of signal-to-noise ratio		187
Appendix B In-lens detector histograms		191
Appendix C Fitting SE probability distributions		195
Appendix D MATLAB code		199
D.1	MATLAB code for chapter 2	199
D.2	MATLAB code for chapter 3	214
D.3	MATLAB code for chapter 4	217
D.4	MATLAB code for chapter 5	221
Appendix E The First (and Second) Question		237
Bibliography		257

List of Figures

1-1	Schematic for TEM/STEM	23
1-2	Schematic for SEM	26
1-3	Detectors for SEs	30
1-4	Everhart-Thornley electron detector	32
1-5	Interaction-Free measurement	37
2-1	Conventional and IFM imaging schemes	52
2-2	Comparing conventional imaging schemes with and without D_3	62
2-3	Comparison of posteriors for conventional and IFM imaging	71
2-4	Comparison of P_{err} and \bar{n}_{damage} for the imaging schemes	72
2-5	Conditional re-illumination applied to IFM imaging Scheme C	77
2-6	Error and damage for IFM imaging Scheme C	80
2-7	P_{err} vs. \bar{n}_{damage} for all imaging schemes	81
2-8	Image simulation using conventional and IFM imaging with conditional re-illumination	82

3-1	Contrast for SEM images	90
3-2	Mean absolute relative error for SEM images	93
3-3	SNR for SEM images	98
3-4	Schemes for grayscale conditional re-illumination	103
4-1	Image histograms in SEM	111
4-2	Joy's method of calculating image SNR and SE detector DQE	113
4-3	SE quantization observed on the in-chamber detector in SEM	119
4-4	Statistics of image histogram SE counting	124
4-5	Variation of DQE with working distance for in-chamber and in-lens SE detectors	127
4-6	Oscilloscope outcoupling of SE detector signal	129
4-7	Oscilloscope histograms and their statistics.	132
5-1	Scan waveforms on the SEM	141
5-2	Scheme for oscilloscope synchronization	145
5-3	Acquisition frame alignment and SE pulse extraction	149
5-4	SE count imaging with in-chamber SE detector	154
5-5	Statistics of SE count imaging	155
5-5	Statistics of SE count imaging	156
5-6	Probability distribution of SE emission	160
5-7	SE count imaging with conditional re-illumination	164

5-8	Comparison of conditional re-illumination schemes	166
5-9	Schemes for live SE counting and conditional re-illumination	171
6-1	Mach-Zehnder interferometer in TEM	182
A-1	Example SNR calculation	188
B-1	In-lens image histogram	192
B-2	Joy's method for in-lens detector	193
C-1	Probability distribution of SE emission revisited	196

List of Tables

2.1	List of symbols and abbreviations used in Chapter 2	53
2.2	Possible outcomes at D_1 of STEM imaging with 2 incident electrons.	54
2.3	Decision rule for STEM imaging with 2 incident electrons.	54
2.4	Probabilities at D_1 and D_2 for IFM imaging.	55
2.5	Decision rule for IFM imaging with 2 incident electrons.	56
2.6	Possible outcomes at D_1 for Scheme A.	58
2.7	Decision rule for Scheme A.	59
2.8	Possible outcomes at D_1 and D_3 for Scheme B.	61
2.9	Decision rule for Scheme B.	62
2.10	Decision rule for IFM imaging with Poisson number of incident electrons.	65
2.11	Detection probabilities at D_1 , D_2 and D_3 for Scheme D.	68
2.12	Decision rule for Scheme D.	68
2.13	Detection probabilities at D_1 , D_2 and D_3 for Scheme D.	81
3.1	List of symbols and abbreviations used in Chapter 3	88

4.1 List of symbols and abbreviations used in Chapter 4 110

Chapter 1

Introduction

The electron microscope is a powerful and versatile tool that is used to image and characterize organic and inorganic with sub-nanometer resolution [1]. The diverse imaging modalities available on modern electron microscopes can be used to perform topographical, phase, and elemental composition analysis on samples. With the introduction of advanced phase retrieval and compressed sensing techniques, electron microscopy has become a high-throughput technique capable of answering a wide variety of questions about the electronic, magnetic, and elemental composition of a sample. Quantum mechanical imaging schemes that exploit the stable, high-coherence electron beams and aberration-corrected optics available in modern electron microscopes have the potential to further extend the types of samples and information obtainable in these tools [2–4]. However, the widespread adoption of these techniques is limited by a lack of analysis of the capabilities of quantum mechanical schemes implementable with current technology, as well as the lack of availability of single-electron sensitive detection in some electron microscopy modalities. Further, the applicability of electron microscopy to the imaging of biological samples remains limited by the challenge of beam-induced sample damage. In this thesis, we will address these challenges by combining ideas from compressed sensing, adaptive illumination, and quantum mechanics to develop new, reduced-incident-electron-dose

imaging algorithms and expand the availability of single-electron-sensitive imaging in electron microscopy.

In this introductory Chapter 1, we will discuss basic electron microscopy techniques, recent ideas and advances towards reducing sample damage in these techniques, and current challenges in their widespread implementation. This chapter is organized into four sections. In Section 1.1, we will introduce the two fundamental electron microscopy modalities: transmission/scanning transmission electron microscopy (TEM/STEM) and scanning electron microscopy (SEM). Following this introduction, we will discuss limitations imposed by sample radiation sensitivity on the types of samples that can be imaged in electron microscopes as well as recently proposed and adopted methods to reduce the imaging dose in electron microscopy in Section 1.2. In Section 1.3 we will discuss challenges in and requirements for the adoption of the low-dose imaging schemes introduced in the previous section. In Section 1.4, we will summarize the work in this thesis that meets these requirements and expands the application of adaptive imaging and quantum mechanical protocols to different electron microscopy modalities.

1.1 Introduction to electron microscopy modalities

In this section we will describe the two fundamental imaging modalities in electron microscopy: the imaging of thin samples in transmission mode (transmission/scanning transmission electron microscopy, TEM/STEM), and the imaging of the surface of thick samples (scanning electron microscopy, SEM). These techniques together can be used to obtain surface and cross-sectional imaging and chemical composition information of a specimen with atomic or close-to atomic resolution. This introduction will form the basis of our discussions of image formation, quality, and sample damage in the rest of this thesis.

1.1.1 Transmission and Scanning Transmission Electron Microscopy (TEM/STEM)

Figure 1-1(a) is a schematic of TEM imaging. Pre-specimen electromagnetic lenses produce a collimated electron beam that is incident on the sample and gets scattered as it transmits through the sample. If the sample is thin (< 100 nm), a small fraction of the electrons scatter inelastically and the rest scatter elastically and undergo diffraction. The transmitted electrons are imaged by post-specimen electromagnetic lenses.

There are several sources of contrast in TEM/STEM images. First, contrast can arise from thickness or atomic mass differences between different parts of the sample, which lead to differences in inelastic scattering. This type of contrast is referred to as mass-thickness or z-contrast. Second, contrast can also arise due to differences in orientation of the atomic lattice in the different parts of the sample, which lead to differences in how electrons are diffracted. This type of contrast is called diffraction contrast. Finally, interference between electron beams diffracted due to phase modulations in the sample can also result in contrast. This type of contrast is referred to as phase contrast. In summary, diffraction and phase contrast result from unscattered and elastically forward-scattered electrons, while z-contrast results from inelastic scattering. TEM images typically show several of these sources of contrast together.

In Figure 1-1(a) we can see how the post-specimen lower objective lens makes beams diffracted from the sample (orange) interfere with each other to form an image at the image plane. Figure 1-1(b) is a high-resolution TEM image of gold nanoparticles deposited on a carbon support membrane suspended over vacuum. The gold nanoparticles are the dark polygonal regions while the carbon membrane is the lighter, grainy region. The nanoparticles appear darker than the carbon membrane because of z-contrast. Inside each nanoparticle the atomic lattice of gold is visible due to phase contrast. TEMs usually operate at an incident electron beam energy between

50 - 300 keV and an incident beam current between tens of picoamperes and a few nanoamperes. With the advent of spherical and chromatic aberration correction, the resolution of TEM images can be lower than 0.1 nm for sufficiently thin (< 50 nm) samples [5].

The imaging detector in a TEM is placed in a plane conjugate with the first image plane of the lower objective lens (indicated in Figure 1-1(a)), after the image has been further magnified by intermediate and projection lenses. TEM detectors need to be spatially resolved, *i.e.*, need to be pixelated, so that they can capture the image of the sample. Charge-coupled device (CCD) cameras, capable of pixel resolutions higher than 2000×2000 pixels at several frames per second, are widely used [6]. More recently, CMOS cameras that detect electrons directly (rather than using scintillators as in CCD cameras), are sensitive to single electrons, and have high frame rates (up to 1000 frames per second), have been used for low-dose cryo-electron microscopy, as we will discuss further in Section 1.2 [7].

Traditionally, phase contrast, the highest resolution mode of TEM imaging, has been implemented by using a combination of beam aberrations and defocus, *i.e.*, the phase changes introduced in the beam from aberrations are balanced by deliberately defocusing the beam to optimize the transfer of contrast in the microscope [8,9]. However, the use of defocus limits the achievable imaging resolution. More recently, phase plates that shift the phase of the undiffracted beam by $\pi/2$ radians relative to the diffracted beams, thereby enabling in-focus Zernike-type phase contrast imaging, have been designed and implemented in the TEM [10,11]. The use of these plates has enhanced both the contrast and resolution available in phase contrast TEM images [12–16].

Figure 1-1(c) is a schematic of STEM imaging. Unlike in the TEM, the incident electron beam is focused to a spot on the sample and scanned across it. We can think of the sample as being divided into pixels, and the incident electron beam raster scans over each sample pixel. The STEM image is a representation of signal intensity

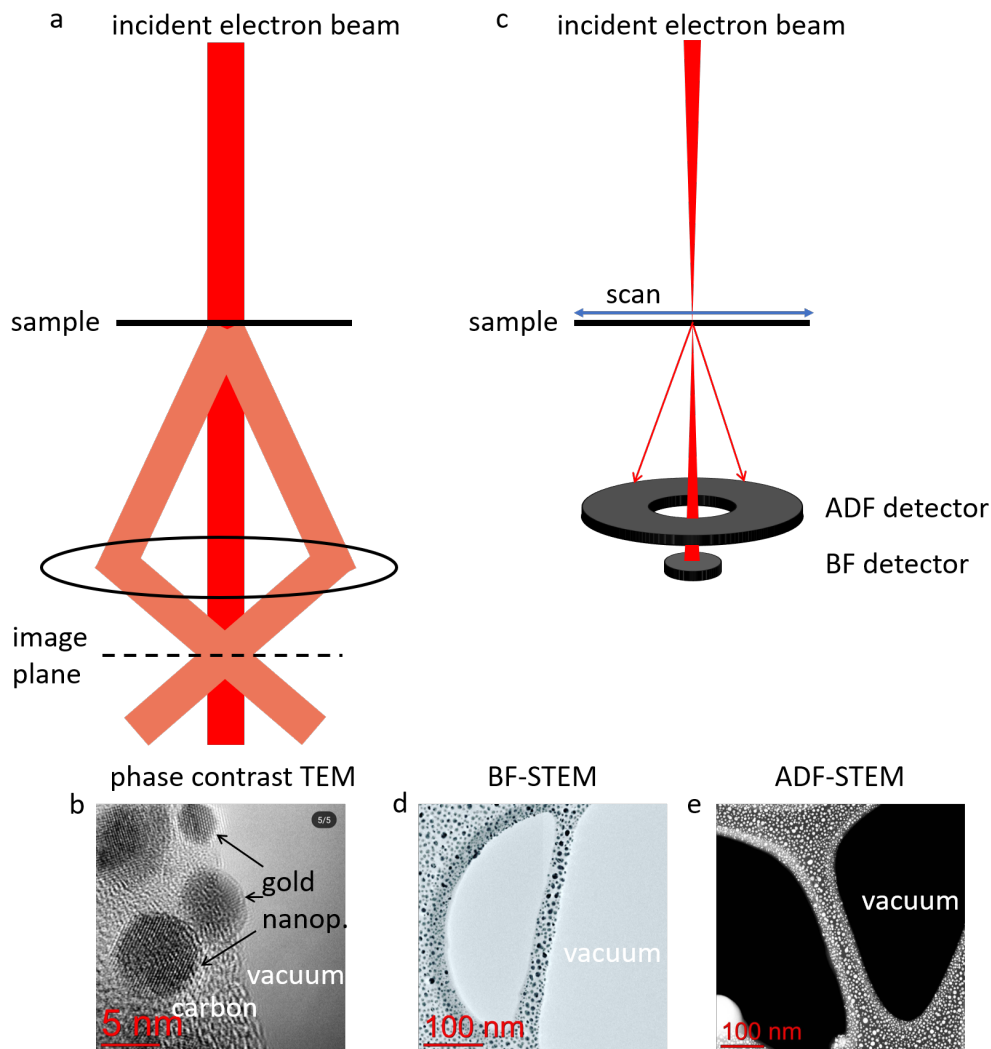


Figure 1-1: Transmission/scanning transmission electron microscopy (TEM/STEM). (a) Schematic for phase-contrast TEM imaging. The collimated incident electron beam is diffracted by the sample, and the diffracted beams are collected and made to re-interfere by the post-specimen objective lens to create an image at the image plane. (b) Phase contrast HRTEM image of gold nanoparticles suspended on a carbon support grid. (c) Schematic for STEM imaging. The focused electron beam scans over the sample, and the annular dark field (ADF) and bright field (BF) detectors collect inelastically scattered and unscattered electrons respectively. (d) BF-STEM and (e) ADF-STEM image of the same gold nanoparticle sample as (b).

from each pixel of the image. Therefore, in this type of imaging, the signal detector does not need to be pixelated (*i.e.*, it does not need to have spatial resolution); it simply collects all the signal from each pixel serially. Instead, spatial resolution is determined by other factors such as the size of a pixel on the sample (*i.e.*, the gap between successive positions of the electron beam), the spot size of the focused electron beam, and the type of signal collected [1]. STEM systems operate at the same ranges of incident beam energies and currents as TEMs. A combination of aberration-correction, advanced phase retrieval techniques, and high-dynamic range electron counting detectors have enabled the resolution of STEM images to be as low as 0.04 nm [17].

A state-of-the-art STEM will have many different modalities to construct images from the various types of signals that arise from the interaction between the incident electron beam and the sample. For example, in STEM-based cathodoluminescence, we map the intensity of photons emitted by the sample in response to the incident electron beam. In electron-energy loss spectroscopy, we map the energy lost by electrons as they are scattered inelastically by the sample pixels. Here, we will focus on two imaging modalities available on all STEMs: bright- and dark-field imaging. The position of the detectors for these imaging modes are shown in Figure 1-1(c).

In bright-field (BF) imaging, the detector detects electrons that transmit through the sample without any scattering, or electrons that scatter at very small angles. Therefore, the image from this detector is a map of the intensity of the electrons transmitted through each sample pixel. The image is bright in regions of the sample that transmit more electrons (very thin regions, regions with low atomic mass elements, or vacuum) and darker in regions that scatter more electrons (thicker regions or regions with high atomic mass elements). Figure 1-1(d) is a BF-STEM image of the same sample of gold nanoparticles deposited on a carbon support membrane as the TEM image. The gold nanoparticles appear as dark circles or polygons because they scatter more electrons, while the carbon support grid appears brighter. The background vacuum over which the carbon membrane is suspended appears brightest

because it transmits all electrons.

In dark field (DF) imaging, the detector detects electrons that are inelastically scattered off the sample (shown with red arrows in Figure 1-1(c)). The detector is annular in shape to allow the unscattered electrons to go through to the BF detector, and the inner and outer angles of the annulus determine the type of scattering process to which the DF detector is sensitive. The position of this annular dark field (ADF) detector is indicated in Figure 1-1(b). Figure 1-1(e) is an ADF-STEM image of a different region of the same sample of gold nanoparticles on a carbon support membrane as the TEM and BF-STEM images. In this image, the contrast is reversed compared to the BF-STEM image. The gold nanoparticles appear brightest because they scatter the incident electrons more than the carbon membrane, which appears darker. The background vacuum, which scatters no electrons, is completely black.

1.1.2 Scanning Electron Microscopy (SEM)

In this section we will introduce SEM imaging and describe the two types of imaging modes used most widely in SEM: secondary electron (SE) imaging and backscattered electron (BSE) imaging. Since the geometry and behavior of SE detectors in an SEM will be an important consideration in chapters 4 and 5 of this thesis, we will also discuss the construction and working of these detectors in this section.

1.1.2.1 Basic SEM operation

Figure 1-2(a) is a schematic representation of SEM. Similar to STEM, the incident electron beam scans over the sample, which can be thought of as being divided into pixels. A computer builds the image of the sample serially, and the image is a representation of the signal level on the detector from each pixel [19]. Unlike the STEM, the SEM images electrons emitted from the surface of the sample (instead of electrons transmitted through the sample). Since the electron beam does not need to go

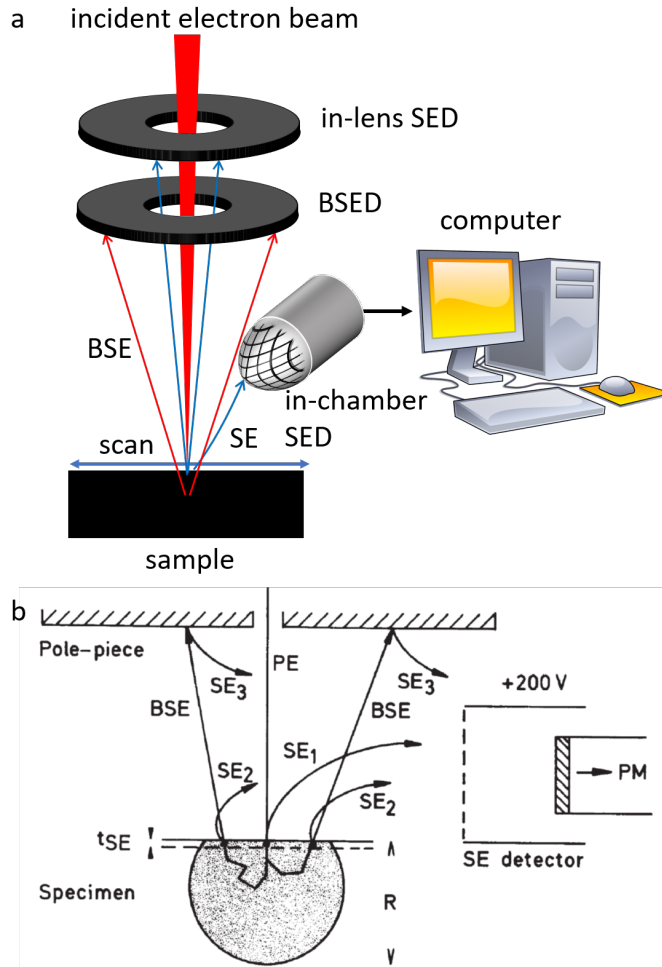


Figure 1-2: Schematic for Scanning Electron Microscopy (SEM). (a) The focused incident electron beam raster scans over the sample and generates SEs and BSEs. SEs get detected by either the in-chamber SE detector or the in-lens SE detector, and BSEs get detected by the BSE detector. A computer receives the signal from these detectors serially and generates an image of the sample. (b) Generation of SEs and BSEs in SEM. BSEs are generated within a micron-sized volume in the sample due to the incident electrons (labelled PE) undergoing multiple scattering events. SEs generated by the incident electron beam (PE) in the sample are called SE₁s, those generated by BSEs in the sample are called SE₂s, and those generated by BSEs on striking the lens polepiece and SEM chamber walls are called SE₃s. Figure reproduced from [18].

through the sample, the sample can be a bulk material and need not be thinned down. Therefore, sample preparation is more straightforward for SEM than STEM. Further, since the incident electrons are not required to go through the sample, they can be of lower energy; SEM imaging is typically done at electron beam energies between 1 and 30 keV, as opposed to 50-300 keV and above for STEM. Typical values of the incident beam current are in the range of 50 pA - 1 nA, and typical pixel dwell time are in the range of 5 μ s - 100 μ s.

There are two types of electrons that are emitted from the surface of samples and imaged in SEMs: secondary electrons (SEs, shown by the blue arrows in Figure 1-2(a)) and backscattered electrons (BSEs, shown by the red arrows in Figure 1-2(a)) [18]. SEs are electrons that are part of the sample, get excited by the incident electron beam and are ejected from the sample surface. The generation of SEs is depicted schematically in Figure 1-2(b), which is reproduced from *Scanning Electron Microscopy* by L. Reimer [18]. SEs typically have energies in the range of 2-10 eV; conventionally the upper bound on SE energies is placed at about 50 eV. Although the incident-beam electrons deposit their energy and excite sample electrons in a large, micron scale volume inside the sample (depicted by R in Figure 1-2(b)), only electrons from within the first few nanometers of the surface can escape (depicted by t_{SE} in Figure 1-2(b)) [19]. Therefore, SE imaging is very sensitive to changes in surface topography: sharp edges or corners offer a greater surface area for SEs to escape and show up as brighter than surrounding regions in SE images. Hence, SE imaging is best used for mapping the sample topography. The resolution of SE imaging is typically on the order of a few nanometers, determined by the sample material, imaging conditions, and type of detector. The yield of SEs (*i.e.*, the mean number of SEs excited by each incident electron) is very sensitive to the energy of the incident electrons. At typical SEM energies (between 1-30 keV) it is less than 1 for most materials [20]. In this range of energies SE yield decreases as energy increases and vice versa. The SE yield shows some dependence on the sample atomic number, but this dependence is highly irregular [18]. Therefore, SEs are typically not used to map

the material composition of the sample.

BSEs are incident electrons that undergo several small-angle nuclear scattering events inside the sample and eventually get scattered back out of the top surface of the sample at an angle to it. The generation of BSEs is depicted schematically in Figure 1-2(b). Since they undergo several scattering events inside the sample before turning back, they are emitted over a micron-scale volume in the sample. Further, because they are generated due to nuclear scattering inside the material, their yield is much more sensitive to the material composition of the sample than its topography. Hence, BSE imaging is best used to map sample material composition. The resolution of BSE imaging is typically lower than SE imaging due to the large volume over which BSEs are emitted [19].

As we had discussed earlier, the resolution of SE imaging depends on several factors, including the type of electron source, imaging conditions, type of sample, and type of detector. The type of electron source and imaging conditions such as the beam current, beam energy, and working distance determine the size of the incident electron beam on the sample surface. Another factor that affects resolution is the source of SEs. SEs are classified into different types based on their source. SEs emitted directly from the sample surface by the incident beam are called SE_{1s}. Since these SEs are excited directly from the small volume within the escape depth probed by the incident beam, they offer the highest resolution SE imaging. BSEs also emit SEs when they are within the escape depth of the sample surface on their way out. Due to their lower energy and the oblique angle, BSEs are more efficient at generating SEs than the incident-beam electrons [21]. The SEs generated by BSEs are called SE_{2s}. BSEs can also emit SEs after emerging from the sample surface, upon striking the walls of the SEM chamber, the lens polepieces, etc. These SEs are called SE_{3s}. The generation of SE_{1s}, SE_{2s}, and SE_{3s} is depicted schematically in Figure 1-2(b). Although SE_{2s} and SE_{3s} increase the signal from each pixel of the image, they offer lower resolution SE imaging due to the large escape region of BSEs. However, due to the larger SE yield of BSEs, SE_{2s} and SE_{3s} can dominate the total SE yield unless care

is taken about the placement of the SE detector and other imaging conditions [22,23]. We will now turn to a discussion of SE detectors. The detection mechanism as well as the geometry and placement of these detectors will be important in our discussion of SE counting and imaging in Chapters 4 and 5.

1.1.3 Detectors for SEs

SE detectors register the intensity of the SE signal for every pixel to generate the SE image. SE detectors are typically placed in one or both of two locations in an SEM: in-chamber and in-lens. These two detectors are shown schematically in Figure 1-2(a). Figure 1-3(a) indicates the positions of the objective lens polepiece, the two SE detectors, and the BSE detector in the chamber of the SEM used in this work (Zeiss LEO 1525). This image was captured with the sample stage (attached to the vacuum chamber door) pulled out, which is why the sample is absent. We have indicated the typical position of the sample with a black box. We will first discuss the geometry of each detector and then the common mechanism by which these detectors register the SE signal.

The in-chamber SE detector is placed inside the vacuum chamber of the SEM at an angle to the sample, as shown schematically in Figure 1-2(a). As we can see in Figure 1-3(a), this detector has a Faraday cage around it on which a positive voltage of several hundred volts is applied. This positive bias attracts SEs towards the detector. Due to its placement in the SEM chamber, the in-chamber detector does not discriminate between SE_{1s} , SE_{2s} , and SE_{3s} . Consequently, it typically offers lower resolution images than the in-lens detector. Further, since the in-chamber detector is placed at an angle to the sample, SEs emitted from sample surfaces facing towards the detector can reach the detector with greater probability than SEs emitted from surfaces facing away from the detector. Therefore, SE images generated by this detector tend to show shadowing effects. Figure 1-3(b) (reproduced from [22]) is an in-chamber SEM image of a carbon-coated, polished copper standard sample

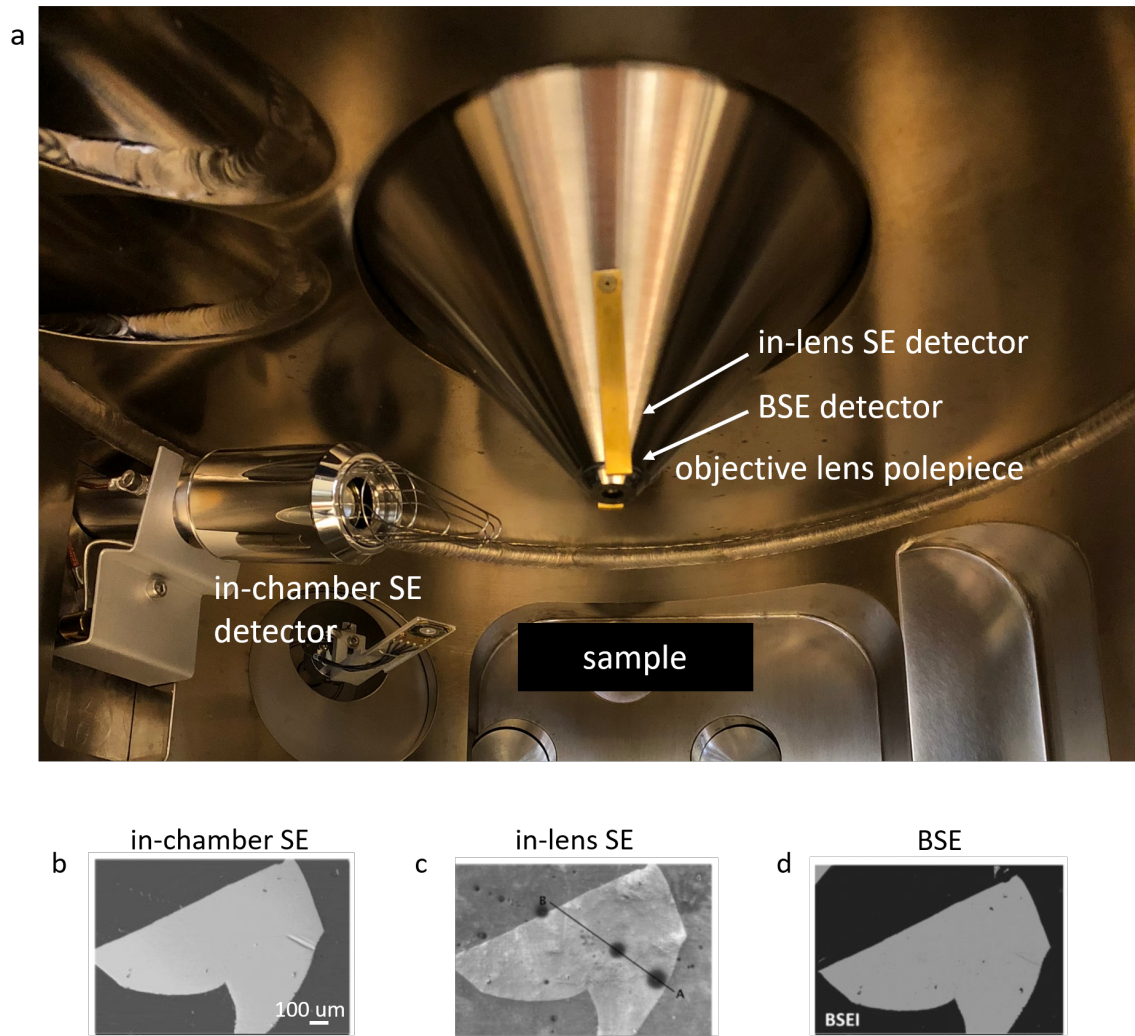


Figure 1-3: Detectors for SEs. (a) View inside an SEM chamber, showing the objective lens polepiece and in-chamber SE detector. The positions of the in-lens SE detector, the BSE detector, and the sample are also indicated. (b) In-lens, (c) in-chamber, and (d) BSE images of a carbon-coated, polished copper standard sample embedded in epoxy resin and mounted on a brass strip. These images are reproduced from [22].

embedded in epoxy resin and mounted on a brass strip. We can see some of the surface topography of the sample in this image. Further, due to the influence of SE_2 s and SE_3 s generated by BSEs, we can also see contrast between the copper sample and the brass mount. This material contrast is not as high as in the BSE image (Figure 1-3(d)) but is much greater than in the in-lens image.

The in-lens SE detector is placed inside the objective lens polepiece above the sample, as shown schematically in Figure 1-2(a). In Figure 1-3(b) we have indicated the position of this detector. The detector components are inside the polepiece and cannot be seen in this image. The detector is annular in shape and is placed symmetrically around the incident beam optical axis. In the SEM used in this work, the in-lens detector uses an 8 keV electrostatic field to attract SEs towards it. Due to its position close to the sample as well as the large electrostatic field to attract SEs, the in-lens detector tends to be more efficient at collecting SEs than the in-chamber detector. Also, because of its symmetrical position around the beam optical axis, in-lens detector SE images do not have shadowing effects. Further, due to its position inside the lens polepiece, the solid angle subtended on it by BSEs is small. Therefore, the in-lens detector is much better at collecting SE_1 s preferentially over other types of SEs. Consequently, in-lens detector images can have higher resolution than in-chamber images [22]. Figure 1-3(c) (reproduced from [22]) is an in-lens image of the same polished copper sample as in the previous paragraph. We can observe more surface details in this image and lesser contrast between the copper and brass, indicating that SE_1 s make a greater contribution to this image compared to the in-chamber detector image.

The most popular detection method for electrons, common to both the in-chamber and in-lens detectors, is based on a scintillator - photomultiplier setup first introduced in SEM imaging by Everhart and Thornley [25]. This detection method is depicted schematically in Figure 1-4 (image reproduced from *Scanning Electron Microscopy* by L. Reimer [24]). SEs emitted from the sample strike a scintillator plate biased at a positive bias of 8-10 keV and generate photons. These photons are

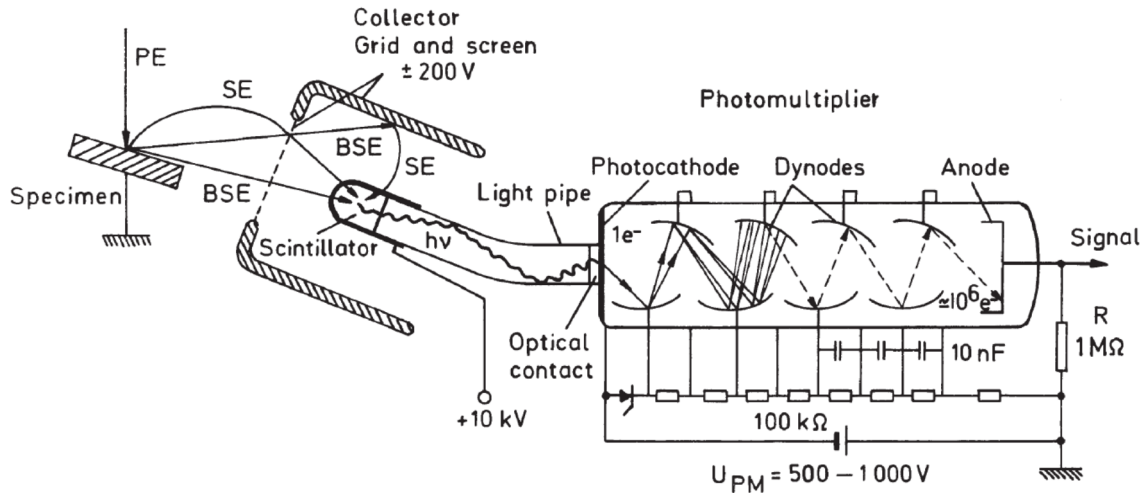


Figure 1-4: Schematic representation of an Everhart-Thornley electron detector. A combination of a scintillator and photomultiplier detects SEs from each pixel of the sample to produce the image. Figure reproduced from [24].

directed to a photomultiplier through a light pipe. On striking the photocathode of the photomultiplier, the photons generate photoelectrons which are guided through a series of dynode stages biased at increasingly high voltages up to 1 kV. The dynode stages amplify the photoelectron signal. The amplified signal is coupled out of the SE detector. Following this outcoupling, the signal is filtered, amplified further, quantized to 8-bits, and displayed on the SEM computer screen for each pixel. The internal quantum efficiency of detection is close to 1, meaning that almost every SE that is incident on the SE detector contributes to the detector signal [26–29].

Although these SE detector systems are capable of counting individual SEs [24, 27], they are usually used in analog mode, meaning that they integrate the electron signal. The scintillator materials commonly used in these detectors have an excitation decay time on the order of 50-100 ns [24], meaning that for each SE that strikes the scintillator, photons are produced up to 100 ns after the initial excitation. Therefore, if a second SE excites the detector within the decay time of the first SE, the signal from these two SEs will overlap and may not be distinguishable. For 100 pA incident beam current and SE yield $\delta = 0.2$ we would expect to receive ~ 125 SEs per μs [27]. This rate of SEs would be far too high for the detector to count each SE, and it would be

more accurate to instead find the analog signal from all the detection events. Further, in many SEM systems, including the Zeiss LEO 1525 used in this work, the SEM computer software displays the detector signal for every pixel on the screen averaged over the pixel dwell time. This *signal-time averaging* is performed to prevent under- or over-saturation of the image when the pixel dwell time is changed. For example, suppose the signal level from a particular sample pixel is 10 units at a pixel dwell time of 5 μs , and it corresponds to an 8-bit pixel brightness level of 150 on the image displayed on the SEM computer. Now, if the pixel dwell time is doubled to 10 μs , the signal level from the same pixel would be expected to double to 20 units, which would correspond to a pixel brightness level of 300. However, an 8-bit image only has 256 levels. Therefore, this pixel would appear to be saturated in the longer dwell time image. Similarly, as the dwell time is lowered, the pixel brightness would get lower until it reduces to 0. To prevent this saturation, the SEM displays the signal from every pixel averaged over the pixel dwell time, so that the expected pixel brightness level stays constant as the pixel dwell time is changed. Signal-time averaging will have important consequences in our implementation of SE counting, as we will describe in Chapter 4.

In the next section, we will use the understanding of electron microscopy developed in this section to discuss sample radiation damage, which restricts the types of samples that can be imaged in an electron microscope, and techniques to lower the incident electron dose and mitigate this damage.

1.2 Techniques for reducing incident electron dose

We discussed in Section 1.1 how electron microscopes operate by radiating the specimen with a high energy (50 keV or more for TEM, 1-30 keV for SEM) incident beam of electrons and collecting the electrons transmitted and/or scattered from the specimen. We also saw the different imaging modalities that arise from the nature of the signal collected. In TEM imaging, the incident-beam electrons that are transmitted

or forward-scattered through a thin (≤ 100 nm) specimen are collected. Transmitted and elastically forward scattered electrons are used to form phase-contrast images, while inelastically forward-scattered electrons are used to image the specimen (z-contrast TEM imaging and bright- and dark-field scanning transmission electron microscopy (STEM) mode imaging) and also to study its crystal structure and chemical composition. In SEM imaging, both the SEs generated from the specimen by the incident-beam electrons (SE imaging), as well as incident-beam electrons that are backscattered from the sample (BSE imaging) are used for imaging.

An inherent disadvantage of electron microscopy is damage to the specimen from the highly energetic incident-beam electrons. Typical beam currents are in the range of ~ 100 pA to a 10 nA. Focused down to a beam size of 0.01 nm^2 (typical in STEM imaging), or 1 nm^2 (typical in SEM imaging), these currents correspond to electron doses of $10^5 - 10^7$ electrons per square nanometer per microsecond for STEM and $10^3 - 10^5$ electrons per square nanometer per microsecond for SEM. These electron doses can damage the specimen through two different mechanisms: knock-on damage and radiolysis. Knock-on damage refers to the direct displacement of sample atoms by the high-energy electrons in the incident beam, and radiolysis refers to ionization and consequent dissociation of chemical bonds in the sample due to the incident beam. Depending on the operating voltage of the microscope and the chemical composition of the sample, one or both of these mechanisms may be significant [30,31]. The high electron dose in electron microscopy is tolerable for many inorganic and non-biological samples but has been a major problem in the application of electron microscopy in imaging biological samples for which this radiation dose is damaging to the carbon-based structure [32,33]. To reduce sample damage, we could reduce the imaging current; however, this reduction would lead to less signal from the sample, and consequently lower signal-to-noise ratio. This tradeoff between image quality and sample damage limits the resolution of electron microscope imaging of biological samples [30].

The effect of radiation damage on the imaging of samples in electron mi-

croscopy can be quantified as a critical dose D_c , defined as the dose at which the relative intensity of a ring or spot in the diffraction pattern of the sample fades by a factor of $1/e$ [34, 35]. Although D_c varies over several orders of magnitude for different molecules (and also depends on the beam energy and operating temperature), 0.01 C/cm^2 is a typical value at 100 keV beam energy [30]. This value equals about 6×10^3 electrons per square nanometer, which, for a pixel dwell time of 1 μs , is in the range of electron dose for SEM and one order of magnitude below the dose in STEM specified in the previous paragraph. Therefore, such a sample would undergo severe radiation damage during electron beam imaging. For many organic samples, the critical dose is even lower than 6×10^3 electrons per square nanometer, and it can be difficult to image such samples in STEM or SEM.

As a consequence of electron-beam-induced sample damage, most live-sample biological imaging currently uses optical microscopy, where the conventional resolution limit is given by Abbe's criterion and is about 200 nanometers for visible light. Although several techniques have been used in recent years to overcome this limit [36, 37], the best achievable resolution is still in the range of tens of nanometers. Therefore, for true atomic sub-nanometer-scale biological imaging, an electron beam imaging modality is essential.

Recently, cryogenic electron microscopy (cryo-EM) [38] has been used to image biological molecules at resolutions lower than 0.3 nm [39]. A major advantage of performing electron microscopy at cryogenic temperatures is that D_c can be more than one order of magnitude higher at 100 K than 300 K [34]. In cryo-EM, the sample consists of hundreds of thousands of particles of the biomolecule being imaged. The electron beam is spread out over this ensemble, and each individual particle gets a small electron dose which limits damage. An imaging algorithm reconstructs a 3-D electron density map of the biomolecule using several thousands of noisy, low-dose images of the biomolecule in different orientations. Since the technique depends on acquiring images of an ensemble of nanoparticles, it is susceptible to inhomogeneities in the particle size and composition. Further, the requirement of cryogenic tempera-

tures precludes any possibility of imaging nanostructures within a live cell.

In this section, we will discuss two techniques that have been proposed and used for reduced-dose electron microscopy: interaction-free-measurement (IFM) based quantum electron microscopy (QEM) and adaptive illumination. While QEM is a proposed electron microscopy scheme, adaptive illumination has already been employed in STEM and SEM to reduce the electron dose for imaging by several orders of magnitude [40, 41].

1.2.1 IFM-based QEM

Interaction-free measurement (IFM) was first proposed by Elitzur and Vaidman in 1993 as a thought experiment for detecting the presence of a 100% absorbing or scattering sample pixel (exemplified by a single-photon-sensitive bomb) without interacting with it [42]. In their scheme, sketched in Figure 1-5, the sample being imaged is placed in one of the arms of a Mach–Zehnder interferometer. We assume the sample to be made up of opaque (scattering) pixels (shown in black) and completely transparent pixels (shown in white). The Mach–Zehnder interferometer consists of two beamsplitters and two mirrors. The first beamsplitter divides the amplitude of the incident probe particles along two ‘arms’ of the interferometer. These two arms of the interferometer are redirected by the two mirrors and made to interfere by the second beamsplitter. Detectors D_1 and D_2 count the particles at the two output ports of the interferometer.

We denote the photon creation operator along the beam path incident on the first beamsplitter as \hat{y}^\dagger , along the upper interferometer arm as \hat{a}^\dagger , the lower arm as \hat{b}^\dagger , the upper output from the second beamsplitter as \hat{c}^\dagger , and the lower output with \hat{d}^\dagger . Kets $|0\rangle$ and $|1\rangle_s$ represent 0 photons and 1 photon along path s respectively; thus $\hat{s}^\dagger |0\rangle = |1\rangle_s$. Here, $s \in \{a, b, c, d\}$. For 50% transmitting beamsplitters, an input photon has equal probabilities of being in either of the interferometer arms. Hence,

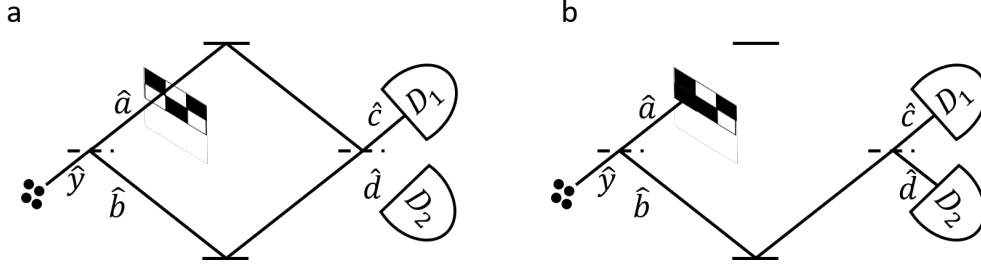


Figure 1-5: Interaction-Free measurement. The sample being imaged is placed in one of the arms of a Mach-Zehnder interferometer, consisting of two beamsplitters and two mirrors. (a) When the sample pixel is transparent, the two photon paths constructively interfere with each other along the upper output port leading to each incident photon being counted at detector D_1 . (b) When the sample pixel is opaque, the interference between the two paths is broken. The incident photon scatters off the opaque pixel with probability 0.5 and gets detected on detectors D_1 and D_2 with probability 0.25 each. A photon detection at D_2 indicates that the pixel is opaque without the photon having interacted with the pixel.

the creation operator at the input transforms as:

$$\hat{y}^\dagger \rightarrow \frac{\hat{a}^\dagger + \hat{b}^\dagger}{\sqrt{2}}.$$

Similarly at the second beamsplitter,

$$\hat{a}^\dagger \rightarrow \frac{\hat{c}^\dagger - \hat{d}^\dagger}{\sqrt{2}}.$$

$$\hat{b}^\dagger \rightarrow \frac{\hat{c}^\dagger + \hat{d}^\dagger}{\sqrt{2}}.$$

where the change in sign for \hat{a}^\dagger occurs because reflection along the upper arm leads to a phase change of π while reflection along the lower arm does not. When the sample pixel is transparent and a single photon enters the interferometer along \hat{y} ,

$$|1\rangle_y \rightarrow \hat{y}^\dagger |0\rangle \rightarrow \frac{\hat{a}^\dagger + \hat{b}^\dagger}{\sqrt{2}} |0\rangle \rightarrow \frac{1}{\sqrt{2}} \left\{ \frac{\hat{c}^\dagger - \hat{d}^\dagger}{\sqrt{2}} - \frac{\hat{c}^\dagger + \hat{d}^\dagger}{\sqrt{2}} \right\} |0\rangle \rightarrow \hat{c}^\dagger |0\rangle \rightarrow |1\rangle_c. \quad (1.1)$$

Thus, the photon always exits at the upper output of the interferometer, as shown in Figure 1-5(a). Physically, this phenomenon occurs because of constructive interference in the direction of the upper output and destructive in the direction of the lower output port of the interferometer. Detector D_1 , placed at the upper output of

the interferometer, always registers a count for every input photon while detector D_2 at the lower output never registers a count.

Now, we place a sample pixel that is opaque (*i.e.*, it absorbs or inelastically scatters all incident particles) in the upper arm of the interferometer as depicted in Figure 1-5(b). A photon that takes the upper arm gets scattered by the sample pixel. Therefore, the interference between the two arms is broken. We get:

$$\begin{aligned}
|1\rangle_y \rightarrow \hat{y}^\dagger |0\rangle &\rightarrow \frac{\hat{a}^\dagger + \hat{b}^\dagger}{\sqrt{2}} |0\rangle \\
&\rightarrow \frac{\hat{a}^\dagger}{\sqrt{2}} |0\rangle + \frac{|\text{scattering}\rangle}{\sqrt{2}} \\
&\rightarrow \frac{\hat{c}^\dagger - \hat{d}^\dagger}{2} |0\rangle + \frac{|\text{scattering}\rangle}{\sqrt{2}} \\
&\rightarrow \frac{|1\rangle_c}{2} - \frac{|1\rangle_d}{2} + \frac{|\text{scattering}\rangle}{\sqrt{2}}
\end{aligned}$$

Now an input photon will be counted at detectors D_1 and D_2 with probability 0.25 for each and will be scattered by the sample pixel with probability 0.5. Counts at detector D_1 do not provide us any new information since this detector clicked for a transparent pixel too. However, counts at D_2 tell us that the sample pixel was opaque, since this detector cannot register counts for transparent pixels as seen in Equation (1.1). Further, photons registered at detector D_2 could not have been scattered by the sample pixel since they reached the detector. Hence, we have inferred the presence of the opaque pixel without interacting with or depositing energy in it with the photon. Photon detection at D_2 only happens in 25% of the cases; 50% of the time photons still hit opaque sample pixels. By scanning the beam over all sample pixels and checking which detector the photon is counted at, we can generate an image of the sample. In generating this image, we would only be sure of the opacity of pixels for which there was a detection in D_2 , or for which there was scattering. For pixels where there was a detection at D_1 , we would have to make a guess. We will discuss strategies to make and improve this guess in Chapter 2.

IFM with photons was first demonstrated in 1998 by Kwiat and co-workers [43],

who also proposed a scheme for improving the efficiency of IFM based on the quantum Zeno effect by cascading several Mach–Zehnder interferometers and reducing the transmissivity of the beamsplitters [44]. Putnam and Yanik [45] suggested a scheme for implementing high-efficiency IFM with electrons, following which designs for such a ‘Quantum Electron Microscope’ (QEM) were outlined by Kruit and co-workers [2, 46]. In these designs, the electron beam is confined inside a resonant cavity with a beamsplitting element (such as a crystalline grating or a nanofabricated diffractive electron mirror [47–49]). The beamsplitting element creates two interferometer arms, and the sample is placed in one of these arms. The electron beam starts off completely in one arm of the cavity, and its intensity transfers quadratically to the other arm with increasing circulations in the cavity in the absence of the sample, or if the sample pixel being imaged is transparent to electrons. If the sample pixel is opaque, this quadratic buildup does not happen, and sample damage increases linearly with the number of circulations. Therefore, as the number of passes increases, the advantage of reduced damage offered by this scheme builds up linearly as well. Such a microscope would potentially enable atomic-resolution imaging of the specimen with beam-induced damage reduced by several orders of magnitude due to the reduced interaction between the specimen and incident beam [38].

In parallel with these developments, theoretical work also focused on analyzing the limits of IFM for imaging semitransparent phase and amplitude objects [50–54], objects with non-uniform transparency distribution [55, 56], and incorporating non-ideal detectors and system losses [57, 58]. This body of work introduced the idea of a finite acceptable rate of object misidentification (*i.e.* error probability) as a trade-off for lowered sample damage. These studies established that in some cases, quantum imaging protocols can offer an advantage in terms of reduced sample damage for the same error probability [59–61], for example, when distinguishing semitransparent samples from completely transparent or opaque samples, measuring sample phase in addition to amplitude, detecting the presence of a single defect, or working with Poisson sources.

With recent progress in nanofabrication, it has become possible to perform amplitude-division interferometry with a Mach–Zehnder interferometer in a standard TEM and STEM. In our previous work, we demonstrated electron interference in a standard TEM using a monolithic grating consisting of two 40 nm thick single-crystal silicon membranes as beamsplitters, fabricated using focused ion-beam milling [62,63]. Tavabi and co-workers also reported electron interference using a similar crystalline grating [64]. Following this work, Yasin and co-workers demonstrated electron holography in a STEM using a nanofabricated phase grating as the beamsplitter [4,65–67]. Nanofabricated, free-standing amplitude gratings have also been previously used as electron beamsplitters in a custom-made setup at lower electron beam energies [68]. Therefore, single-stage Mach–Zehnder based IFM can be implemented in an SEM or STEM with current technology [69].

1.2.2 Adaptive and Structured Illumination

Adaptive and structured illumination of the sample is based on the idea that the illumination on the sample in electron microscopy need not be a collimated beam (for TEM) or a focused beam that scans all the specimen pixels (for STEM and SEM). By structuring the illumination such that we extract only the information we desire from the sample, we can reduce the total incident dose during imaging. Similarly, by adapting the illumination to a fraction of the sample pixels and using prior information about the sample, we can reconstruct an image of the whole sample at a much lower dose.

Multipass TEM has recently been proposed as a way of obtaining the same reduction in incident electron dose as in QEM without the need for beamsplitting [3, 70]. Just as in QEM, the electron beam and the sample are placed in a resonant cavity inside which the electron beam circulates [71]. The electron optics inside the cavity is configured such that the sample is imaged onto itself at each circulation of the electron beam. Therefore, the electron beam incident on the sample is structured

to be an image of the sample itself. This repeated re-imaging builds up contrast in the sample image quadratically, while the sample damage only builds up linearly with the number of circulations. This buildup mirrors the intensity build up in the QEM and offers the same reduction in sample damage [72].

The recent creation and use of electron beams with orbital angular momentum (OAM) in STEM is another example of structured illumination [73,74]. Conventional electron probes do not possess magnetic moment and are insensitive to the magnetic properties of materials. The deployment of OAM beams in STEM has enabled the exploration of magnetic properties of different materials [75]. Such beams have been created by the use of nanofabricated phase masks placed in the path of the electron beam. More generally, there has been progress towards the development of the equivalent of spatial light modulators for electrons, *i.e.*, phase masks that can give electron beams a desired arbitrary phase profile [76]. Such phase masks have the potential to reduce the required incident dose for certain kinds of imaging experiments significantly. For example, by shaping the electron wavefront to match specific molecular arrangements or orientations, the number of electrons required for finding these arrangements in an ensemble could theoretically be reduced to 1 [59–61]. 4-D STEM techniques such as matched illumination and detector interferometry (MIDI)-STEM and STEM holography, aimed at enhancing phase contrast in STEM (and thereby reducing dose) are also enabled by nanofabricated phase plates that structure the incident electron beam [4,65–67,77].

After early work on adapting the incident beam current and pixel dwell time to meet the critical dose requirements of the sample [78], adaptive illumination has been implemented in STEM through sparse sampling techniques. In these illumination algorithms, a randomly selected subset of sample pixels is illuminated by the focused STEM beam. An image of the whole sample is reconstructed from this undersampled image by inpainting the missing pixels, using prior knowledge about the beam scan coils, sample, and detectors. The fraction of sample pixels illuminated can be as low as 6.25% of the overall pixels. In combination with adaptive re-illumination techniques,

where the pixels are re-illuminated based on the results of previous illuminations, lattice-resolved images have been obtained at doses less than 100 electrons per square nanometer [40, 79].

Adaptive illumination schemes that use information about the scan coils and detectors have not been implemented as widely in SEM as in STEM. Work in this field has focused more on computational methods of reconstructing whole images from sparse sampled datasets using inpainting and denosing algorithms [80]. In other work, an algorithm where a low beam current, fast pixel dwell time image of the sample was used to identify regions of interest within the sample which were then re-sampled at higher pixel dwell times was implemented and resulted in 3 times higher SNR than conventional SEM images at the same incident dose [41].

1.3 Requirements for implementation of adaptive illumination and quantum imaging in electron microscopy

In the previous section, we described quantum imaging and adaptive illumination protocols that are being implemented in electron microscopy to reduce the incident electron dose on a sample. With the implementation of electron interferometry in TEM/STEM, an analysis of the advantages offered by these schemes in TEMs is required. Further, adaptive illumination techniques have been much more widely implemented in high-energy STEM than lower-energy SEM. One of the main reasons for this disparity is the availability of electron counting detectors in STEM. As we had discussed in Section 1.1.1, single-electron-sensitive pixel array detectors with frame rates above 400 frames per second and dynamic ranges up to $10^6 : 1$ are used in cryo-EM, adaptive illumination and phase-retrieval STEM imaging [7, 17, 40, 81]. Further, software-based electron counting using the conventional ADF detectors on the STEM has also been used to implement low-dose imaging [82–84]. Electron

counting detectors will also play an important role in the implementation of quantum mechanical schemes such as QEM and multipass TEM. However, the capability of counting electrons has not been readily available at voltages below 20 keV for SEM imaging, particularly for counting SEs. Although SE counting has been used in the past to characterize SEM detectors and perform imaging, this lack of widespread availability of electron counting on SEMs has been the reason for greater emphasis on the use of computational techniques for implementing low-dose imaging. In this section, we will review the history of SE counting and discuss requirements for the implementation of adaptive illumination schemes at lower incident electron beam voltages in SEM. We will also discuss requirements for the combination of adaptive illumination and quantum imaging techniques achievable with current technology in STEM.

1.3.1 History of electron counting in SEM

SE counting on SEMs has been used as a means of characterizing both SE emission from materials and detectors for SEs since the early days of SEM. A central question of interest to investigators since the late 1930's has been the nature of noise in SE emission and the deviations of this emission from an ideal Poisson distribution. Experimental work by Kurrelmeyer and Hayner [85], and later theoretical analysis by Everhart and co-workers [86], revealed significant deviations from Poisson statistics in the SE emission. Later experimental and theoretical work by Oatley [28, 87], Baumann and Reimer [88, 89], and more recently Novák [29], Frank [21], and Sakakibara [90] further characterized these deviations and established that they arise because the emission of SEs is the result of two successive processes with a Poisson probability distribution: first, the generation of the incident beam at the electron gun, and second, the emission of SEs by each incident-beam electron. The resulting distribution from two coupled Poisson distributions is not a Poisson distribution since its variance is higher than its mean. However, if the SE yield δ is low (< 0.4 or so), the probability of one incident electron resulting in the emission of more than one

SE is also low. In this case, the emission of SEs for each incident electron can be approximated as a Bernoulli process with a probability of success equal to the SE yield δ , and the overall emission statistics of SEs will be approximately Poisson [21]. The assumption of low δ is true at high incident beam energies (for example, the SE yield of aluminum at 10 keV incident beam energy is ~ 0.2 [20,21]). Hence, deviations from Poisson statistics in the SE emission are small at these energies. However, at lower incident beam energies δ is higher (for aluminum, $\delta = 1$ at 300 eV) which explains the larger deviations seen in the earlier lower-energy observations of Kurrelmeyer and Hayner [85] and Everhart [86].

The development and characterization of scintillator-photomultiplier based electron detectors, particularly the Everhart-Thornley detector [25], was another motivation to study SE emission and statistics through counting. Early work by Pawley [91], Comins [92], and Oatley [28, 87] measured the noise in such detectors and established the Detection Quantum Efficiency (DQE) as a measure of the efficiency of various scintillator materials and detector geometries. In his analysis of the noise in scintillator-based detectors, Oatley used electron count measurements to evaluate the number of photoelectrons generated at the photomultiplier cathode per SE incident on the scintillator and concluded that a large fraction (up to 85%) of the incoming SEs produced at least one photoelectron and are consequently detected [28,87]. Therefore, we can conclude that the contribution of missed detections and dark counts to noise in these detectors should be quite low, and the non-unity DQE of these detectors is primarily due to geometrical constraints. Later work by Novák [29] can also be used to reach the same conclusion.

Measurement of the DQE of SE detectors has also been a focus of work by Joy and co-workers [26,27]. Joy used SEM image histograms of uniform samples to find the DQE of different types of SE detectors. We will detail Joy's technique for measuring DQE in Chapter 4 Section 4.1.1.2 and use it to benchmark our results for SE detector DQE in Section 4.1.3.2 of the same chapter. Joy also observed hints of SE quantization in the image histograms at very low beam currents, but did not use

the quantized peaks in his analysis. Joy, as well as Griffin [22], also reached the same conclusion about the non-ideal DQE arising from the geometrical placement of the SE detector as we discussed in the last paragraph.

The use of electron counting for improving imaging in SEM was pioneered by the work of Yamada and co-workers [93–97]. In their work, they coupled the signal from the SE detector to a discriminator-pulse counter circuit to count the number of SE for every scan position on the object and generate an image. The collection and readout of pulses for each pixel was synchronized with the SEM scan. The discriminator filtered out background low-voltage thermal noise pulses generated in the SE detector (the discrimination voltage was set by a preliminary statistical analysis of the voltage level of the output pulses), and the counter shaped and registered the filtered pulses. This circuit was used to generate SE count images of different types of organic and inorganic samples. The authors also extracted the SNR for a chosen point in the scan area using multiple SE count images and showed that it was up to 4.4 times higher than the SNR for imaging with the advantage being larger at lower incident beam currents. They used very long pixel dwell times (typically 41 μ s) and relied on low beam currents (down to 0.1 pA) to achieve the required low number of incident-beam electrons. They also reported some evidence of deviations from Poisson statistics in the distribution of the SEs.

1.3.2 Challenges and requirements

Having discussed the current state of quantum imaging and adaptive illumination in STEM and SEM imaging, we will discuss challenges and opportunities in these fields in this section. We will first focus on STEM, where, as we had discussed in Section 1.1.1, electron counting detectors have been enabling the implementation of dose-efficient structured and adaptive illumination schemes as well as quantum imaging protocols. Next, we will discuss SEM, where SE count imaging is not widely available which limits the application of advanced imaging techniques.

As we discussed in Section 1.2.1, quantum imaging schemes are starting to be implemented in STEM. Therefore, an analysis of the performance of schemes such as IFM in a Mach–Zehnder interferometer is required to establish their advantages compared to conventional imaging. Although such analyses exist for advanced schemes such as QEM [2, 54] and multipass microscopy [3, 72], they are needed for the lower-efficiency schemes that can be realized with current technology on STEM systems. Due to the underlying probabilistic nature of quantum imaging protocols, adapting the illumination at each pixel to prior statistics could be a way to further maximize the benefits of quantum protocols. Therefore, an analysis of how well quantum imaging schemes can perform when combined with adaptive illumination would also be of interest.

For SEM imaging, the development of protocols for SE count imaging would allow the adoption of structured illumination and quantum imaging schemes to lower voltages and extend the already existing adaptive illumination schemes discussed in Section 1.2.2. Although SE count imaging was implemented by Yamada and co-workers, a simpler scheme that does not require external circuits and nanosecond synchronization would enable more widespread adoption of SE count imaging. As we had discussed in Section 1.1.3, current conventional SE imaging uses analog signal averaging to create images due to the high rate of SEs incident on the detector. Therefore, any implementation of SE counting would need to use much lower beam currents than conventional imaging. For example, a beam current of 1 pA and $\delta = 0.2$ would result in ~ 1 SE per μs , which should be countable on SE detectors with scintillator decay times on the order of 100 ns. However, such low currents would result in noisy images due to the inherent shot noise in both the incident beam and SE emission. To improve the image quality, a protocol for SE counting over multiple imaging frames and longer dwell times would be needed. Such an SE count scheme would also mitigate noise due to SE detector background and dark counts, which can be significant at low beam currents.

1.4 Work in this thesis

This thesis addresses the challenges and requirements discussed in the previous section for STEM and SEM imaging. The thesis is divided into six chapters. Following this introductory chapter, in Chapter 2 we will theoretically analyze the advantages of IFM-based quantum imaging over conventional STEM imaging. We will also present a scheme to adaptively illuminate each pixel based on the statistics from previous illuminations and calculate the reduction in incident electron dose and sample damage enabled by this scheme. In chapters 3, 4 and 5, we will turn our attention to SE counting in SEM. In preparation for our implementation of SE count imaging, in Chapter 3 we will analyze image quality metrics for characterizing and comparing grayscale images and schemes for extending adaptive re-illumination to SEM imaging. In Chapter 4, we will present two methods of counting SEs in an SEM: image histograms and oscilloscope outcoupling. We will present evidence of SE counting for both methods and compare their ease of implementation and versatility. We will use the two schemes to characterize the detection quantum efficiency (DQE) of both the in-chamber and in-lens SE detectors and map its variation with the working distance. In Chapter 5, we will use the oscilloscope outcoupling scheme to implement offline SE count imaging. We will describe our code for taking the oscilloscope outcoupling datasets for several frames and counting SEs from every pixel for each frame. We will also implement the offline conditional re-illumination schemes developed in Chapter 3 and demonstrate reduction in the incident electron dose using the image quality metrics from Chapter 3. In the concluding Chapter 6, we will discuss extensions of the work presented in this thesis, including recent schemes for phase contrast IFM and SE counting in helium ion microscopy. Appendices A through D will present data, methods, and code that supplement the discussion in the main thesis chapters.

Finally, teaching has been an important aspect of my PhD and has brought me just as much joy and opportunities for self-reflection and improvement as my research. Appendix E is the final paper for a teaching class I took at the Harvard Graduate

School of Education (T.440: Teaching and Learning: The Having of Wonderful Ideas).
In this essay I describe my journey to understanding the importance of complexity,
confusion, trust, and emotion in the process of teaching and learning.

Chapter 2

Reduced-dose electron microscopy through conditional sample re-illumination

In Chapter 1 we introduced quantum electron microscopy schemes and adaptive illumination schemes as a means of reducing the incident electron dose on the sample and mitigate sample damage during imaging. As we had discussed in that chapter, recent progress in nanofabrication has enabled the implementation of Mach-Zehnder interferometry in a standard TEM/STEM and SEM [62, 64, 65, 68]. Therefore, a comparison of the performance of a Mach-Zehnder-based IFM setup with that of conventional STEM imaging is important since such a setup can be implemented in a TEM with current technology. In this chapter we will combine IFM-based imaging with a sample illumination scheme that uses Bayesian inference to take the counts at the imaging detectors from each round of illumination into account, to further reduce the sample damage for the same probability of imaging error [51, 57]. This *conditional re-illumination* scheme ties in with previous research in imaging and image processing schemes that take advantage of prior information about the source, the object, the imaging apparatus, as well as information gained during the experiment, to adap-

tively illuminate the sample and use maximum-likelihood reconstruction to improve the image signal-to-noise ratio at low incident electron doses [40,41,61,79,80,98–103]. We will calculate the damage suffered by the sample and the errors in the image generated in conventional STEM (or classical) imaging as well as IFM imaging for opaque-and-transparent samples using this conditional re-illumination scheme. Our results indicate that the sample damage is significantly lower for IFM-based imaging, particularly when combined with conditional re-illumination, compared to conventional imaging.

This chapter is divided into three sections. In Section 2.1, we will introduce the various conventional and IFM imaging setups considered in this chapter and derive expressions for the sample damage and errors made while imaging opaque-and-transparent samples with these schemes. Next, in Section 2.2 we will introduce the conditional re-illumination and calculate error and damage for the conventional and IFM imaging schemes with conditional re-illumination. Finally, in Section 2.3 we will summarize the results of this chapter and discuss methods of implementing the conditional re-illumination scheme developed in this chapter. In Section D.1 of Appendix D we list the MATLAB scripts used to perform the simulations in this chapter. Our work in the remaining chapters of this thesis is motivated by the need to overcome challenges of low-dose imaging and fast beam blanking required for the implementation of conditional re-illumination in SEM.

The text and figures from this chapter are reproduced from [104]. The theory and simulations in this chapter were performed in collaboration with Yuri van Staaden (Delft University of Technology), Prof. Vivek Goyal (Boston University) and Prof. Karl K. Berggren.

2.1 Error and damage in STEM and IFM imaging

In order to compare STEM and IFM imaging, we need to develop metrics for calculating imaging error and sample damage. In this section, we will describe our calculation of error and damage in conventional STEM and IFM imaging. In Section 2.1.1, we will introduce the STEM and IFM imaging schemes considered in this paper as well as the terminology used in the results we have derived. To motivate the need for conditional re-illumination, we will discuss the simplest case of unconditional re-illumination, where each pixel is illuminated by 2 electrons, with and without IFM, in Section 2.1.2. In Section 2.1.3 we will discuss the most general case, where the number of electrons illuminating each pixel is derived from a Poisson distribution.

2.1.1 Apparatus and Terminology

Before analyzing the STEM and IFM schemes with conditional re-illumination, we introduce the setup of these schemes as well as the notation that is used in the rest of this paper. In Figure 2-1, we show the STEM and IFM imaging schemes considered in this paper. In each scheme, the sample is placed in the path of the incident electron beam. Detectors at the outputs count electrons emerging from the imaging scheme. In our analysis, we denoted the detector for electrons transmitted through the sample as D_1 . This detector is analogous to the bright-field detector in conventional microscopes. We denoted the analogous detector to the dark-field detector in conventional microscopes, *i.e.* the detector for electrons scattered from the sample, as D_3 . The electrons that damage the sample lose energy to and scatter off of it. Therefore, we also used the counts at D_3 as a measure of the damage suffered by the sample. IFM imaging requires another detector at the second output port of the beamsplitter; we denoted this detector as D_2 . In our analysis, we considered these detectors to be 100% efficient, with no dark counts. We also assumed that the imaging system had no losses. Since a counting detector for scattered electrons is not always available on typical TEMs/STEMs, we have considered four imaging schemes in total

in this paper. Scheme A, depicted in Figure 2-1(a), is STEM imaging without D_3 . Scheme B, depicted in Figure 2-1(b), is STEM imaging with D_3 . Scheme C, depicted in Figure 2-1(c), is IFM imaging without D_3 . Scheme D, depicted in Figure 2-1(d), is IFM imaging with D_3 . The presence of D_3 in the imaging schemes eliminated errors due to the Poisson nature of the electron beam, resulting in fewer electrons required to achieve a desired error rate.

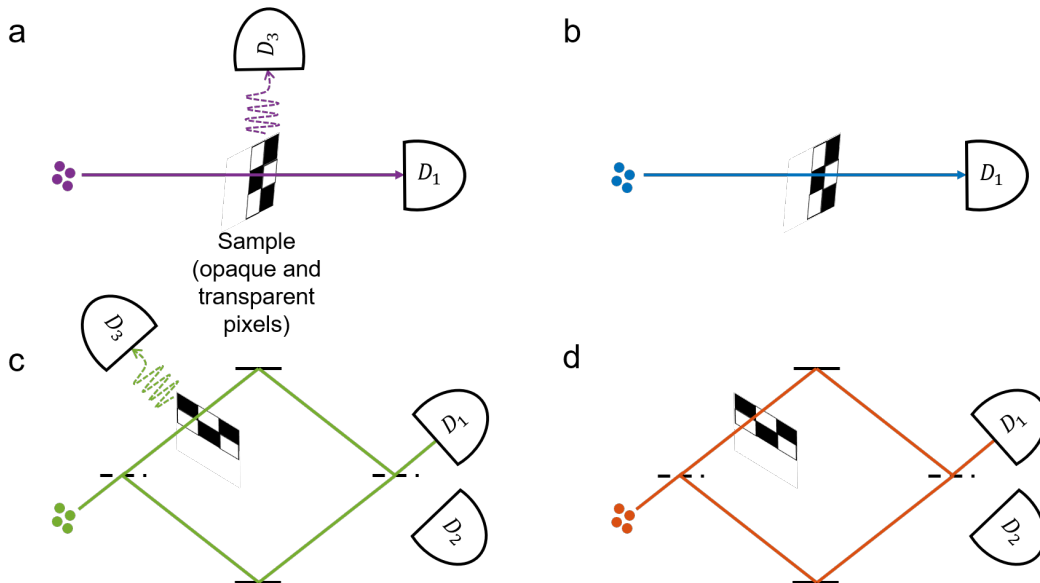


Figure 2-1: Conventional and IFM imaging schemes. (a) Classical imaging without an additional scattering detector D_3 . D_1 registers a count when the object is transparent to electrons. (b) Classical imaging with D_3 . D_3 registers a count every time an electron scatters off the object. (c) IFM without D_3 . D_1 registers a count every time when the object is transparent and with probability $\frac{1}{4}$ when the object is opaque. D_2 does not register a count when the object is transparent, and registers a count $\frac{1}{4}$ th of the times the object is opaque. (d) IFM with D_3 : D_3 registers a count with probability $\frac{1}{2}$ when the object is opaque, and does not register a count when the object is transparent.

As we had mentioned before, we considered only opaque-and-transparent samples in our analysis. Pixels are imaged independently, so we considered any one arbitrary pixel. We use a random variable X to represent the opacity of the sample: $X = 1$ denotes an opaque pixel, and $X = 0$ denotes a transparent pixel. We denote the prior probability of an opaque pixel with q . The number of electrons in the incident beam is denoted by N . In calculations that include the Poisson nature of the electron beam, N becomes a Poisson random variable with mean λt , where λ denotes

X	a pixel's true opacity: 0 when transparent, 1 when opaque
\hat{X}	our inference for the pixel's opacity: 0 when transparent, 1 when opaque
q	prior probability of opaque pixel
λt	mean number of electrons in Poisson beam
N	actual number of electrons in the beam
D_i	imaging detectors; $i = 1, 2, 3$
n_i	electron counts at detector D_i
P_{err}	total probability of misidentifying a pixel
P_{MD}	probability of inferring an opaque pixel as transparent
P_{FA}	probability of inferring a transparent pixel as opaque
\bar{n}_{damage}	mean number of electrons scattered by opaque pixels

Table 2.1: List of symbols and abbreviations used in this chapter.

the beam current and t the illumination time per pixel. The number of electrons detected at D_1 is denoted by n_1 , at D_2 by n_2 , and at D_3 by n_3 . In our calculations, we inferred whether the pixel being examined was opaque or transparent based on the values of n_1 , n_2 , and n_3 for that pixel. This inference, also 1 or 0, is denoted by another binary-valued random variable, \hat{X} . Our analysis of the different imaging schemes involved evaluation of two quantities for each scheme: the total probability of misidentifying a pixel, P_{err} , and the average number of electrons scattered by an opaque pixel, \bar{n}_{damage} . We split P_{err} into two components: P_{MD} , the probability of missed detections (opaque pixels inferred as transparent), and P_{FA} , the probability of false alarms (transparent pixels inferred as opaque).

Table 2.1 summarizes the abbreviations and symbols used in this chapter.

2.1.2 Analysis of STEM and IFM approaches with single-shot illumination and $N = 2$ electrons

Before we consider Poisson-distributed illumination, we will develop our methodology for calculating P_{err} and \bar{n}_{damage} by considering the case of $N = 2$ for STEM and IFM imaging. The insights from this calculation will inform our consideration of the more general case. In the case of $N = 2$, since N is exactly known, we can make

two simplifying observations. First, the scattering detector D_3 does not provide any additional benefit, since any electron that was not detected by D_1 or D_2 must have been scattered. Hence, we expect the same results from Schemes A and B, and from Schemes C and D. Second, illuminating each pixel with one electron twice is equivalent to illuminating it once with two electrons. Therefore, we will work out the theory for simultaneous illumination with two electrons.

2.1.2.1 STEM imaging

Figure 2-1(a) and (b) show the STEM imaging Schemes A and B. If the pixel is opaque, neither of the 2 incident electrons will be detected at D_1 . If it is transparent, both the electrons will be detected. We summarize these observations in Table 2.2.

X	n_1
0	2
1	0

Table 2.2: Possible outcomes at D_1 of STEM imaging with 2 incident electrons.

Therefore, it is straightforward to design a decision rule for \hat{X} . Two detections at D_1 implies that the pixel was transparent. No detections imply that the pixel was opaque. This decision rule is summarized in Table 2.3.

n_1	\hat{X}
0	1
2	0

Table 2.3: Decision rule for STEM imaging with 2 incident electrons.

Here we will never make any errors, so $P_{\text{err}} = 0$. We can also evaluate $\bar{n}_{\text{damage}} = E[N \mid X = 1] = 2$. Thus, even though we get error-free detection, we also damage the opaque pixels in our sample with both electrons.

2.1.2.2 IFM imaging

Figure 2-1(c) and (d) show the IFM imaging Schemes C and D. When $X = 0$, constructive interference leads to both incident electrons being detected at D_1 . When $X = 1$, a given incident electron is detected at D_1 or D_2 with probability $\frac{1}{4}$ each and scattered off the pixel with probability $\frac{1}{2}$. Since the detection is probabilistic, we cannot be sure of how many electrons will be detected at either detector. Hence, we summarize the probabilities of detection of each incident electron at D_1 and D_2 in Table 2.4.

X	D_1	D_2
0	1	0
1	$\frac{1}{4}$	$\frac{1}{4}$

Table 2.4: Probabilities at D_1 and D_2 for IFM imaging.

Any D_2 counts tell us that the pixel was opaque, and hence we set $\hat{X} = 1$. Similarly, if there were no counts at both detectors, or only one count at either detector, one or both of the electrons must have been scattered by the pixel. Therefore, $\hat{X} = 1$ again. However, an ambiguity arises when $n_1 = 2$ and $n_2 = 0$, since this outcome is possible with both $X = 0$ and $X = 1$. We denote the probability that the pixel was transparent, given that $n_1 = 2$ and $n_2 = 0$, by $P(X = 0 | n_1 = 2, n_2 = 0)$, which we can evaluate using Bayes' rule, as follows:

$$P(X = 0 | n_1 = 2, n_2 = 0) \tag{2.1}$$

$$\begin{aligned}
 &= \frac{P(n_1 = 2, n_2 = 0 | X = 0)P(X = 0)}{P(n_1 = 2, n_2 = 0 | X = 0)P(X = 0) + P(n_1 = 2, n_2 = 0 | X = 1)P(X = 1)} \\
 &= \frac{1 - q}{(1 - q) + (1/16)q} = \frac{1}{1 + q/(16(1 - q))}. \tag{2.2}
 \end{aligned}$$

If $P(X = 0 | n_1 = 2, n_2 = 0) > P(X = 1 | n_1 = 2, n_2 = 0)$, the decision $\hat{X} = 0$ has a higher chance of being correct. Using the expression for $P(X = 0 | n_1 = 2, n_2 = 0)$ in Equation (2.2), we get the final decision rule given in Table 2.5.

n_1	n_2	\hat{X}
0	0	1
0	1	1
0	2	1
1	0	1
1	1	1
2	0	0, $q \leq 16/17$ 1, $q > 16/17$

Table 2.5: Decision rule for IFM imaging with 2 incident electrons.

The decision rule for $n_1 = 2$ and $n_2 = 0$ implies that unless the prior probability of the pixel being opaque is large ($q > 16/17$), the decision $\hat{X} = 0$ has a higher probability of being correct with two detections at D_1 . Physically, the reason that the decision $\hat{X} = 0$ produces fewer errors is that the outcomes $n_1 = 2$ and $n_2 = 0$ occur with certainty for a transparent pixel, but with a probability of $1/16$ for an opaque pixel. This intuition holds unless we were already very sure of the pixel being opaque ($q > 16/17$) prior to the experiment. Although the event $n_1 = 2$ and $n_2 = 0$ reduced our confidence that the pixel was opaque, $\hat{X} = 1$ still had the greater probability of being correct.

We can now evaluate P_{MD} and P_{FA} :

$$\begin{aligned}
P_{\text{MD}} &= P(\hat{X} = 0 \mid X = 1) \\
&= \begin{cases} P(n_1 = 2, n_2 = 0) = 1/16, & \text{for } q \leq 16/17; \\ 0, & \text{otherwise,} \end{cases} \\
P_{\text{FA}} &= P(\hat{X} = 1 \mid X = 0) \\
&= \begin{cases} 0, & \text{for } q \leq 16/17; \\ 1, & \text{otherwise.} \end{cases}
\end{aligned}$$

The total error probability is given by $P_{\text{err}} = qP_{\text{MD}} + (1 - q)P_{\text{FA}}$. Hence,

$$P_{\text{err}} = \begin{cases} q/16, & \text{for } q \leq 16/17; \\ 1 - q, & \text{otherwise.} \end{cases}$$

This result implies that for most values of q , up to $q = 16/17$, the error probability increases linearly but remains small ($P_{\text{err}} \leq 1/17$). The only kind of error we can make in this regime is a missed detection, which happens when $n_1 = 2$ and $n_2 = 0$ for an opaque pixel. This kind of error becomes more probable as q increases, since the number of opaque pixels in the sample increases. Beyond $q = 16/17$, we can only have false alarms, since now we switch to guessing that the pixel is opaque for the case when $n_1 = 2$ and $n_2 = 0$. However, since most of the pixels are opaque anyway, the total probability of error reduces.

We can evaluate $\bar{n}_{\text{damage}} = E[N | X = 1] = 1$, since the probability of scattering for each incident electron is $\frac{1}{2}$. Thus, the IFM imaging Schemes C and D provide lower \bar{n}_{damage} than the STEM imaging Schemes A and B, at the cost of non-zero P_{err} .

This example illustrates the fundamental trade-off that appears in all of our results: accepting a small error probability led to reduction in the expected damage on the sample. Further, the introduction of a second electron reduced the error probability, at the cost of increased damage.

2.1.3 Analysis of STEM imaging schemes with single-shot illumination and $N \sim \text{Poisson}(\lambda t)$ electrons

We will now derive analogous results for the more general case of Poisson illumination, where the number of electrons in the beam (N) is not determinate. The probability of having exactly n electrons in the beam is given by:

$$P(N = n) = e^{-\lambda t} \frac{(\lambda t)^n}{n!}.$$

Here, λt is the mean number of electrons in the beam.

2.1.3.1 Scheme A: STEM imaging without D_3

In the absence of an object, each of the N incident electrons will be detected at D_1 , while in the presence of an object none of them will. These observations are summarized in Table 2.6.

X	n_1
0	N
1	0

Table 2.6: Possible outcomes at D_1 for Scheme A.

Since N is Poisson distributed, we do not know beforehand exactly how many electrons were in the beam. For any $n_1 \geq 1$, the inference $\hat{X} = 0$ (*i.e.* the pixel is transparent) would always be correct. However, ambiguity arises when $n_1 = 0$. The lack of detections at D_1 could be because of an opaque pixel ($X = 1$), or it could be because the beam did not contain any electrons ($N = 0$).

We expect our final decision rule for $n_1 = 0$ to depend on both the prior q and mean number of electrons in the beam λt . For example, if λt was high, the probability of there being no electrons in the beam would be low. Therefore, the lack of detections at D_1 is more likely to have been caused by an opaque pixel, and we would expect $\hat{X} = 1$ to be the inference that leads to fewer errors. The opposite would be true for small λt . Similarly, increasing q would indicate greater confidence that $X = 1$, and we would make that inference for more of the ambiguous cases where $n_1 = 0$. We refer to the conditional probability that $X = 0$, given the value of n_1 , as $\eta_A(n_1, q, \lambda t)$ (anticipating its dependence on q and λt). Then $\eta_A(n_1, q, \lambda t) = 1$ for

$n_1 > 0$. To determine the decision rule for the case when $n_1 = 0$, we calculate

$$\begin{aligned}
\eta_A(0, q, \lambda t) &= P(X = 0 \mid n_1 = 0) \\
&= \frac{P(n_1 = 0 \mid X = 0)P(X = 0)}{P(n_1 = 0 \mid X = 0)P(X = 0) + P(n_1 = 0 \mid X = 1)P(X = 1)} \\
&= \frac{e^{-\lambda t}(1 - q)}{e^{-\lambda t}(1 - q) + q} = \frac{1}{1 + e^{\lambda t}q/(1 - q)}. \tag{2.3}
\end{aligned}$$

This expression for η_A is comparable to the expression for $P(X = 0 \mid n_1 = 2, n_2 = 0)$ in Equation (2.2). Just as in the $N = 2$ case, if $P(X = 0 \mid n_1 = 0) > P(X = 1 \mid n_1 = 0)$, we would want $\hat{X} = 0$, and vice-versa. Therefore, we get as our decision rule (for $n_1 = 0$):

$$\hat{X} = \begin{cases} 1, & \text{for } \eta_A(0, q, \lambda t) < \frac{1}{2}; \\ 0, & \text{otherwise.} \end{cases} \tag{2.4}$$

As we had anticipated, this decision rule depends on both q and λt . This decision rule is summarized in Table 2.7.

n_1	\hat{X}
0	1, $\eta_A(0, q, \lambda t) < \frac{1}{2}$ 0, otherwise
≥ 1	0

Table 2.7: Decision rule for Scheme A.

We plot $\eta_A(0, q, \lambda t)$ as a function of q , for different values of λt between 0 and 5, in Figure 2-2(a). We also depict the decision threshold $\eta_A(0, q, \lambda t) \leq \frac{1}{2}$ by the horizontal dashed line. The probability of the beam having zero electrons is given by $e^{-\lambda t}$. Therefore, for low values of λt the probability of no detections at D_1 ($n_1 = 0$) due to the beam having zero electrons is high. Hence, we gain little information from the illumination experiment, and it makes sense to infer \hat{X} based on q . Therefore, $\eta_A(0, q, \lambda t) = 1 - q$ for $\lambda t = 0$ in Figure 2-2(a). As λt increases, the probability of zero electrons in the beam reduces. Therefore, the probability of $n_1 = 0$ being due to an opaque pixel increases. Hence, we can conclude that $\hat{X} = 1$ over a wider range

of the prior q . As a result, $\eta_A(0, q, \lambda t) < \frac{1}{2}$ over an increasingly wider range of q in Figure 2-2(a) for $\lambda t = 0.5, 2$ and 5 .

We can now look at the probabilities of missed detections and false alarms, P_{MD} and P_{FA} . When the pixel is opaque ($X = 1$), we do not get detections at D_1 ($n_1 = 0$). Hence, we either always make a mistake (when $\eta_A(0, q, \lambda t) \geq \frac{1}{2}$) or never make one (when $\eta_A(0, q, \lambda t) < \frac{1}{2}$). Thus,

$$\begin{aligned} P_{\text{MD}} &= P(\hat{X} = 0 \mid X = 1) \\ &= \begin{cases} 0, & \text{for } \eta_A(0, q, \lambda t) < \frac{1}{2}; \\ 1, & \text{otherwise.} \end{cases} \end{aligned}$$

When the pixel is transparent ($X = 0$), if the beam has electrons ($N > 0$), we never make a mistake. Errors arise only when $N = 0$. In this case, if $\eta_A(0, q, \lambda t) \geq \frac{1}{2}$, $\hat{X} = 0$ and our inference is still correct. If $\eta_A(0, q, \lambda t) < \frac{1}{2}$, $\hat{X} = 1$ and we have a false alarm. Hence,

$$\begin{aligned} P_{\text{FA}} &= P(\hat{X} = 1 \mid X = 0) \\ &= \begin{cases} P(N = 0), & \text{for } \eta_A(0, q, \lambda t) < \frac{1}{2}; \\ 0, & \text{otherwise} \end{cases} \\ &= \begin{cases} e^{-\lambda t}, & \text{for } \eta_A(0, q, \lambda t) < \frac{1}{2}; \\ 0, & \text{otherwise.} \end{cases} \end{aligned}$$

The total error probability P_{err} is given by:

$$P_{\text{err}} = \begin{cases} (1 - q)e^{-\lambda t}, & \text{for } \eta_A(0, q, \lambda t) < \frac{1}{2}; \\ q, & \text{otherwise.} \end{cases}$$

The condition for $\eta_A(0, q, \lambda t)$ can be recast into one for q using Equation (2.3), as follows:

$$\eta_A(0, q, \lambda t) < \frac{1}{2} \Rightarrow e^{\lambda t} \frac{q}{1 - q} > 1 \Rightarrow q > \frac{1}{1 + e^{\lambda t}}.$$

Hence,

$$P_{\text{err}} = \begin{cases} q, & \text{for } q \leq \frac{1}{1+e^{\lambda t}}; \\ (1-q)e^{-\lambda t}, & \text{otherwise.} \end{cases}$$

This expression is similar to the expression for P_{err} in the $N = 2$ case, with the addition of the statistics of the incident beam (through the $e^{-\lambda t}$ term).

We can evaluate $\bar{n}_{\text{damage}} = E[N \mid X = 1] = \lambda t$. Hence, P_{err} can also be expressed as

$$P_{\text{err}} = \begin{cases} q, & \text{for } q \leq \frac{1}{1+e^{\lambda t}}; \\ (1-q)e^{-\bar{n}_{\text{damage}}}, & \text{otherwise.} \end{cases} \quad (2.5)$$

As an example, consider the case of $\lambda t = \frac{1}{2}$ and $q = \frac{1}{2}$. From the equations above, $\frac{1}{1+e^{\lambda t}} = \frac{1}{1+e^{1/2}} \approx 0.378$, and $\bar{n}_{\text{damage}} = \frac{1}{2}$. Since $q > \frac{1}{1+e^{\lambda t}}$, $P_{\text{err}} = \frac{1}{2}e^{-1/2} \approx 0.303$.

2.1.3.2 Scheme B: STEM imaging with D_3

In this scheme, we detect every electron in the beam in one of the two detectors D_1 and D_2 . The possible detection events are summarized in Table 2.8.

X	n_1	n_3
0	N	0
1	0	N

Table 2.8: Possible outcomes at D_1 and D_3 for Scheme B.

Just as for Scheme A, if $n_1 > 0$, we can correctly infer that $\hat{X} = 0$. Similarly, if $n_3 > 0$, we can infer that $\hat{X} = 1$. The only case in which we need to guess is when $n_1 = 0$ and $n_3 = 0$. Due to the presence of D_3 , we can be sure that all electrons in the incident beam were counted. Hence, $n_1 = 0$ and $n_3 = 0$ is only possible if $N = 0$. In this case, we do not gain any information about the sample from our experiment. Therefore, we would assign \hat{X} based on the known prior q , which is unchanged:

$$\eta_B(0, q, \lambda t) = P(X = 0 \mid n_1 = 0, n_3 = 0) = 1 - q. \quad (2.6)$$

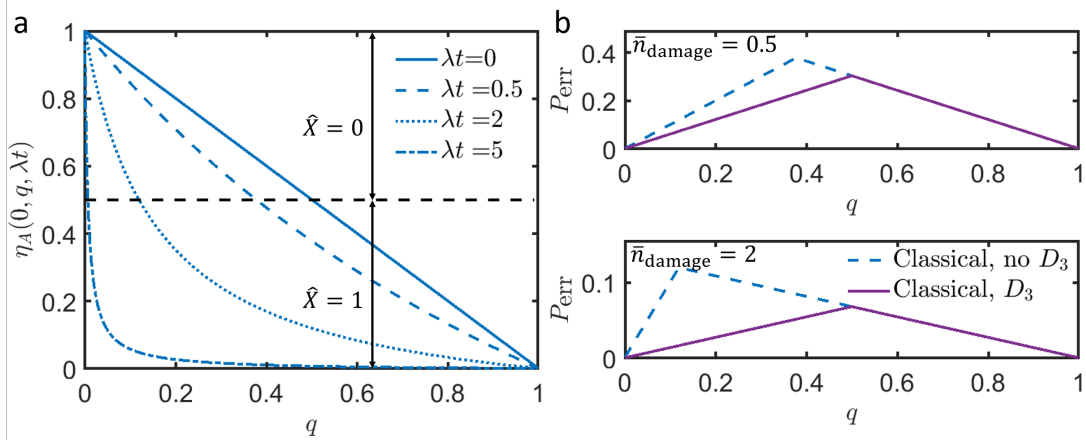


Figure 2-2: Comparing conventional imaging schemes with and without D_3 . (a) $\eta_A(0, q, \lambda t)$, the probability of the pixel being transparent ($X = 0$) given $n_1 = 0$, vs. the known prior q , for λt ranging from 0 (no beam) to 5 electrons in the beam on average. We infer $\hat{X} = 1$ if $\eta_A(0, q, \lambda t) < \frac{1}{2}$ and $\hat{X} = 0$ otherwise. The horizontal black dashed line indicates this threshold for inferring \hat{X} , $\eta_A(0, q, \lambda t) = \frac{1}{2}$. As λt increases, the value of q at which $\eta_A(0, q, \lambda t)$ is less than $\frac{1}{2}$ decreases and P_{err} is minimized by the decision $\hat{X} = 1$ over a wider range of q . (b) Comparing P_{err} vs. q for Schemes A and B, for (a) $\bar{n}_{\text{damage}} = 0.5$, and (b) $\bar{n}_{\text{damage}} = 2$. The presence of D_3 reduces P_{err} for $q < 0.5$. Beyond $q > 0.5$, the two schemes give the same P_{err} .

$\hat{X} = 0$ if $q \leq \frac{1}{2}$ and $\hat{X} = 1$ if $q > \frac{1}{2}$. The final decision rule is summarized in Table 2.9.

n_1	n_3	\hat{X}
0	≥ 1	1
≥ 1	0	0
0	0	0 $q \leq \frac{1}{2}$ 1 $q > \frac{1}{2}$

Table 2.9: Decision rule for Scheme B.

We make errors only for pixels where $n_1 = 0$ and $n_3 = 0$. In this case,

$$\begin{aligned}
 P_{\text{MD}} &= P(\hat{X} = 0 \mid X = 1) = \begin{cases} e^{-\lambda t}, & \text{for } q \leq \frac{1}{2}; \\ 0, & \text{otherwise,} \end{cases} \\
 P_{\text{FA}} &= P(\hat{X} = 1 \mid X = 0) = \begin{cases} 0, & \text{for } q \leq \frac{1}{2}; \\ e^{-\lambda t}, & \text{otherwise.} \end{cases}
 \end{aligned}$$

Here, as in Scheme A, the $e^{-\lambda t}$ term comes from the probability that $N = 0$. Using

these results, we can evaluate P_{err} as follows:

$$P_{\text{err}} = \begin{cases} qe^{-\lambda t}, & \text{for } q \leq \frac{1}{2}; \\ (1 - q)e^{-\lambda t}, & \text{otherwise.} \end{cases} \quad (2.7)$$

Compared to the expression for P_{err} for Scheme A (Equation (2.5)), we see from Equation (2.7) that the error probability in Scheme B is reduced by a factor of $e^{-\lambda t}$ for small values of q . This reduction demonstrates the benefit of the addition of D_3 in Scheme B.

We can rewrite Equation (2.5), for the case $q < \frac{1}{1+e^{-\lambda t}} < \frac{1}{2}$, as

$$\bar{P}_{\text{err}} = q = qe^{-\lambda t} + q(1 - e^{-\lambda t}).$$

The first term in this equation is the same as P_{err} in Equation (2.7) for $q \leq \frac{1}{2}$ and arises when the beam has no electrons and we guess \hat{X} incorrectly. The second term is due to errors made when the beam has electrons, but they are scattered by an opaque pixel. Since $q < \frac{1}{1+e^{-\lambda t}}$, we decide that $\hat{X} = 0$, which is an error. These additional errors in Scheme A are eliminated by having an additional detector for scattered electrons in Scheme B.

Damage is the same as Scheme A: $\bar{n}_{\text{damage}} = \lambda t$. Hence, P_{err} can also be expressed as

$$P_{\text{err}} = \begin{cases} qe^{-\bar{n}_{\text{damage}}}, & \text{for } q \leq \frac{1}{2}; \\ (1 - q)e^{-\bar{n}_{\text{damage}}}, & \text{otherwise.} \end{cases} \quad (2.8)$$

In the example case outlined for Scheme A ($\lambda t = \frac{1}{2}$ and $q = \frac{1}{2}$), $P_{\text{err}} = \frac{1}{2}e^{-1/2} \approx 0.303$. Hence, for this particular case, there is no advantage in using D_3 . This result occurs because $q = \frac{1}{2} > \frac{1}{1+e^{-\lambda t}}$ for any $\lambda t > 0$. As we have seen above, for $q > \frac{1}{1+e^{-\lambda t}}$ the expressions for error probability for the two schemes are identical. Physically, this result makes sense when we consider the scenarios in which an error could be made with $q = \frac{1}{2}$. For Scheme A, when the beam contains no electrons ($N = 0$), we would

get $n_1 = 0$ and hence assign $\hat{X} = 1$ (since $q = \frac{1}{2} > 0.378$). For $q = \frac{1}{2}$, this inference is incorrect half the time. If the beam contains at least one electron and we get $n_1 = 0$, we would again assign $\hat{X} = 1$. This would always be correct, since $n_1 = 0$ with $N \neq 0$ is only possible when $X = 1$. For Scheme B, with $n_1 = 0$ and $n_3 = 0$, we would assign $\hat{X} = 0$, in accordance with the decision rule above (alternatively, we could guess \hat{X} at random since $q = \frac{1}{2}$). Both these decision rules would also be incorrect half the time. When $N \neq 0$, we would get counts at either D_1 or D_3 . Hence, we would again never make an error for any q . Therefore, in both schemes, with $q \geq \frac{1}{2}$, the only case in which we make errors is when $N = 0$. Hence, P_{err} is equal for both schemes for $q = \frac{1}{2}$.

In Figure 2-2(b), we compare P_{err} for Scheme B (solid purple curve) and Scheme A (dashed blue curve), as a function of q . The top plot in Figure 2-2(b) is for $\bar{n}_{\text{damage}} = 0.5$, and the bottom plot is for $\bar{n}_{\text{damage}} = 2$. The addition of D_3 lowers P_{err} for Scheme B compared to Scheme A, for $q < \frac{1}{2}$. For $q \geq \frac{1}{2}$, D_3 offers no advantage, as explained previously.

Scheme C: IFM imaging without D_3

For this scheme, due to the possibility of detections at D_1 (*i.e.* $n_1 > 0$) with both opaque and transparent pixels, there exists a threshold for the number of detections at D_1 below which the decision that the pixel was opaque ($\hat{X} = 1$) is a better choice and vice-versa. We have summarized the detection probabilities at D_1 and D_2 for Scheme C in Table 2.4. In the most general case, we will have to infer \hat{X} with $n_1 \geq 0$ and $n_2 \geq 0$ such that $n_1 + n_2 \leq N$. If $n_2 > 0$, regardless of n_1 , we can decide that $\hat{X} = 1$, and we would never make an error since this event is impossible if $X = 0$. The event $n_2 = 0$ is possible in two cases: when $X = 0$, or when $X = 1$ but no electrons reach D_2 . In the first case, all incident electrons will be detected at D_1 with probability 1, while in the second case this probability is $\frac{1}{4}$ for each electron. Hence, we would expect fewer counts at D_1 for $X = 1$ compared to $X = 0$. Therefore, there

should exist a threshold count at D_1 below which $\hat{X} = 1$ is a better decision and above which $\hat{X} = 0$ is better. We denote this threshold by k^* . This decision rule is summarized in Table 2.10.

n_1	n_2	\hat{X}
any	≥ 1	1
$< k^*$	0	1
$\geq k^*$	0	0

Table 2.10: Decision rule for IFM imaging with Poisson number of incident electrons.

To find k^* , we first look at the conditional probability $\eta_C(n_1, q, \lambda t)$ that $X = 0$ given the specified value of n_1 and $n_2 = 0$, similar to the analysis for Scheme A.

$$\begin{aligned}
\eta_C(n_1, q, \lambda t) &= P(X = 0 \mid n_1, n_2 = 0) \\
&= \frac{P(n_1, n_2 = 0 \mid X = 0)P(X = 0)}{P(n_1, n_2 = 0 \mid X = 0)P(X = 0) + P(n_1, n_2 = 0 \mid X = 1)P(X = 1)} \\
&= \frac{(e^{-\lambda t}(\lambda t)^{n_1}/n_1!)(1 - q)}{(e^{-\lambda t}(\lambda t)^{n_1}/n_1!)(1 - q) + (e^{-\lambda t/4}(\lambda t/4)^{n_1}/n_1!)e^{-\lambda t/4}q} \\
&= \frac{1}{1 + (e^{\lambda t/2}/4^{n_1})(q/1 - q)}. \tag{2.9}
\end{aligned}$$

Here, the third equality results from the fact that the counts at D_1 and D_2 are independent Poisson processes. When $X = 0$, the mean of the Poisson process at D_1 is λt , while $n_2 = 0$ is a probability 1 event. When $X = 1$, the means of the Poisson processes at both D_1 and D_2 are $\lambda t/4$.

The decision rule for \hat{X} is the same as that in Equation (2.4). We can also use the expression for $\eta_C(n_1, q, \lambda t)$ to find k^* . From Equation 2.9, we get

$$\eta_C(n_1, q, \lambda t) \geq \frac{1}{2} \Rightarrow \frac{e^{\lambda t/2}}{4^{n_1}} \frac{q}{1 - q} \leq 1.$$

Solving $(e^{\lambda t/2}/4^{n_1})(q/1-q) = 1$ for $n_1 = k^*$, we get

$$k^* = \frac{\lambda t}{2} \log_4 e + \log_4 \left(\frac{q}{1-q} \right). \quad (2.10)$$

We can now work out the error probabilities:

$$\begin{aligned} P_{\text{MD}} &= P(\hat{X} = 0 \mid X = 1) \\ &= P(n_1 \geq k^*, n_2 = 0 \mid X = 1) \\ &= P(n_1 \geq k^* \mid X = 1)P(n_2 = 0 \mid X = 1) \\ &= \left(\sum_{k \geq k^*} e^{-\lambda t/4} \frac{(\lambda t/4)^k}{k!} \right) e^{-\lambda t/4}, \\ P_{\text{FA}} &= P(\hat{X} = 1 \mid X = 0) \\ &= P(n_1 < k^*, n_2 = 0 \mid X = 0) \\ &= P(n_1 < k^* \mid X = 0)P(n_2 = 0 \mid X = 0) \\ &= \sum_{k < k^*} e^{-\lambda t} \frac{(\lambda t)^k}{k!}. \end{aligned}$$

Combining these gives the total error probability, P_{err} :

$$\begin{aligned} P_{\text{err}} &= q \left(\sum_{k \geq k^*} e^{-\lambda t/4} \frac{(\lambda t/4)^k}{k!} \right) e^{-\lambda t/4} \\ &\quad + (1-q) \left(\sum_{k < k^*} e^{-\lambda t} \frac{(\lambda t)^k}{k!} \right). \end{aligned}$$

In these equations, k is a non-negative integer that represents the possible values of n_1 .

Since on average only half of the incident electrons scatter off the sample,

$\bar{n}_{\text{damage}} = \lambda t/2$. Hence,

$$\begin{aligned}
P_{\text{err}} &= q \left(\sum_{n > k^*} e^{-\bar{n}_{\text{damage}}/2} \frac{(\bar{n}_{\text{damage}}/2)^k}{k!} \right) e^{-\bar{n}_{\text{damage}}/2} \\
&+ (1 - q) \left(\sum_{k < k^*} e^{-2\bar{n}_{\text{damage}}} \frac{(2\bar{n}_{\text{damage}})^k}{k!} \right) \\
&= q e^{-\bar{n}_{\text{damage}}} \left(\sum_{k > k^*} \frac{(\bar{n}_{\text{damage}}/2)^k}{k!} \right) \\
&+ (1 - q) e^{-2\bar{n}_{\text{damage}}} \left(\sum_{k < k^*} \frac{(2\bar{n}_{\text{damage}})^k}{k!} \right). \tag{2.11}
\end{aligned}$$

The first term in Equation (2.11) decays as $e^{-\bar{n}_{\text{damage}}}$, which is the same decay as Equations (2.5) for Scheme A and (2.8) for Scheme B. The second term decays as $e^{-2\bar{n}_{\text{damage}}}$, which is faster than the decay for the STEM Schemes A and B. Therefore, we expect this factor to lower P_{err} for IFM below that for Schemes A and B.

As an example, consider the case of $\lambda t = 1$ and $q = \frac{1}{2}$. We take $\lambda t = 1$ instead of $\frac{1}{2}$ (as in the examples for Schemes A and B) to keep $\bar{n}_{\text{damage}} = \frac{1}{2}$. From Equation (2.10), $k^* = \frac{1}{2} \log_4 e \simeq 0.36$. Since k in Equation (2.11) can only take non-negative integer values, the first term in the equation will have all values of k greater than 1, and the second will have just a single term, $k = 0$. Hence, we get

$$\begin{aligned}
P_{\text{err}} &= \frac{1}{2} \left(\sum_{n \geq 1} e^{-1/4} \frac{\left(\frac{1}{4}\right)^n}{n!} \right) e^{-1/4} \\
&+ \frac{1}{2} e^{-1} = \frac{1}{2} (1 - e^{-1/4}) e^{-1/4} + \frac{1}{2} e^{-1} \approx 0.27.
\end{aligned}$$

Note that P_{err} here is lower than that for the STEM imaging Schemes A and B (for which $P_{\text{err}} = 0.303$), for the same $\bar{n}_{\text{damage}} = \frac{1}{2}$. This lower damage illustrates the advantage offered by IFM imaging.

Scheme D: IFM imaging with D_3

Here, we add D_3 to count scattered electrons, just as in Scheme B. The detection probabilities are summarized in Table 2.11.

X	D_1	D_2	D_3
0	1	0	0
1	$\frac{1}{4}$	$\frac{1}{4}$	$\frac{1}{2}$

Table 2.11: Detection probabilities at D_1 , D_2 and D_3 for Scheme D.

If we observe counts at D_2 or D_3 , *i.e.* either $n_2 \geq 1$ or $n_3 \geq 1$ (or both), we decide that $\hat{X} = 1$, regardless of the counts on D_1 , and we would never make an error. Ambiguity only arises if $n_2 = 0$ and $n_3 = 0$. As in Scheme C, there should exist a threshold count k^* at D_1 below which $\hat{X} = 1$ is a better decision and above which $\hat{X} = 0$ is better. Table 2.12 summarizes this decision rule.

n_1	n_2	n_3	\hat{X}
any	any	≥ 1	1
any	≥ 1	any	1
$< k^*$	0	0	1
$\geq k^*$	0	0	0

Table 2.12: Decision rule for Scheme D.

Using the same approach for finding k^* as before, we begin with

$$\begin{aligned}
\eta_D(n_1, q, \lambda t) &= P(X = 0 \mid n_1, n_2 = 0, n_3 = 0) \\
&= \frac{P(n_1, n_2 = 0, n_3 = 0 \mid X = 0)P(X = 0)}{P(n_1, n_2 = 0, n_3 = 0 \mid X = 0)P(X = 0) + P(n_1, n_2 = 0, n_3 = 0 \mid X = 1)P(X = 1)} \\
&= \frac{(e^{-\lambda t}(\lambda t)^{n_1}/n_1!)(1 - q)}{(e^{-\lambda t}(\lambda t)^{n_1}/n_1!)(1 - q) + (e^{-\lambda t/4}(\lambda t/4)^{n_1}/n_1!)e^{-\lambda t/4}e^{-\lambda t/2}q} \\
&= \frac{1}{1 + (1/4^{n_1})(q/1 - q)}. \tag{2.12}
\end{aligned}$$

Again, the second equality results from the fact that the counts at each of the three detectors are independent Poisson processes (with means $\lambda t/4$ at D_1 and D_2 , and $\lambda t/2$ at D_3 , when $X = 1$). We can solve for $\eta_D(n_1, q, \lambda t) = \frac{1}{2}$ to obtain the value of k^* :

$$k^* = \log_4 \left(\frac{q}{1 - q} \right). \tag{2.13}$$

This expression is the same as the second term in Equation (2.10) for Scheme C. Here, we see that k^* does not depend on the mean number of incident electrons. This is because by adding D_3 , we have eliminated uncertainty from the Poisson statistics of the beam, since each input electron is detected. The only case in which the beam statistics matter is when there are no electrons in the beam ($N = 0$).

In Figure 2-3(a), we plot $\eta_A(n_1, q, \lambda t)$, $\eta_C(n_1, q, \lambda t)$ and $\eta_D(n_1, q, \lambda t)$ as functions of the prior q . The curves are plotted at $\lambda t = 2$, for $n_1 = 0$ (Figure 2-3(a)) and $n_1 = 2$ (Figure 2-3(b)). When $n_1 = 0$, for Scheme D, we gain no new information in the experiment. Hence $\eta_D(n_1, q, \lambda t) = 1 - q$. For Scheme C, the possibility that $n_1 = 0$ due to $X = 1$ is not ruled out. Therefore, the range of q over which inferring $\hat{X} = 1$ gives fewer errors is larger than that for Scheme D. In Schemes C and D, on average half the incident electrons interact with the sample, while in Scheme A all of them do. Therefore, if we observe $n_1 = 0$ with Scheme A, inferring $\hat{X} = 1$ leads to fewer errors over a wider range of q than with Schemes C and D. When $n_1 = 2$, the value of $\eta_A(n_1, q, \lambda t)$ remains the same in Scheme A since $\eta_A(n_1, q, \lambda t)$ is the same for

all $n_1 > 0$. However, for both Schemes C and D, we can be much more certain that the pixel is transparent for $n_1 = 2$ than for $n_1 = 0$. Therefore, the range of q over which we infer $\hat{X} = 0$ increases.

We can compute the error probabilities for Scheme D in the same way as for Scheme C:

$$\begin{aligned}
P_{\text{MD}} &= P(\hat{X} = 0 \mid X = 1) \\
&= P(n_1 \geq k^*, n_2 = 0, n_3 = 0 \mid X = 1) \\
&= P(n_1 \geq k^* \mid X = 1)P(n_2 = 0 \mid X = 1) \\
&\quad P(n_3 = 0 \mid X = 1) \\
&= \left(\sum_{k \geq k^*} e^{-\lambda t/4} \frac{(\lambda t/4)^k}{k!} \right) e^{-\lambda t/4} e^{-\lambda t/2}, \\
P_{\text{FA}} &= P(\hat{X} = 1 \mid X = 0) \\
&= P(n_1 < k^*, n_2 = 0, n_3 = 0 \mid X = 0) \\
&= P(n_1 < k^* \mid X = 0)P(n_2 = 0 \mid X = 0) \\
&\quad P(n_3 = 0 \mid X = 0) \\
&= \sum_{k < k^*} e^{-\lambda t} \frac{(\lambda t)^k}{k!}, \\
P_{\text{err}} &= q \left(\sum_{k \geq k^*} e^{-\lambda t/4} \frac{(\lambda t/4)^k}{k!} \right) e^{-3\lambda t/4} \\
&\quad + (1 - q) \left(\sum_{k < k^*} e^{-\lambda t} \frac{(\lambda t)^k}{k!} \right).
\end{aligned}$$

We note that the false alarm probability P_{FA} is the same as for Scheme C, since $P(n_3 = 0 \mid X = 0) = 1$. However, the missed detection probability P_{MD} is reduced by a factor of $e^{-\lambda t/2}$ due to the presence of D_3 . Intuitively, some of the pixels for which we incorrectly inferred $\hat{X} = 0$ without D_3 are now correctly assigned as opaque due to detections at D_3 , lowering the rate of missed detections.

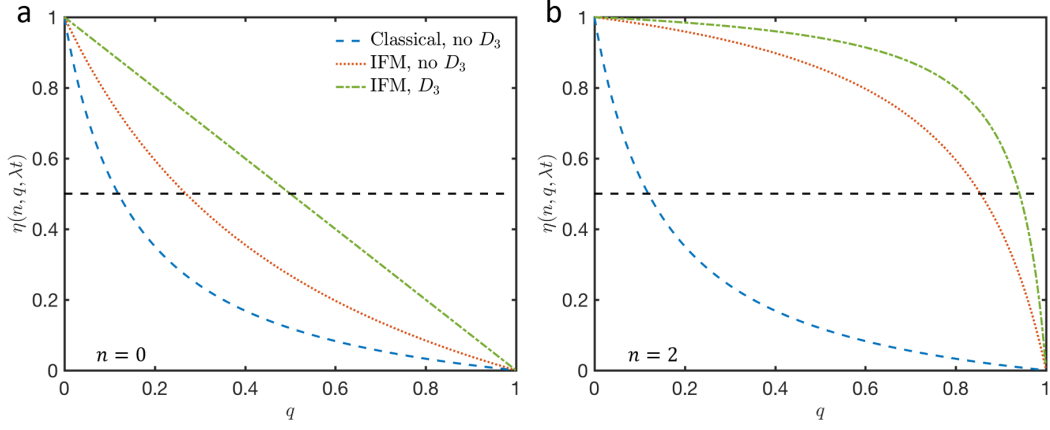


Figure 2-3: Comparison of posteriors for conventional and IFM imaging. $\eta(n_1, q, t)$ vs. q at $\lambda t = 2$ for conventional imaging Scheme A, and IFM imaging Schemes C and D, for (a) $n_1 = 0$ and (b) $n_1 = 2$. Also indicated by the horizontal dotted black line is the threshold for inferring \hat{X} , $\eta(n_1, q, \lambda t) = \frac{1}{2}$. For Scheme A, η_A is the same for all n_1 , and remains unchanged in (a) and (b). For Schemes C and D, as n_1 increases, the probability of the pixel being transparent increases, and hence the range of q for which inferring $\hat{X} = 0$ leads to lower P_{err} grows larger.

\bar{n}_{damage} is the same as for Scheme C, *i.e.* $\lambda t/2$. Hence,

$$\begin{aligned}
P_{\text{err}} &= q \left(\sum_{k \geq k^*} e^{-\bar{n}_{\text{damage}}/2} \frac{(\bar{n}_{\text{damage}}/2)^k}{k!} \right) e^{-3\bar{n}_{\text{damage}}/2} \\
&+ (1 - q) \left(\sum_{k < k^*} e^{-2\bar{n}_{\text{damage}}} \frac{(2\bar{n}_{\text{damage}})^k}{k!} \right) \\
&= q e^{-2\bar{n}_{\text{damage}}} \left(\sum_{k \geq k^*} \frac{(\bar{n}_{\text{damage}}/2)^k}{k!} \right) \\
&+ (1 - q) e^{-2\bar{n}_{\text{damage}}} \left(\sum_{k < k^*} \frac{(2\bar{n}_{\text{damage}})^k}{k!} \right). \tag{2.14}
\end{aligned}$$

Equation (2.14) has two terms, both with a decay factor of $e^{-2\bar{n}_{\text{damage}}}$. Just as for Equation (2.11) in Scheme C, we can expect this factor to lower P_{err} for Scheme D below that for Schemes A and B (Equations (2.5) and (2.8)). Further, since this factor is present in both terms (as opposed to just the second term in Equation (2.11)), we can expect P_{err} for Scheme D to be lower than in Scheme C as well. From Equation (2.13), with the same example parameters as Scheme C ($\lambda t = 1$ and $q = \frac{1}{2}$),

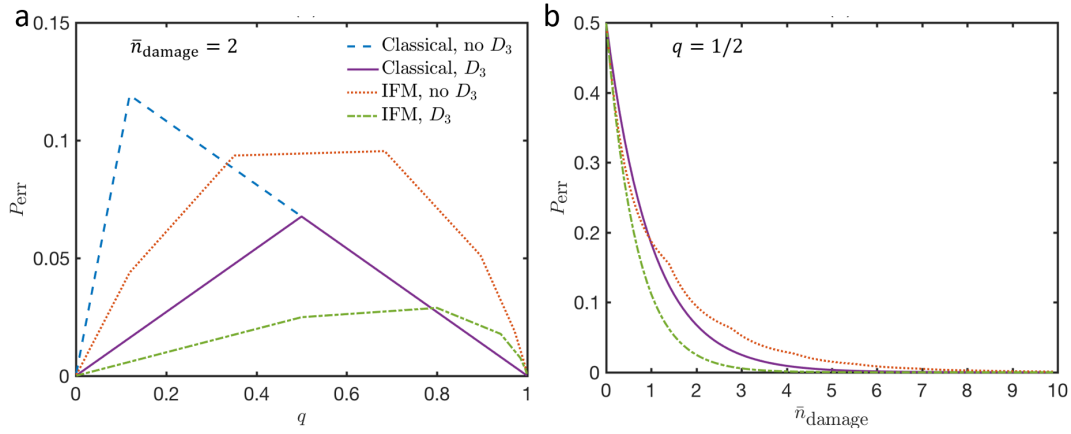


Figure 2-4: Comparison of P_{err} and \bar{n}_{damage} for the imaging schemes. (a) P_{err} vs. q for the four imaging schemes. Scheme D gives the lowest P_{err} . (b) P_{err} vs. \bar{n}_{damage} for the imaging schemes. The curve for Scheme B overlaps with that for Scheme A. Again, Scheme D gives the lowest P_{err} for a given value of \bar{n}_{damage} .

$k^* = 0$. This value of k^* eliminates the second term from the expression for P_{err} , and we get

$$P_{\text{err}} = \frac{1}{2} \left(\sum_{k \geq 0} e^{-1/4} \frac{\left(\frac{1}{4}\right)^k}{k!} \right) e^{-3/4} = \frac{1}{2} e^{-3/4} \approx 0.236.$$

We see that P_{err} for Scheme D is lower than Schemes A, B and C, for the same value of \bar{n}_{damage} .

Figure 2-4(a) is a comparison of P_{err} vs. q for the four different schemes outlined above. Each curve was plotted for $\bar{n}_{\text{damage}} = 2$, to compare the schemes at constant damage. The kinks in the curves are due to changes in the optimal decision scheme (and therefore, the expression for P_{err}) as a function of q (see Equations (2.5), (2.8), (2.11) and (2.14)). For Schemes C and D, there are multiple kinks due to the dependence on q of k^* (see Equations (2.10) and (2.13)).

The advantage of the scattering detector D_3 in terms of lowering P_{err} for both STEM and IFM imaging is apparent in Figure 2-4(a). Further, the error for Scheme D is the lowest of all four schemes for a broad range of q . This range of q includes two important regimes: low q , which is applicable to most electron microscopy samples, and $q = \frac{1}{2}$, which is a reasonable initial guess for a completely unknown sample.

We see that Scheme C offers an advantage over Scheme A for low values of q as well, although the reduction in P_{err} here is not as large as the reduction in P_{err} for Scheme D. Finally, Scheme C has a larger error than Scheme B for all values of q . For $q > 0.5$, the error in Scheme C is larger than all other schemes, because of missed detections due to scattering from opaque pixels.

Figure 2-4(b) shows P_{err} as a function of \bar{n}_{damage} for all the schemes, at $q = \frac{1}{2}$. As described earlier, for all $\lambda t > 0$, $e^{\lambda t} > 1$, and hence $\frac{1}{1+e^{\lambda t}} < \frac{1}{2}$. Therefore, the expressions for P_{err} are identical for Schemes A and B. Hence, the two curves overlap in Figure 2-4(b). We see that Scheme C provides a lower P_{err} than STEM imaging for $\bar{n}_{\text{damage}} < 0.93$. Beyond this value of \bar{n}_{damage} , missed detections due to scattering from the sample result in a greater P_{err} than Schemes A and B. Since q is constant, the kinks in the curve for Scheme C indicate the values of the mean number of beam electrons λt (and correspondingly, \bar{n}_{damage}) at which the threshold k^* changes, in accordance with Equation (2.10). As in Figure 2-4(a), the optimal decision scheme evolves, this time with λt . We had already made this observation in Figure 2-3. Removing missed detections by introducing D_3 in Scheme D further reduces P_{err} below Schemes A and B for all values of \bar{n}_{damage} . As we had noted earlier, the expression for k^* (Equation (2.13)) for Scheme D does not depend on λt . Therefore, k^* does not change with \bar{n}_{damage} , leading to a smooth curve for P_{err} for Scheme D.

2.2 Conditional re-illumination

As seen above, the Poisson distribution of the source creates an ambiguity in the interpretation of the electron counts at the detectors, leading to errors. One possible strategy to reduce these errors is to re-illuminate each pixel with the same beam. In this case, the error would be equivalent to single-shot illumination with a beam that has twice the dose (*i.e.* twice the λt). As seen from the expressions for the error probability P_{err} in each scheme, an increase in λt would lead to a reduction in P_{err}

for a given value of prior q .

However, we do not need to re-test each pixel. Pixels that we are sure are either opaque or transparent (*i.e.* the inference of \hat{X} for those pixels is not made on the basis of a probabilistic decision rule) need not be re-tested. For example, for Scheme C (IFM imaging without D_3), we would re-test pixels for which the number of counts on detector D_2 , $n_2 = 0$ (for any value of the counts on D_1 , n_1), since this was the only case in which the pixel value is not known with surety. We will refer to such a re-illumination scheme as *conditional re-illumination*.

Even after re-illumination, some pixel values will not be known with surety. For some of the pixels for which $n_2 = 0$ in Scheme C, the probability of making an incorrect inference for \hat{X} will be low. For example, if the number of detections at D_1 is high, we can be confident that the pixel is transparent. One way to use a confidence level is to set a *re-illumination threshold*, ϵ , such that if $\eta(n_1, q, \lambda t) < \epsilon$ or $\eta(n_1, q, \lambda t) > 1 - \epsilon$, we do not re-test the pixel under consideration. Thus, we only re-illuminate pixels for which $\eta(n_1, q, \lambda t) \in [\epsilon, 1 - \epsilon]$. Note that here we have used a general $\eta(n_1, q, \lambda t)$ to refer to the probability of a pixel being transparent given n_1, q and λt , since these considerations can apply to any of the schemes considered in Section 2.1.3.

A sequence of illuminations updates our belief on the opacity of the pixel. Starting with prior q_{m-1} on the probability that the pixel is opaque before the m th round of illumination, we again use Bayes' rule to update the prior to

$$q_m = 1 - \eta(n_1, q_{m-1}, \lambda t),$$

after the m th round of illumination. Note that we now use λt to refer to the mean electron number per pixel per illumination. The initial prior is $q_0 = q$, and based on the re-illumination threshold above, we re-illuminate when $q_m \in [\epsilon, 1 - \epsilon]$, which we call the *range of uncertainty*. Illuminations are repeated until q_m falls outside the range of uncertainty, or a pre-defined maximum number of illuminations M is

reached.

Before considering the general case of a Poisson-limited beam for all four imaging schemes, we illustrate the idea of conditional re-illumination through two short examples, for Schemes A (STEM imaging without D_3) and C (IFM imaging without D_3).

Example 1: Scheme A

We consider the imaging Scheme A with $\lambda t = 2$ and $q_0 = \frac{1}{2}$ and set the re-illumination threshold at $\epsilon = 0.1$. After the first round of illumination, we would infer that any pixels for which $n_1 > 0$ are transparent ($\hat{X} = 0$); this decision is always correct, and no re-testing is required. For pixels where $n_1 = 0$, we have

$$\begin{aligned} q_1 &= 1 - \eta_A(n_1, q_0, \lambda t) = 1 - \eta_A(0, \frac{1}{2}, 2) \\ &= 1 - \frac{1}{1 + e^{2 \frac{1}{2}/(1 - \frac{1}{2})}} \approx 0.881, \end{aligned}$$

by substituting in Equation (2.3). Since q_1 falls in the range of uncertainty, we re-test each of these pixels.

In the second round of illumination, if $n_1 > 0$ for any of the re-tested pixels, $\hat{X} = 0$ as before. If $n_1 = 0$ again,

$$\begin{aligned} q_2 &= 1 - \eta_A(n_1, q_1, \lambda t) = 1 - \eta_A(0, 0.881, 2) \\ &= 1 - \frac{1}{1 + e^{2 (0.881/0.119)}} \approx 0.992. \end{aligned}$$

Now, since q_2 falls outside the range of uncertainty, we will not re-test any of these pixels and assign $\hat{X} = 1$. The probability of error is still non-zero, but smaller than that with just one round of illumination. In this case all the opaque pixels will be re-tested, and on average we will not gain any advantage in terms of reduced damage.

As a final remark, we note that if $\lambda t = 3$, $\eta_A(n_1, q_0, \lambda t) \approx 0.047$ for pixels for

which $n_1 = 0$, after the first round of illumination. Thus, we would not re-test any pixel. As λt increases, the probability that there was at least one electron in the beam increases. Therefore, if $n_1 = 0$, there is a smaller chance of making an error if we set $\hat{X} = 1$ with increasing λt .

Example 2: Scheme C

We consider the imaging Scheme C with $\lambda t = 10$ and $q_0 = \frac{1}{2}$. Ambiguity arises when $n_2 = 0$. We can evaluate $\eta_C(n_1, q_0, \lambda t)$ for these parameters using Equation (2.9):

$$\eta_C(n_1, q_0, \lambda t) = \eta_C(n_1, \frac{1}{2}, 10) = \frac{1}{1 + e^5/4^{n_1}}.$$

In Figure 2-5(a), we plot $\eta_C(n_1, q_0, \lambda t)$ as a function of the counts at D_1 , n_1 . This figure shows that $\eta_C(n_1, q_0, \lambda t)$ is small for low values of n_1 , and increases to ≈ 1 for $n_1 \geq 7$. If we detect few electrons at D_1 , it is more probable that an opaque pixel is scattering the incident electrons than for the pixel to be transparent and the number of illumination electrons being very low. Therefore, we can be confident that $X = 1$. If we detect more electrons at D_1 , it is more probable that the pixel was transparent. In these limits, the probability of making an error is low. The solid orange horizontal lines in Figure 2-5(a) show the re-illumination thresholds with $\epsilon = 0.05$. We can see that the re-illumination condition is satisfied for $2 \leq n_1 \leq 5$. Instead, if we use $\epsilon = 0.25$, as shown by the dashed orange horizontal lines in Figure 2-5(a), the re-illumination condition is satisfied for $3 \leq n_1 \leq 4$. For each value of ϵ , outside the corresponding range of n_1 , the probability of incorrectly inferring \hat{X} is below our re-illumination threshold. For example, if $n_1 = 2$ for a particular pixel, $\eta_C(n_1, q_0, \lambda t) = 0.097$ (hence $q_1 = 0.903$), and this pixel would be re-tested if we work with $\epsilon = 0.05$. In the second round, if $n_1 = 2$ again for this pixel, $\eta_C(n_1, q_0, \lambda t) = 0.044$. Hence we would assign $\hat{X} = 1$ with a very low P_{err} . However, if we work with $\epsilon = 0.25$, this pixel would not be re-tested. Hence, \bar{n}_{damage} with $\epsilon = 0.25$ would be lower than that with $\epsilon = 0.05$, at the cost of increased P_{err} .

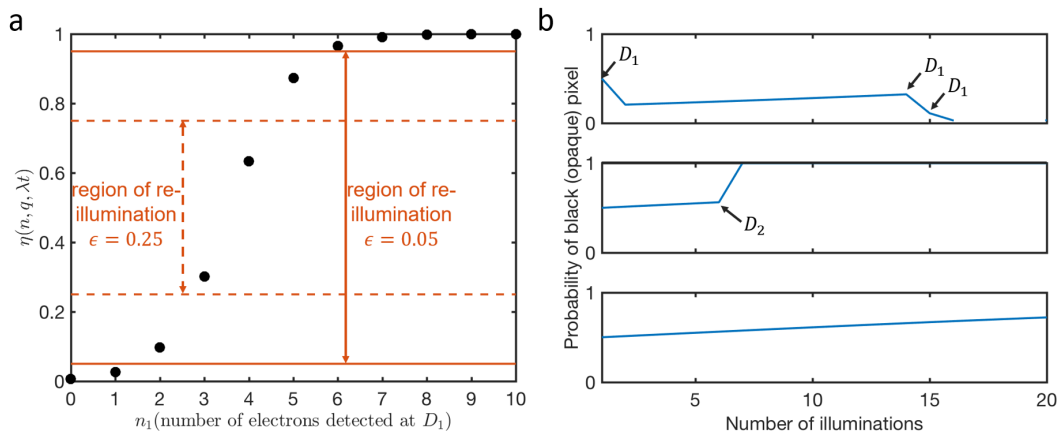


Figure 2-5: Conditional re-illumination applied to IFM imaging Scheme C. (a) $\eta_C(n_1, q_0, \lambda t)$ (black dots) as a function of n_1 , with $\lambda t = 10$ and $q_0 = \frac{1}{2}$. Also indicated are re-illumination ranges corresponding to two values of the re-illumination threshold ϵ : $\epsilon = 0.05$ (solid orange line) and $\epsilon = 0.25$ (dashed orange line). (b) Three examples of the evolution of q with multiple illuminations for Scheme C. These q trajectories were obtained using Monte Carlo simulations, with a maximum of $M = 20$ illuminations, a dose per illumination $\lambda t = 0.1$ electrons per pixel, and $\epsilon = 0.05$. The top panel is for a transparent pixel ($X = 0$); q_m decreased with each detection at D_1 , and dropped below $\epsilon = 0.05$ after the third D_1 detection. For the pixel in middle panel, a D_2 detection at the 7th round of illumination confirmed $q_m = 1$ (hence $\hat{X} = 1$). For the pixel in the lower panel, there were no detections in any of the illuminations. q_m slowly increased but did not cross the error threshold. Therefore, at the end of the 20th illumination, we were forced to make a guess for this pixel. Since $q_{20} > 0.5$, we guessed $\hat{X} = 1$.

2.2.1 Evolution of q_m

As we had discussed before, the basis of conditional re-illumination is the varying trajectories of q_m for different sample pixels. In order to visualize this variation in the trajectory of q_m , in Figure 2-5(b) we plot the evolution of q_m for three sample pixels over multiple rounds of conditional re-illumination, for Scheme C. We obtained this plot using a Monte Carlo simulation, the details of which are described later, and Bayesian inference to update q_m as described before. For this simulation, we chose the dose per illumination $\lambda t = 0.1$, $M = 20$, and $\epsilon = 0.05$.

For the pixel in the top plot in Figure 2-5(b), there was a detection at D_1 on the first illumination. Hence, q_1 reduced from its initial value of $\frac{1}{2}$. Following this

detection, there were no further detections till the fourteenth illumination. However, since this imaging scheme does not have a D_3 , the lack of detections could be because of electrons scattering off the pixel. Therefore, q_m slowly increases to account for this possibility. Further D_1 detections in the fourteenth and fifteenth illuminations reduced q_{15} to below ϵ , and we inferred $\hat{X} = 0$. This pixel was not illuminated in future rounds.

For the pixel depicted in the middle plot in Figure 2-5(b), there were no detections until the seventh round of illumination, when there was a detection at D_2 . This detection set q_7 to 1. Hence, we inferred that $\hat{X} = 1$ and stopped illuminating this pixel in future rounds.

For the pixel in the bottom plot, there were no detections in any of the twenty rounds of illumination. Just as for the pixel in the top panel, q_m slowly increased, but did not cross $1 - \epsilon$. At the end of the twentieth round, we were forced to make a guess for \hat{X} . Since q_{20} is closer to 1, we guessed $\hat{X} = 1$, which was correct in this case.

These three examples demonstrate different trajectories that the prior q can take for different pixels. Conditional re-illumination ensures that the illumination strategy for each pixel is tailored to the trajectory being followed by that pixel's prior.

2.2.2 Error and damage in conditional re-illumination

The acceptable ranges of the error probability P_{err} and scattered electrons \bar{n}_{damage} dictate the parameter space for designing a conditional re-illumination experiment. Figure 2-6(a) shows P_{err} as a function of the maximum number of illuminations M for $\epsilon = 0.05$ (solid orange curve with cross markers) and $\epsilon = 0.25$ (dashed orange curve with circular markers), for $q = \frac{1}{2}$, $\lambda t = 0.2$. As M increased, P_{err} continuously decreased. This trend is as we would expect; more illuminations drive q_m for each

pixel closer to 0 or 1, reducing errors. Figure 2-6(b) shows the corresponding values of \bar{n}_{damage} ; we see that \bar{n}_{damage} increased with increasing M , saturating to 0.95 for $\epsilon = 0.25$ and 1.8 for $\epsilon = 0.05$. This saturation occurs because as the number of illuminations increases, the number of pixels being re-tested reduces, and hence the contribution of each successive round of illumination to the damage reduces. Therefore, Figure 2-6 illustrates the trade-off between error probability and sample damage with increasing conditional re-illumination. Further, this figure also shows the impact of the acceptable re-illumination threshold on error probability and damage: a larger re-illumination threshold leads to a greater probability of error but a smaller amount of sample damage, and vice-versa. For example, suppose for a particular imaging experiment, an acceptable value of P_{err} is ≈ 0.16 . As can be seen from Figure 2-6(a), we can obtain this value by choosing $M \approx 30$ and $\epsilon = 0.25$, or $M \approx 16$ and $\epsilon = 0.05$. From Figure 2-6(b), we see that the value of \bar{n}_{damage} for the first choice of parameters would be ≈ 0.95 , while for the second choice of parameters it would be ≈ 1.15 . Hence, the first choice seems preferable. However, there might be other experimental constraints that influence the choice of parameters (for example, data collection time, and therefore M , might be limited by sample drift).

In order to determine the optimal set of parameters to obtain a given P_{err} and \bar{n}_{damage} point, we performed Monte Carlo simulations of the conditional re-illumination process for all four imaging schemes. We use an object with 10^6 pixels and an initial $q = \frac{1}{2}$. In our simulations, we picked the number of electrons incident on each pixel per illumination from a Poisson distribution with mean λt . Then, we allocated electrons to each detector for the imaging scheme under investigation (IFM without D_3), based on the detection probability at that detector. At the end of each round of illumination, we used the expressions for $\eta(n_1, q, \lambda t)$ derived for each scheme (Equations (2.3), (2.6), (2.9) and (2.12)) to update q_m for each pixel. We used this updated q_m as the prior for the next round of illumination. During the simulation, we used counts at D_3 to keep track of the number of electrons incident on each opaque pixel, even for schemes in which we did not use the counts at D_3 to update q_m . We

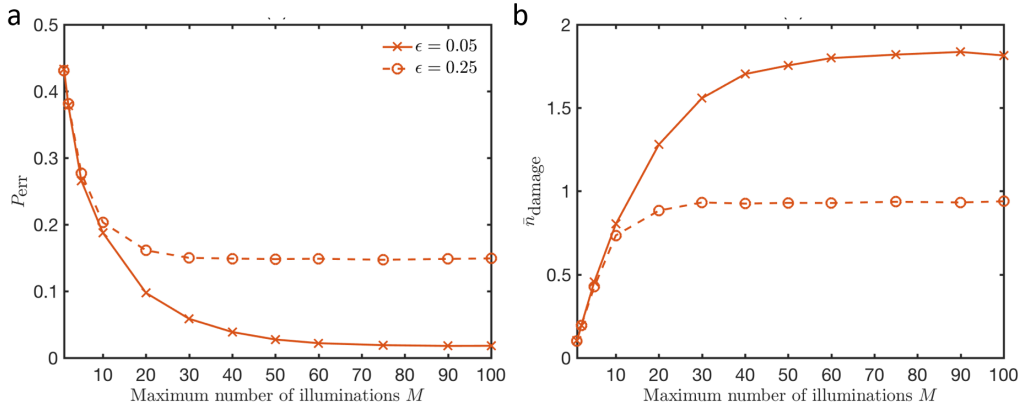


Figure 2-6: Error and damage for IFM imaging Scheme C. λt is kept constant at 0.2 for these simulations. (a) P_{err} as a function of the maximum number of illuminations M , for both re-illumination thresholds in Figure 2-5(a). The solid orange curve with cross markers is for $\epsilon = 0.05$, and the dashed orange curve with circular markers is for $\epsilon = 0.25$. P_{err} decreased with increasing illuminations for both values of ϵ . Increasing the re-illumination threshold ϵ from 0.05 to 0.25 led to an increase in the values of P_{err} (b) \bar{n}_{damage} vs. M . \bar{n}_{damage} increased with increasing illuminations, saturating at $\bar{n}_{\text{damage}} \approx 1.8$ for $\epsilon = 0.05$, and $\bar{n}_{\text{damage}} \approx 0.95$ for $\epsilon = 0.25$.

repeated this process for each pixel until one of two stopping conditions were met: either the updated q_m fell outside the re-illumination range, or the number of illuminations reached a predefined maximum, M . At the end of the simulation, we made an inference for pixels for which q_m was still inside the re-illumination range based on whether q_m was greater or less than $\frac{1}{2}$. Following this decision, we calculated P_{err} by averaging the absolute difference between the actual pixel value X and the inferred value \hat{X} over all the pixels. We calculated \bar{n}_{damage} by dividing the total counts at D_3 for all the pixels by the number of opaque pixels. We performed these simulations for $\lambda t \in [0.1, 2]$, $M \in [1, 100]$, and $\epsilon \in [0, 0.2]$, for each imaging scheme.

In Figure 2-7 we plot the convex hull of the $(\bar{n}_{\text{damage}}, P_{\text{err}})$ points obtained from these simulations for each scheme. As an example, for Scheme D (IFM imaging with D_3 , green curve with square markers in Figure 2-7), the 10 points with the smallest P_{err} values on the convex hull, along with the $(M, \epsilon, \lambda t)$ values at these points, are summarized in Table 2.13.

The general trend in these values is for ϵ to reduce towards 0, λt to increase,

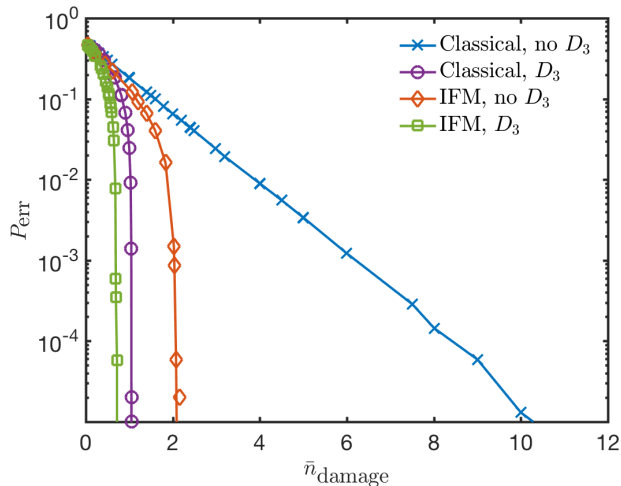


Figure 2-7: P_{err} vs. \bar{n}_{damage} for all 4 imaging schemes, with varying ϵ , λt and M . Each curve represents the convex hull of $(\bar{n}_{\text{damage}}, P_{\text{err}})$ points obtained from Monte Carlo simulations, whose details are described in the text. For schemes B, C and D, \bar{n}_{damage} saturates (at $\bar{n}_{\text{damage}} = 1$ for Scheme B, 2 for Scheme C and $\frac{2}{3}$ for Scheme D).

and M to increase towards 100 as P_{err} reduces and \bar{n}_{damage} increases. The choice of parameters in a potential experiment would depend on the acceptable P_{err} and \bar{n}_{damage} values, along with the achievable λt and M values in the experimental setup.

n_{damage}	$P_{\text{err}}(\times 10^{-2})$	M	ϵ	λt
0.5686	8.783	25	0.15	0.1
0.5883	7.834	25	0.05	0.1
0.5958	6.900	30	0.15	0.1
0.6261	4.495	40	0.10	0.1
0.6458	3.079	100	0.10	0.1
0.6796	0.778	100	0.05	0.1
0.6901	0.059	90	0	0.1
0.6917	0.035	100	0	0.1
0.7172	0.0058	60	0	0.2
0.7184	0.0006	75	0	0.2

Table 2.13: Detection probabilities at D_1 , D_2 and D_3 for Scheme D.

As can be seen in Figure 2-7, there appears to be no advantage of using condi-

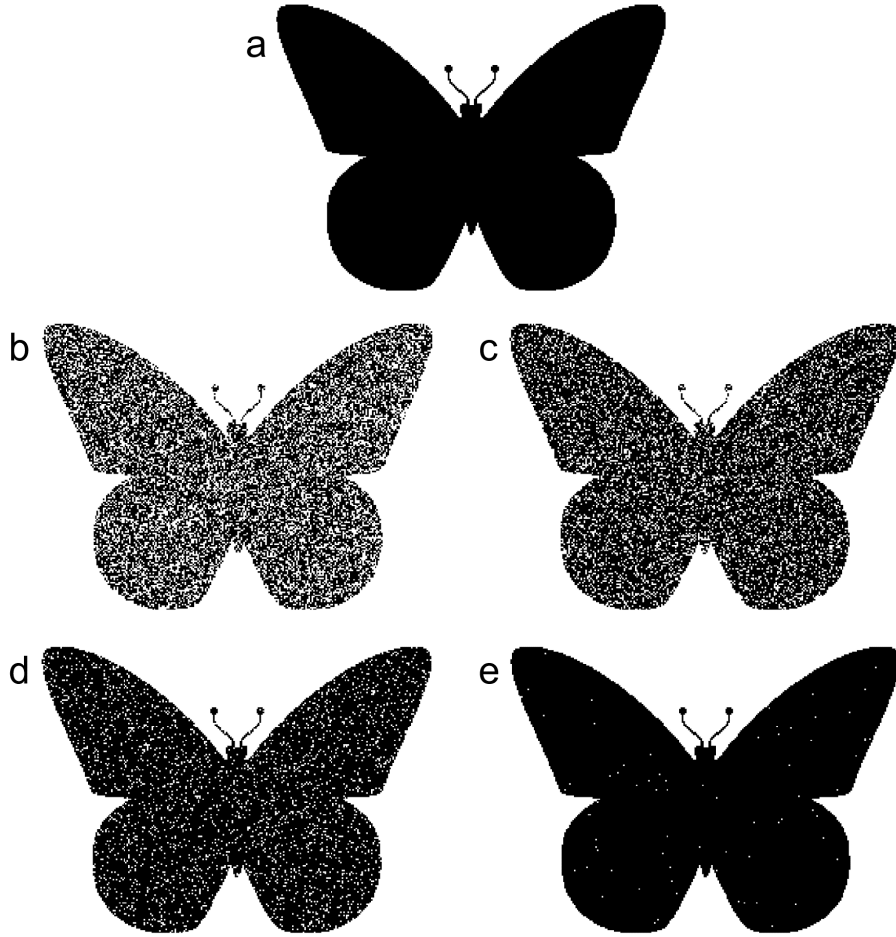


Figure 2-8: Image simulation using conventional and IFM imaging with conditional re-illumination. We performed all simulations at $\bar{n}_{\text{damage}} = 1$ electron per opaque pixel, and $M = 10$. (a) Original object used for image simulations. The object has an equal number of opaque (black) and transparent (white) pixels. (b) Simulated image using Scheme B, without conditional re-illumination. $P_{\text{err}} = 0.18$ for this image. (c) Simulated image using Scheme D, without conditional re-illumination. $P_{\text{err}} = 0.11$ for this image. (d) Simulated image using Scheme B with conditional re-illumination. $P_{\text{err}} = 5.1 \times 10^{-2}$ for this image. (e) Simulated image using Scheme D with conditional re-illumination. $P_{\text{err}} = 1.3 \times 10^{-3}$ for this image.

tional re-illumination for Scheme A (STEM imaging without D_3) – the curve for this scheme is identical to the one in Figure 2-4(b). We had already made the observation that conditional re-illumination does not benefit Scheme A in Example 1 earlier in this section. However, for the other three schemes, we obtain a saturation in \bar{n}_{damage} with increasingly low values of P_{err} . This saturation occurs for the same reasons as for Figure 2-6(b). For Scheme B (STEM imaging with D_3), \bar{n}_{damage} saturated to ~ 1 at low P_{err} . This value makes sense because for correct identification of an opaque pixel, we would ideally need only one electron. For Scheme C (IFM imaging without D_3), \bar{n}_{damage} saturated at 2. In this scheme, we want a detection at D_2 to correctly identify an opaque pixel. The probability of this event is $\frac{1}{4}$. On average, we need 4 electrons to identify an opaque pixel, 2 of which will scatter off the sample. For Scheme D (IFM imaging with D_3), \bar{n}_{damage} saturated at $\sim \frac{2}{3}$. This value also makes sense: to correctly identify an opaque pixel, we want a detection at either D_2 or D_3 in this scheme. The total probability of a detection at D_2 or D_3 is $\frac{3}{4}$. Therefore, on average, we need $\frac{4}{3}$ electrons to identify an opaque pixel. Half of these electrons will scatter off and damage the sample, giving $\bar{n}_{\text{damage}} = \frac{2}{3}$. Overall, Scheme D also gives the lowest \bar{n}_{damage} for a given P_{err} , which demonstrates the benefits of IFM imaging.

In Figure 2-8, we show simulated images of a butterfly, using STEM and IFM imaging schemes with and without conditional re-illumination. Figure 2-8(a) is the original object we used in our imaging simulations. We added an equal number of transparent (white) pixels outside the opaque (black) butterfly pixels, so that $q = \frac{1}{2}$. We performed imaging simulations using the same Monte Carlo method as before. We varied λt to ensure that $\bar{n}_{\text{damage}} = 1$ for all simulations, and we fixed M at 10 and $\epsilon = 0.01$. Figure 2-8(b) is the simulated image using Scheme B (STEM imaging with D_3) without conditional re-illumination. The image reproduces the general shape of the butterfly, but has a lot of missed detections; $P_{\text{err}} = 0.18$. Figure 2-8(c) is the simulated image using Scheme D (IFM imaging with D_3) without conditional re-illumination. It has fewer errors than Figure 2-8(b); $P_{\text{err}} = 0.11$. Figure 2-8(d) is the simulated image using Scheme B with conditional re-illumination. The use

of conditional re-illumination reduced P_{err} to 5.1×10^{-2} . Finally, Figure 2-8(e) is the simulated image using Scheme D with conditional re-illumination. This imaging scheme produced the fewest errors, with $P_{\text{err}} = 1.3 \times 10^{-3}$. Therefore, these imaging simulations again demonstrate the error reduction in IFM imaging and conditional re-illumination.

2.3 Conclusions

In this chapter, we analyzed the performance of conventional and IFM imaging, with and without a detector for scattered electrons. We found that for a given rate of misidentifying sample pixels (P_{err}), the additional detector reduces the required electron dose, and hence the damage suffered by the sample (\bar{n}_{damage}). We also presented a sample re-illumination scheme, where the decision to re-illuminate the sample is made based on the result of previous illuminations. This conditional re-illumination scheme can be applied to both classical and IFM imaging. We showed that this scheme further reduces \bar{n}_{damage} for a given P_{err} . We reduced \bar{n}_{damage} to ≈ 1 for Scheme B, ≈ 2 for Scheme C, and $\approx \frac{2}{3}$ for Scheme D, for $P_{\text{err}} \leq 10^{-3}$. Our imaging simulations further confirmed the advantages of using IFM and conditional re-illumination.

In order to implement conditional re-illumination on an electron microscope, we would need to address two major issues. The first is the requirement of fewer than one electron per pixel to reach low damage values, as shown in Figure 2-7. With a pixel dwell time of 0.2 μs , a dose of 1 electrons/pixel would require an incident beam current of 0.64 pA. Although these dwell times and currents are achievable on current STEMs [78, 84], getting lower doses would be challenging. One possible solution could be the employment of fast electron gated mirrors [2]. The second issue is the requirement of a fast beam blanker. Ideally, we would want to blank the electron beam before changing the voltages on the beam deflector coils to move it to the next pixel to be imaged, to avoid exposing the sample during the beam motion. The speed of this blanking would need to be on the order of nanoseconds, to ensure

that the probability of the sample being exposed while the beam is being blanked is small. A possible solution to this challenge is to perform re-illumination experiments at lower electron beam energies (lower than 30 kV), to make fast beam blanking easier. Recent implementation of sub-ns beam blanking on an SEM [105, 106] would enable our conditional re-illumination scheme.

A major limitation of our analysis is the treatment of the object. Our assumption of opaque-and-transparent pixels is an inherent limitation of IFM [42]. Semitransparent objects would require higher dose to distinguish between areas with similar transparencies. We expect that our re-illumination scheme would need to be modified for semitransparent objects, since we would not be inferring a binary-valued random variable (\hat{X}) anymore [107, 108]. Instead, \hat{X} would now take continuous values between 0 and 1, which would require a more sophisticated probabilistic decision scheme. We expect that the incorporation of conditional re-illumination into existing investigations of IFM imaging with semitransparent objects [50–54], as well as with Quantum Zeno-enhanced IFM [2, 43–45] will be an interesting area of future research. A related issue is the assumption that opaque pixels in the object remain opaque upon being scattered by electrons. In real microscopy experiments, beam-induced damage degrades sample contrast [30]. This loss of contrast would increase the error probability P_{err} , and accounting for would again require extension of our formalism to semitransparent samples.

A second major limitation of this work is the exclusion of the effect of the object on the phase of the electron beam. Interferometric schemes are ideally suited for detecting phase, and previous work [53] has shown that IFM imaging provides an advantage for phase objects. A third limitation is the assumption of perfect detectors (no losses or dark counts) and a lossless system. We will address the impact of object phase, as well as lossy beamsplitters and detectors on the efficiency of our re-illumination scheme in future work.

Our work in the rest of this thesis is aimed at addressing these challenges to-

wards the implementation of conditional re-illumination. In our work we will use an SEM as a testbed for implantation of low-dose imaging and conditional re-illumination schemes. We chose to use an SEM for implementing low-dose imaging due to the ease of setting up different configurations of the sample and detectors in it. In chapters 4 and 5, we will address the challenges posed by the requirement of low incident dose by implementing SE count imaging on an SEM. We will use fast pixel dwell times (0.44 μ s) and low incident beam currents (< 5 pA) to ensure that the incident dose on the sample and the number of generated SEs are low. Further, in Chapter 4, we will implement offline conditional re-illumination with SE counting on an SEM. We will also discuss schemes for implementation of live conditional re-illumination on an SEM in chapters 3 and 5. In Chapter 3, we will propose schemes for conditional re-illumination for grayscale SEM imaging. We will also describe three metrics for characterizing the image quality in grayscale images which we will use in our implementation of offline conditional re-illumination for grayscale samples in Chapter 5. These schemes and metrics for grayscale SEM samples can be extended to semitransparent STEM samples as well

The conditional re-illumination scheme outlined in this chapter provides microscopists with a method of using both prior knowledge about the sample and information gained during the experiment to reduce sample damage and allow the investigation of radiation-sensitive samples, such as organo-metallic frameworks, proteins and biomolecules. The scheme could also be combined with existing schemes of sparse sampling, and using denoising and inpainting algorithms for low-dose STEM and SEM imaging [40, 41, 79, 80].

Chapter 3

Image quality metrics and schemes for conditional re-illumination for grayscale samples in an SEM

In Chapter 2, we introduced the idea of conditional reillumination and evaluated the reduction in sample damage from this scheme for opaque-and-transparent samples with STEM and IFM imaging. However, almost all real-world samples of interest in electron microscopy are grayscale and have many pixel intensity levels. Therefore, the simple re-illumination schemes we had proposed in Chapter 2 based on two possible pixel intensity levels have to be modified. We cannot define an error probability of misidentifying opaque pixels as transparent and vice-versa, since we now have multiple grayscale levels. As a consequence, the magnitude of the error depends on the difference between the estimated pixel value and the real value.

In this chapter, we will analyze image quality and accuracy metrics for samples with more than two pixel brightness levels and discuss conditional re-illumination schemes for such grayscale samples. As we will describe in Chapter 5, we implemented these re-illumination schemes on an SEM, so we will focus on describing the schemes for an SEM. However, since these schemes are based on making decisions on illumi-

MARE	Mean Absolute Relative Error
$a(n)$	1-dimensional signal
$r_a(m)$	Autocorrelation of $a(n)$ at offset m
$\mathbf{E}[a(n)]$	Expectation value of $a(n)$
$N(\mu, \sigma^2)$	Gaussian distribution with mean μ and variance σ^2
Poisson(λ)	Poisson distribution with mean λ
τ	Pixel dwell time
$\phi(m, n)$	2-dimensional image autocorrelation at offset (m, n)
$\phi_{NF}(m, n)$	2-dimensional noise-free image autocorrelation at offset (m, n)
$\phi_N(m, n)$	2-dimensional noise autocorrelation at offset (m, n)
$\hat{\phi}_{NF}(m, n)$	Estimator for 2-dimensional noise-free image autocorrelation at offset (m, n)
$\hat{\phi}_N(m, n)$	Estimator for 2-dimensional noise autocorrelation at offset (m, n)
A	Scaling factor for 8-bit image
M	Maximum number of illuminations
N_{ill}	Number of illuminations
N_{SE}	Number of SEs per pixel
$N_{\text{SE,T}}$	Threshold number of SEs per pixel

Table 3.1: List of symbols and abbreviations used in this chapter

nation depending on the current pixel intensity level, they can be adapted to TEM and STEM as well, similar to the scheme we described in Chapter 2.

This chapter is organized into three sections. In Section 3.1 we will describe three metrics that can be used to characterize image quality of noisy, grayscale images: contrast, mean absolute relative error (MARE), and signal-to-noise-ratio (SNR). In Section 3.2 we will describe schemes for conditional re-illumination imaging of grayscale objects in an SEM, where the image quality metrics we introduce in Section 3.1 would be used to characterize the images. These conditional re-illumination schemes were developed in collaboration with John Simonaitis (Massachusetts Institute of Technology). Finally, in Section 3.3, we will summarize our results from this chapter.

Table 3.1 lists the abbreviations and symbols used in this chapter. MATLAB scripts used to generate the plots in this chapter are reproduced in Section D.2 of Appendix D.

3.1 Image quality metrics for grayscale images

In this section we will show how contrast, MARE, and SNR can be calculated using real SEM images and discuss the conditions under which their use is appropriate. We will use these metrics in Chapter 5 when we compare the image quality and incident electron dose of conventional and SE count images and conditional re-illumination. Note that we did not consider the dependence of the spatial resolution of our SEM images on the incident electron dose in this thesis. Therefore, we did not use techniques such as Fourier-ring-correlation [109] to characterize the resolution of our images, nor did we compute the contrast transfer function (CTF) of our SEM [110].

3.1.1 Contrast

The contrast of a feature or region of interest in an image is a measure of how clearly the feature can be seen against its background or another adjacent feature. There are many different ways of defining contrast depending on the precise imaging situation and type of sample [111]. The common thread among these measures of contrast is that it is usually defined as a ratio of the difference between the intensities of the feature of interest and the background, and the background intensity. In this thesis, we will use the Michelson contrast, which is defined as follows. Suppose the pixels representing the feature of interest have a mean pixel value of I_{sample} and the pixels representing the background have a mean value $I_{\text{background}}$. The Michelson contrast K is defined as:

$$K = \frac{I_{\text{sample}} - I_{\text{background}}}{I_{\text{sample}} + I_{\text{background}}}$$

If $I_{\text{sample}} \gg I_{\text{background}}$, K will be close to 1. If the $I_{\text{background}} \approx I_{\text{sample}}$, K will be close to zero. This type of contrast is often used in optical lithography and microscopy systems, where it is calculated as a function of feature size and is called the modulation transfer function (MTF) [112]. It is an appropriate contrast measure when the difference between the sample and the background levels is substantial or when the

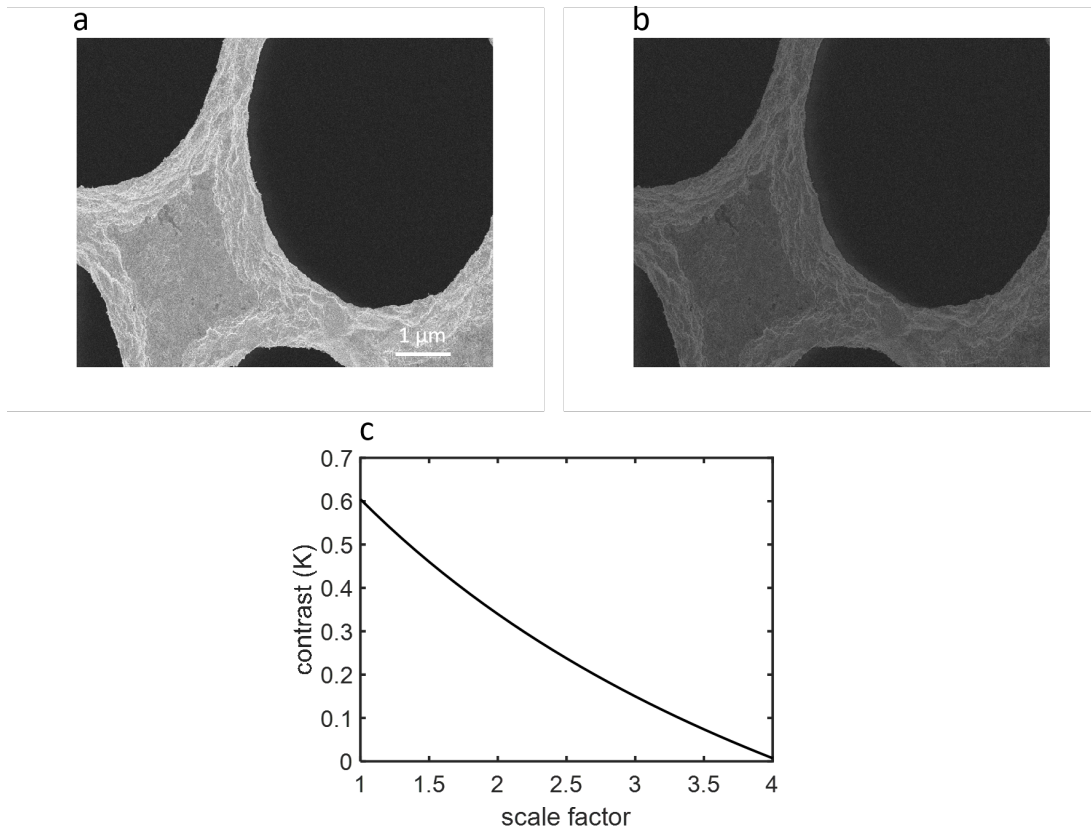


Figure 3-1: Contrast for SEM images.(a) SEM image of a TEM support grid suspended in vacuum, courtesy Navid Abedzadeh. (b) Simulated lower contrast image, generated by scaling down the intensities of the pixels corresponding to the TEM grid by 2. (c) Contrast as a function of the scaling factor used to generate the simulated image. As the scaling factor increased from 1 to 4, the contrast reduced from 0.61 to almost 0.

sample being imaged is periodic. We chose to use this type of contrast in our work because, as we will discuss in more detail in Chapter 5, the sample we imaged was a copper grating suspended over vacuum, where the difference between the brightness of the pixels representing copper and those representing the background vacuum was large.

Figure 3-1 shows an example of the calculation of contrast. Figure 3-1(a) is an SEM image of the supporting bars of a TEM grid, courtesy Navid Abedzadeh. We can see that there are two types of pixels in this image: bright pixels representing the support grid and dark pixels representing the background. Figure 3-1(b) is a simulated image of the same sample, where we scaled the intensities of the bright

pixels by a factor of 2. We can see that the support grid appears to be much dimmer with respect to the background, *i.e.*, its contrast is lower. As the scale factor is increased, we would expect the contrast to reduce. Figure 3-1(c) is a plot of the contrast K as a function of the scale factor. We can see that as the scale factor increases from 1 to 4 and the support grid becomes dimmer against the background, the contrast reduces from 0.61 to nearly 0, as expected.

As we had discussed earlier, the Michelson contrast is appropriate if there are clearly demarcated sample and background pixels which can be used to measure I_{sample} and $I_{\text{background}}$. Further, the distribution of the pixel values in the sample and background should be relatively narrow so that defining I_{sample} and $I_{\text{background}}$ is meaningful. In our discussion of SE count imaging in Chapter 5, we will use the contrast to quantify the advantage of SE count imaging compared to conventional imaging.

3.1.2 Mean absolute relative error

There are several error-based metrics that are used to characterize the quality of images, such as the mean squared error (MSE) and the root mean squared error (RMSE) [113]. In this work, we will consider the mean absolute relative error (MARE). MARE is a measure of the relative error between the pixel values in a noisy image of a sample and in the ‘ground truth’ [113,114], which is an image of the same sample that contains the correct pixel values. We suppose that the image is a matrix of size $R \times S$ with pixel values $A(i, j)$, $1 \leq i \leq R$ and $1 \leq j \leq S$, and the ground truth image is represented by $T(i, j)$. Then, MARE is given by [113,115]:

$$\text{MARE} = \sum_{i=1}^R \sum_{j=1}^S \frac{|A(i, j) - T(i, j)|}{T(i, j)}.$$

Therefore, MARE measures the mean of the absolute error at a pixel as a fraction of the ground truth value of that pixel and can be thought of as a percentage error

relative to the ground truth image. As stated earlier, MARE extends the definition of P_{err} from Chapter 2, being linearly dependent on the absolute difference between the experimental image and the ground truth. MARE is a widely applicable image quality metric and can be calculated for any type of image.

By virtue of its definition, MARE requires knowledge of the ground truth image, which is rarely available in a real-world imaging scenario. Due to this requirement, MARE differs from other image quality metrics, such as contrast (discussed in Section 5.3.2.1) and signal-to-noise-ratio (discussed in Section 5.3.2.2), which do not require a ground truth image. The need for a ground truth limits the applicability of MARE to comparing different microscopy techniques on known, well-characterized samples for which the ground truth is known, rather than a technique to compare the quality of micrographs of real samples that have not been imaged before.

A second disadvantage of MARE is that due to the scaling by the ground truth pixel intensity $T(i, j)$, MARE gives greater weight to errors on pixels that have a low ground truth intensity. This overemphasis on dimmer pixels could lead to an inaccurate error metric for electron microscopy images, where samples are often suspended over vacuum. For some imaging modes (such as ADF imaging as discussed in Chapter 1), vacuum regions provide very little signal. Consequently, errors/noise in such pixels would be greatly overemphasized by MARE. Conversely, in other types of samples, dim regions might correspond to the thinnest, most interesting regions of the sample. In such cases, a greater weight on errors made on dim pixels would be advantageous.

Figure 3-2 shows an example MARE calculation. Figure 3-2(a) is an SEM image of tin nanoparticles attached to a copper support grid, courtesy Navid Abedzadeh. We used this image as the ground truth and generated noisy versions of it to calculate the MARE. Figure 3-2(b) is an example of such a noisy image. In this image each pixel value was one trial of a Poisson-distributed random variable with mean equal to the corresponding pixel value in the ground truth image. The MARE of this image

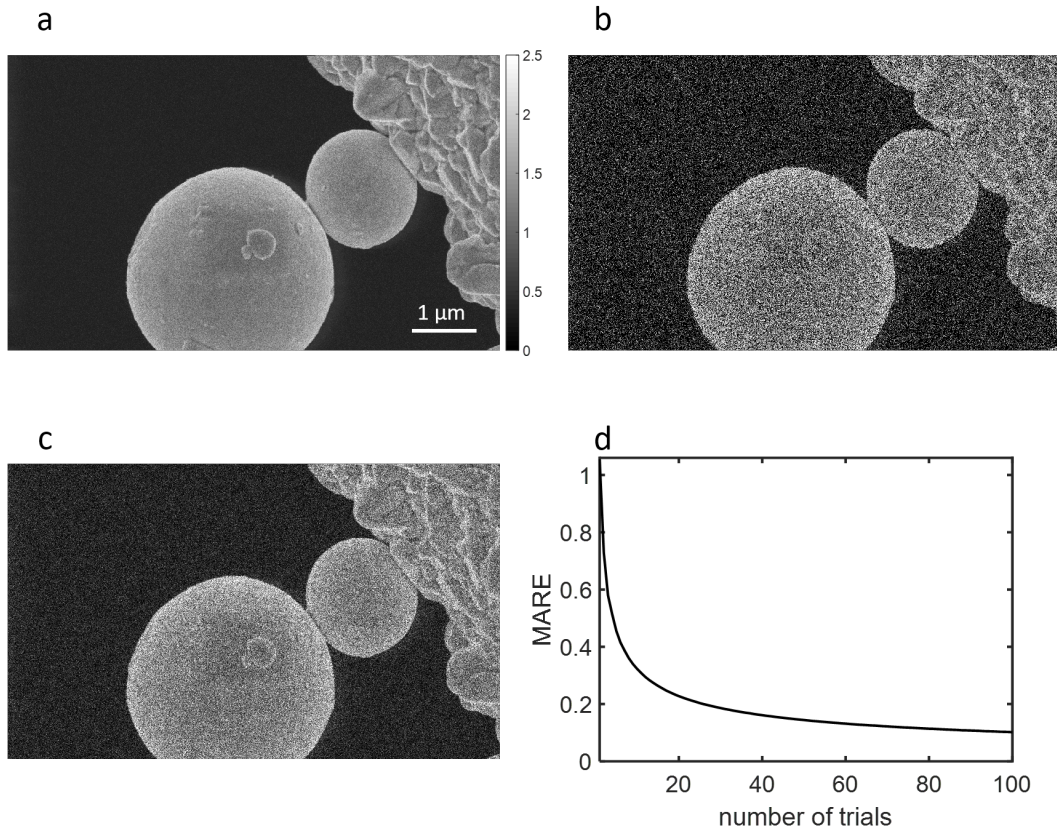


Figure 3-2: Mean absolute relative error for SEM images. (a) SEM image of tin nanoparticles on a copper support grid, courtesy Navid Abedzadeh. We used this image as the ‘ground truth’ in our calculation. (b) Noisy version of the image in (a), where each pixel value is the result of one trial of a Poisson process with mean value equal to the corresponding pixel value in (a). (c) Same as (b), except the pixel values are averaged over 5 trials. The image is less noisy than (b) due to averaging. (d) Mean relative absolute error as a function of the number of trials used to generate the noisy images. As the number of trials increases, the MARE reduces due to increasing image accuracy.

was 1.06. Figure 3-2(c) is another noisy image generated in the same way as 3-2(b), except that each pixel value was the average of five trials of a Poisson-distributed random variable instead of one. Consequently, the image was less noisy and had a MARE of 0.41. Figure 3-2(d) is a plot of the MARE as a function of the number of trials used to form the noisy images. We can see that as the number of trials increases, the MARE drops due to the improvement in the accuracy of the generated image.

In our analysis of different schemes for conditional re-illumination in Chapter 5,

we will use the MARE to characterize the accuracy of the generated images. In this case, we will have a ground truth available (an SE count image of the same sample generated without re-illumination) which we will use to calculate the MARE for the conditional re-illumination schemes.

3.1.3 Signal-to-noise ratio

The SNR is a standard measure used in many fields of signal processing and imaging to characterize the quality of a signal. However, defining SNR for a single SEM image is challenging, because of the difficulty in differentiating signal from noise in an image of an unknown sample. A method for solving this problem was proposed by Thong et al. [116], who developed an SNR measure for a single SEM image by looking at the autocorrelation of the image. The autocorrelation function can be thought of as a measure of how similar an image is to an offset copy of itself. Here, we note that the autocorrelation is defined for a probabilistic model of a random process. From a single realization of a random process, we cannot compute the autocorrelation, but we can compute an estimate of the autocorrelation of the underlying random process. Here, we will model a noise-free image as a realization of a two-dimensional wide-sense stationary random process, and an observed signal is another two-dimensional wide-sense stationary random process with statistical dependence on the noise-free image.

The autocorrelation $r_a(m)$ of a one-dimensional wide-sense stationary random signal $a(n)$ is defined as:

$$r_a(m) = \mathbf{E} [a(n)a(n - m)] \quad (3.1)$$

Here m is called the offset or lag, and n and $n - m$ are two points along the signal. \mathbf{E} denotes expectation value. Note that the lack of dependence of the expectation on n is a requirement of wide-sense stationarity. We would find the autocorrelation function of a physical image for a given pixel offset by multiplying it by a duplicate of itself offset by the required number of pixels. If the image has features that extend over a many pixels, a displaced copy of the image will have similar intensities in the

same pixels as the original image. Therefore, the autocorrelation of such an image would be high. Conversely, if the pixel values in the image vary rapidly over a few pixels, the autocorrelation will be small.

Here, we will describe Thong et al.'s SNR measure and present a new, rigorous justification behind the measure. This SNR measure is based on the assumption that the contribution to the image autocorrelation from the 'signal' component of the image varies slowly (*i.e.*, over several pixels), whereas the 'noise' component of the autocorrelation varies rapidly and is zero for $m \neq 0$ in the definition of autocorrelation in Equation 3.1. This difference in the nature of signal and noise allows the extraction of their relative contributions to the autocorrelation, and the ratio of these contributions is a measure of the image SNR.

We will first consider an ideal Poisson signal derived from an underlying ground truth image and analyze its autocorrelation. Then, we will introduce some of the non-idealities present in an SEM and derive Thong et al.'s expression for the SNR measure. Finally, we will demonstrate the effectiveness of the SNR measure by calculating it for SEM images taken at different pixel dwell times.

Let $f(n) \sim \text{Poisson}(s(n))$ be a Poisson process derived from $s(n)$. We assume that if $s(n)$ is known, the values of $f(n)$ at two points n_1 and $n_2, n_1 \neq n_2$, would be independent of each other. This assumption is equivalent to assuming that the noise for any pair of pixels is uncorrelated (and hence has an expected value of zero). We want to find the autocorrelation of $f(n)$, *i.e.*, we want to find $r_f(m) = \mathbf{E}[f(n)f(n-m)]$. We consider two cases: $m \neq 0$ and $m = 0$.

Case 1: $m \neq 0$

$$\begin{aligned}
 \mathbf{E}[f(n)f(n-m)] &= \mathbf{E}[\mathbf{E}[f(n)f(n-m)|\{s(n)\}]] \\
 &= \mathbf{E}[\mathbf{E}[f(n)|s(n)] \mathbf{E}[f(n-m)|\{s(n)\}]] \\
 &= \mathbf{E}[s(n)s(n-m)] \\
 &= r_s(m)
 \end{aligned}$$

Here, the second equality results from our assumption about the independence of $f(n_1)$ and $f(n_2)$, and the third equality results from the definition of $f(n)$. Therefore, we conclude that $r_f(m) = r_s(m)$ for $m \neq 0$.

Case 2: $m = 0$

$$\begin{aligned}
\mathbf{E}[f(n)f(n-m)] &= \mathbf{E}[f(n)^2] \\
&= \mathbf{E}[\mathbf{E}[f(n)^2|\{s(n)\}]] \\
&= \mathbf{E}[s(n)^2 + s(n)] \\
&= r_s(0) + \mathbf{E}[s(n)]
\end{aligned}$$

Here, the third equality again results from the definition of $f(n)$. Therefore, we finally get:

$$r_f(m) = \begin{cases} r_s(m), & m \neq 0; \\ r_s(0) + \mathbf{E}[s(n)], & m = 0. \end{cases}$$

Hence, the autocorrelation $r_f(m)$ of the noisy image $f(n)$ derived from the ground truth $s(n)$ will be the same as the autocorrelation of $s(n)$ everywhere except at $m = 0$, where there is an additional term due to the fact that $f(n)$ is derived from a random process $s(n)$ and is therefore noisy. As we had stated earlier, the assumption we made about the independence of values of $f(n)$ at different pixels is equivalent to assuming that the noise is uncorrelated between neighbouring pixels, which is why the contribution due to noise only affects the autocorrelation at zero offset. At zero offset, we expect the autocorrelation to have a sharp peak due to the additional noise contribution. At non-zero offsets, this noise contribution is zero because the noise in neighbouring pixels is uncorrelated.

Our assumption that $f(n) \sim \text{Poisson}(s(n))$ is not justified for SEM imaging. A conventional SEM image is not a count of SEs per pixel. As we had discussed in Chapter 1 Section 1.1.3, the SEM image is a map of the average signal level from the SE detectors for every pixel, which is quantized and displayed as an 8-bit image. Further, in addition to noise due to the randomness inherent in the generation of SEs,

the SE image can also have noise due to imperfect detection of SEs, background counts in the detector, variation in the signal waveform from the detector (see Chapter 4 Section 4.2), and quantization of the SE signal. We can model the scaling to 8-bit and noise addition in an SEM as a linear scaling of the number of SEs observed for that pixel, along with zero mean Gaussian noise, as follows:

$$f(n) \sim A \cdot \text{Poisson}(s(n)) + N(0, \sigma^2)$$

Here, the factor A accounts for scaling to 8 bits [117], and $N(0, \sigma^2)$ accounts for the additional sources of noise discussed above. Using the same process to find the autocorrelation $r_f(m)$, we get:

$$r_f(m) = \begin{cases} A^2 r_s(m), & m \neq 0; \\ A^2 r_s(0) + A \mathbf{E}[s(n)] + \sigma^2, & m = 0. \end{cases} \quad (3.2)$$

Hence, for a real image, we would still expect the autocorrelation to show a sharp peak at zero offset. Now, the peak at zero offset has contributions from both noise due to the Poisson process and the variance of the additional Gaussian noise. Thong's method provides a way to estimate the "noise-free" component of the autocorrelation, at zero offset ($\hat{\phi}_{NF}(0,0)$, an estimator for the true noise-free autocorrelation $\phi_{NF}(0,0) = A^2 r_s(0)$) from the observed autocorrelation at zero offset ($\phi(0,0)$) and estimate both the signal and noise contributions in the image to derive SNR for a single SEM image. Note that our SEM images are two-dimensional and hence we specify the offset along both dimensions in our notation. We will demonstrate this method through an example.

Figures 3-3(a) and (b) are two SEM images of the same region of a bulk copper sample, taken at the same incident beam current. We acquired Figure 3-3(a) at a pixel dwell time of 3.6 μs and Figure 3-3(b) at a pixel dwell time of 28 μs . The longer dwell time we used to acquire Figure 3-3(b) resulted in a less noisy image.

In Figure 3-3(c), we plot the autocorrelations of these two images. The full

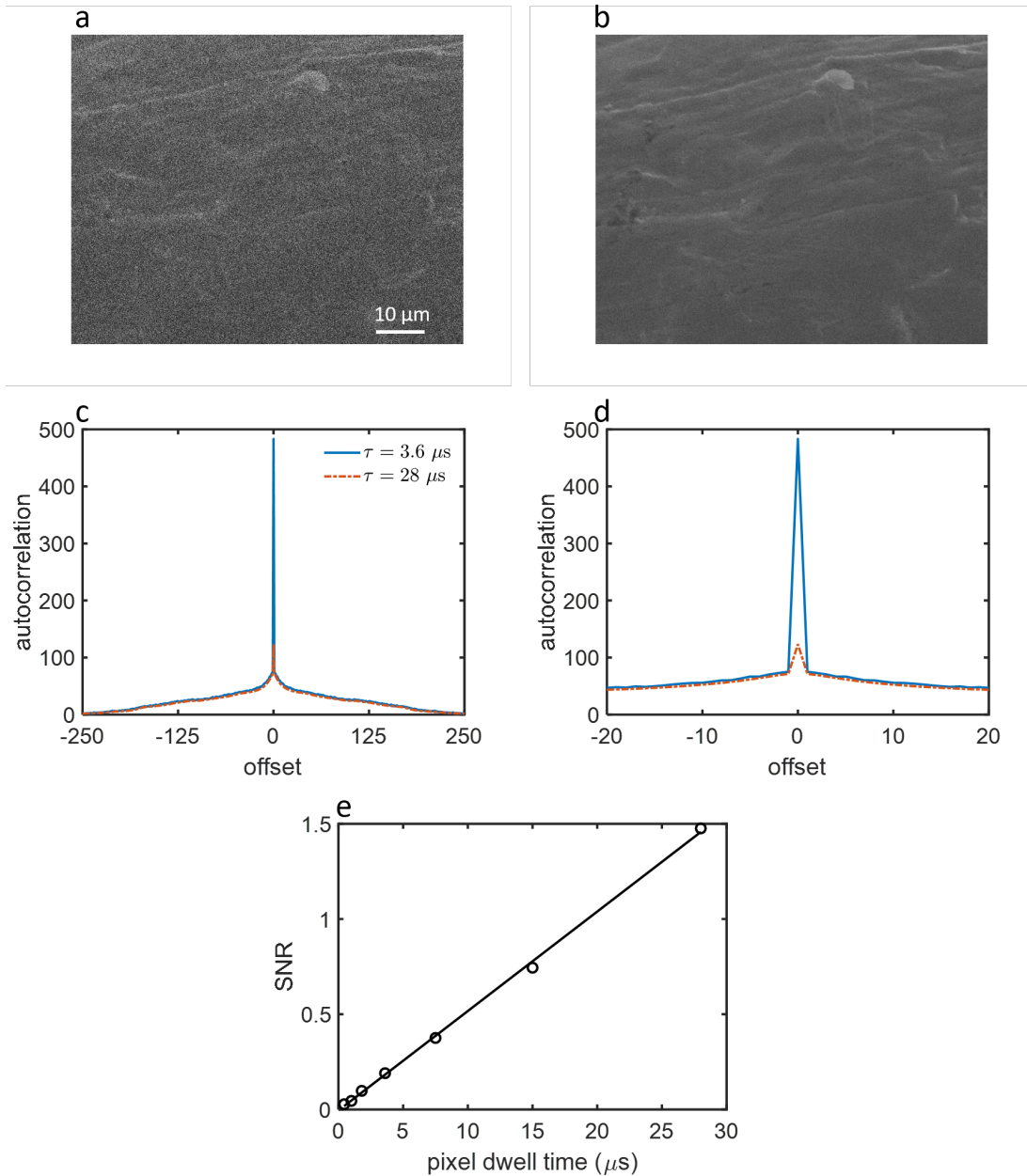


Figure 3-3: SNR for SEM images. (a) SEM image of bulk copper, taken at a pixel dwell time of 3.6 μs . (b) SEM image of the same sample as (a), taken at a pixel dwell time of 28 μs . (c) Autocorrelation of the 3.6 μs dwell time image (solid blue curve) and the 28 μs dwell time image (dash-dotted orange curve). The autocorrelation is almost identical except at zero pixel offset. (d) Autocorrelation of the two images around zero pixel offset. The sharp peak at zero offset is because of image noise. The peak is lower for the 28 μs pixel dwell time image because it is less noisy. (e) SNR extracted from the autocorrelation of SEM images acquired with pixel dwell times between 0.44 μs and 28 μs . The SNR scales linearly with pixel dwell time.

autocorrelation is a three-dimensional function since the images can be offset in two dimensions. In Figure 3-3(c) we have plotted the autocorrelation for offsets in the horizontal direction; the offset in the vertical direction is zero. The solid blue curve is the autocorrelation of the image in Figure 3-3(a), and the dash-dotted orange curve is the autocorrelation of the image in Figure 3-3(b). We can see that the autocorrelation values for the two images are almost identical at all offsets except 0. Figure 3-3(d) is a magnified view of the autocorrelations around zero offset. We can see that the less noisy, longer pixel dwell time image has a smaller autocorrelation peak at zero offset compared to the higher noise, shorter pixel dwell time image.

From Figure 3-3(d) we can also see that the autocorrelation curves for small, non-zero offsets are pretty flat, especially when compared to the sharp peaks at zero offset. For example, between pixel offset values of 1 and 10, the autocorrelation of the $\tau = 3.6 \mu\text{s}$ image reduces from 75 to 46.8 (an average reduction of 3.1 per additional pixel offset), whereas it jumps to 483.4 at zero offset (an increase of 408.4 from the value at pixel offset of 1). We can use this observation to estimate the noise-free autocorrelation at zero offset, $\hat{\phi}_{NF}(0, 0)$. Thong discusses two methods of finding $\hat{\phi}_{NF}(0, 0)$. The first method is to simply set it to be equal to the value of the autocorrelation at an offset of 1 pixel, *i.e.*, $\hat{\phi}_{NF}(0, 0) = \phi(1, 0)$. The second method of estimating $\hat{\phi}_{NF}(0, 0)$ is to use linear extrapolation of the values of the autocorrelation for small pixel offsets. Both these methods are justified because, as we had discussed, the autocorrelation value does not change significantly between consecutive pixels. We decided to use the second method to extract $\hat{\phi}_{NF}(0, 0)$ because, as we can see in Figure 3-3(d), the autocorrelation is close to linear at small pixel offsets.

Once we have extracted $\hat{\phi}_{NF}(0, 0)$, we can obtain an estimate of the noise contribution $\hat{\phi}_N(0, 0)$ to $\phi(0, 0)$: $\hat{\phi}_N(0, 0) = \phi(0, 0) - \hat{\phi}_{NF}(0, 0)$. The ratio of these two quantities gives us a measure of the image SNR:

$$\text{SNR} = \frac{\hat{\phi}_{NF}(0, 0)}{\hat{\phi}_N(0, 0)}$$

We used this method to find the SNR for images of the same sample of bulk copper as in Figure 3-3 for pixel dwell time between 0.44 μs and 28 μs . Figure 3-3(e) is a plot of the extracted SNR values, indicated by unfilled black circles. The solid black line is a least-squares linear fit to the extracted values. We can see that the extracted SNR values scale almost linearly (correlation coefficient $r^2 > 0.99$) with the pixel dwell time. We can derive this linear scaling from our expression for $r_f(m)$. As discussed in Chapter 1, due to the fact that the SEM image pixel intensity is the average value of the detector signal observed for that pixel, increasing the pixel dwell time does not change the mean value of the pixel intensities: although the total signal observed for each pixel increases, the pixel dwell time increases by the same factor. Therefore, the mean pixel value remains the same. We can include this effect in our model of a real SEM image as follows: let the two pixel times t_1 and t_2 correspond to two images f_1 and f_2 . Let $t_2/t_1 = \alpha$. On changing the dwell time from t_1 to t_2 , the raw signal from the SE detector will scale by α . Therefore, we have:

$$f_1(n) \sim A_1 \cdot \text{Poisson}(s(n)) + N(0, \sigma)$$

$$f_2(n) \sim A_2 \cdot \text{Poisson}(\alpha s(n)) + \alpha N(0, \sigma)$$

Due to signal averaging, $\mathbf{E}[f_1(n)] = \mathbf{E}[f_2(n)]$. Hence, $A_1/A_2 = \alpha$. Using Equation (3.2) to find the autocorrelation $r_f(0)$, we get:

$$\begin{aligned} r_{f_1}(0) &= A_1^2 r_s(0) + A_1^2 \mathbf{E}[s(n)] + \sigma \\ r_{f_2}(0) &= \alpha^2 A_2^2 r_s(0) + \alpha A_2^2 \mathbf{E}[s(n)] + \alpha^2 \sigma \end{aligned}$$

Here, the expression for $r_{f_2}(0)$ results from the fact that scaling a random variable by k scales its variance by k^2 . Simplifying this expression for $r_{f_2}(0)$, we get:

$$r_{f_2}(0) = A_1^2 r_s(0) + A_1^2 \mathbf{E}[s(n)] / \alpha + \alpha^2 \sigma$$

Comparing this expression to the expression for $r_{f_2}(0)$, we can see that the noise-free component of the autocorrelation is the same for both but the contribution due to noise due to the Poisson nature of the signal has scaled down by α . The noise from other sources in the SEM scales by α^2 . For the imaging conditions normally used in an SEM, the contribution of noise from other sources on the SEM is small [27] and the σ^2 term can be ignored. Consequently, the SNR scales linearly with the pixel dwell time, just as we had observed in Figure 3-3(e).

In summary, this SNR measure provides another way to characterize image quality and scales linearly with the incident electron dose. We require two conditions to be fulfilled for this method to work: the noise autocorrelation must be non-zero only at a pixel offset of 0, and the autocorrelation of the ground truth image must vary much more slowly than the noise autocorrelation. From the autocorrelation curves in Figure 3-3(c) and (d) we can see that noise in the SEM images does not show correlation for any non-zero pixel offsets. We also confirmed that this was the case by scanning the beam over a region of vacuum and checking the autocorrelation of such images. Further, we ensured that all samples we scanned had features that extended over many pixels so that the image autocorrelation varied slowly at non-zero pixel offsets. We note that the absolute value of this SNR measure for a particular SEM image is not very informative. For example, the SNR value for the long-dwell time image in Figure 3-3(b) is about 1.5, which would be considered low in other scenarios. It is the change in the value of this SNR metric upon varying the imaging conditions which provides useful information about changes in the image quality. We will use this SNR measure to quantitatively compare the SE count images we will generate in Chapter 5 with conventional SEM images and also to compare different schemes for conditional re-illumination on the SEM. In these comparisons, we will look at the relative values of the SNRs of the images being compared rather than the absolute values.

Although the example image we considered in Figure 3-3 is fairly uniform and does not have a lot of features, the SNR measure works equally well for all types of

SEM images. Appendix A presents an example calculation of this SNR measure for an SEM image with more features.

Having defined metrics for grayscale images, we now turn to devising schemes for conditional re-illumination imaging of such samples in the next section. The schemes that we develop will be based on the conditional re-illumination schemes we had developed for opaque-and-transparent samples in Chapter 2, modified to account for the grayscale nature of the samples.

3.2 Schemes for implementation of grayscale conditional re-illumination for grayscale objects

In Chapter 2 the stopping criterion of our conditional re-illumination scheme was determined by either the number of detected electrons or the number of illuminations. In this section we will adapt these ideas to conditional re-illumination in SEM imaging. As we had discussed in Chapter 1, conventional SEM imaging gives us average SE signal for every pixel. In chapters 4 and 5 we will show that we can count SEs in an SEM and that the SE count images have better SNR and contrast than conventional images taken under the same conditions. Further, just as for STEM imaging in Chapter 2, we can spread out the total incident electron dose over several rounds of illumination instead of illuminating the sample with a high dose once. These possibilities motivated the two SEM re-illumination schemes we will develop here. The first scheme, which we will call M -limited conditional re-illumination, uses a stopping criterion based on the number of illuminations. The second scheme, which we will call N_{SE} -limited conditional re-illumination, uses a stopping criterion based on the number of SEs detected for each pixel. For each scheme, we will assume that we have a high-dose reference image to benchmark the errors and incident electron dose for the scheme.

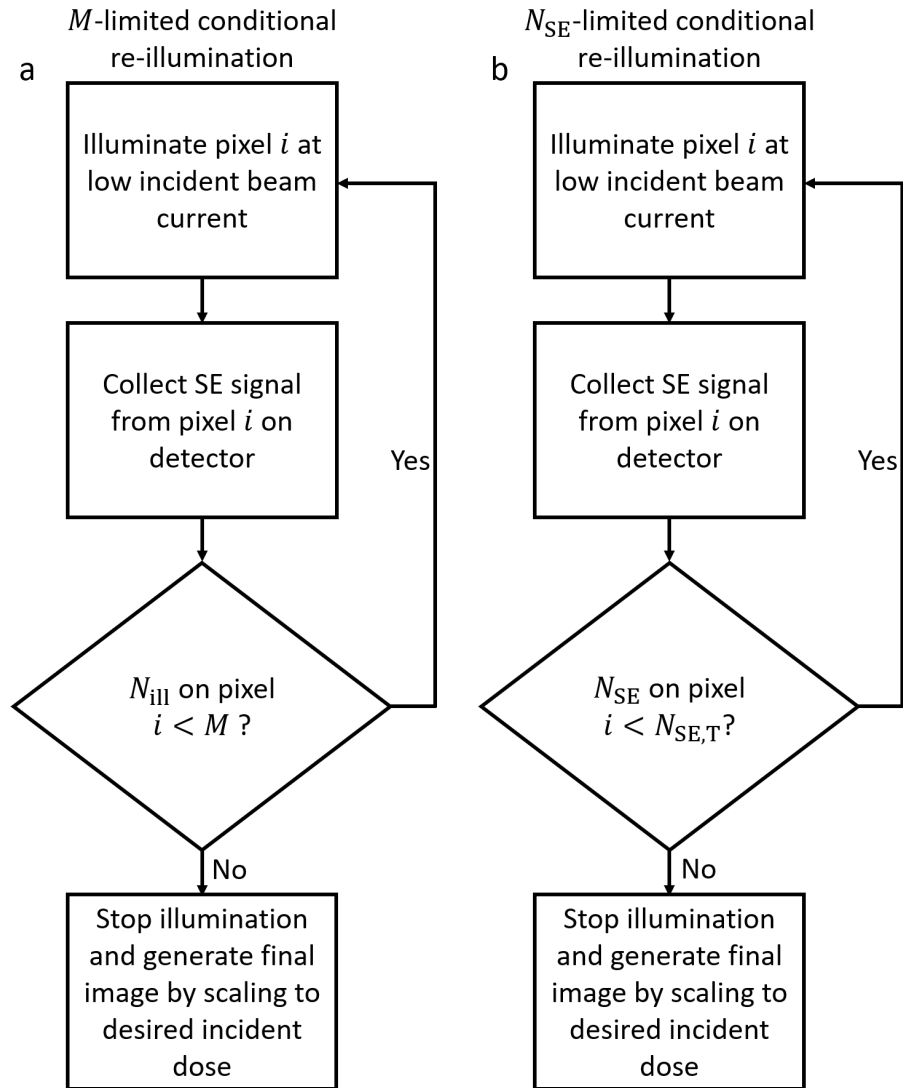


Figure 3-4: Schemes for grayscale conditional re-illumination. (a) M -limited scheme. Each pixel is illuminated and the SE signal from it recorded until the number of illuminations N_{ill} reaches a threshold M . (b) N_{SE} -limited scheme. Each pixel is illuminated and the SE signal from it recorded until the number of secondary electrons N_{SE} reaches a threshold $N_{\text{SE},T}$.

3.2.1 M -limited conditional re-illumination

This scheme is depicted for one pixel of the image in Figure 3-4(a). The pixel is illuminated by a low current incident beam and the number of SEs emitted from that pixel recorded on the SE detector. If the number of illuminations N_{ill} on that pixel is less than a threshold M , we continue illuminating it. Once the $N_{\text{ill}} = M$, we stop illuminating the pixel. In other words, the total number of illuminations for every pixel is limited by M . Therefore, the ‘conditioning’ or stopping criterion in this scheme is simply an upper bound on the number of sample illuminations. Each pixel would receive the same average dose, equal to M times the dose from one illumination. At the end of the imaging process, we scale the number of SEs recorded for every pixel to correspond to the incident electron dose in the reference image for comparison.

This scheme appears to be equivalent to illuminating the sample once with M times the dose. However, in Chapter 4 we will show that SE counting becomes inaccurate due to non-linearities at higher currents (above 8 pA under the conditions we used). Therefore, limiting the current to low values (we will use 2 pA in Chapter 5 for SE count imaging) gives accurate SE counts per pixel as the image builds up over M illuminations. Further, spreading the dose out over several illuminations lowers the dose rate on the sample which is an important factor when considering sample damage [31].

3.2.2 N_{SE} -limited conditional re-illumination

This scheme is depicted for one pixel of the image in Figure 3-4(b). The pixel is illuminated by a low current incident beam and the number of SEs recorded on the SE detector. If the number of SEs from the pixel is below a certain threshold $N_{\text{SE},T}$, we illuminate the pixel in the next round. If N_{SE} crosses $N_{\text{SE},T}$, we skip the pixel in future rounds of illumination. We continue re-illuminating until all pixels have

$N_{\text{SE}} \geq N_{\text{SE,T}}$ or a maximum number of illuminations is reached. After each round of illumination we have a map of the pixels that need to be skipped in the next round. At the end of the imaging process, we know the number of illuminations it took for each pixel to achieve $N_{\text{SE}} \geq N_{\text{SE,T}}$.

In this scheme the dose per pixel will be variable. On average, pixels on the sample with higher SE yield will require fewer illuminations than pixels with lower SE yield. Just as for the M -limited scheme, we create a final image by scaling N_{SE} for every pixel to correspond to the incident electron dose for the reference image. However, unlike the M -limited scheme, the scaling factor will vary for every pixel. Due to the accounting of signal for every pixel and possibility of non-uniform number of illuminations over the sample, this scheme is similar to the conditional re-illumination scheme from Chapter 2.

3.3 Conclusions

In this chapter we described three metrics for evaluating image quality: mean absolute relative error (MARE), contrast, and signal-to-noise-ratio (SNR). We evaluated these metrics for example SEM images, and we also discussed requirements for using these metrics and the types of samples and imaging setups each of the metrics is best suited for. We also presented two schemes to adapt conditional re-illumination to SEM imaging. These schemes were inspired by the conditional re-illumination scheme of Chapter 2, adapted to account for the number of SEs.

We will use the image quality metrics from this chapter throughout Chapter 5 to characterize our SE count images as well as compare the two SEM re-illumination schemes. We will show that SE count imaging has a better contrast and SNR than conventional imaging under identical imaging conditions. Through our implementation of both these conditional re-illumination schemes, we will calculate the reduction in electron dose enabled by these schemes by accepting a lower SNR or higher MARE.

We will show that there is no clear advantage of using one scheme as opposed to the other in all cases. The choice of scheme depends on the type of sample and which image quality metric is important. Our implementation of the two schemes will be offline (*i.e.*, the schemes will not be implemented on live SE images but instead in post-processing) due to limitations of the setup we had available. However, we will propose schemes for live, online conditional re-illumination that could be achieved with a modified SEM setup.

Chapter 4

Histogram- and oscilloscope-based secondary electron counting in SEM

In this chapter, we will demonstrate SE counting in an SEM using two techniques: image histograms and oscilloscope outcoupling. Our primary motivation for developing the image-histogram and oscilloscope-based electron counting methods described in this chapter was to implement the low-dose imaging and conditional re-illumination techniques described in Chapter 3. As discussed in Section 3.2 of that chapter, the implementation of these techniques relies upon counting the number of SEs in order to be as efficient as possible with the incident electron dose on the specimen. As we had discussed in Chapter 1, although circuit-based SE counting has been used to characterize SE detectors, image histograms have not been used for this purpose. Therefore, we wanted to develop an electron counting method that could be easily implemented on any SEM without the need to develop complicated external circuitry.

In Chapter 1, we saw how Yamada and co-workers [93–97] implemented SE count imaging on the SEM using external discriminator and pulse counting circuits coupled and synchronized with the SEM and showed that the SNR for electron count-

ing images was better than the SNR for conventional SEM images. However, this implementation did not lead to electron count imaging being incorporated into commercial SEM imaging. One factor that was responsible for this lack of incorporation was the complicated external circuitry required for counting SEs and synchronizing the counting with the SEM scan coils. Developing these external circuits and making them compatible with different SEM softwares and configurations is a challenge. Further, the long pixel dwell times required for this implementation of electron count imaging limited the application of this technique to radiation-damage-resistant samples. For the kind of low-dose imaging of radiation-sensitive samples that we are interested in, fast pixel dwell times need to be coupled with low incident beam currents to limit the damage imparted to the sample during imaging and allow the microscopist to engineer both the total electron dose (number of incident electrons) and the dose rate (incident electron current) incident on the specimen [31].

In this chapter, we will demonstrate an alternative implementation of SE counting in the SEM using image histograms. For low-dose SE count imaging we aimed to maximize the number of detected SEs from every pixel. Hence, we implemented the histogram-based SE counting technique for both the in-chamber and in-lens detectors. This implementation requires no external circuits and utilizes histograms of the live SEM images which are available in the SEM software directly. Therefore, this technique could easily be incorporated into commercial SEM software and used to perform live electron count imaging. We will also extend Joy's analysis of the DQE of SE detectors [26, 27] (as discussed in Section 1.3.1 of Chapter 1) by using our histogram counting technique to measure the DQE at various operating conditions. Further, we will verify the results we obtain from image histograms by outcoupling the signal from the SE detectors onto an oscilloscope and analyzing the statistics of the observed SE pulses. This outcoupling technique is a simplified version of Yamada's implementation [95, 97]. We will perform our electron counting and analysis at pixel dwell times down to 1.8 μs . Coupled with the low incident beam currents used in Yamada's work, this work extends electron count imaging to

be applicable to radiation-sensitive biological samples. In Chapter 5, we will use these histogram and oscilloscope-based SE counting techniques to implement offline low-dose and conditional re-illumination imaging schemes.

This chapter is organized into three sections. We will introduce image histograms and provide an example of their use by implementing Joy’s method of calculating DQE [26,27] in Section 4.1.1. Following this introduction to image histograms, in Section 4.1.2, we will describe our SE counting results, discuss the optimization of imaging conditions to obtain the SE quantization, analyze the statistics of our image histograms, use this analysis to calculate the DQE for both the in-lens and in-chamber SE detectors, and check these results with those obtained in Section 4.1.1.2 using Joy’s method. We will also analyze the effect of changing working distance on the DQE. In Section 4.2, we will verify our histogram counting results by coupling the SE detector signal onto an oscilloscope and comparing the statistics of the histograms obtained from this signal with the image histogram statistics. Finally, in Section 4.3, we will summarize our results and discuss possible extensions and implementation in commercial SEM software. The measurements reported in this chapter were performed in collaboration with John Simonaitis and Navid Abedzadeh (Massachusetts Institute of Technology).

Table 4.1 lists the abbreviations and symbols used in this chapter. Section D.3 of Appendix D lists the MATLAB scripts used to generate image histograms and analyze oscilloscope signals in this chapter.

4.1 SE counting using image histograms

In this section, we will first take a detailed look at the histograms of conventional SEM images and their use in quantifying the DQE of SE detectors using Joy’s method. Then, we will consider how the histogram changes when microscope settings such as the brightness, contrast, beam current, and scan speed are changed. We will see how

DQE	Detection Quantum Efficiency
N	Mean number of incident-beam electrons
I_B	Incident electron beam current
e	Fundamental unit of charge; 1.6×10^{-19}
δ	Secondary electron yield
$N_{\text{SE,object}}$	Mean number of SEs emitted per pixel
N_{SE}	Mean number of SEs detected per pixel
SNR_{exp}	SNR from image histogram
$\text{SNR}_{\text{ideal}}$	Ideal SNR for a given I_B and δ
V_{sup}	Suppressor voltage
WD	Working distance
FWHM	Full-width at half maximum

Table 4.1: List of symbols and abbreviations used in this chapter

optimizing these conditions allows us to see SE quantization in the histogram with both the in-chamber and in-lens detectors. Finally, we will consider the statistics of the SE distributions obtained from these detectors and use these statistics to calculate the DQE of the detectors.

4.1.1 Image histograms in SEM

In this section we will introduce histograms in the SEM and describe what they represent. As an example of the application of image histograms, we will quantify the DQE of both the in-lens and in-chamber SE detectors on our SEM using Joy's method. Our discussion of image histograms in this section will form the basis of the results in the rest of this chapter.

4.1.1.1 Introduction to histograms of SEM images

Figure 4-1(a) shows an SEM image of spherical tin nanoparticles attached to a copper support structure on a standard TEM grid (image courtesy Navid Abedzadeh). This image, as well as all other SEM images used in this chapter, has a pixel resolution of 1024×768 . Each pixel of the image has an 8-bit pixel brightness value, which means that the pixel brightness lies in the range $[0, 255]$. Figure 4-1(b) is the histogram of

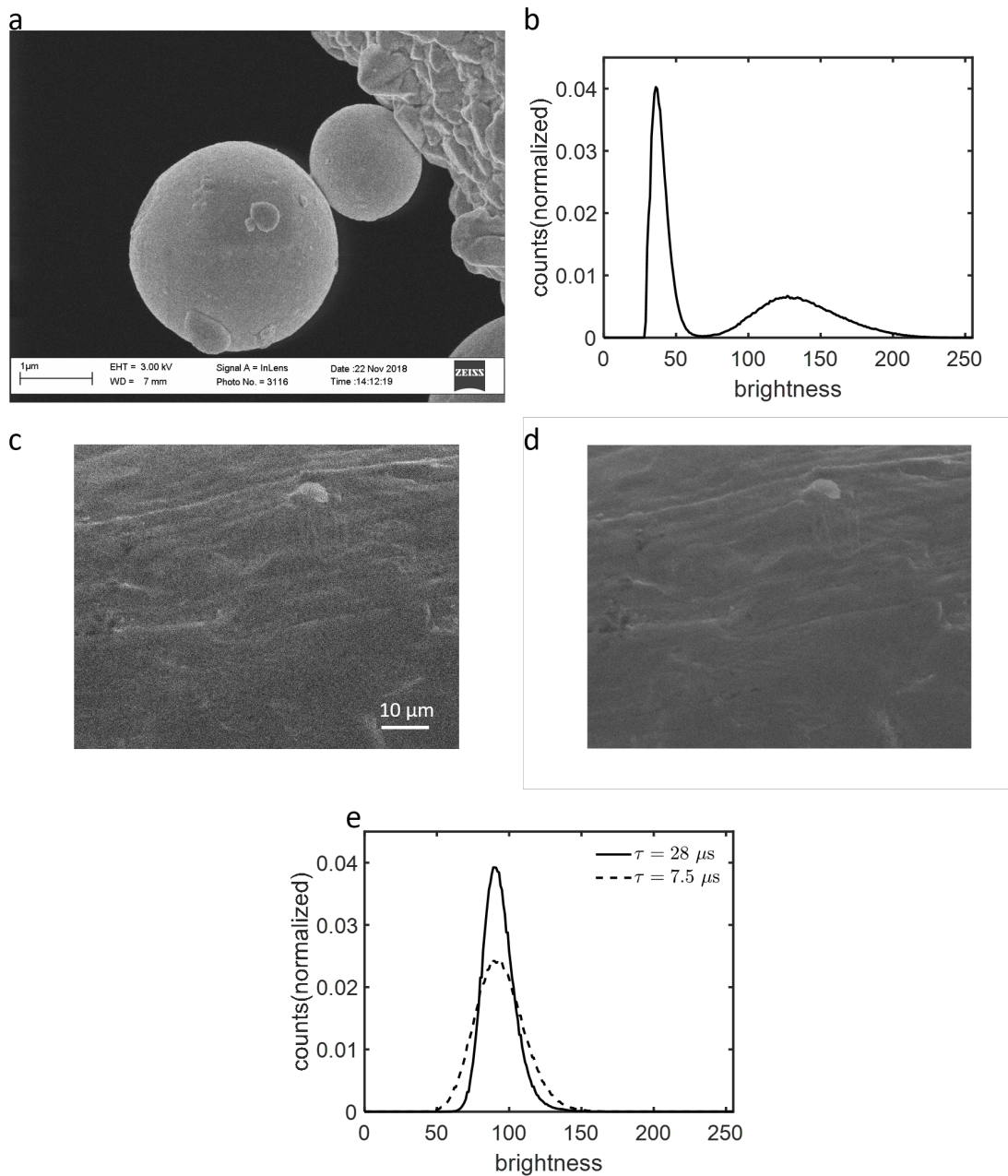


Figure 4-1: Image histograms in SEM. (a) SEM image of spherical tin nanoparticles on a copper TEM support grid, courtesy Navid Abedzadeh. (b) Histogram of the SEM image in (a). The pixels fall into two broad peaks: darker pixels representing the background and brighter pixels representing the sample. (c) SEM image of a uniform region of copper taken at a pixel dwell time τ of 7.5 μs . (d) SEM image of the same uniform region of copper as (c) taken at a pixel dwell time τ of 28 μs . The image is less noisy than (c). (e) Image histograms of the SEM micrographs in (c) (solid curve) and (d) (dashed curve). The less noisy image (d) has a narrower image histogram.

this image. It is a plot of the number of pixels with a certain pixel brightness versus the range of pixel brightnesses. We can see that the pixel brightnesses fall into two broad peaks corresponding to the darker (lower pixel brightness) background pixels and the brighter (higher pixel brightness) pixels representing the tin nanoparticles and copper support structure. Therefore, the histogram reveals the distribution of pixel brightnesses in the image and can be used to quantify noise in it. For example, Figures 4-1(c) and 4-1(d) are SEM images of the same uniform region of copper, taken at two different pixel dwell times τ . Figure 4-1(c) was taken at a small pixel dwell time $\tau = 7.5 \mu\text{s}$, meaning that fewer beam electrons were incident on each pixel of the image, than Figure 4-1(d), for which $\tau = 28 \mu\text{s}$. As we will discuss in Section 4.1.1.2, fewer incident electrons lead to a more noisy signal, and the image in Figure 4-1(c) looks noisier than 4-1(d). Figure 4-1(e), which shows the histogram of these two images, confirms this observation. The image histogram for Figure 4-1(c) (dashed curve) is broader than that for Figure 4-1(d) (solid curve) indicating that the pixel brightness distribution is narrower for the less noisy image in Figure 4-1(d). Note that the means of the two image histograms are the same (pixel brightness level of 90) due to signal time-averaging, as discussed in Section 1.1.3 of Chapter 1. As shown by Joy et al. [26, 27], we can use the width of the histogram to characterize the SNR of the image and the DQE of the SE detectors. We will demonstrate this method in the next section as an example of the utility of histograms in SEM.

4.1.1.2 Joy's method of calculating image SNR and DQE in SEM

Before describing Joy's method of calculating DQE, we will describe the basic statistics of SE emission and introduce terminology that we will use in the rest of this chapter.

The average number of incident electrons N on the object is given by:

$$N = \frac{I_B \tau}{e}. \quad (4.1)$$

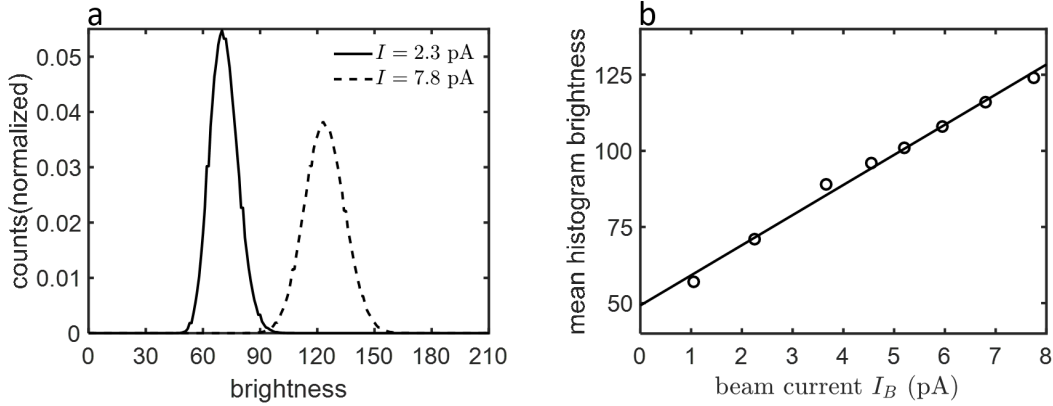


Figure 4-2: Joy’s method of calculating image SNR and SE detector DQE. (a) Histograms of two SEM images of the same uniform aluminum sample taken at two incident beam currents: 2.3 pA and 7.8 pA. The higher current histogram has a higher mean pixel brightness as well as higher width. (b) Variation of mean histogram brightness with incident beam current. The vertical intercept of the least-square fit line is the offset level due to the image brightness and contrast settings.

Here, I_B is the incident beam current, τ the pixel dwell time, and e the unit of electron charge; $e = 1.602 \times 10^{-19}$ C. Then, the average number of SEs emitted by an object pixel, $N_{SE,object}$, is given by:

$$N_{SE,object} = N \cdot \delta = \frac{I_B \tau}{e} \cdot \delta.$$

Here, δ is the total SE yield of the object pixel. Finally, the average number of SEs detected by the SE detector from that pixel, N_{SE} , is given by:

$$N_{SE} = N \cdot \delta \cdot \text{DQE} = \frac{I_B \tau}{e} \cdot \delta \cdot \text{DQE}. \quad (4.2)$$

Here, DQE is the detection quantum efficiency and measures the fraction of the SEs produced per object pixel that are detected by the SE detector.

Note that we only discussed the mean number of incident and SEs. As discussed in Section 1.3.1 of Chapter 1, the full distribution of SEs is complicated, with several reports detailing deviations from ideal Poisson statistics. These deviations manifest as an increase in the observed variance of the distribution of SEs [21,90]. In this chapter, we will only use the mean SE counts.

Joy's method of finding the DQE of SE detectors in SEM relies on using image histograms to calculate the signal-to-noise-ratio (SNR) at different imaging currents. Note that SNR here is unrelated to the SNR metric introduced in Chapter 3, and it is related to the mean and width of the image histogram, as we will describe below.

Using the regular SEM imaging process (as described in Chapter 1), we generated histograms for in-chamber and in-lens SE detector images. Figure 4-2(a) shows image histograms for the in-chamber detector from a uniform region of aluminum foil obtained at an incident beam energy of 10 kV and $\tau = 28 \mu\text{s}$, a working distance of 13 mm, at two beam currents: $I_B = 2.3 \text{ pA}$ (solid black curve) and $I_B = 7.8 \text{ pA}$ (dashed black curve). The mean pixel brightness for the low-current histogram for is 71 and for the high-current histogram is 124. We expect the mean pixel brightness to be higher for the image histogram at higher incident beam current due to higher $N_{SE,\text{object}}$. Further, the histogram for $I_B = 2.3 \text{ pA}$ is narrower than the histogram for $I_B = 7.8 \text{ pA}$; the full-width-at-half maximum (FWHM) for the $I_B = 2.3 \text{ pA}$ histogram is 18 pixel brightness units, while the FWHM for the $I_B = 7.8 \text{ pA}$ histogram is 24 pixel brightness units. For a Poisson distributed random variable, the variance is equal to the mean. Hence, the width of its probability distribution increases as the square root of the mean. Therefore, as $N_{SE,\text{object}}$ increases due to higher current, we expect the histogram mean to increase linearly and the histogram FWHM to increase as the square root of the current. For an ideal detector (DQE = 1), assuming Poisson statistics, we would expect the SNR to be equal to $\sqrt{N_{SE,\text{object}}}$. We will refer to this quantity as $\text{SNR}_{\text{ideal}}$.

However, before we can use our image histograms to calculate SNR, we have to correct the histograms for the image brightness and contrast settings we used. From Equation (4.2), we would expect the image histogram mean to go to zero as the beam current I_B reduces to zero. However, the specific image brightness and contrast settings we use might offset this value and make it non-zero. In order to find what this offset level is, we plot the image histogram mean as a function of the incident beam current in Figure 4-2(b). As expected, the variation of the image histogram

mean with I_B was linear. We extrapolated the least-square fit line (shown in black) to zero current to find the offset level. In this case, the offset level was 49 pixel brightness units. We will see in Section 4.1.2 that this value is close to the noise level for the in-chamber detector at these settings. Next, we subtracted the offset level from the image histogram means to find the true means at zero offset. The ratio of the corrected histogram mean to the FWHM gave us SNR_{exp} , which is the experimental SNR. SNR_{exp} includes the effect of the non-unity DQE and is equal to $\sqrt{N_{SE}}$, the SNR for a Poisson distribution with mean equal to the number of SEs that are detected at the in-chamber detector. From Equation (4.2),

$$N_{SE} = N_{SE,\text{object}} \cdot \text{DQE}.$$

Using our definitions of $\text{SNR}_{\text{ideal}}$ and SNR_{exp} , we get

$$\text{SNR}_{\text{exp}}^2 = \text{SNR}_{\text{ideal}}^2 \cdot \text{DQE}.$$

Hence,

$$\text{DQE} = \text{SNR}_{\text{exp}}^2 / \text{SNR}_{\text{ideal}}^2.$$

From the image histograms for the different incident beam currents shown in Figure 4-2 we extracted a DQE between 0.15 and 0.22 depending on the incident beam current. We ascribe this variation to small non-linearities in the detector at higher currents as discussed further in sections 4.1.3.1 and 4.2.2. We also performed a similar analysis for the in-lens detector and obtained a DQE between 0.3 and 0.6. Note that in these calculations, we used $\delta = 0.2$ for our aluminum sample [18, 20, 21]. The values of DQE extracted from our implementation of Joy's method are in the range reported previously for well-designed in-chamber and in-lens detectors [26, 27] and will serve as a benchmark for our technique of calculating DQE in Section 4.1.3.2.

4.1.2 SE quantization in SEM image histograms

In this section, we will demonstrate our observation of distinct peaks in the image histogram due to the quantization of SEs. As described in Chapter 1, we used a Zeiss LEO 1525 with a Gemini column in our experiments. The native Zeiss SEM interface (SmartSEM, V05.01.08) was used to form SEM images. We scanned a featureless sample of aluminum foil at low magnification (pixel size $> 1 \mu\text{m}$) at an incident beam energy of 10 keV. In order to observe SE quantization, we needed to be careful about the imaging conditions we used. Therefore, we will first discuss the optimization of imaging parameters: the number of incident electrons on the sample, the image brightness, image contrast, detector suppressor voltage, and beam blanking. We will show how peaks due to SE quantization emerged in our image histograms when the parameters were optimized. Note that in this section we will discuss the optimization of these parameters for the in-chamber SE detector. We performed a similar analysis for the in-lens detector, as discussed in Appendix B.

4.1.2.1 Number of incident electrons

As specified in Equation (4.2), the number of SEs detected by the SE detector is given by $N_{SE} = \frac{I_B \tau}{e} \cdot \delta \cdot \text{DQE}$. As we had discussed in Section 1.3.1 of Chapter 1, the SE distribution is close to Poisson for the range of incident beam energies we are working with. A Poisson distribution resembles a normal distribution at high mean; Joy reported the transition from normal to Poisson-like in the SE image histogram [27]. In order to observe SE quantization, we ensured that N_{SE} was low by lowering the incident beam current I_B and/or the pixel dwell time τ . Further, we also chose an incident beam energy of 10 keV to ensure that δ was low enough to resolve single SEs, as discussed in Section 1.1.2 of Chapter 1. We also used the smallest condenser aperture (diameter $7.5 \mu\text{m}$) on our SEM to limit I_B . With the smallest aperture, we further optimized N by tuning the gun extraction voltage and the pixel dwell time τ to obtain SE in the image histogram.

Figure 4-3(a) shows the image histograms for a featureless aluminum sample for different values of τ . This experiment was carried out at $I \approx 2.3$ pA. The different histograms correspond to a τ of 28 μs (blue curve), 15 μs (orange curve), 7.5 μs (purple curve), 3.6 μs (green curve), and 1.8 μs (dark red curve). Note that each histogram in this chapter is plotted with the bins on the horizontal axis centered at each integer between 0 and 255. Further, each histogram, unless stated otherwise, is normalized so that the total area under the histogram sums to 1. Stated another way, each histogram is an empirical probability mass function.

As we lowered τ from 28 to 15 μs the histograms became wider but retained the same mean, just as the histograms in Figure 4-1(e) for the images in Figures 4-1(c) and (d). When we reduced the dwell time to 7.5 μs , a series of sharp peaks appeared in the histogram. The first of these peaks was centered at a brightness level of 44, the second at 51, and the third at 58. Upon reducing τ to 3.6 μs , the first peak remained at 44, but the second shifted to 58, and the third to 73. This shift continued on further reducing the dwell time to 1.8 μs , in which case the second peak appeared at 73 and the third at 105. Simultaneously, as τ was reduced, the first peak at brightness 44 increased in intensity.

We attributed the peaks that emerged in the histogram at small dwell times to SE quantization [27]. As we will discuss in greater detail in Section 4.1.2.5, the constant sharp peak at pixel brightness 44 can be attributed to noise and corresponds to pixels with zero detected SEs. The shifting of the other peaks' pixel brightness levels when the dwell time was lowered can be explained as a consequence of signal time-averaging. Suppose a pixel that emitted two SEs on average when $\tau = 7.5$ μs had a brightness of 58. The difference in pixel brightness between the two-SE level and the noise level would be 14. When $\tau = 3.6$ μs , this pixel would have emitted one SE on average. However, due to signal time-averaging, the brightness of this pixel would have remained 58. Therefore, a brightness of 58 would now have corresponded to one emitted SE, and the gap between the noise level and the one-SE level would have been 14. In the histogram in 4-3(a), we see that at $\tau = 3.6$ μs (purple curve)

the first peak is at pixel brightness 58, as we would have predicted from the above example. At $\tau = 1.8 \mu\text{s}$, we would predict the gap between the zero and one-SE levels to double to 28 and the one electron level to be at pixel brightness 72. This is very close to the observed peak at 73. By the same logic, whenever the dwell time is halved, we would expect the pixel brightness level of each of the SE peaks to double, leading to doubling of the gap between successive electron peaks observed in Figure 4-3(a).

In Figure 4-3(b) we show the variation of the histogram with incident beam current I_B . We controlled I_B by changing the gun extraction voltage. These measurements were made at $\tau = 3.6 \mu\text{s}$. The values of I_B for which we plotted histograms in this figure are 5.6 pA (dashed blue curve), 3.9 pA (dash-dotted orange curve), and 1 pA (solid purple curve). We can see that as I_B reduces, the one-SE peak at pixel brightness 58 becomes stronger, while the three and higher SE peaks become weaker. The two-SE peak is stronger for 3.9 pA than the other incident beam current values. These trends indicate that the mean number of detected SEs reduced on reducing I_B . In Section 4.1.3.1 we will analyze this reduction quantitatively and see that it is linear (as expected from Equation (4.2)) at low incident beam currents. This linear trend supports our conclusion that the peaks in the histogram arise due to integral number of SEs.

Based on the results in Figures 4-3(a) and (b), we decided to use $\tau = 3.6 \mu\text{s}$ as the pixel dwell time for future experiments since this dwell time gave us strong multi-electron peaks that are well-separated. We varied I_B depending on the desired mean number of SEs per pixel by tuning the gun extraction voltage.

4.1.2.2 Image brightness

The image brightness specifies the DC offset applied on the signal coming from the SE detector. It is different from the pixel brightness which is the 8-bit value of each pixel in the image. The SEM software displays the image brightness as a number

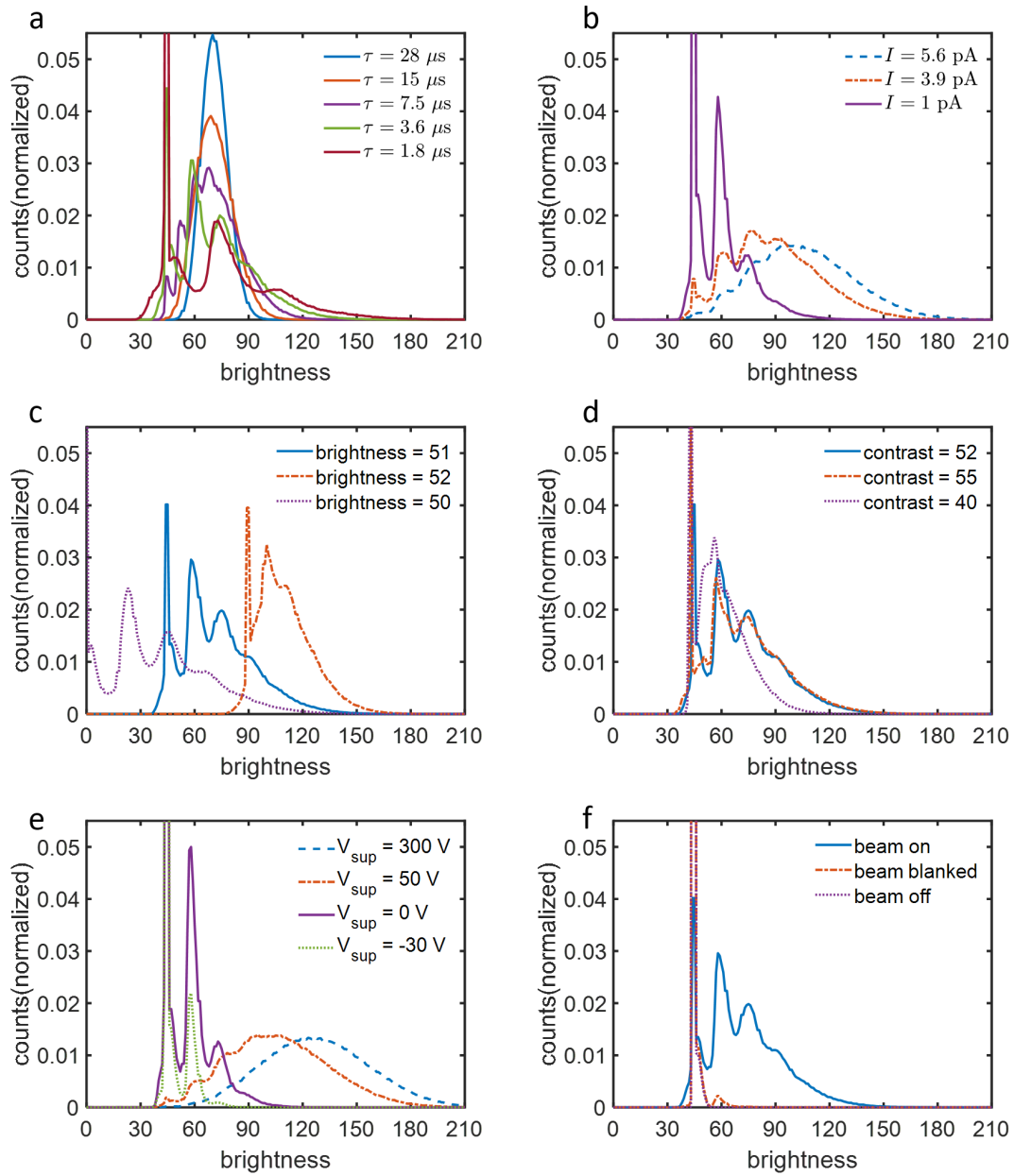


Figure 4-3 (*previous page*): SE quantization observed on the in-chamber detector in SEM. (a) Variation of the image histogram with pixel dwell time τ . As we reduced τ , distinct peaks appeared in the image histogram corresponding to integral numbers of detected SEs. (b) Variation of the image histogram with incident beam current I_B for constant τ . As I_B reduced, the SE peaks became sharper and the histogram transitioned from nearly Gaussian to Poisson-type. (c) Optimization of image brightness. An image brightness of 51 (solid blue curve) ensured that the sharp noise peak was well-resolved (unlike image brightness 50, dotted purple curve) and the SE peaks did not merge into one another (unlike brightness 52, dash-dotted orange curve). (d) Optimization of image contrast. A contrast of 52 (solid blue curve) ensured that the peaks did not merge into one another (unlike contrast 40, dotted purple curve) and the noise-artifacts did not become significant (unlike contrast 55, dash-dotted orange curve). (e) Variation of image histogram with in-chamber detector suppressor voltage. As the suppressor voltage was reduced, the SE peaks became more distinct and the mean SE count reduced since fewer SEs were attracted to the detector. (f) Image histograms for beam on (solid blue curve), beam blanked (dash-dotted orange curve), and beam off (dotted purple curve). When the beam is blanked, the SE peaks disappear except for a small residual one-SE peak which disappears when the beam is turned off. The remaining sharp peak corresponds to the zero-SE noise level.

between 0 and 100. We obtained the data shown in Figures 4-3(a) and (b) at an image brightness of 51.

Figure 4-3(c) shows the change in the image histogram on changing the image brightness on the SEM software. The image brightness values shown are 51 (solid blue curve), 52 (dash-dotted orange curve), and 50 (dotted purple curve). As we would expect from adding a DC offset, the histogram shifted to higher pixel brightness values for higher image brightness, and vice versa. Further, the peaks in the histogram merged with each other at 52 image brightness. As we will show in Section 4.2.1, the maximum voltage output from the SE detector at the image contrast settings we used was about 5.6 V. Therefore, as we increased the image brightness, the range over which the signal from the detector could vary reduced. The peak merging was a result of this reduced dynamic range of the detector signal. Conversely, at image brightness 50 and below, the sharp noise peak shifts to zero pixel brightness and can no longer be clearly resolved. Based on the results of Figure 4-3(c), we decided to use an image brightness of 51 for all experiments to clearly visualize the zero-SE peak and avoid artifacts in our analysis due to some pixels being saturated at zero pixel brightness but not lose the quantization of the peaks due to reduced dynamic range

at higher image brightnesses.

4.1.2.3 Image contrast

The image contrast specifies the overall dynamic range over which the signal from the SE detector can vary. On the SEM software, the image contrast is specified as a value between 0 and 100. We obtained the data in Figures 4-3(a),(b), and (c) at an image contrast of 52.

Figure 4-3(d) shows the image histograms for different values of image contrast. These histograms were obtained at an image brightness of 51. The values of image contrast in this plot are 52 (solid blue curve), 55 (dash-dotted orange curve), and 40 (dotted purple curve). We see that reducing the contrast reduced the peak separation and the peaks merged with each other at image contrast of 40. The merging is a result of a lower dynamic range, similar to the effect in our discussion about image brightness in Section 4.1.2.2. At contrast 55, we started seeing shoulders on both sides of the one-SE peak around pixel brightnesses 50 and 70. We suspect that these shoulders were due to detector noise that gets amplified at high contrast. Based on the results of Figure 4-3(d), we decided to use a brightness of 52 for all experiments to get well-separated SE quantization peaks without introducing artifacts due to detector noise.

4.1.2.4 Detector suppressor voltage

The suppressor voltage V_{sup} is applied to the external cage on the in-chamber SE detector to accelerate and attract the low-energy SEs towards it. In Figure 4-3(e), we plot the image histograms for $V_{\text{sup}} = 300$ V (dashed blue curve), $V_{\text{sup}} = 50$ V (dash-dotted orange curve), $V_{\text{sup}} = 0$ V (solid purple curve), and $V_{\text{sup}} = -30$ V (dotted purple curve). The change in mean SE count was small when we reduced V_{sup} from 300 V to 50 V. At $V_{\text{sup}} = 300$ V, $N_{SE} = 5.59$ and at $V_{\text{sup}} = 50$ V,

$N_{SE} = 4.18$. Most SEs have energies less than 50 eV, so an accelerating voltage above 50 V should be sufficient to attract them to the detector. However, the histogram changed dramatically on reducing V_{sup} from 50 V to 0 V; $N_{SE} = 0.78$ at 0 V. Between 50 V and 0 V, the suppressor voltage was in the range of SE energies, and the detector missed more and more of the SEs as the voltage was reduced. At $V_{sup} = 0V$, there was no voltage to attract the SEs to the detector, and only SEs that were emitted with sufficient energy and in the direction of the detector were detected. Hence, the mean number of SEs went down, and very few pixels registered two or three SEs as seen in the purple curve. On reducing the suppressor voltage to negative values, the electron peaks were further suppressed, and at $V_{sup} = -30$ V only a small fraction of the pixels registered one SE ($N_{SE} = 0.18$). In this condition the detector repelled most SEs and only a very small fraction of them made it to the detector. The contribution of SE₃s (as described in Chapter 1 Section 1.1.2.1) was much more significant in this condition due to the relative lack of SE₁s and SE₂s at the detector. The sequential suppression of the histogram peaks as the suppressor voltage was reduced is more evidence towards their origin being due to SE quantization.

We decided to use a suppressor voltage of 300 V (the maximum possible value) to maximize the number of SEs that were registered on our detector. However, in experiments where the electromagnetic field in the vicinity of the sample was important (such as SE yield measurements), we reduced this voltage to 50 V since the statistics of SEs remained almost the same at this lower suppressor voltage.

4.1.2.5 Beam blanking

In Figure 4-3(f), we plot the image histogram in three cases: beam on (solid blue curve), beam blanked (dash-dotted orange curve), and beam off (dotted purple curve). We see that when the beam was blanked, most of the pixels had a brightness of 44 except for a small peak at the one SE brightness level of 58. When the incident beam was switched off this small peak disappeared. When the incident beam is blanked in

the SEM, deflection plates near the electron gun prevent it from reaching the sample; however, the beam is still on. Therefore, it is possible for stray SEs from higher up in the column to make it to the detector leading to the small peak. Note the similarity between this histogram and the histogram obtained at $V_{\text{sup}} = -30$ V in Figure 4-3(e). In both cases, a few SEs made it onto the detector leading to the small one-SE peak. When the beam was switched off, no secondaries were generated anywhere in the column which led to the one-SE peak disappearing. The only peak now was at pixel brightness 44. From this observation, we concluded that this peak was due to detector noise and corresponds to the zero-SE level. As we had discussed in Section 4.1.2.2, the exact position of this peak was determined by the image brightness setting.

4.1.3 Characterization of in-chamber and in-lens detectors using SE counting

In the previous section, we showed how quantized SE peaks emerged in the image histogram when the number of incident electrons, image brightness, image contrast, and detector suppressor voltage were optimized. In this section, we will use the image histogram peaks to analyze the statistics of the SEs. We will look at the mean SE number N_{SE} obtained from the image histograms and use it to calculate the DQE of the in-chamber and in-lens detectors. We will compare the DQE obtained for these detectors with the value obtained in Section 4.1.1.2 using Joy's method. We will also look at the variation of the DQE with sample working distance.

4.1.3.1 SE counting for in-chamber detector image histograms

Figure 4-4(a) is an image histogram for the in-chamber detector at an incident beam energy of 10 keV, $I_B = 7.5$ pA, $\tau = 3.6$ μ s, image brightness of 51, contrast of 52, and a working distance of 13 mm. We can treat this histogram as a probability mass function and find the mean pixel brightness. Knowing the zero-, one-, and two-SE

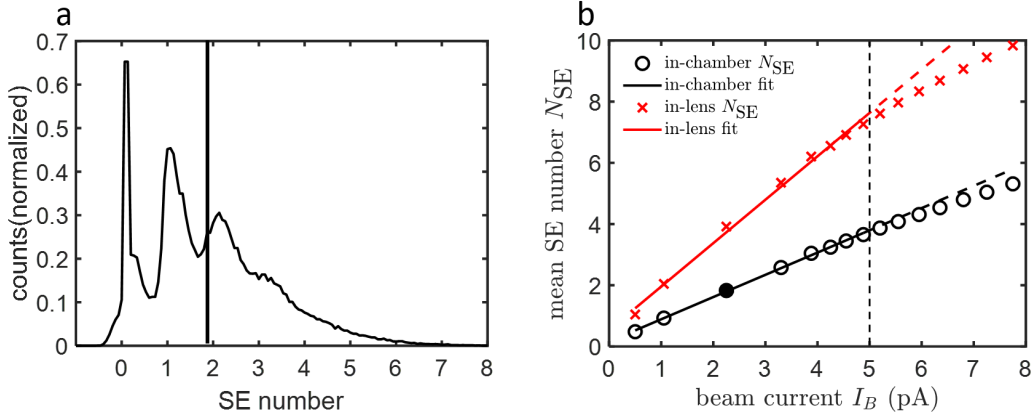


Figure 4-4: Statistics of image histogram SE counting. (a) Image histogram with the mean pixel brightness level of 1.91, marked with a vertical line. (b) Variation of mean SE number with incident beam current for the in-lens and in-chamber detectors. Unfilled black circles indicate extracted N_{SE} values for the in-chamber detector, and red crosses indicate N_{SE} values for the in-lens detector. Filled black circle indicates N_{SE} for the histogram in (a). The least-squares fit lines (black for the in-chamber detector and red for the in-lens detector) are for $I_B < 5$ pA, indicated by the vertical dashed black line. Above this incident beam current, the extracted N_{SE} values deviate from this fit due to signal pileup. The DQE extracted from the slope of these lines is 0.16 for the in-chamber detector and 0.32 for the in-lens detector.

levels, we can translate this brightness to a mean SE number N_{SE} . For the histogram in Figure 4-4(a), this mean SE number is 1.91, indicated by the dotted black vertical line.

In Figure 4-4(b), we plot the mean SE number extracted from image histograms for a range of incident beam currents, for both the in-chamber detector (unfilled black circles) and the in-lens detector (red crosses). The data point corresponding to the histogram in Figure 4-4(a) is indicated with a filled black circle. As we lowered the beam current from 7.8 pA to 0.5 pA, the mean SE number reduced from 5.31 to 0.48 for the in-chamber detector and from 9.83 to 1.04 for the in-lens detector. We see that the mean SE number varies linearly with I_B for low currents and shows some non-linearity at higher currents for both detectors. The solid black line is a least-square fit to the extracted SE number for $I_B < 5$ pA (indicated by the vertical dotted black line) for the in-chamber detector, and the solid red line is a fit to the extracted SE number for the same range of incident beam current for the in-lens

detector. We expect that the non-linearity at higher currents is caused by increasing incidents of multiple SEs hitting the detector within a fraction of the pixel dwell time, causing signal pileup and consequent incorrect extracted SE values. We will discuss the mechanism for this pileup in more detail in Section 4.2.2. In all our applications of electron counting in this chapter and Chapter 5, we will restrict ourselves to a very small probability of multiple incidence by either using low currents ($I_B < 5$ pA) to extract detector parameters and/or using very fast scans (as in Chapter 5).

We note that the mean SE number is higher by a factor of 2 for the in-lens detector than for the in-chamber detector. The higher mean SE number indicates that the in-lens detector is more efficient at collecting SEs than the in-chamber detector, as reported previously [22, 26].

4.1.3.2 DQE from in-chamber and in-lens detector image histograms

From Equation (4.2), the mean SE number N_{SE} is given by:

$$N_{SE} = N \cdot \delta \cdot \text{DQE} = \frac{I\tau}{e} \cdot \delta \cdot \text{DQE}$$

As mentioned before, we used $\tau = 3.6$ μs for all the image histograms used to extract the data shown in Figure 4-4. We used a value of 0.2 for the SE yield of our aluminum sample at 10 kV [18, 20, 21]. Knowing these values, we extracted the DQE for both the in-chamber and in-lens detectors from the slope of the best-fit lines for the mean SE number N_{SE} versus beam current I_B plots in Figures 4-4(b) and (c). The extracted values were 0.16 for the in-chamber detector and 0.32 for the in-lens detector. These values are close to the range of DQE values we had obtained using Joy's method in Section 4.1.1.2 and are also in the range of reported values in the literature for these detectors [26, 27]. As discussed by Joy, DQE values can vary by orders of magnitude depending on the detector geometry and age [27]. As an example of another source of this variation, in the next section we will see how the DQE of both detectors varied with the working distance.

4.1.3.3 Variation of DQE with working distances

We investigated the variation of the in-chamber and in-lens detector DQE as a function of the working distance as an application of this technique of finding the DQE. As discussed in Section 1.1.3 of Chapter 1, our SEM has an 8 kV electrostatic field along the optical axis to attract SEs to the in-lens detector. Working with a similar column design, Griffin [22] has previously reported qualitative improvement in the fine details observable in the in-chamber detector image with increasing working distance. All results reported in this section were obtained with the incident beam energy at 10 kV, $I_B = 2.3$ pA, and $\tau = 3.6$ μ s.

In Figure 4-5(a) we plot the image histograms for the in-chamber detector at two working distances (WD): 13 mm (solid black curve) and 34 mm (dash-dotted black curve). We see that the SE peaks are well-defined for the lower working distances but not the higher working distance. This observation indicates that the mean SE number was higher at WD = 34 mm than at WD = 13 mm. From the histograms, $N_{SE} = 5.78$ for WD = 34 mm and $N_{SE} = 1.66$ for WD = 13 mm. This increase in mean SE number (and consequent increase in DQE) translates to higher SNR, consistent with Griffin's observation.

In Figure 4-5(b) we plot the image histograms at WD = 13 mm (solid red curve) and WD = 34 mm (dash-dotted red curve) for the in-lens detector. Contrary to our observations with the in-chamber detector, for the in-lens detector N_{SE} was lower at WD = 34 mm, where it is 0.32, than at WD = 13 mm, where it was 4.42. This effect was not reported by Griffin, who noted little variation in the in-lens image with increasing working distance.

Figure 4-5(c) is a plot of the DQE for both detectors for working distances between 13 mm and 34 mm. Once again, we can see the trend of increasing DQE for the in-chamber detector and decreasing DQE for the in-lens detector with increasing WD. We believe that the reduction in DQE for the in-lens detector with increasing WD is a result of the diminishing effect of the 8 kV electrostatic field designed to

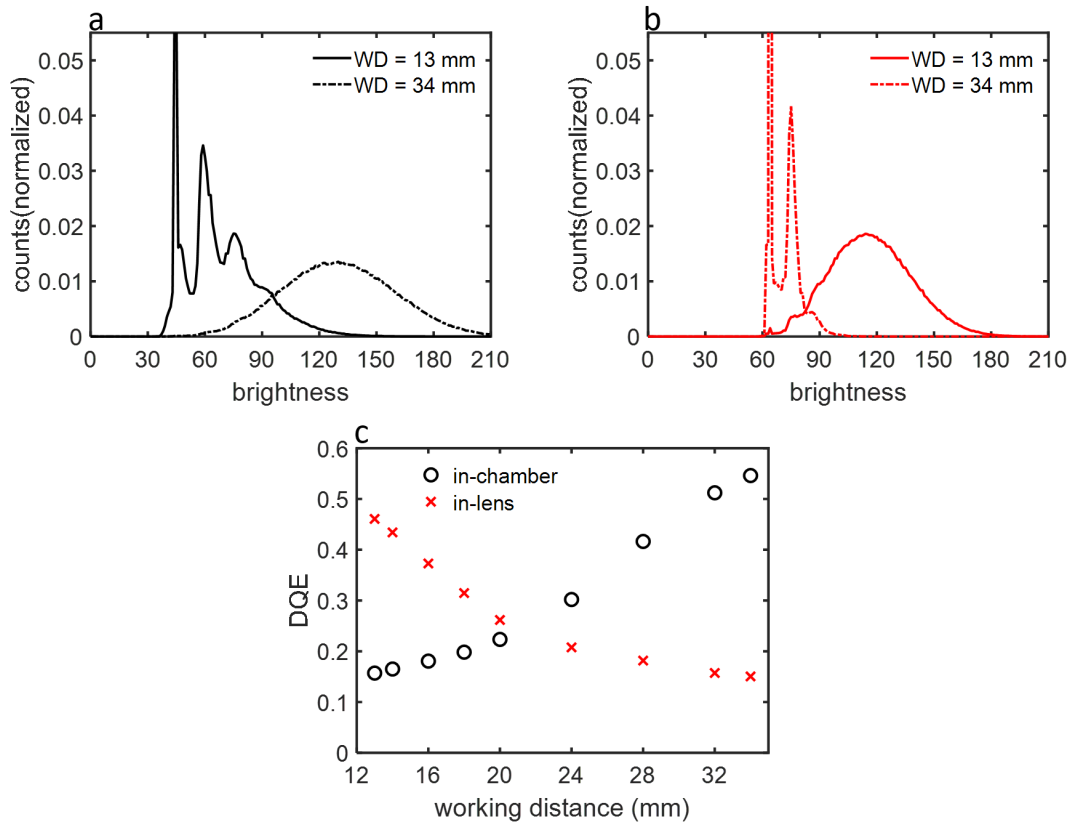


Figure 4-5: Variation of DQE with working distance for in-chamber and in-lens SE detectors. (a) Image histograms for SEM images captured using the in-chamber detector for working distances of 13 mm (solid black curve) and 34 mm (dash-dotted black curve). The mean SE number is higher at 34 mm than at 13 mm. (b) Image histograms for SEM images captured using the in-lens detector for working distances of 13 mm (solid red curve) and 34 mm (dash-dotted red curve). The mean SE number is lower at 34 mm than at 13 mm. (c) DQE for the in-chamber detector (unfilled black circles) and in-lens detector (red crosses) at different working distances. The DQE for the in-chamber detector increases with working distance, while the DQE for the in-lens detector goes down.

attract SEs to the in-lens detector. At higher working distances this field would be weaker and less effective at drawing SEs back up the column to the in-lens detector. The weaker field would also result in more electrons being available to be detected by the in-chamber detector which explains part of the increase in its DQE with increasing working distance. A second reason for the increase in the DQE of the in-chamber detector with working distance could be that at larger working distances, the detector geometry and location with respect to the sample becomes more favorable and allows more SEs to reach the detector. Further, as the working distance increases, the

solid angle within which most of the BSEs are emitted covers more of the surface of the objective lens polepiece and chamber walls of the SEM. Therefore, the BSEs can generate more SE_3 s which would be detected by the in-chamber detector. The in-lens detector, placed along the optical axis so that it is much less sensitive to SE_3 s by design, would not see this increase. We believe that the reduction in in-lens detector DQE was not seen by Griffin because of higher incident beam currents which ensured that even at large working distances, sufficient SEs were detected at the in-lens detector to generate a high-SNR image.

4.2 SE counting using oscilloscope outcoupling

In Section 4.1 we described our scheme and observations of SE quantization using the image histogram. We presented evidence for the observed histogram peaks arising due to SEs and applied these findings to calculate the DQE of the in-chamber and in-lens SE detectors and map the variation of the DQE with working distance. In this section, we will extend the histogram technique by directly analyzing the signal from the SE detectors by outcoupling it onto an oscilloscope. We performed this outcoupling to reproduce the image histograms using the direct time-domain signal from the SE detector and rule out the possibility of the histogram peaks arising from an artifact of the SEM imaging algorithm. Therefore, this outcoupling provides further evidence of SE quantization in the image histogram and suggests extensions of this work towards live electron count imaging and implementation of the conditional re-illumination schemes described in Chapter 3. We will consider these extensions in more detail in Chapter 5. As we had done in the discussion of the image histogram technique, we will focus on the in-chamber SE detector here; we obtained similar results for the in-lens detector.

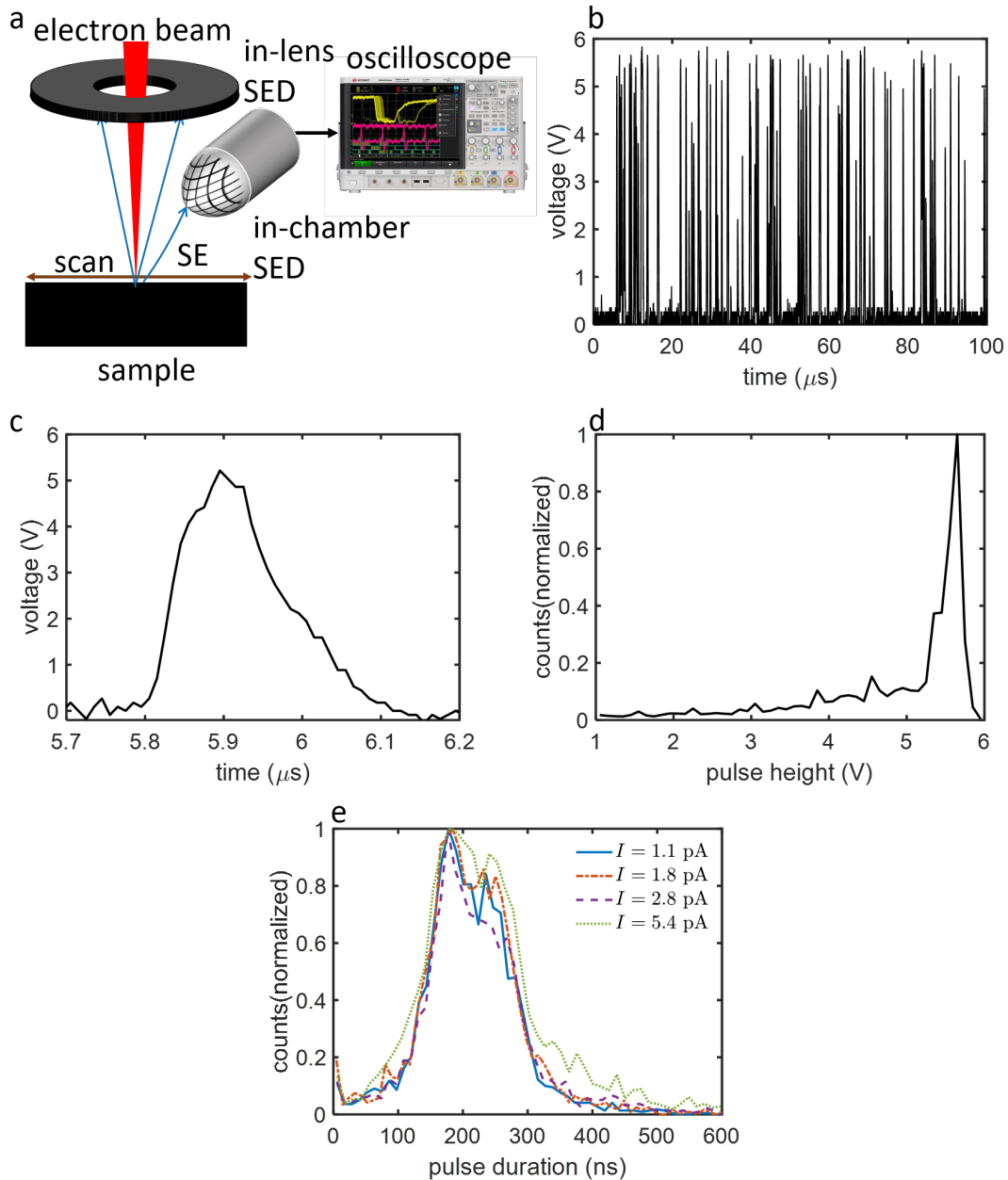


Figure 4-6: Oscilloscope outcoupling of SE detector signal. (a) Scheme for oscilloscope outcoupling. The signal from the SE detector is directly analyzed on an oscilloscope. (b) 100 μs output signal from the in-chamber detector on the oscilloscope (sampled at 10 ns) showing pulses due to detected SEs. (c) A single signal pulse with a FWHM time duration of 148 ns. (d) Histogram of signal pulse heights showing that most pulses are saturated at 5.6 V. (e) Histograms of the FWHM pulse durations for I_B between 1.1 pA and 5.4 pA. All histograms have a mean of 180 ns.

4.2.1 Introduction to oscilloscope outcoupling

Figure 4-6(a) is a schematic of the oscilloscope outcoupling scheme we will use in this section. In this experiment, we held the incident beam stationary over one spot on a uniform sample of aluminum. Since the sample was uniform and the beam was held stationary, we did not need to synchronize the collection of detector signals on the oscilloscope with the SEM scanning; we assumed that the expected number of SEs for a time window corresponding to the pixel dwell time did not vary over the collection period. The SE signal from the in-chamber detector was coupled to a 2 GHz LeCroy WaveRunner 6200A oscilloscope through a standard BNC cable. As described in more detail in Section 4.2.2, we used the outcoupled signal to generate histograms on the oscilloscope and compared these histograms with the image histograms generated from the SEM image.

The outcoupling port on our detector was present after a pre-amplification stage which meant that the signal we obtained on the oscilloscope was not the raw signal from the photomultiplier tube. Oatley [28,87], Baumann and Reimer [89], and Novák [29] have quantified the number of photoelectrons generated at the photocathode per incident SE on the scintillator of the SE detector; at 10 kV bias voltage the mean number of photoelectrons is between 5-10 depending on the material of the photocathode and configuration of the photomultiplier. Each of these photoelectrons will create a voltage pulse in the raw signal from the photomultiplier with a pulse time duration on the order of 10-20 ns [29,97]. However, as we will describe in more detail later in section, we observed one pulse per incident SE with a mean time duration of ≈ 180 ns. These longer pulses were a result of the low-pass filtering and amplification applied at the pre-amplification stage. Therefore, we did not observe pulses from individual photoelectrons excited by each detected SE. However, for the purpose of SE counting, the longer-time pulse generated by each detected SE was sufficient as long as pulses from successive SEs did not overlap with each other. At the end of this subsection we will show how the settings we used ensured that the probability of pulses overlapping with each other was very low.

From Figure 4-6(b) we can also see that the pulses had varying time durations. In Figure 4-6(e), we plot histograms of the pulse time duration of 2×10^4 observed pulses, with the time duration measured at the pulse FWHM, for incident beam currents between 1.1 pA and 5.4 pA. The distribution of pulse time duration was approximately Gaussian with a mean duration of 180 ns. Moreover, the distribution remained the same for different incident beam currents up to 8 pA (not plotted here). As the current increased, the average number of pulses per time window increased, but their width followed the same distribution as in Figure 4-6(e). Therefore, we concluded that each pulse was the result of a single SE detection, and the number of pulses in each time window corresponded to the number of SEs incident on the detector in that time.

As described in Section 4.1, the maximum beam current we used in our experiments was 8 pA and $\tau = 3.6 \mu\text{s}$. Using Equation (4.2) and assuming that $\delta = 0.2$ and the DQE for the in-chamber detector is 0.16, $N_{SE} = 5.7$. Therefore, at this beam current, there is a high probability of multiple SEs incident on the detector within the pixel dwell time, which increases the probability of overlap between the pulses generated by these SEs. We ascribed the deviation from linearity of our SE count measurements in Figure 4-4 to this increasing probability of pulse overlap at higher incident beam currents. Lowering the beam current reduces the probability of pulse overlap and results in linear scaling of SE count with beam current.

4.2.2 Oscilloscope histograms and statistics

Once we had determined the origin of the pulses in the outcoupled signal on the oscilloscope, we could start comparing its statistics to those of the image histograms we had analyzed in Section 4.1.3.1. As described in Section 1.1.3 of Chapter 1, the brightness of each pixel on the SEM image corresponds to the average signal level from that pixel. Therefore, we collected a series of 10^4 signal windows on the oscilloscope, each of time duration $5 \mu\text{s}$, sampled at 10 ns. The total collection time for all the signal

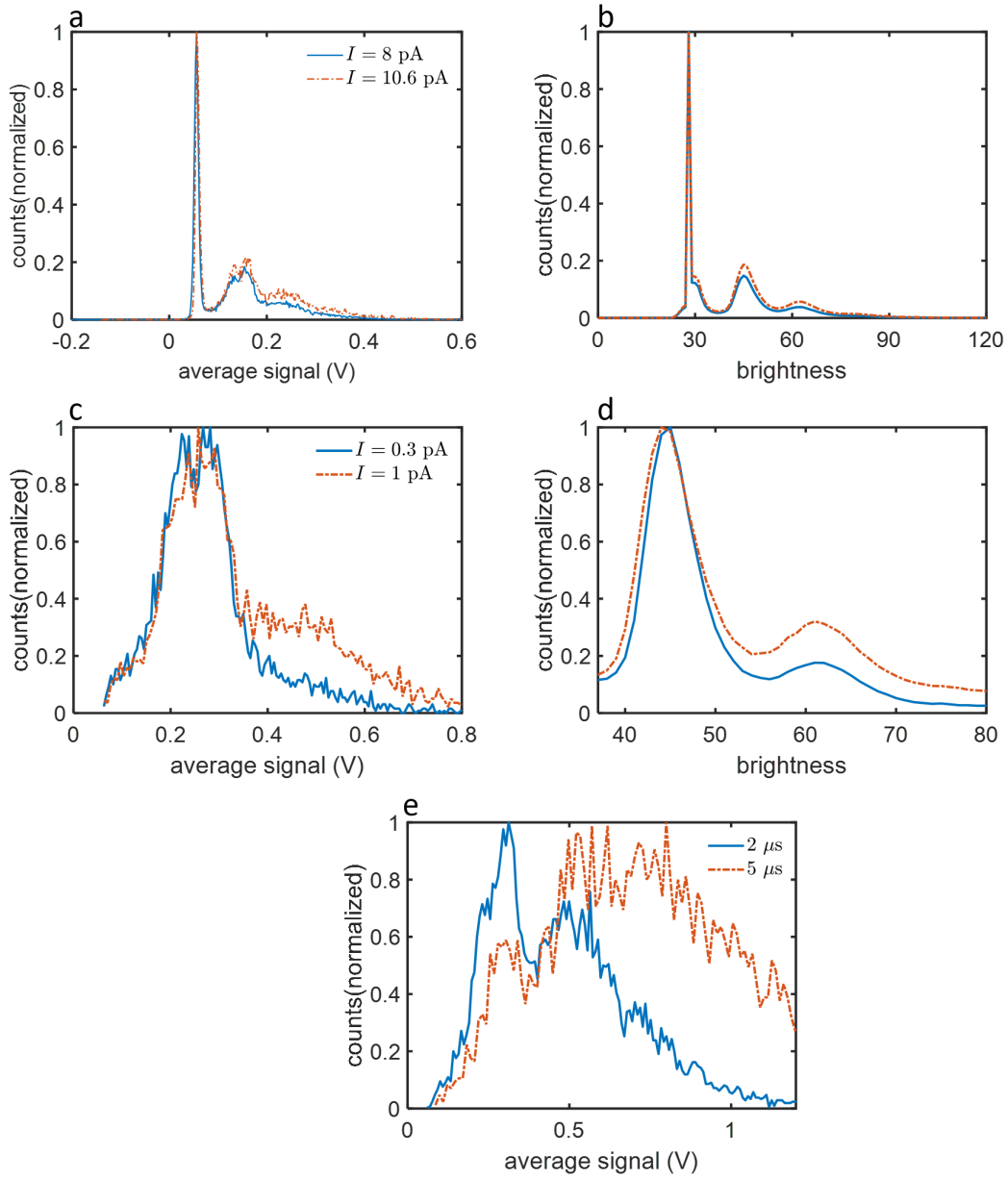


Figure 4-7 (*previous page*): Oscilloscope histograms and their statistics. (a) Histogram of the average signal level from 10^4 , 5 μ s signal collection windows on the oscilloscope for $I_B = 8$ pA (solid blue curve) and $I_B = 10.8$ pA (dash-dotted orange curve). Both histograms show a sharp noise peak and two broad integral SE peaks with the intensity of the SE peaks being higher for the higher incident beam current histogram. The mean SE number for the $I_B = 8$ pA histogram was 0.94 and for the $I_B = 10.8$ pA it was 1.24. (b) Image histograms for the same object region at the same incident beam currents as (a). The mean SE number for the $I_B = 8$ pA histogram was 1.07 and for the $I_B = 10.8$ pA it was 1.25. (c) Oscilloscope histogram for 5×10^3 , 5 μ s detector signal windows, acquired with an oscilloscope trigger voltage of 0.6 V, for $I_B = 0.3$ pA (solid blue curve) and $I_B = 1$ pA (dash-dotted orange curve). The higher current histogram shows higher counts in the two-SE peak region. (d) Image histograms for the same object scan regions for the same incident beam currents as (c). The ratio of the one- and two-SE peaks is ~ 5 at $I_B = 0.3$ pA and ~ 2.5 at $I_B = 1$ pA for both the oscilloscope and image histograms. (e) Oscilloscope histograms for 5×10^3 detector signal windows of duration 2 μ s (solid blue curve) and 5 μ s (dash-dotted orange curve) with trigger voltage of 0.6 V. Both histograms show distinct SE peaks, and the higher duration histogram has higher intensity for two-SEs and higher SE numbers indicating a higher mean SE count.

windows was about 40 minutes. We were limited in the number of signal windows we could collect by the memory of the oscilloscope and contamination buildup as discussed later in this section. We used random triggering on the oscilloscope to ensure that the collected signal was not biased. However, a small fraction ($< 2\%$) of the signal windows had incomplete SE pulses at either the beginning or end of the window collection time. We did not consider these windows in our analysis of oscilloscope histograms. Since the fraction of such windows was small, we do not expect their omission to impact the statistics we will report here.

In Figure 4-7(a), we plot the histogram of the average signal level from the collected signal windows. Note that this histogram (and others in this figure) is normalized to the height of the highest peak instead of the histogram area which was the case for the earlier histograms we have discussed in this chapter. We made this change to make it easier to visualize the differences between the histograms at different incident beam currents. The solid blue curve in Figure 4-7(a) corresponds to a beam current of 8 pA and the dash-dotted orange curve corresponds to 10.8 pA. The histograms for both currents exhibited a sharp peak at an average voltage value of 0.06 V and two broad peaks at average voltages of 0.15 V and 0.24 V. For

comparison, in Figure 4-7(b) we plot image histograms for the same currents with the same settings. Note that the image brightness in this histogram was slightly different than in Figures 4-4 and 4-5 (50.9 instead of 51) leading to different peak positions. In the discussion on image brightness in Section 4.1.2.2, we had described how sensitive the exact peak positions are to image brightness. The image histograms show the usual sharp noise peak and distinct one- and two-SE peaks. The presence of these peaks in the histogram generated from the oscilloscope signal, as well as the similarity between the overall shape and regular spacing of the peaks in the two types of histograms, provides further evidence that the origin of these peaks is SE quantization. We also note that the oscilloscope histogram appears to be noisier because of the fewer signal windows used to generate it (10^4) compared to the SEM images which have a size of 1024×768 pixels.

We can use the oscilloscope histograms to estimate the mean number of SEs using the same procedure we had discussed for image histograms in Figure 4-4. Using this process, the mean SE count for the 8 pA oscilloscope histogram was 0.94. The mean SE count for the 10.8 pA oscilloscope histogram was 1.24. In comparison, the mean SE count for the 8 pA image histogram was 1.07, and the mean SE count for the 10.8 pA image histogram was 1.25. Apart from fluctuations due to the fewer number of signal windows used to generate the oscilloscope histogram, the deviations between the oscilloscope and image histogram SE counts were caused by two additional reasons. First, there was significant sample contamination buildup during the long (40 minute) data collection time. We noticed a significant change in the mean SE count from image histograms taken at the start of the data collection and the end. For example, for the 10.8 pA dataset, the mean SE count changed from 1.43 at the start of the data collection to 0.86 by the end. The image histograms in Figure 4-7(b) are the average of two histograms taken at the start and end of the data collection, as are the mean SE counts reported from these averaged image histograms. Since the statistics for the oscilloscope histograms in Figure 4-7(a) build up over the data collection time, we compared the mean SE number from these histograms to the av-

eraged image histograms. The second reason for deviations between the oscilloscope and image histogram mean values is signal pileup, *i.e.*, the non-linearity due to overlapping pulses at high incident beam currents that we had noted in Figure 4-4(b). At beam currents of 8 pA and 10.8 pA the non-linearity can be significant leading to distortion in the oscilloscope and image histograms and their statistics.

Figure 4-7(c) shows oscilloscope histograms of 5×10^3 signal windows of duration 5 μs taken at lower beam currents to mitigate the effect of contamination buildup and detector non-linearity. The solid blue curve is for a beam current of 0.3 pA, and the dash-dotted orange curve is for a beam current of 1 pA. Further, to collect this data we used a trigger voltage of 0.6 V on the oscilloscope (instead of using random triggering as in Figure 4-7(a)) to filter out the noise pulses and get better statistics on the higher SE number pulses. The oscilloscope for $I_B = 1$ pA shows a higher signal in the two-electron peak region. Due to the lack of pulses lower than 0.6 V we could not obtain a mean SE count from these histograms. However, we can compare the ratio of the one- and two-SE peaks from these oscilloscope histograms to the values from the image histograms. Figure 4-7(c) is an image histogram for the same scan region under the same settings. The ratio of the one- and two-SE peak for both the oscilloscope and image histograms at 0.3 pA was approximately 5, and the ratio for the 1 pA histograms was approximately 2.5. Although the SE peaks in the oscilloscope histogram are not as well resolved as in the image histogram due to fewer samples, this equality between the one- and two-electron peak ratios indicates that the statistics from both types of histograms are equivalent.

In Figure 4-7(e), we plot the oscilloscope histogram for 5×10^3 pulses for sampling window times of 2 μs (solid blue curve) and 5 μs (dash-dotted red curve). We obtained both histograms with the oscilloscope trigger voltage set to 0.6 V for an incident beam current of 4 pA. Note that we used a larger aperture on the SEM (20 μm instead of 7.5 μm for all earlier results) to get higher SE signal levels. The 2 μs histogram shows two clear peaks at average signal levels 0.27 V and 0.51 V. The 5 μs histogram also shows peaks at these values and higher signal at 0.51 V and above.

Again, these results are consistent with our interpretation of the peaks as arising from single SEs. The reduction in histogram counts in going from 5 μs to 2 μs is similar to the emergence of SE peaks in Figure 4-3(a), showing the consistency between these two techniques.

4.3 Conclusions

In this chapter, we have shown how SE counting can be performed using two methods—image histograms and outcoupling of detector signal on an oscilloscope. The image histogram method builds on work by Joy et al. [26,27] and Timischl et al. [118], while the oscilloscope outcoupling method builds on work by Oatley [28,87], Baumann and Reimer [89], and Novák [29]. We used the oscilloscope outcoupling method to verify the results of the histogram method and also proved the utility of the histogram method by using it to calculate the DQE of the in-chamber and in-lens SE detectors and characterize its variation with working distance.

Our analysis of the variation of the detector DQE with working distance revealed that the DQE for the in-chamber detector increases and the DQE for the in-lens detector falls with increasing working distance. We speculated that the increase in the in-chamber detector DQE arose from greater availability of SEs due to the reduced effectiveness of the 8 kV in-lens detector attraction field at higher working distances as well as greater generation of SE_{3s} by BSEs. Establishing which of these effects is dominant by, for example, varying the in-lens detector field would be an interesting extension of this work.

Unlike the work of Joy and co-workers, we did not use image histograms to find an SNR in our work. We found that the variances of the quantized-SE count image histograms were much higher than the means. Although we found deviation from Poisson statistics in the SE emission, as we will detail in Section 5.3.3 of Chapter 5, the deviations from Poisson statistics in the histogram variances were much larger

than those reported in Chapter 5. Due to these large deviations we could not extract reliable SNR values from the image histograms. A more detailed analysis of higher-order statistics of the image histograms would be an interesting extension of this study.

The histogram SE counting method is more direct, requires no external circuitry, and could be incorporated into commercial SEM software easily to understand the statistics of the images being generated and use those statistics to optimize the image SNR. The histogram method could potentially also be used to generate electron count images by assigning an SE number to each pixel in the image based on its pixel brightness knowing the positions of the quantized electron peaks. However, as can be seen from the image histograms in Figures 4-3, 4-4, and 4-5, there is significant overlap between the one-, two-, and three-SE peaks, and assigning an SE number to pixels with brightnesses intermediate between the distinct peak regions would require a probabilistic decision scheme. Such a scheme would lead to errors in the assignment of some pixels. However, if a few errors are acceptable as a trade-off for ease of implementation, a histogram electron count imaging scheme is an attractive option for extending conventional SEM imaging. In designing such a scheme, the range of incident beam currents would be limited by the non-linearities introduced by overlapping SE pulses at high incident beam currents; the exact value of the beam current at which the non-linearity becomes significant would depend on the dead-time of the SE detector. We also showed that the single electron signal is observable in the image histogram for pixel dwell times down to 1.8 μs . Although we did not use currents as low as in Yamada's work [95,97] (the lowest current we used was 0.3 pA compared to 0.1 pA by Yamada), combining these conditions could lead to imaging of radiation-sensitive samples such as proteins and biomolecules at extremely low incident electron doses and dose rates. Such low dose-rate imaging could also be applied to time-resolved SEM imaging [107,108].

The outcoupling method, on the other hand, requires an external oscilloscope. Although we used a 2 GHz oscilloscope for the experiments reported here, the mini-

imum sampling time we used was 10 ns, which corresponds to a bandwidth of 100 MHz. Therefore, oscilloscope outcoupling could be achieved with a much cheaper oscilloscope with the tradeoff that signal dynamics faster than 10 ns (such as the response of individual photoelectrons) would not be observable. The oscilloscope outcoupling method is more versatile than the histogram method because it can allow for discrimination between signal pulses generated by SEs from the sample and background counts in the detector based on voltage levels, thereby lowering imaging noise. This method also gives us direct access to the detector signal which allows us to design custom signal processing algorithms as detailed in Chapter 5. We also note that this setup is simpler than the circuitry developed by Yamada and co-workers [95,97] for electron counting which required several filters, a discriminator, and a pulse counter. In the next chapter, we will show how outcoupling both the SEM scan waveform and the SE detector signal allows us to perform offline SE count imaging and conditional re-illumination and propose a setup for online SE count imaging and conditional re-illumination.

Chapter 5

Electron count imaging and conditional re-illumination for reduced-dose SEM

In Chapter 4, we described image histogram- and oscilloscope-based SE counting and used these techniques to find the DQE of the SE detectors in the SEM. In this chapter, we will extend the oscilloscope outcoupling technique to generate offline SE count images and implement conditional re-illumination. We will describe how this implementation achieves the incident electron dose reduction discussed in chapters 2 and 3 and propose a scheme for implementing online SE count imaging and conditional re-illumination in the SEM.

This chapter is organized into six sections. In Section 5.1, we will discuss the SEM scan algorithm and waveforms and describe how we outcoupled the SE detector signal in synchronization with the scan waveform. In Section 5.2, we will describe the code we developed to generate SE count images from the outcoupled detector data. In Section 5.3 we will show the generated SE count images and compare the contrast and SNR of SE count images with conventional SEM images. We will also use the SE count images to extract SE emission distributions and discuss their statistics.

Next, in Section 5.4, we will describe the implementation of offline conditional re-illumination using the SE detector signal and compare the MARE and SNR of images generated with re-illumination and without. In Section 5.5, we will propose an online implementation of SE count imaging and conditional re-illumination and describe the required hardware components and their specifications. Finally, we will discuss conclusions and extensions of this work in Section 5.6. In Section D.4 of Appendix D we list the MATLAB scripts used to generate SE count and conventional SEM images, calculate image quality metrics for these images, and implement offline conditional re-illumination.

The measurements reported in this chapter were performed in collaboration with John Simonaitis (Massachusetts Institute of Technology).

5.1 Scan waveforms on the SEM

In this section we will describe the features of the horizontal and vertical SEM scan waveforms. Understanding the shape and timing characteristics of these waveforms was an important step in our implementation of SE count imaging. We will also discuss how we used these features to synchronize the outcoupling of the SE detector signal with the SE scan to implement SE count imaging and conditional re-illumination.

5.1.1 Analysis of SEM scan waveforms

Figure 5-1 (a) is a schematic of scanning in an SEM. The rectangle represents the area on the sample over which the SEM beam scans. An SEM image of this sample area consists of sequentially scanned lines (demarcated by horizontal bars in Figure 5-1(a)) with a certain number of image pixels on each line (indicated by the vertical bars within the first scan line in Figure 5-1(a)). There are two types of scan functions in all SEMs: the fast, horizontal scan and the slow, vertical scan. The horizontal scan

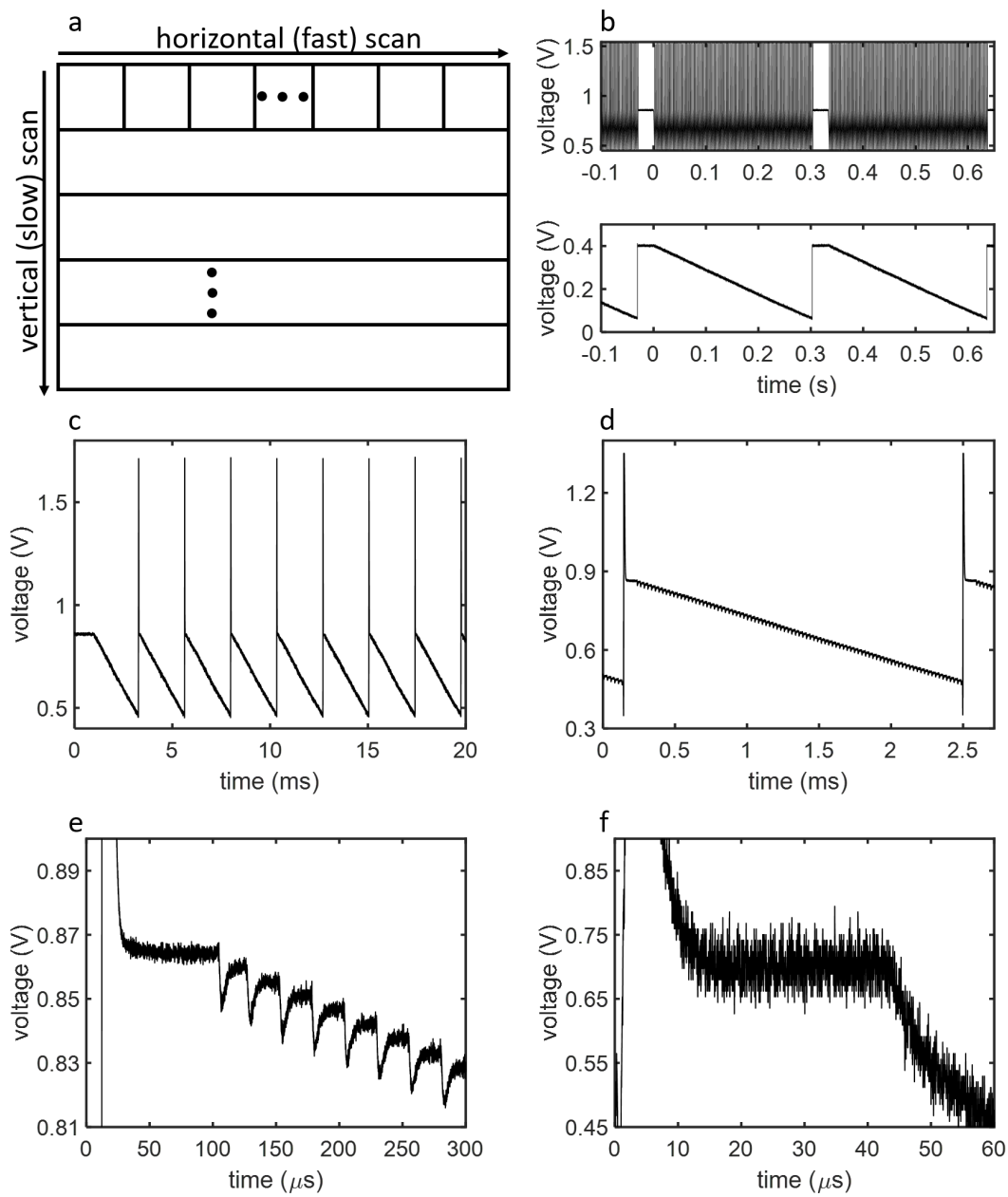


Figure 5-1 (*previous page*): Scan waveforms on the SEM. (a) Schematic of SEM scanning, showing the two scan directions in an image frame: the fast horizontal scan which defines lines in a frame and the slow vertical scan which defines the whole frame. (b) Horizontal (top) and vertical (bottom) scan waveforms for a pixel dwell time of 28 μs and a pixel resolution of 129 lines by 88 pixels per line. Both the horizontal and the vertical scan waveforms are sawtooth-shaped. The total duration of the image frame in this example was 304 ms. (c) First few lines in the horizontal scan. There is a 0.9 V spike at the end of each linescan, during the period where the electron beam is retraced to its horizontal starting position. (d) One linescan, showing the retrace spike, 70 μs front porch, and trace region. The trace region has discrete steps corresponding to image pixels on the line. (e) Start of one linescan, showing the retrace spike, front porch, and trace with discrete steps. Before each step there is a transition region with a local minimum. The time duration between successive minima is 26 μs , close to the pixel dwell time. (f) Start of one linescan for a pixel dwell time of 440 ns. Unlike (e), there are no discrete steps in this faster linescan.

defines one line in an image frame while the vertical scan defines one image frame. Here, an image frame refers to one scan of the incident electron beam over every pixel on the sample area being imaged. Therefore, within each image frame, the horizontal scan repeats for every line, while the vertical scan occurs once per image frame.

Figure 5-1(b) is an example of the horizontal (top) and vertical (bottom) scan waveforms on the SEM. We obtained these waveforms for a scan area consisting of 129 lines by 88 pixels per line at a pixel dwell time of 28 μs . The figure contains the last few lines of one image frame followed by two full image frames separated by a 30 ms frame reset time (the flat parts in the horizontal and vertical scans). Both the horizontal and vertical scans consist of sawtooth waveforms. The horizontal scan has many repeated sawtooths in every image frame with each sawtooth waveform corresponding to one linescan. The resolution in the top image is too low to distinguish between the linescans. The vertical scan consists of one sawtooth waveform per image frame. The total duration of the image frame was 304 ms excluding the frame reset time at the start of every frame.

In Figures 5-1(c) and (d) we take a more detailed look at the horizontal linescans of the first frame. Figure 5-1(c) shows the first few linescan waveforms, and Figure 5-1(d) shows one linescan. The total duration of each linescan is 2.45 ms. In these and the following figures, we will see that each linescan consists of three

regions, which we will call the retrace spike, front porch, and trace regions, following the terminology used for video scan signals. At the end of each linescan there is a 0.9 V voltage spike, lasting for 30 μs , before the scan waveform resets to the voltage at the start of the line. This resetting corresponds to the electron beam retracing to its horizontal starting position after every line. We can see these spikes at 0.1 and 2.5 ms in Figure 5-1(d). This voltage spike occurs because of ringing in the voltage of the scan electronics as it resets at the end of each line. Following the voltage spike there is a 70 μs ‘plateau’ (which we will call the front porch region) where the scan voltage is relatively flat. This region allows the scan voltage to settle to its starting value after the retrace spike and before the trace across the line on the sample begins. The front porch is followed by the trace region where the incident electron beam actually scans over the sample. This section of the scan waveform consists of a series of decreasing voltage steps, with each step corresponding to one pixel on the scan line.

We can see these steps, along with the retrace spike and front porch regions of the linescan, in greater detail in Figure 5-1(e). Each step had a size of 4 mV and a time duration of 26 μs , measured at the valleys between each step. Since the number of pixels in each line was 88, we would expect the total voltage swing for one linescan to be 352 mV. This value is close to the observed swing of 380 mV in one linescan. Further, the time duration of each step was close to the pixel dwell time of 28 μs calculated from the frame time specified for the scan speed chosen in the SEM software. Both these observations provide evidence for our assertion that these voltage steps corresponded to the individual pixels on each line of the image. We can also see that the steps are not completely flat; at the end of each pixel step there was a transition period before the scan waveform voltage level reached the value corresponding to the next pixel. This transition period was approximately 10 μs long for the settings used in Figure 5-1(e) and was probably caused by the inherent speed of the scan coil electronics. Due to the presence of this transition period, we observed the discrete pixel steps for linescan waveforms corresponding to relatively long pixel dwell times only. For pixel dwell times below $\sim 7.5 \mu\text{s}$, we did not observe this

discretization and the trace decreased continuously. Figure 5-1(f) is an example of such a scan waveform at pixel dwell time of 440 ns. This difference between slow and fast scans was important in the code we used to implement EC imaging, as we discuss more extensively in Section 5.2.1.

5.1.2 Synchronizing SEM scan with oscilloscope frame capture

Having discussed the features of the SEM scan waveforms in Section 5.1.1, we will now focus on how we used these features to synchronize the SEM scan with the collection of SE detector signal on an oscilloscope. This synchronization would be a requirement in any implementation of SE count imaging, since it provides a reference time axis for segmentation of the continuous-time detector signal into pixels on the image.

Figure 5-2 is a schematic of our scan synchronization method. When we started scanning the sample, the SEM computer sent the scan start signal to the SEM scan coils. We outcoupled the signal from the SE detector as well as the SEM scan coil voltage waveforms to two channels of an oscilloscope (2 GHz LeCroy WaveRunner 6200A) using BNC cables. We configured the data collection on the oscilloscope to be triggered by the scan coil voltage channel and set the trigger voltage to be close to the peak of the retrace spike present at the end of the first linescan in the frame. This trigger voltage setting ensured that the oscilloscope began data collection on all channels at the start of the image frame, thereby providing a common time axis for both the SEM linescan waveform and the SE detector signal. There was some variation in the exact time at which signal collection was triggered on the oscilloscope due to noise in the linescan waveform signal. In Section 5.2.2 we will discuss how this variation affected the data we collected and how we corrected for it in the SE count imaging code.

We specified the total data collection time on the oscilloscope to be a few

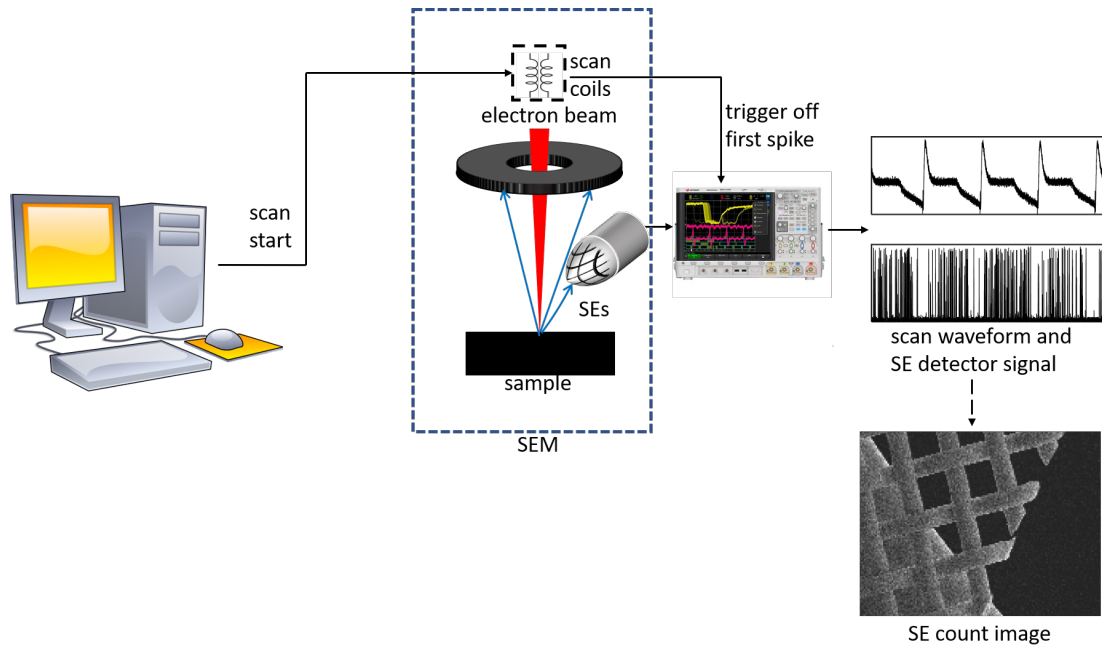


Figure 5-2: Scheme for oscilloscope synchronization. The scan start signal from the SEM computer to the scan coils initiates the beam scan over the sample. We outcoupled both the scan coil voltages and the SE detector signal onto our oscilloscope and set the trigger voltage for data collection on all channels of the oscilloscope to be very close to the peak of the retrace spike before each linescan. Therefore, this spike served as an absolute time reference for all the collected data. Each acquisition frame consisted of the scan waveform and the SE detector signal with their time axes referenced to the same retrace spike. We used several such acquisition frames to form the final SE count image offline (dashed black arrow).

ms larger than the image frame time for the area we were scanning to ensure that the entire image frame was contained in the collection time. We will refer to the SEM scan voltage signal and the SE detector signal collected over one such collection time as an *acquisition frame*. The typical frames we imaged had a pixel resolution of around 200×200 pixels, and we used a pixel dwell time of 440 ns for all data acquisition. Therefore, the total acquisition frame time was on the order of 20 ms. As discussed in Chapter 4, we found an oscilloscope sampling time of 10 ns to be adequate for sampling the SE detector signal pulses. Over a total collection time of 20 ms, this sampling rate corresponded to 2×10^6 signal samples. This number is close to the maximum number of samples that could be stored on our oscilloscope per acquisition frame (4×10^6 samples). This limitation in the maximum number of samples per acquisition frame limited the pixel resolution of the images we could

capture.

We collected several acquisition frames from the same scan area to construct SE count images of that area. We note that saving the data corresponding to each acquisition frame on the oscilloscope took several seconds. We manually blanked the incident electron beam during this time. In Section 5.5.1 we will discuss schemes for live, online implementation of SE count imaging where the beam blanking can be automated and which do not require an oscilloscope. Therefore, these schemes would overcome both the limitations of long acquisition frame save times, as well as limited acquisition frame sizes mentioned in the previous paragraph.

5.2 Analysis of acquisition frames

So far, we have discussed features of the SEM scan waveform and how we used these features to synchronize the acquisition of SE detector data with the SEM scan on the oscilloscope. The acquisition frames we collected contained the SEM linescan as well as the detector signal referenced to a common time axis. The next step was to use the acquisition frames to generate SE count images. In this section, we will describe the MATLAB code we used to generate SE count images from these acquisition frames.

In the MATLAB code we addressed several challenges in order to generate SE count images. First, we needed to find the number of lines and number of pixels per line in the acquisition frames. We will describe how we used the linescan waveform to determine these parameters in Section 5.2.1. Second, we needed to account for slight variations in the triggering time on the oscilloscope due to noise in the linescan waveform, which we will describe in Section 5.2.2. Finally, we needed to extract the section of the SE detector signal that corresponded to the trace section of the linescan where the incident beam was actually scanning over the sample. We will describe this extraction in Section 5.2.3. With these challenges addressed, we counted the number of SE pulses for every pixel in each acquisition frame. We will describe our counting

algorithm in Section 5.2.4. The MATLAB code described in this section is reproduced in Section D.4 of Appendix D.

5.2.1 Calculating image resolution from linescan waveforms

In our SE imaging code we used the linescan waveform to calculate the number of lines and the number of pixel per line in the image. As we had discussed in Section 5.1.1, each line in the horizontal scan was preceded by a retrace spike associated with the resetting of the scan voltage. We can see these spikes in Figures 5-1(c), (d) and (e) for a pixel dwell time of 28 μs and in 5-1(f) for a pixel dwell time of 440 ns. Since one spike was associated with the end of one line, a count of the number of spikes was also a count of the number of lines in the image. Therefore, in the SE count imaging code, we used threshold discrimination to determine the number of spikes and hence the number of scan lines in the scanned sample area.

We used a similar technique to calculate the number of pixels in every line. As we had discussed in Section 5.1.1, each pixel step in the trace section of a slow linescan was followed by a transition period during which the scan voltage transitioned to the next pixel. In Figure 5-1(d) we can see the scan voltage during this transition period had a minimum from which the voltage reached the next pixel voltage value in 10 μs . We used a count of these minima to count the number of pixels for each linescan. Discrete steps in the linescan corresponding to pixels were only present for slow linescans, and we did not observe them for linescans that corresponded to a pixel dwell time faster than 7.5 μs . This pixel dwell time was an order of magnitude larger than the pixel dwell time of 440 ns we used to generate the SE count images. Figure 5-1(f) shows the trace portion of the linescan sawtooth waveform for a pixel dwell time of 440 ns, and we can see that it does not show discrete steps corresponding to each pixel in the linescan. Therefore, to count the number of pixels in the linescan, we acquired a slow linescan waveform (at pixel dwell time 28 μs) at the same image pixel resolution. Since we were only interested in collecting the scan waveform and

not the SE signal from the object, we collected this slow linescan with the incident electron beam turned off to prevent unnecessary incident electron dose on the sample.

5.2.2 Aligning acquisition frames and finding linescan period

The next challenge we addressed in the SE count imaging code was temporal alignment of all the acquisition frames. Figure 5-3(a) shows the linescan waveforms for the first few lines for the first (solid orange curve) and second (solid blue curve) acquisition frames captured on the oscilloscope during one imaging experiment. Note that in this figure we added a vertical voltage offset to the scan waveform for the first acquisition frame for ease of viewing. We can see that the two frames were misaligned by a time duration corresponding to one linescan. As we had discussed in Section 5.1.2, we set the trigger level on the oscilloscope to be close to the peak voltage of the spike that followed each linescan. The misalignment in Figure 5-3(a) was caused by noise in the linescan waveform. This noise caused the exact trigger level to be first reached on different spikes for different frames. Each acquisition frame still had SE detector signal and scan waveform referenced to the same time axis, but the misalignment caused the time axis to differ for different frames. We ensured that this misalignment between frames was small enough that the signal from the whole image frame was still captured in the acquisition frame on the oscilloscope.

In the SE count imaging code, we decided to use the linescan waveform for the first frame as the absolute reference to measure the misalignment of all other frames. We used the one-dimensional cross-correlation between the linescans for first frame and those for each of the succeeding frames to measure the misalignment between that frame and the first frame. Figure 5-3(b) is the cross-correlation between the linescans for the two acquisition frames from Figure 5-3(a). The cross-correlation of two input signals is the product of the two signals as a function of a delay introduced in one of the signals. As the delay changes, one signal ‘slides over’ the other, and the cross-correlation magnitude depends on how similar the two signals are at that delay.

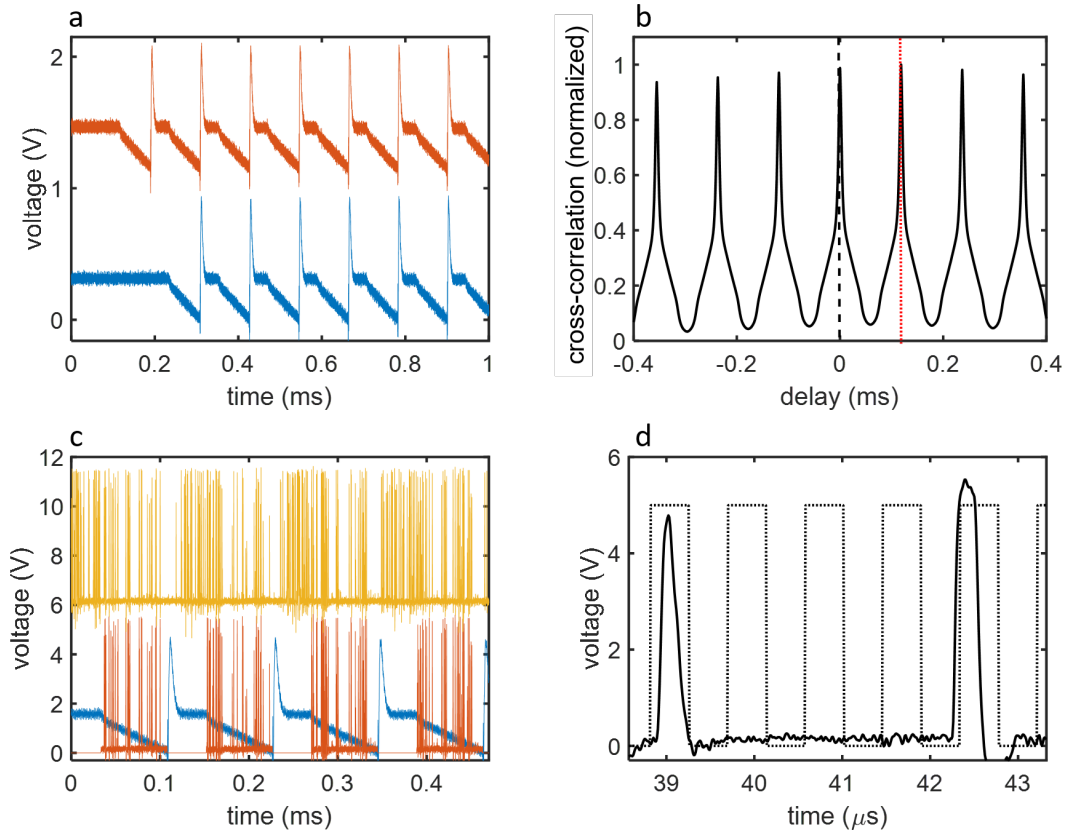


Figure 5-3: Acquisition frame alignment and SE pulse extraction. (a) Linescans from two acquisition frames at a pixel dwell time of 440 ns. The top linescan (orange) is misaligned with the bottom linescan (blue) by one line. We added a vertical offset of 1.1 V to the orange linescan for ease of viewing. (b) Cross-correlation of the two linescans in (a). The offset between zero delay (indicated by the dashed black line) and the highest cross-correlation peak (indicated by the dotted red line) equals the misalignment of 118.4 μs between the two linescans. (c) Extraction of useful SE signal, *i.e.*, the sections of the raw SE signal (yellow) corresponding to the trace section of the linescans, during which the incident beam scans over the sample (orange). We added a vertical offset of 6 V to the raw SE detector signal for ease of viewing. (d) Counting SE pulses. The dotted black square waveform shows successive image pixels, with even pixels assigned a value of 0 and odd pixels a value of 5. The first of the SE pulses (solid black) is within an odd pixel. However, although the second pulse originates in an even pixel, most of its intensity is present in the next (odd) pixel.

Since the two linescan waveforms were periodic, the cross-correlation showed periodic peaks. Figure 5-3(b) shows a few of these peaks around zero delay. The highest of these peaks occurred for a delay at which the two linescans were exactly aligned with each other. In Figure 5-3(b), we have indicated zero delay with a dashed black vertical line. The delay for the highest peak was 118.4 μs , indicated by the dotted red vertical line. The lower bound on the alignment precision of this technique was equal to the sampling time of 10 ns. Using this technique we extracted the misalignment for the linescan in each acquisition frame and delayed or advanced the scan waveform and the SE detector signal for that frame by this misalignment to ensure that all frames were aligned to the same time axis.

An additional advantage of calculating the cross-correlation was that the gap between successive peaks of the autocorrelation gave us the periodicity of the linescan waveform. We averaged the values of the gap between the 20 highest cross-correlation peaks to get the value of the linescan period. This period would have been much more difficult to extract from the waveform directly due to noise on the signal, and the cross-correlation was a much more accurate way to measure the periodicity. For the linescans shown in Figure 5-3(a), we measured this period to be 118.4 μs .

5.2.3 Finding linescan duration and extracting SE signal during scanning

The final step before counting the number of SE pulses for each image pixel was determining the start and end time of the trace section of each linescan in every acquisition frame. This step was important because, in addition to the expected signal pulses during the trace section of the linescan, the SE detector also recorded signal pulses during the retrace spike and front porch periods between successive trace sections. Figure 5-3(c) shows the raw signal from the in-chamber SE detector (in yellow) and the scan waveform (in blue). Note that in this figure we added an offset of 6 V to the raw SE signal for ease of viewing. We can see that there are signal

pulses during the spike and front porch sections of the linescan, in addition to the pulses in the trace region. These signal pulses originated from the sample material at the rest position of the incident electron beam before it started the next linescan. Since this signal does not correspond to the sample region being imaged, it should not be used to generate the image. By finding the start and end time of the trace sections in all the linescans, we can exclude this signal from our analysis and count only the pulses that were recorded when the beam was scanning. Further, having determined the number of pixels per line as described in the previous section, we can use these start and end times as references to segment the signal from one linescan into pixels.

We found the start and end time of the trace section of first linescan in the first acquisition frame manually. With all the acquisition frames aligned and knowing the period of the linescan waveform (as discussed in the previous section), the SE count code automatically determined the start and end times of the trace sections in all other linescans in all frames. Once we had determined these times we could determine which sections of the SE signal were acquired during the trace sections and ignore the rest of the detector signal. Figure 5-3(c) shows the sections of the in-chamber detector signal acquired during the trace section in red (without any offset). These sections line up with the trace section of the linescan waveform. After extracting these sections, we divided the trace period into pixels using the extracted number of pixels as described in the previous section. With this segmentation done, our code was ready to count the number of pulses in each pixel.

5.2.4 Counting SE pulses

We generated SE count images by counting the number of SE pulses in each pixel in our code. As described in Chapter 4 Section 4.2.2, we used contrast and brightness settings so that most of the SE pulses were saturated at a voltage of 5.6 V. This saturation enabled us to use a simple threshold in our code to filter out low voltage

noise pulses and count SE pulses originating from the sample. In the SE code we set this threshold voltage to be 1 V.

Figure 5-3(d) shows an example of the in-chamber detector signal pulses (solid black). In this figure, we have also plotted a square waveform corresponding to successive pixels that the code segmented the trace section of the linescan into (dotted black curve), with odd pixel numbers arbitrarily assigned a value of 5 and even pixels a value of 0 for ease of viewing. We can see that the first SE detector pulse originates in one of the odd pixels and is fully contained within it. The SE imaging code counted one SE in that pixel for this frame. There were no SE pulses for the next 6 pixels. The next SE pulse originated close to the end of an even pixel, but most of its intensity was present in the next (odd) pixel. We assigned this pulse to the even pixel it originated in. The conventional imaging scheme used by the SEM computer would have accounted most of its intensity in the next, odd pixel, leading to inaccuracy in the displayed intensity of that pixel. This ‘spillover’ effect has been discussed in the context of STEM imaging [84] and is one of the reasons we expect SE count images to be more accurate than conventional SEM images.

5.3 Results of SE count imaging

Having described our MATLAB imaging code, we can now discuss the results of applying this code to the acquisition frames collected on our SEM. In this section, we will describe the SE count images we generated using the oscilloscope acquisition frames on one or both SE detectors. We acquired our frames at $I = 2$ pA, pixel dwell time $\tau = 440$ ns, incident beam energy 10 keV, using the smallest (7.5 μm) condenser aperture, a working distance of 13 mm, an image brightness of 51, and an image contrast of 52. We chose the beam current and dwell time settings to ensure that the number of SEs per pixel was low enough that we could resolve the individual pulses. In Section 4.1.3 of Chapter 4, we noted that overlap between pulses introduced errors in the SE counting for $I > 5.5$ pA. Therefore, we chose a current much lower than this

value. Using Equation (4.1), the number of incident electron per pixel $N = 5.5$ at the settings we used. We saw in Chapter 4 that the DQEs of the in-chamber and in-lens detectors at this working distance were 0.16 and 0.32 respectively. Assuming an SE yield of 0.3, we get $N_{SE} = 0.26$ for the in-chamber detector and $N_{SE} = 0.68$ for the in-lens detector using Equation (4.2). Therefore, we expect most acquisition frames to have fewer than 2 SEs in one pixel for both detectors. From Chapter 4 Section 4.2.1, we also know that the average width of the SE pulse is 180 ns. Therefore, even if some of the pixels record 2 SE pulses, we expect to be able to resolve them. To generate the SE count images reported in this section, we recorded 32 acquisition frames on the oscilloscope and summed the SE counts for all pixels over these frames.

We will first show the SE count images generated using just the in-chamber detector in Section 5.3.1. Then, in Section 5.3.2, we will show the the SE count image generated from combining the signal from the in-lens and in-chamber detectors and demonstrate that the contrast and SNR are both higher for the SE count images than conventional images. We will also analyze the statistics of the SE emission distribution extracted from these images and measure their deviation from ideal Poisson statistics in Section 5.3.3.

5.3.1 SE count imaging with in-chamber detector

Figure 5-4(a) is an SE count image of a freestanding copper mesh with a period of 120 μm , generated using the SE signal on the in-chamber detector. The pixel resolution of this image is 262×188 . The colorbar in Figure 5-4(a) indicates the number of SEs for a given pixel greyscale level. The maximum number of SEs for any pixel in the image was 26 (summed over all 32 acquisition frames), and the mean number of SEs per pixel in the image was 3.13.

Figure 5-4(b) is an image of the same sample generated by finding the average signal for every pixel using the same acquisition frame dataset as 5-4(a). This image represents a conventional SEM image; we checked that the statistics of this image

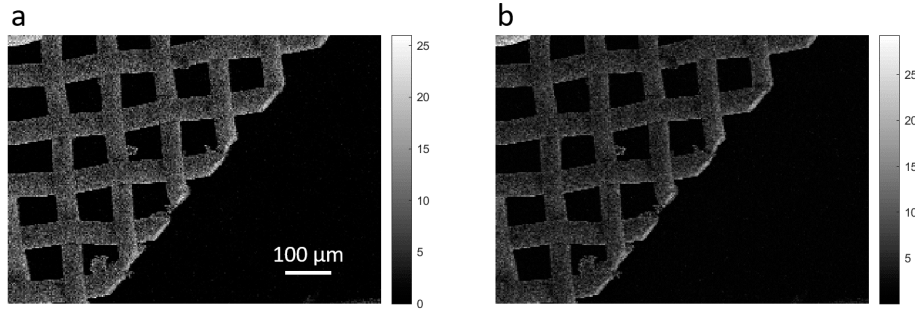


Figure 5-4: SE count imaging with in-chamber SE detector. (a) SE count image of a 120 μm period copper mesh suspended over vacuum. We collected the 32 acquisition frames used to generate this image at an incident beam current of 2 pA, energy of 10 keV, and a pixel dwell time of 440 ns. The image pixel resolution is 262×188 . The mean SE count per pixel in the image was 3.13. (b) Conventional image of the same copper mesh grating under the same imaging conditions as (a). We scaled this image so that it has the same mean pixel intensity as the mean SE count in (a). The contrast between the copper mesh and the background vacuum appears to be lower in this image than in (a).

were close to those of an image of this sample generated by the SEM computer. We scaled the pixel intensities in this image so that the mean intensity in this image was equal to the mean SE count in Figure 5-4(a), 3.13. We can see that the contrast of the copper mesh compared to the background vacuum appears to be lower than the contrast in the SE count image. In Section 5.3.2 we will quantitatively analyze the contrast and SNR of the SE count and conventional images generated by combining the counts from both SE detectors. We will show that both the contrast and the SNR for the SE count images was higher than for the conventional images.

5.3.2 SE count imaging with in-chamber and in-lens detectors

Figure 5-5(a) is an SE count image obtained by adding the number of SE counts from the in-chamber and in-lens detectors on the SEM, using the same imaging conditions as in Section 5.3.1. The mean number of SE counts from just the in-lens detector signal was 5.05, compared to 3.13 from the in-chamber detector image in Figure 5-

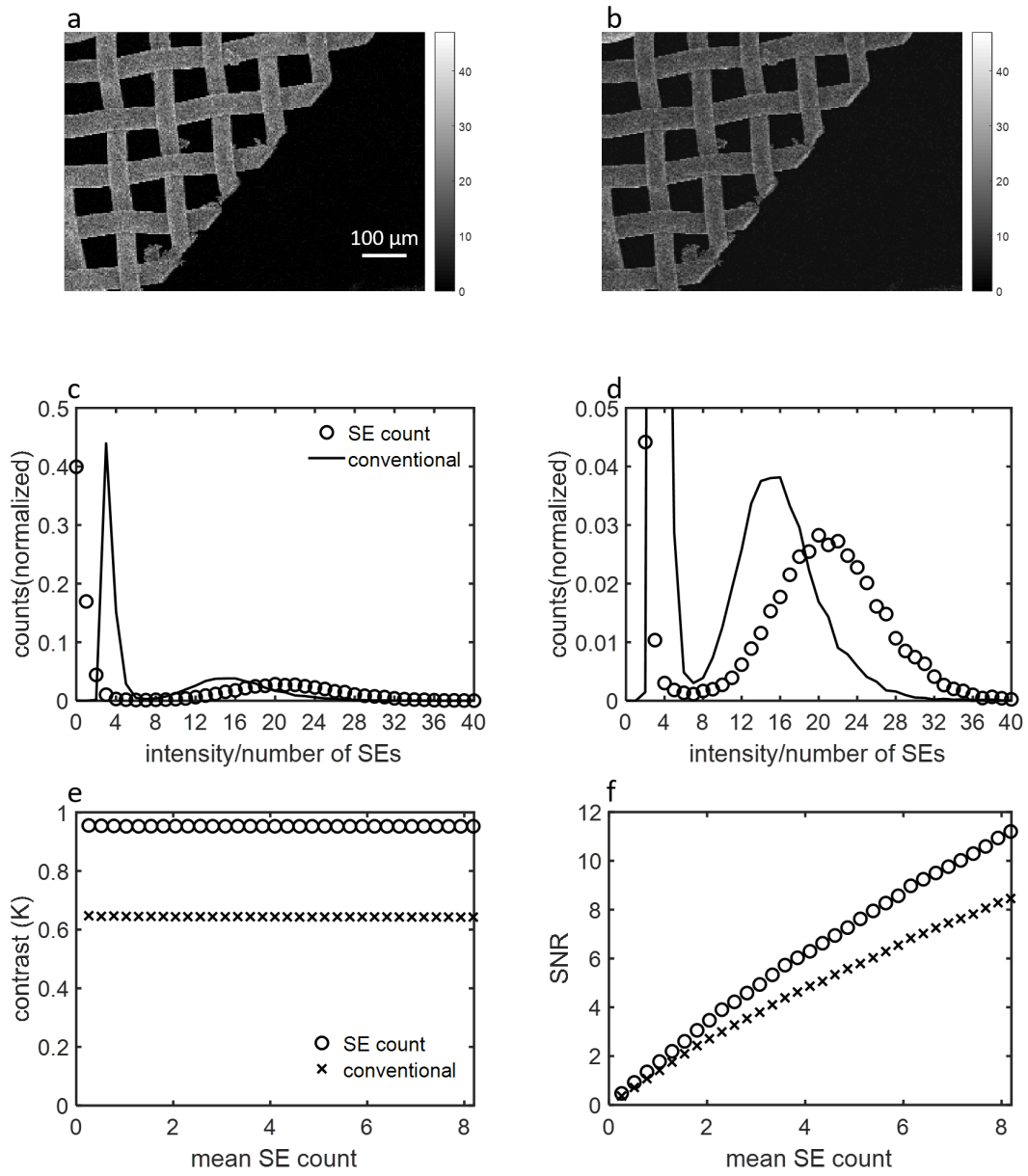


Figure 5-5 (*previous page*): Statistics of SE count imaging. (a) SE count image generated by adding the counts from the in-chamber and in-lens detectors over all 32 acquisition frames. The mean SE count in the image is 8.18. (b) Conventional image scaled to the same mean SE count, showing lower contrast between the copper mesh and background than (a). (c) Histogram of the SE number (for the SE count image, unfilled circles) and the pixel intensity (for the conventional image, solid line). The histogram shows two peaks, corresponding to the darker background pixels and the brighter copper mesh pixels. The gap between the dark and bright peaks is higher for the SE count image than the conventional image, indicating that the SE count image has higher contrast. (d) Magnified view of the peak corresponding to the copper mesh pixels, again showing that the mean of the peak in the SE count image histogram is higher than the mean in the conventional image histogram. (e) Contrast K (refer text for definition) as a function of mean SE count for the SE count (unfilled circles) and conventional (crosses) images. We varied the mean SE count by varying the number of acquisition frames used to generate the final images. The contrast stays constant as the mean SE count increases and is always higher for the SE count image (0.95) compared to the conventional image (0.64). (f) SNR (refer text for definition) as a function of the mean SE count for the SE count and conventional images. The SNR increases for both images with mean SE count and is always $\sim 30\%$ higher for the SE count image. The SNR for the SE count image is also more linear than the SNR for the conventional image.

4(a). The higher mean SE count again demonstrates the higher DQE of the in-lens detector at this working distance, as we had discussed in Chapter 4 Section 4.1.3. Figure 5-5(b) is a conventional image of the same sample. Just as in Section 5.3.1, we scaled this image so that its mean was equal to the mean of the SE count image in Figure 5-5(a). Again, the contrast of the copper mesh compared to the background appears to be lower in the conventional image than in the SE count image.

In Figure 5-5(c), we plot the image histogram of the SE count image (unfilled circles) and the conventional image (solid curve). In Figure 5-5(d) we plot the same histogram scaled to make viewing of the counts at higher intensities easier. Note that in case of the SE count histogram, the horizontal axis represents the number of SEs detected at a particular pixel, while for the conventional image, the horizontal axis represents a scaled pixel intensity. Both histograms show two prominent peaks: at low intensities due to the background (vacuum) pixels, and at higher intensities due to the copper mesh. We used an SE count/pixel intensity of 7 as a threshold between these two types of pixels, since both histograms had local minima at this value. There are two important features in these histograms. First, the peak in the

SE count histogram due to the copper mesh is at higher counts than the peak for the conventional histogram. The mean SE count for the pixels containing the copper mesh is 21.29, compared to a mean intensity of 16.17 in the corresponding pixels in the conventional image. Second, the mean SE counts in the pixels representing vacuum is 0.52 in the SE count image, compared to a mean intensity of 3.52 in the conventional image. Therefore, the mean level of the background pixels is higher in the conventional image than in the SE count image.

We will now compare SE count imaging to conventional imaging using the image quality metrics we had introduced in Chapter 3. In that chapter, we discussed three metrics: contrast, SNR, and MARE. While contrast and SNR can be evaluated for a single image, to calculate MARE we need a ‘ground truth’ image with which to compare the SE count and conventional images we generated. Using a long-pixel-dwell-time conventional SEM image of the sample as the ground truth would bias the results in favor of the generated conventional image since they would both use the same method to assign pixel intensities. Therefore, in the absence of a ground truth, we will use the contrast and SNR to compare the two images.

5.3.2.1 Comparison of contrast for SE count and conventional imaging

As we had stated in Chapter 3 Section 3.1.1, we can calculate the Michelson contrast K of the sample pixels against the background pixels, as follows:

$$K = \frac{N_{\text{SE,sample}} - N_{\text{SE,background}}}{N_{\text{SE,sample}} + N_{\text{SE,background}}}$$

Here, $N_{\text{SE,sample}}$ is the mean number of SEs in the sample pixels, and $N_{\text{SE,background}}$ is the mean number of SEs in the background pixels. In the SE count and conventional images we have generated, we can use the pixels that represent the copper grid as the sample and the pixels that represent vacuum as the background. Using the mean values of the histogram peaks for these two types of pixels in the equation for contrast, we get $K = 0.95$ for the SE count image and $K = 0.64$ for the conventional image.

Hence, the contrast between sample and background pixels was almost 50% higher for the counting image than the conventional image.

Figure 5-5(e) shows the contrast in the SE count image (unfilled circles) and the conventional image (crosses) as a function of the mean SE count in the image. We varied the mean SE count by varying the number of acquisition frames used to generate the final image; the mean SE count varied linearly with the number of acquisition frames. We can see that the contrast remains constant for both the SE count image and the conventional image as the acquisition frames build up to form the final image. This constant behavior of the contrast indicates that we can choose the incident electron dose we want to work with independent of contrast. In the next section, we will consider the SNR, which provides another way to quantify the image quality with respect to the incident electron dose.

5.3.2.2 Comparison of signal-to-noise-ratio for SE count and conventional imaging

A second metric for the quality of the SE count and conventional images is the SNR. In the SNR measure we introduced in Chapter 3 (based on work by Thong et al. [116]), we estimated the signal and noise by considering the image autocorrelation near zero offset. Figure 5-5(f) is a plot of the SNR for the SE count (unfilled circles) and conventional image (crosses) as a function of the mean SE count. We can see that for both images the SNR increases as a function of the mean SE count. Further, the SNR for the SE count image is always $\sim 30\%$ higher than the SNR for conventional imaging. For example, an SNR of 8 is first achieved for SE count imaging at a mean SE count of 5.38, while for conventional imaging it is achieved at an SE count of 7.68. Since the mean SE count scales linearly with the incident beam current (as discussed in Chapter 4), this difference represents an incident electron dose reduction of 30% due to SE count imaging for the same SNR. We also note that the conventional image SNR shows some non-linearity in the high-mean SE count region, while the SE count

SNR is much more linear for the entire range of mean SE count. Such non-linearity in the SNR of conventional images was also observed by Yamada et al. [95,97].

Taken together, our results show that SE count imaging can lead to significant reduction of the incident electron dose for the same image quality, compared to conventional imaging. We considered two metrics for the image quality: contrast and SNR. Both metrics were higher for the SE count image compared to the conventional image. Although we did not implement a live SE count imaging scheme, the live implementation scheme we will outline in Section 5.5.1 would achieve these benefits of SE count imaging.

5.3.3 Probability distribution of SEs

In the previous section, we compared the mean SE signal of image pixels corresponding to the sample (copper mesh) with image pixels corresponding to the background (vacuum) to obtain the contrast. Segmenting the pixels in this way also allowed us to analyze the statistics of the SE distribution and quantify its deviations from an ideal Poisson process. We recall from Chapter 1 Section 1.3.1 that this question has motivated a lot of work into SE counting. Oatley, Frank, Baumann and Reimer, and Sakakibara have all reported varying degrees of deviation from ideal Poisson statistics in the SE emission distribution [21,28,87,89,90].

Figure 5-6(a) is a plot of the relative count of pixels that represent the background vacuum (unfilled blue circles) as a function of the number of SEs in those pixels. In this plot, we have normalized the counts so that they sum to 1 over the different numbers of SEs. Therefore, this plot can be thought of as a probability distribution of the number of SEs. As we had noted in Section 5.3.2, the mean SE counts for these background pixels was 0.52. To visualize the deviation from an ideal Poisson process, we have also plotted the probabilities for a Poisson process with the same mean (orange crosses). We can see that the probability of 0 SEs is higher and that of 1 SE is lower for the distribution we extracted from our data than for the ideal

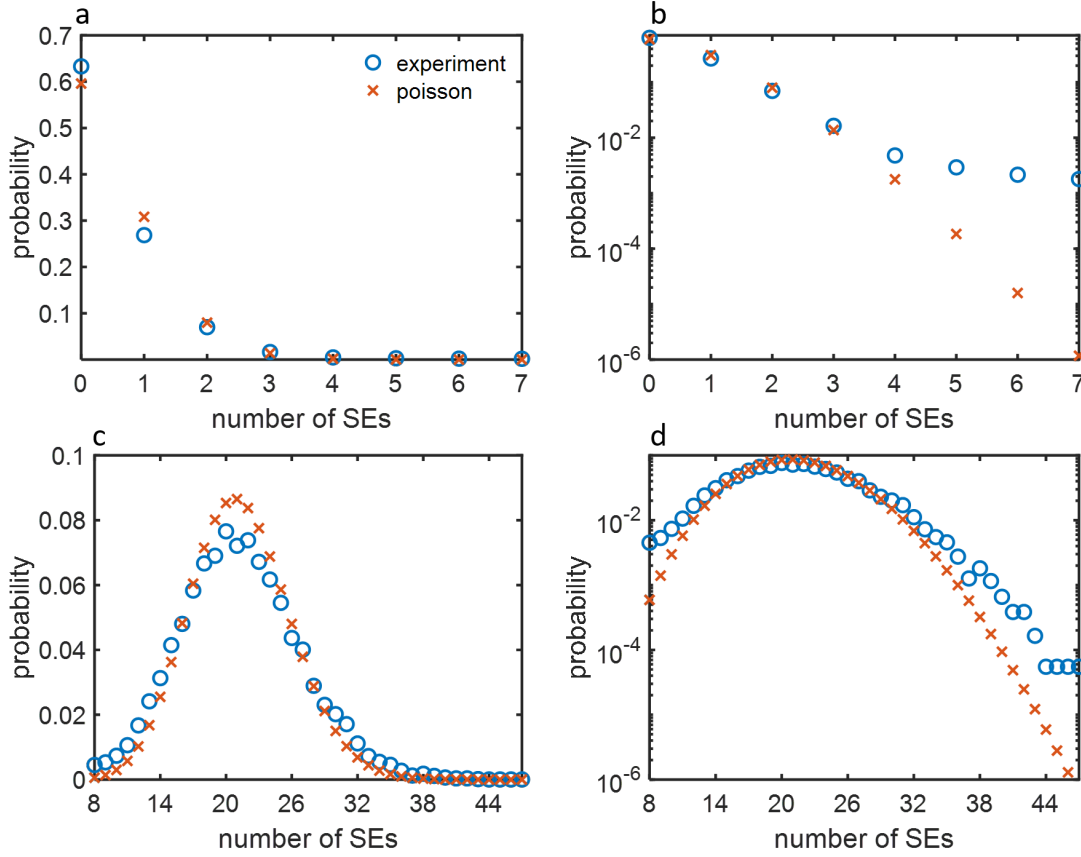


Figure 5-6: Probability distribution of SE emission. (a) Distribution of the number of SEs extracted from the background (vacuum) pixels in Figure 5-5(a) (unfilled blue circles). The mean SE count for this distribution is 0.52 and the variance was 0.74. The orange crosses indicate the probabilities of a Poisson process with the same mean SE count. (b) Same as (a) with the y-axis on a log scale. The extracted SE distribution deviates significantly from an ideal Poisson distribution beyond 3 SEs, reflecting its larger variance. (c) Distribution of the number of SEs extracted from the sample (copper mesh) pixels in Figure 5-5(a) (unfilled blue circles). The mean SE count for this distribution is 21.29 and the variance was 29.8. The orange crosses indicate the probabilities of a Poisson process with the same mean SE count. The Poisson distribution has a higher and narrower peak than the extracted SE distribution. (d) Same as (c) with the y-axis on a log scale. The extracted SE distribution deviates significantly from the ideal Poisson distribution above 30 SEs and below 14 SEs, reflecting its larger variance.

distribution. Figure 5-6(b), which is the same as 5-6(a) but with the y-axis on a log scale, shows that at higher SE numbers the extracted probabilities are much higher than the probabilities from the Poisson distribution. From these plots, we would expect the variance of the extracted probabilities to be higher than the variance for an ideal Poisson process, which should be equal to 0.52. The variance of the extracted distribution is 0.74, confirming this intuition. From these numbers, the B-factor [21] of this process is 0.42.

We performed a similar calculation for the pixels representing the copper mesh. Figure 5-6(c) is a plot of the relative number of copper mesh pixels (unfilled blue circles) as a function of the number of SEs in those pixels. Figure 5-6(d) is the same plot with the y-axis on a log scale. Just as in Figure 5-6(a) and (b), we scaled the pixel numbers so that they summed to 1. We have also plotted the probabilities of an ideal Poisson process with the same mean as the extracted distribution (21.29) using orange crosses. From these plots we can see that the extracted distribution was wider than an ideal Poisson distribution. The variance of the extracted distribution was 29.8. This variance value gave us a B-factor of 0.4, which is very close to the B-factor we had extracted from the vacuum pixel distribution. We note that this B-factor is about 2 times larger than that reported by Frank for copper at 10 keV [21]. We expect this deviation to be caused by small non-uniformities in the sample, as well as the enhancement of SE yield at the edges of the copper grid.

In appendix C, we will show that we can fit the extracted SE distributions much more accurately with a type of compound Poisson distribution called a Neyman type-A distribution. Such compound Poisson distributions, consisting of a sum of k Poisson random variables (where k is itself a Poisson random variable), have been used previously to model the emission of SEs [21, 29]. Our extracted SE distributions provide further experimental evidence towards their applicability. This preliminary analysis indicates that our method of SE count imaging is a promising way of characterizing the statistics of SE emission.

5.4 Offline conditional re-illumination

We have described our implementation of offline SE count imaging and showed that SE count images can achieve the same SNR as conventional images at a 30% lower incident electron dose. In this section, we will use the same acquisition frame dataset to evaluate if the SEM conditional re-illumination schemes we had outlined in Chapter 3 can further reduce this incident electron dose. We recall that conditional re-illumination schemes are based on trading off some error in the image for reduced incident electron dose. We will evaluate this tradeoff for the two conditional re-illumination schemes we had described: M -limited schemes, where we stop illuminating all pixels after a pre-defined maximum number of illuminations, and N_{SE} -limited schemes, where we stop illuminating a given pixel if the number of SEs from it reaches a pre-defined threshold $N_{\text{SE},T}$. In M -limited schemes the incident electron dose is constant for all pixels, while in N_{SE} schemes it varies from pixel to pixel.

In Section 5.3 of this chapter, we used contrast and SNR to compare SE count and conventional SEM images. We did not use MARE to compare the images because we did not have a ‘ground truth’ image. In this section, we will use the SNR and MARE. Due to the low number of background counts in the SE count images in Figures 5-4 and 5-5 we found that the contrast was close to 1 for both re-illumination schemes and was not a very useful metric to compare them. However, now that we have generated an SE count image, we can use it as the ground truth to compare SE count images with conditional re-illumination. The implementation of any re-illumination scheme on the same acquisition frame dataset would introduce errors in the number of SEs in some of the image pixels, and the SE count image from Figure 5-5(a), generated using the SE counts from both detectors and all acquisition frames, is a good reference ground truth with which to compare the re-illumination images.

We will use the *relative incident dose* to compare the incident electron dose for the ground truth and re-illumination images. The relative incident dose is the

ratio of the mean electron dose per pixel for a particular re-illumination scheme to the maximum possible electron dose per pixel. The maximum possible dose per pixel is achieved when we use all 32 acquisition frames to generate the SE count image; in this case the relative incident dose is 1. Any re-illumination technique would use at most 32 frames for generating the SE count image. Therefore, the relative incident dose for the re-illumination schemes would be less than or equal to 1. Our aim in this section will be to calculate MARE and SNR as a function of the relative incident dose for the two re-illumination schemes.

5.4.1 Images from conditional re-illumination schemes

Figure 5-7 shows the results of conditional re-illumination experiments on the same acquisition frames as Figures 5-4 and 5-5. Figure 5-7(a) is the same image as Figure 5-5(a) and will be the ground truth image. This image has an SNR of 11.2 and a relative incident dose of 1, meaning that all pixels receive the maximum possible incident electron dose.

Figure 5-7(b) is an M -limited conditional re-illumination image with $M = 14$. We generated this image by limiting M to 14 (instead of 32 as in Figure 5-7(a)) and scaling the SE counts for every pixel by $32/M$ so that we can compare it to the ground truth. This image has an SNR of 5.73, a MARE of 0.21, and a relative incident dose of 0.44. Therefore, we have reduced the incident electron dose by 56% at the cost of reducing SNR by a factor of 2.

Figure 5-7(c) is an N_{SE} -limited conditional re-illumination image with $N_{\text{SE},T} = 8$. As discussed in Section 5.3, the mean number of SEs per pixel per frame was less than 1, and most pixels received either 1 or zero SEs in every frame. Once the number of SEs for a given pixel had reached 8, we recorded the number of acquisition frames it took to reach 8 SEs for that pixel and did not consider SEs on that pixel in the following frames. As a result, we made a map of the number of acquisition frames it took to reach 8 SEs for every pixel. For the background, vacuum pixels, which

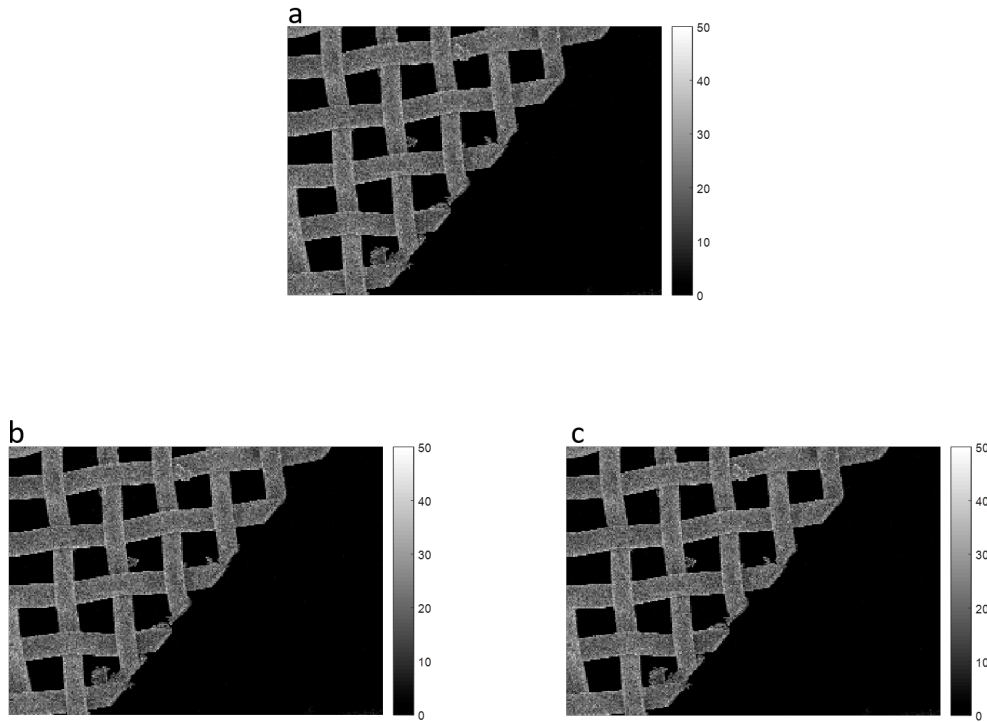


Figure 5-7: SE count imaging with conditional re-illumination. (a) SE count image using SE counts from both detectors from all 32 acquisition frames. Same image as Figure 5-5(a). The SNR for this image is 11.2 and the MARE is 0 at a relative electron dose of 1 (*i.e.*, all pixels received the maximum possible dose). We used this image as the ground truth. (b) SE count image generated using M -limited conditional re-illumination, with $M = 14$. This image has an SNR of 5.73 and a MARE of 0.21, at a relative dose of 0.44. (c) SE count image generated using N_{SE} -limited conditional re-illumination, with $N_{SE,T} = 8$. This image has an SNR of 5.68 and a MARE of 0.18, at a relative dose of 0.79.

typically had between zero to 5 SEs over all frames (see Figure 5-5(c)), this number was 32. Then, we scaled each pixel value by the ratio of 32 to the number of frames it had taken to reach 8 SEs to get the final SE count image. The SNR for this image was 5.68 (close to the value for Figure 5-7(b)), the MARE was 0.18, and the relative incident dose was 0.79. Therefore, in this image we have reduced the incident electron dose by 21% at the cost of reducing SNR by a factor of 2.

From the colorbar in 5-7(c), we note that a few pixels had many more counts than the corresponding pixels in the ground truth image. There was a (small) probability that a given pixel received more than 1 SE in a given frame, and for a small number of pixels this event happened in multiple acquisition frames and the number of SEs reached 8 in relatively few frames. Consequently the scaled SE counts on these pixels were larger than 60 in some cases (the maximum pixel SE count in the ground truth image was 45).

We can see that the tradeoff between SNR and relative incident dose is worse for the N_{SE} -limited scheme than in the M -limited scheme, since the relative incident dose in that scheme was lower (0.44 for M -limited vs 0.79 for N_{SE} -limited) for the same SNR of about 5.7. However, the N_{SE} -limited scheme produced a lower MARE than the M -limited scheme (0.21 for M -limited vs 0.18 for N_{SE} -limited) for the same SNR. In the next section we will take a more detailed look at the SNR and MARE as functions of the relative incident dose for these schemes.

5.4.2 Analysis of image quality and relative incident dose for conditional re-illumination schemes

In Figure 5-8 we compare the SNR and MARE for the two conditional re-illumination schemes as a function of the relative incident dose. For the M -limited scheme we varied the relative incident dose by varying the number of acquisition frames used to generate the final image (*i.e.*, M). For the N_{SE} -limited scheme we varied the relative

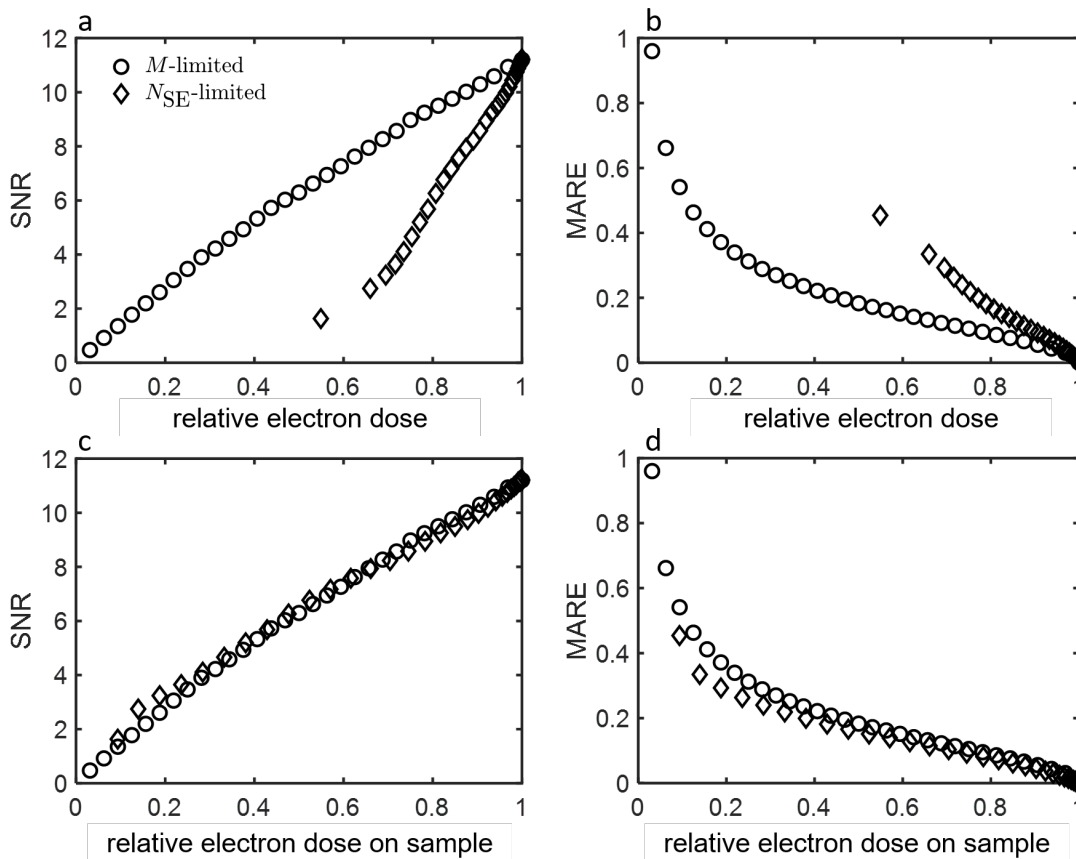


Figure 5-8: Comparison of conditional re-illumination schemes. (a) SNR as a function of the relative electron dose for M -limited and N_{SE} -limited conditional re-illumination. The M -limited scheme shows higher SNR at the same relative dose than the N_{SE} -limited scheme. (b) MARE as a function of the relative electron dose for M -limited and N_{SE} -limited conditional re-illumination. The M -limited scheme shows lower MARE at the same relative dose than the N_{SE} -limited scheme. (c) SNR as a function of the relative electron dose on the sample pixels for M -limited and N_{SE} -limited conditional re-illumination. The SNR for both schemes is almost equal, with the N_{SE} -limited scheme showing slightly higher SNR for relative dose on sample below 0.3. (d) MARE as a function of the relative electron dose on the sample pixels for M -limited and N_{SE} -limited conditional re-illumination. The N_{SE} -limited scheme showed slightly lower MARE than the M -limited scheme for the same relative dose on the sample.

incident dose by varying the threshold number of SEs above which counts from further acquisition frames were not considered (*i.e.*, $N_{SE,T}$). From Figure 5-8(a), we can see that the SNR drops much more rapidly for the N_{SE} -limited scheme as we lower the relative incident dose than the SNR for the M -limited scheme. Similarly, in Figure 5-8(b) we can see that the MARE for the M -limited scheme is always lower than the MARE for the N_{SE} -limited scheme. Both these plots indicate that the simpler M -limited scheme gives a better tradeoff of SNR and MARE vs relative incident dose than the more complicated N_{SE} -limited scheme.

So far, we have considered the relative incident dose averaged over the entire scan region. A lot of the scan pixels generated very few SEs because they represented the background vacuum. These pixels made a big contribution to the relative incident dose for the N_{SE} -limited re-illumination scheme. However, the high dose over these pixels did not correspond to actual sample damage. Therefore, it makes sense to limit our analysis of the relative dose to just the pixels representing the sample (copper mesh). For M -limited conditional re-illumination the relative incident dose will be unchanged because it is the same over all pixels. However, for N_{SE} -limited conditional re-illumination the relative dose will be much lower because we will have removed the background pixels and would only consider the higher SE yield sample pixels. Figure 5-8(a) shows that when we plot the SNR as a function of the relative dose on sample pixels only, the SNR for both schemes is almost identical as a function of the relative incident dose on the sample. In fact, at low values of SNR, the relative incident dose for the N_{SE} -limited scheme is slightly lower than that for the M -limited scheme. For example, the relative dose for the M -limited scheme is 0.19 at an SNR of 2.61 while the relative dose for the N_{SE} -limited scheme is 0.14 (*i.e.*, 26% lower) at an SNR of 2.75. Figure 5-8(b) shows that the MARE for the N_{SE} -limited scheme is also lower than that for the M -limited scheme as a function of the relative incident dose on the sample. For example, at a relative incident dose of 0.19, the MARE is 0.37 for the M -limited scheme and 0.29 for the N_{SE} -limited scheme, a reduction of 22%. We can see that the N_{SE} -limited scheme offers a significant reduction in dose

(81% in this case) at the cost of a moderate MARE of 0.29.

Together, these plots show that when dose on the high-SE-yield parts of the sample is important, the two re-illumination schemes perform comparably, with the N_{SE} -limited scheme enabling lower dose at low SNRs. If the dose over the entire illumination region, including the low-contrast parts of the sample, is important, the M -limited scheme outperforms the N_{SE} -limited scheme. Depending on which part of the sample and image quality metric is more important for the type of sample we are imaging, we could choose one or the other of these re-illumination schemes.

5.5 Schemes for online electron counting and conditional re-illumination

In sections 5.2, 5.3 and 5.4, we implemented offline SE counting and conditional re-illumination using a 32-acquisition-frame dataset that we acquired by synchronizing the collection of SE detector signal and the SEM scan function on an oscilloscope. Using this dataset we evaluated the reduction in incident dose in SE count imaging compared to conventional imaging at the same image quality, and compared the image quality obtained from the two conditional re-illumination schemes at reduced relative incident doses. However, we cannot use the imaging setup shown in Figure 5-2 to realize this dose reduction in practice because the scanning of the beam over the sample was not turned off automatically between acquisition frames. Saving each acquisition frame on the oscilloscope took a few seconds, and the beam was scanning over the sample for some part of this time before we turned it off manually. Therefore, the sample was exposed to the electron beam between acquisition frame collections on the oscilloscope. This additional electron dose offset any reduction in dose we might have obtained with SE count imaging.

As we had discussed in Chapter 1 Section 1.3.1, Yamada and co-workers [93–97] implemented live SE count imaging in the early 1990s. Their implementation

consisted of filters, pulse counting circuits, and registers to store the pulse counts. The data storing and readout was carefully synchronized with the SEM scan waveforms. Although this implementation was fast, it required the design and implementation of complicated circuitry as we discussed in Chapter 4. With the availability of cheap, high-speed computation, we believe that most of the synchronization requirements can be incorporated into the acquisition frame dataset processing code.

In Chapter 4, we also described how SE count imaging could be implemented using image histograms. Such an implementation would be live and not require any external hardware. From the known positions of the quantized SE histogram peaks, we could assign the image pixels an SE count number based on their histogram brightness level. However, as discussed in Chapter 4, this technique would lead to some errors in the SE count assignment because of the overlap between successive SE count histogram peaks, which is caused by the spread in width of the SE pulses (see Figure 4-6 in Chapter 4). However, the probability of making such errors would be known, and the SE count assignment algorithm could be designed to minimize it. Such histogram-based SE count imaging could be used to monitor detector DQEs and image SNRs for optimizing the imaging conditions on the SEM but may not be suitable for high-SNR SEM imaging.

Ideally, we would want each imaging frame (corresponding to the beam scanning over the sample) on the SEM to correspond to an acquisition frame in the dataset. Therefore, the ideal workflow would be to blank the beam while an acquisition frame is being recorded by the oscilloscope, and unblank the beam when the oscilloscope is ready to receive the next frame. This blanking would need to be synchronized with the SEM scan waveforms so that each of the acquisition frames begins from the first line of the scanned area. In this section, we will discuss schemes to implement live, online SE counting and conditional re-illumination that achieve this workflow. The schemes we will propose are enabled by the use of a beam blanker in the SEM. For the live SE count scheme the built-in beam blanker on the SEM is fast enough, while for conditional re-illumination we need ns-timescale beam blanking to allow the electron

beam to be blanked over any desired pixel in the scan area.

5.5.1 Scheme for online SE count imaging

Our scheme for live SE count imaging is shown in Figure 5-9(a). The hardware required is the same as the offline SE imaging scheme we implemented in this chapter, shown in Figure 5-2, with the addition of a beam blanker in the SEM column. At the start of the imaging process, the SEM computer sends a scan start signal to the SEM scan coils to start the first frame. The oscilloscope (as discussed in Chapter 4, the required oscilloscope bandwidth is 100 MHz) captures the scan waveform and the synchronized SE detector signal pulses. The only addition in this scheme compared to the one we have implemented in this chapter would be a beam blanking signal sent from the SEM scan computer to the beam blanker after every acquisition frame. From our study of the scan waveform as discussed in Section 5.1.1, we know the total acquisition frame time and the frame reset time for a given image resolution. Therefore, the scan start signal from the SEM computer, with an added delay equal to the acquisition frame time, can serve as the blanking signal the beam blanker. This signal is shown by the green arrow in Figure 5-9(a). This delay could be introduced using a simple delay line generator or a comparator circuit. On receiving this signal, the beam blanker blanks the SEM before the linescans for the next frame can begin, thereby protecting the sample from additional electron dose while the previous acquisition frame is being saved. As we had described in Section 5.1.2, noise in the scan signal can lead to variation in which voltage spike triggers data collection on the oscilloscope. With the trigger voltage set precisely, we observed that this uncertainty was less than 10 lines, which corresponds to a time delay of ~ 1 ms. Since the frame reset time is around 30 ms depending on the pixel dwell time and scan area size, we have sufficient time to send the blanking signal even with possible delays due to noise. The time taken to save an acquisition frame on our oscilloscope was constant for a fixed sampling time and frame size. For example, for the frame parameters in Section 5.3, the time to save was around 5 s. Since we know when scanning began

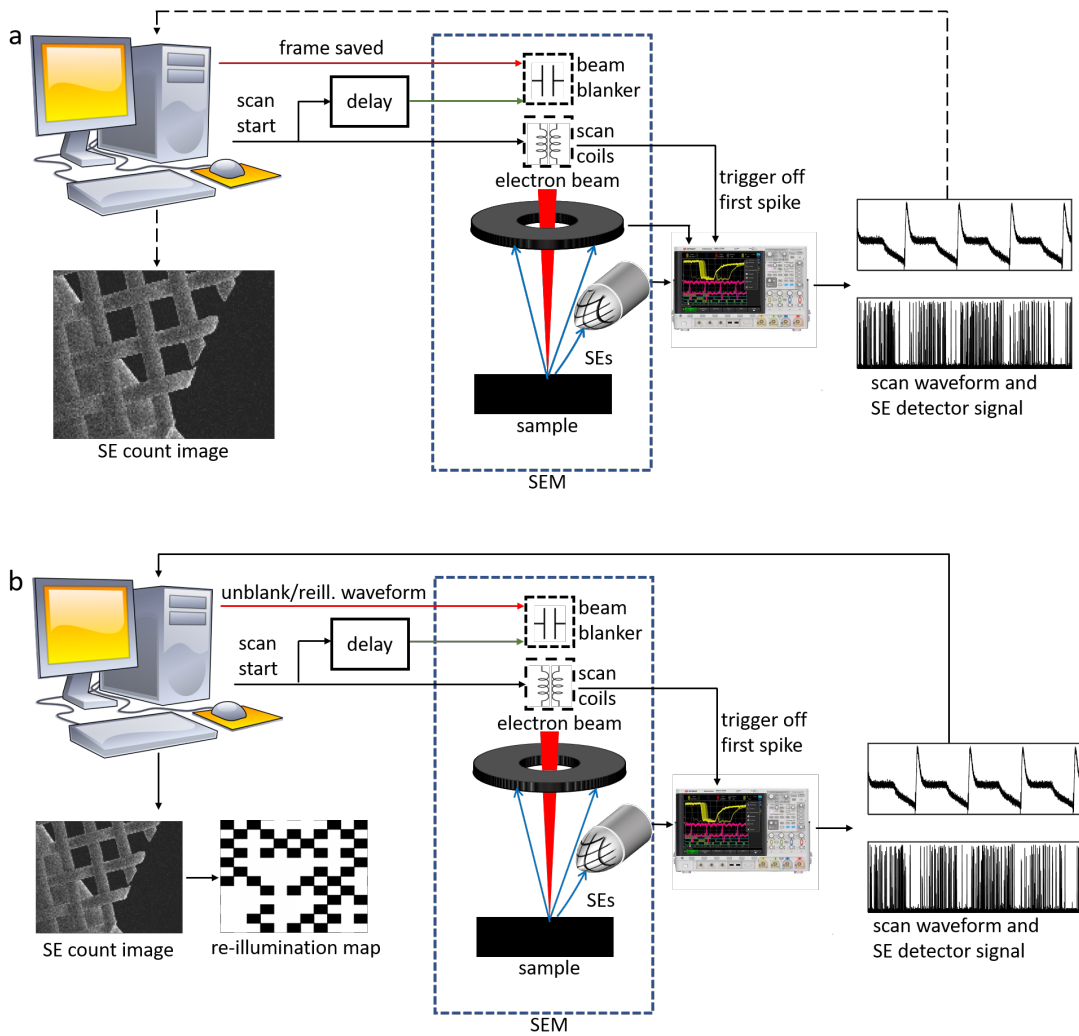


Figure 5-9: Schemes for live SE counting and conditional re-illumination. (a) Live SE counting scheme. Solid black arrows indicate online steps, and dashed black arrows indicate offline steps. The scan start signal from the SEM computer, with a delay equal to the acquisition frame time, activates the beam blanker (green arrow). After the frame is acquired on the oscilloscope, the SEM computer sends an unblanking signal (red arrow) to the beam blanker before the start of the next frame. After all frames have been acquired, the SE count image can be generated on the SEM computer offline. (b) Conditional re-illumination scheme. Now the transfer of acquisition frames and generation of SE count images has to be performed online. From the SE count image the SEM computer generates a reillumination waveform which is sent to the beam blanker to enable blanking of the beam over desired pixels.

and the frame times, the SEM computer already has an internal clock synchronized with the scanning frames. Therefore, after the time to save the previous frame has elapsed, the SEM computer sends an unblinking ‘frame saved’ signal (shown by the red arrow in Figure 5-9(a)) to the beam blanker before the start of the next scan frame. The process repeats for capturing the desired number of acquisition frames. After all the acquisition frames have been collected, the frames are transferred to the SEM computer and the computer processes the frames to generate the final SE count image. These offline processes are indicated with dashed arrows in Figure 5-9(a). Alternatively, they can be brought online and the signal to unblank the beam (indicated in red in Figure 5-9(a)) can be sent after the acquisition frames are transferred to the computer and the count image is generated.

The major advantage of this scheme over Yamada’s live SE counting scheme is that we have captured all the fast timing and processing complexity in the SE count imaging code instead of needing to implement it in hardware circuits as in Yamada’s work. The only hardware timing signal is the one sent to the beam blanker after every acquisition frame. Since each frame typically lasts several tens to hundreds of ms depending on the image size, we do not need any high-speed electronics to implement this signal. As we discussed in the previous paragraph, we need to blank the beam during the frame reset time of 30 ms after the completion of one imaging frame before the next one can begin. The electrostatic beam blanker already built-in the SEM and used for freezing the SEM scan is sufficiently fast to blank the beam during this time. The resonant frequency of the build-in blanker on our SEM was around 10 kHz, and the blanker did not blank the beam effectively above 20 kHz. This speed corresponds to a blanking time of about 50 μ s, which is much lesser than the frame reset time. Therefore, such a blanker would be good enough for this implementation of live SE count imaging.

The major bottleneck in terms of speed of imaging in this scheme is the saving of each acquisition frame on the oscilloscope. Acquisition of the same 32 frame dataset at a speed of 5 seconds per frame would take about 3 minutes. If we have access to the

datastream from the SEM to the SEM computer, which is what the SEM computer would normally use to generate live images, we can take out the oscilloscope entirely from our scheme and use just the computer to create SE counting images. In this case, the SE counting scheme would be truly live, since we would just be processing the same data that the computer would have used anyway to display live images. However, getting access to this datastream may not be straightforward depending on the SEM imaging software, in which case an oscilloscope would be needed to outcouple the detector signal and scan waveform.

The oscilloscope also limits the maximum acquisition frame size. For a 512×384 pixel image, we would need to save 8×10^6 samples per channel for a sampling time of 10 ns. This number is two times the maximum possible number of samples we could save on our oscilloscope. However, other commercially available oscilloscopes can save such large acquisition frames. We should note that as the size of the acquisition frame increases, so does the time required to save it, adding to the total imaging time.

Overall, this proposed scheme of SE count imaging would be slower than Yamada's implementation. However, it would be simpler to implement due to less stringent timing and hardware requirements. The required beam blanking could be achievable with the built-in beam blanker on the SEM, and if access to the datastream from the SEM to the computer is available, an oscilloscope would not be required either.

5.5.2 Scheme for online conditional re-illumination

A similar setup to the one we proposed for live SE count imaging could also be used to implement live conditional re-illumination. This setup is shown schematically in Figure 5-9(b). Implementing M -limited conditional re-illumination is straightforward; we would just blank the beam permanently after the requisite number of acquisition frames had been captured. N_{SE} -limited conditional re-illumination would be enabled by the beam blanker. In this case we would need ns-beam blanking, since we would

be blanking the beam over individual pixels (with dwell times on the order of a few hundred ns) within each frame as opposed to blanking it only at the end of the frame. Recently, sub-ns electrostatic electron beam-blankers have been integrated into the SEM column [105,106]. Such beam-blankers could be used in our scheme too. Further, we would now need to generate SE count images after each frame to decide which pixels to illuminate in the next frame. Therefore, the transferring of acquisition frame data and generation of SE count images would have to be brought online (represented by the solid arrows in Figure 5-9(b)). After the computer has generated an SE count image from one frame, the code decides which pixels are to be re-illuminated and creates a reillumination waveform with the known pixel dwell times. After sending the unblank signal to the beam blanker to start the next frame acquisition, the SEM computer would send the reillumination waveform to the beam blanker in order to blank the beam over the appropriate pixels. This signal is represented with the red arrow in Figure 5-9(b). This process would repeat for every acquisition frame until the SE threshold had been achieved for all pixels.

This implementation of the re-illumination scheme allows flexibility in the exact re-illumination algorithm used. Since none of the components are implemented in hardware, we can easily change the re-illumination criteria in the computer code and no hardware changes would need to be made. Therefore, more complex re-illumination schemes that, for example, take the number of SEs in neighbouring pixels [108] into account or assign different weights to the SE counts from the in-lens or in-chamber detectors could also be implemented.

5.6 Conclusions

In this chapter, we described our implementation of SE count imaging by synchronizing SE detector signal collection with the SEM scan signal using features of the scan waveform. We also described the code we used to generate SE count images from the oscilloscope acquisition frames. Our code incorporated a lot of the ns-synchronization

achieved through external circuitry in Yamada’s implementation of SE count imaging. We used the SNR and contrast metrics introduced in Chapter 3 to show that SE count imaging could produce images with better image quality at the same incident electron dose than conventional imaging. Further, we implemented conditional re-illumination using the two schemes we had described in Chapter 3. Using the SNR and MARE, we showed that image quality metrics can be traded off for reduced incident electron dose in conditional re-illumination schemes. Our results indicated that illuminating all pixels uniformly and stopping after a fixed number of illuminations (M -limited conditional re-illumination) is more effective at reducing incident electron dose than a re-illumination scheme based on stopping at a threshold number of SEs $N_{SE,T}$ (N_{SE} -limited schemes) if we consider average dose over all pixels. If we consider average dose over the (high-contrast) sample only, the N_{SE} -limited scheme gives higher SNR and lower MARE. The choice of scheme would depend on the sample type, image quality metrics and imaging conditions. An interesting extension of this work would be a study of the imaging resolution as a function of the relative incident dose for the two re-illumination schemes. Resolution standards such as the USAF three-bar resolution test chart or diffraction gratings with a known pitch could be used for this work and the resolution of the generated images analyzed using the Fourier-ring correlation technique. More complicated N_{SE} -limited schemes that use non-uniform $N_{SE,T}$, depending on the N_{SE} from a given pixel in previous illuminations, would also be an interesting extension of the re-illumination schemes considered here.

Although the imaging schemes we implemented in this chapter were offline, we proposed schemes for both online SE count imaging and conditional-reillumination that are flexible and can be adapted to a given re-illumination protocol. Our proposed SE count imaging scheme does not require any additional hardware beyond the SEM, the SEM computer, a 100 MHz oscilloscope and a delay element. The built-in beam blanker in the SEM could be used to blank the beam between acquisition frames. Further, our proposed conditional reillumination scheme requires a ns-beam blanker to blank the beam within a frame when it scans over pixels that need to be skipped.

We believe that recent adaptive and sparse-sampling illumination schemes [41, 80] could also be implemented on the SEM using the setup we have proposed here.

We used the SE counts from our images to analyze the statistics of the SE emission distribution and quantified its deviations from an ideal Poisson process. We found a B-factor that was about 2 times larger than previously reported values in literature [21]. More accurate characterization of the SE distribution at different beam energies, incident electron currents and for different materials, as well as investigation of the reasons for the high B-factor would be interesting applications of our technique of SE counting.

Our SE counting re-illumination schemes used very simple estimators for the final pixel SE count. We effectively assumed that the SE count from both detectors on the pixel after a certain number of illuminations was the best estimator for the ‘ground truth’ value. This assumption would be justified if there was no carbon deposition or sample damage, which would cause sample modification during illumination. This assumption was justified for our high-SE-yield copper grid sample. However, for lower-SE-yield organic samples this assumption may not be valid and we might need to assign weights to different acquisition frames since the earlier ones would carry more high-frequency information. Similar frame-weighting techniques have been used in cryo-electron microscopy to improve imaging resolution and corrected for beam-induced motion [7].

As discussed in Chapter 4 Section 4.1.3, the total DQE of our detectors at the working distance we used in this chapter was about 50%. This non-ideal DQE meant that we missed about half of the SEs emitted from the sample. Therefore, we had to illuminate our sample for longer to get the same number of detected SEs, increasing the incident electron dose. To mitigate this effect, we could include the measured value of the DQE in our SE count estimation scheme to improve its accuracy. We could also try to improve DQE by using different detector configurations [26].

In summary, the results of this chapter and Chapter 4 demonstrate that SE

count imaging can be implemented on an SEM to characterize the SE detectors, generate high-SNR images, and analyze the statistics of the SE distribution, using the existing hardware on the SEM. SE count imaging can significantly lower the incident electron dose required for a given image SNR, particularly when combined with conditional re-illumination. In combination with the quantum mechanical electron microscopy schemes considered in Chapter 2, SE counting and re-illumination could lead to an even greater reduction in the incident dose required for SEM imaging.

Chapter 6

Summary and future outlook

In this chapter, we will summarize this thesis and discuss progress towards extensions of this work. This chapter is divided into two sections. In Section 6.1 we will summarize the theoretical and experimental advances made in this thesis, and in Section 6.2 we will discuss possibilities of extending this work to high-efficiency QEM and ion-beam imaging, as well as the status of implementation of these imaging schemes. In this chapter, we will discuss extensions of cross-thesis work; extensions of work in specific chapters were discussed in the respective chapter conclusions.

6.1 Summary of work

In this thesis we have developed adaptive illumination schemes that can be applied to STEM and SEM imaging, as well as single-SE-sensitive imaging on SEM to facilitate the implementation of adaptive and quantum imaging schemes in these microscopes. In Chapter 2, we proposed a scheme called conditional re-illumination, which used the statistics from previous rounds of sample illumination for every pixel to decide which pixels would be illuminated in future rounds. We demonstrated that this scheme allows us to circumvent limitations on sample electron dose due to the Poisson na-

ture of the incident electron beam and achieve close-to-ideal imaging performance for both IFM and STEM imaging for high-contrast samples. In Chapter 3, we extended conditional re-illumination to SEMs by devising metrics for characterizing the quality of grayscale sample images. We analyzed three metrics: contrast, mean absolute relative error (MARE) and signal-to-noise-ratio (SNR, based on Thong et al.'s work [116]) and discussed imaging situations in which each metric would be useful. Further, we developed conditional re-illumination schemes for imaging such grayscale samples in an SEM. Our schemes used two types of criteria for determining if a pixel should be re-illuminated: the number of SEs already detected from it (N_{SE} -limited schemes) and the number of times the pixel had been illuminated (M -limited schemes).

In Chapters 4 and 5, we turned to experimental implementation of the theoretical ideas developed in Chapters 2 and 3. First, in Chapter 4, we developed image histogram- and oscilloscope-based SE counting, and used these techniques to characterize the DQE of the in-chamber and in-lens SE detectors. We also developed an understanding of the voltage and temporal characteristics of the SE pulses. We used this understanding, along with an analysis of the SEM scan waveforms, to develop techniques for offline SE count imaging in Chapter 5. In our SE count imaging algorithm most of the complex nanosecond-scale synchronization required for electron-count imaging was integrated into MATLAB code that processed SEM scan waveforms and SE detector signal to generate images. We compared these SE count images to conventional SEM images using the contrast and SNR metrics described in Chapter 3 and showed a 50% improvement in contrast and 30% improvement in SNR at the same incident electron dose for SE count imaging compared to conventional imaging. We also evaluated the MARE and SNR for the two conditional re-illumination schemes developed in Chapter 3 and showed that the choice of scheme depends upon the type of sample, imaging conditions and type of image quality metric that is important in the experiment. Finally, we proposed online SE count imaging and conditional re-illumination schemes that use existing SEM hardware with the addition of a beam blanker for live implementation of the low-dose imaging schemes

we described in Chapters 3 and 5.

6.2 Future outlook

Having summarized the work in this thesis, we will discuss progress towards implementation of IFM and QEM, extensions of conditional re-illumination to QEM, and other proposed ideas for extending IFM in this section. We will also discuss applications of our SE count imaging techniques to recently proposed time-resolved SEM and helium ion-beam imaging schemes.

6.2.1 Combination of conditional re-illumination with quantum mechanical imaging schemes

In Chapter 2, we calculated the reduction in sample damage enabled by a combination of IFM imaging (using a Mach-Zehnder interferometer) and conditional re-illumination. Further we referred to our implementation of a Mach-Zehnder interferometer in a conventional TEM [62, 63] in Chapter 1. Here, we will discuss this implementation as well as other potential implementations of IFM in more detail and discuss potential extensions of conditional re-illumination to higher-efficiency QEM schemes.

Figure 6-1 is a schematic of our Mach-Zehnder interferometer in a TEM. We fabricated two 45-nm-thick diffraction gratings from a single-crystal silicon TEM support grid (Hitachi Hi-Tech) using gallium focused-ion-beam (FIB) milling. Fabrication from single-crystal-silicon ensured that the two gratings were self-aligned with each other. The gap between the gratings was 20 μm . We placed the two gratings in the sample holder of a TEM (JEOL 2010F HRTEM). We used an electron beam with semi-convergence angle 4 mrad and a 240 nm diameter on the first grating. The first grating acted as beamsplitter and split the incident electron beam into several

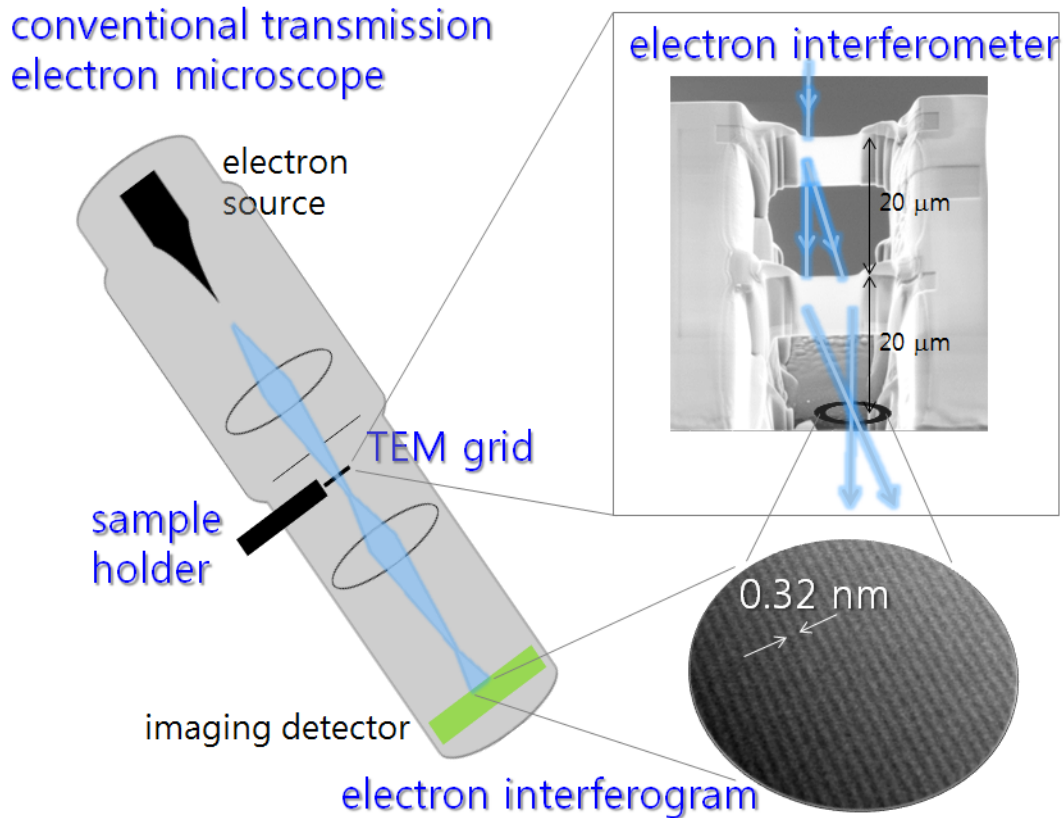


Figure 6-1: Mach-Zehnder interferometer in TEM. The interferometer consists of two silicon diffraction gratings fabricated from a single-crystal silicon TEM support grid using FIB milling. The gratings are mounted into the sample chamber of a TEM, where the split and recombine the electron beam through diffraction to produce 0.32 nm-period interference fringes.

diffraction orders. The 20 μm gap between the gratings ensured that the diffracted beams completely separated from each other when they were incident on the second grating, which diffracted the beams again and caused them to re-interfere at a plane 20 μm below the second grating. On imaging this plane, we observed interference fringes with period 0.32 nm, equal to the silicon $[\bar{1}\bar{1}1]$ lattice spacing. We used the contrast of these fringes to calculate the degree of spatial coherence of the electron beam in our TEM.

The next step to an implementation of IFM using this approach would be the fabrication of a three-grating setup, with the third grating placed in the interference plane of the first two gratings. Modulations in the intensities of the diffracted beams

from this third grating due to the presence of a scattering sample (such as a chunk of platinum deposited between the first two gratings) could be statistically analyzed to demonstrate IFM. As detailed in [63], this approach was hampered by lack of precise control over the thickness of the diffraction gratings, which made it difficult to separate modulation in diffraction beam intensity due to dynamical diffraction effects from modulations due to interference. Although the thicknesses of single membranes can be mapped out using EELS [119], it is challenging to map the thickness of three gratings.

More recently, Turner and co-workers proposed a promising alternative approach to demonstrating IFM, using nanofabricated gratings [69]. Two such gratings, fabricated on SiN using FIB milling, can be placed in the condenser and objective lens apertures of a TEM. The translational degrees of freedom of the mechanical aperture alignment system could be used to align the two gratings. The thickness profiles of these gratings can be individually mapped to model the intensity of diffracted beams. The sample to be imaged can be placed in the regular TEM sample holder which is located between the two aperture planes. Fringes from the interference of electron beams diffracted from the two gratings are imaged on a direct electron detection camera, and modulations in the intensities of the diffracted beams can be used to infer the transparency of the sample pixel being imaged.

Demonstration of IFM with either of these approaches would be a significant step towards the implementation of quantum imaging schemes in TEM. Since these approaches already use conventional TEMs, it would be relatively easy to incorporate conditional re-illumination with these schemes. Especially in the approach with nanofabricated gratings placed in the lens apertures, the sample pixels could be scanned normally once, and the statistics from each pixel could be used to inform future scans. As discussed in Chapter 1, direct electron detectors at TEM energies have a high DQE and fast frame rate, meaning that longer pixel dwell times could be used without compromising the accuracy of electron counting, compared to our implementation of SE counting in Chapters 4 and 5. Therefore, the requirements

for beam blanking speed would not be as high in STEM as in SEM, and existing STEM beam blankers and pattern generators could be used to perform conditional re-illumination.

Recently, Kruit and van Staaden performed an analysis of the performance of conditional re-illumination when combined with the proposed schemes for IFM-based QEM [2]. This analysis also relaxed the assumption of opaque or transparent sample pixels and ideal detectors that we had made in Chapter 2. The major takeaway of this work was that the inclusion of sample grayscale (in the form of both semi-transparency and phase) sustained the benefits of conditional re-illumination imaging. However, the inclusion of QEM schemes with multiple circulations of the electron beam reduced the benefits of re-illumination because this scheme already provides damage-free discrimination between high-contrast sample pixels. With realistically achievable numbers of circulations and typical phases in TEM samples, this analysis reported more than an order of magnitude lower error at a dose of 1 electron per pixel using conditional re-illumination for both STEM and IFM imaging.

A related idea was recently proposed by Kruit et al. [120] to extend the application of QEM to phase-contrast imaging. In this scheme, the transfer of intensity between the two interferometer arms inside the electron cavity is mediated by the phase of the sample pixel being imaged. The number of circulations are chosen such that the intensity transfers completely for a narrow range of pixel phases and does not transfer otherwise. At the end of the imaging process, we have a phase ‘contour’ for the chosen phase. By repeating the experiment for different numbers of circulations, a phase contour map of the entire sample can be created with much lower damage and higher precision than conventional STEM. This scheme could also be combined with conditional re-illumination to, for example, achieve a given phase sensitivity for all pixels.

6.2.2 Extensions of SE counting

In Chapters 4 and 5 of this thesis, we developed SE count imaging and showed that it offers an incident electron dose reduction of up to 30% compared to conventional SEM imaging. As we had discussed in the conclusion sections of these chapters, our work can be extended to more accurately analyze the probability distribution of SEs and characterize deviations from ideal Poisson behavior more accurately. We found some discrepancies in the degree of non-ideality extracted from our experiments and that reported previously [21], and a more accurate analysis to explain this discrepancy would be interesting. Further, we restricted our imaging to SEs. Future extensions could also include counting of BSEs to generate a more complete picture of the statistics of sample-electron interaction and emission.

Recently, there have been proposals to use ideas from the theory of parameter estimation to reduce the required electron dose in SEM and helium ion-beam imaging [107, 108, 121]. These ideas rely on eliminating noise in the image due to the Poisson statistics of the incident ion beam through time-resolved counting of SEs. The extremely low currents used in helium ion-beam imaging (down to 0.1 pA) combined with the high SE yield of ions (much higher than 1 for helium) allow such time-based discrimination between SEs excited by different incident ions. Since our SE counting technique is inherently time-resolved, it could be directly used to implement these proposals.

In conclusion, this thesis extends electron count imaging to SEM and enables its implementation on any SEM system. Further, this thesis also extends adaptive illumination to IFM-based QEM imaging and demonstrates that conditional re-illumination can be used to maximize the benefits of QEM over conventional STEM and SEM imaging. Combined with the many other proposed adaptive illumination and quantum imaging schemes in the literature (as reviewed here and in Section 1.2 of Chapter 1), adoption of the counting techniques developed in this thesis would lead to significant reduction in the electron dose required for electron microscopy.

Appendix A

Example calculation of signal-to-noise ratio

In this Appendix, we will present an example calculation of Thong's SNR metric (discussed in Chapter 3) for an SEM image with more features than that in figure 3-3. The purpose of this Appendix is to demonstrate that the SNR metric works for all kinds of SEM images.

Figure A-1(a) is an SEM image of a brass Faraday cup (the hole in the center of the image is where the incident electron beam would be positioned to measure the current). This Faraday cup was adhered to a stainless steel Kimball physics plate using silver paste, and the assembly was covered by a second Kimball physics plate with a large central aperture (the outline of the aperture is visible to the left of the image). This image was acquired at a pixel dwell time of 1.8 μs . Figure A-1(b) is an SEM image of the same sample, acquired at a pixel dwell time of 3.6 μs . We can see that this image appears to be less noisy. Figure A-1(c) shows the autocorrelation for these images (blue curve for the 3.6 μs -dwell-time image and orange curve for the 1.8 μs -dwell-time image) and figure A-1(d) shows this autocorrelation around zero offset. We can see that the two images have almost identical autocorrelation values at all offsets except zero, where the higher dwell time image has a lower autocorrelation

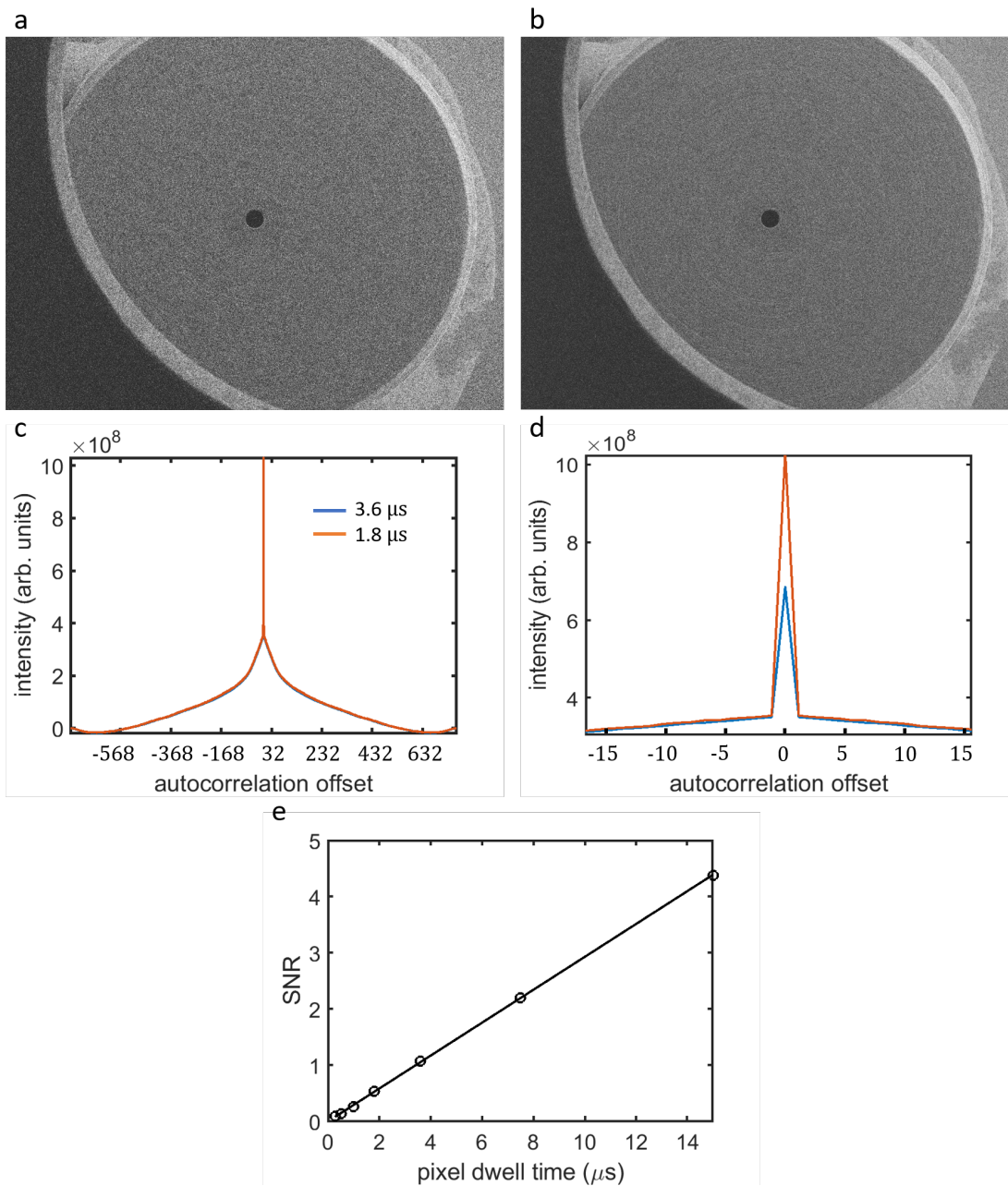


Figure A-1: Example SNR calculation. (a) SEM image of Faraday cup taken at pixel dwell time of 1.8 μs . (b) SEM image of Faraday cup taken at pixel dwell time of 3.6 μs . (c) and (d) Autocorrelation of the images in (a) (solid red curve) and (b) (solid blue curve). (e) Variation of SNR with pixel dwell time, showing linear scaling.

peak. This lower peak shows that the higher dwell time image has higher SNR, as expected. Figure A-1(e) shows the variation of the SNR with pixel dwell time and demonstrates the same linear scaling discussed in Section 3.1.3 of Chapter 4.

Appendix B

In-lens detector histograms

In this appendix, we will show the variation in the image histogram for the in-lens detector with changing imaging conditions. We presented similar data for the in-chamber detector in Chapter 4. This data shows evidence of integral-SE-count peaks in the image histograms for the in-lens detector and supports our conclusions in Chapters 4 and 5.

Figure B-1(a) shows the variation in the in-lens detector image histogram with pixel dwell time. We obtained these histograms by scanning the electron beam over a uniform sample of aluminum at a beam current of 2.2 pA, beam energy of 10 keV, and working distance of 13 mm. Just as for the in-chamber detector, at high pixel dwell time the image histogram is nearly Gaussian. As the pixel dwell time reduces from 28 μs to 7.5 μs , the mean of the histogram remains at 111 but the width increases. At a pixel dwell time of 3.6 μs , we see discrete peaks begin to emerge; there is a sharp peak at brightness 64 and a broader one at brightness 75 in the histogram. The histogram for 1.8 μs shows a sharp peak at 64, and broad peaks at 87 and 112. Finally, the 1.8 μs histogram shows a sharp peak at 64 and a broad peak at 112. The gap between consecutive peaks is 11 pixel brightness units for the 3.6 μs histogram, ~ 24 for the 1.8 μs histogram, and 48 for the 1 μs histogram. Just as we had observed for the in-chamber image histograms, the gap between peaks doubled when the pixel

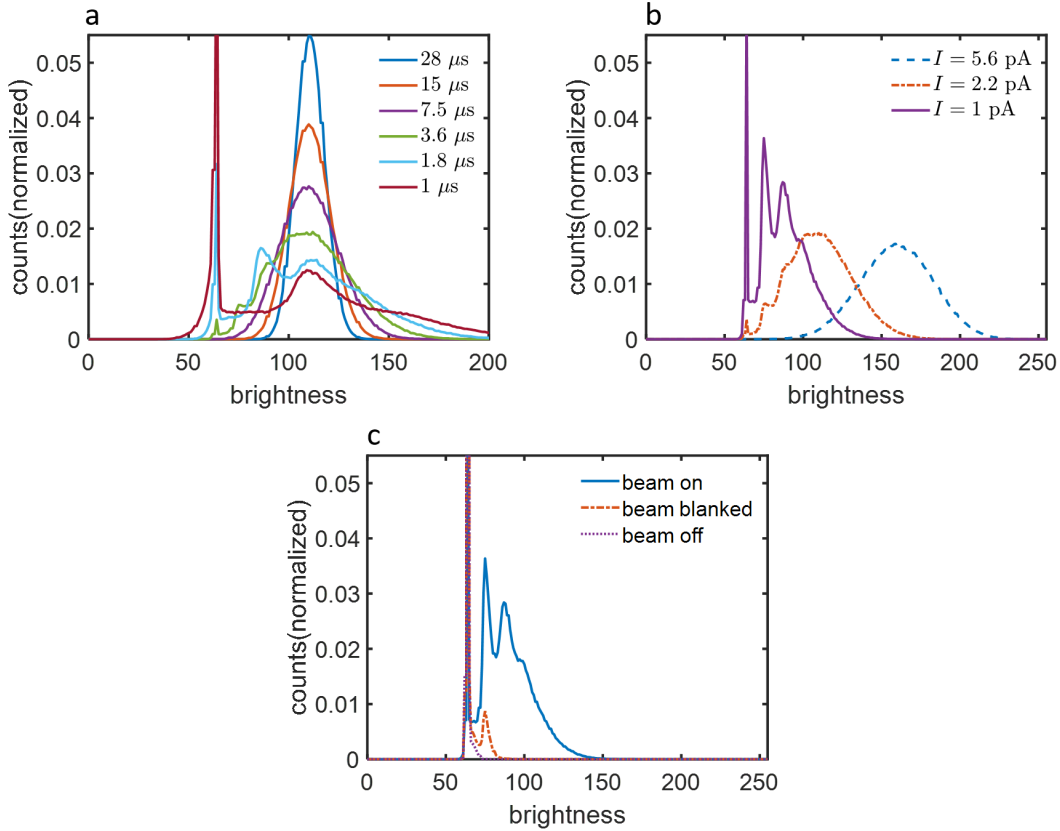


Figure B-1: In-lens image histogram. (a) Variation in image histogram with changing pixel dwell time. As the pixel dwell time was lowered from 28 μs to 1 μs , distinct peaks appeared in the histogram corresponding to 0, 1 and 2 SEs. (b) Variation in image histogram with changing incident electron beam current at a pixel dwell time of 3.6 μs . Discrete peaks appear in the histogram at 1 pA beam current corresponding to integral number of SEs. (c) Variation in the image histogram when the beam is on, blanked and off.

dwell time was halved due to signal time-averaging. Therefore, we can ascribe these peaks to integral number of SEs, with the sharp peak corresponding to 0 SEs.

Figure B-1(b) shows the change in the in-lens image histogram with incident beam current. Each of these histograms was taken at a pixel dwell time of 3.6 μs . As the incident beam current reduces from 5.6 pA to 1 pA, peaks corresponding to integral number of SEs appear in the histogram.

Figure B-1(c) shows the in-lens histogram when the beam is on, blanked and off. Just as for the in-chamber image, a few pixels register one SE when the beam is blanked due to SEs generated in the electron beam column. When the beam is

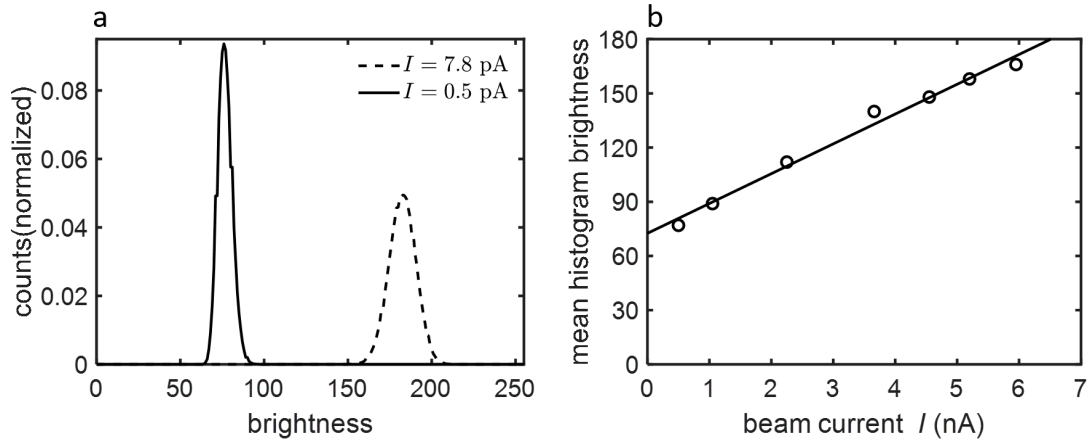


Figure B-2: Joy’s method of finding DQE for the in-lens detector. (a) Change in image histogram on changing the electron beam current from 7.8 pA to 0.5 pA for a pixel dwell time of 28 μ s. The histogram mean lowers from 183 to 76 and the histogram gets narrower. (b) Variation in mean histogram brightness as a function of beam current.

switched off, these SEs disappear and only the sharp, 0 SE peak remains. This result confirms that the sharp peak corresponds to noise and dark counts in the detector.

In Figure B-2, we show the implementation of Joy’s method for finding DQE for the in-chamber detector. The images corresponding to these histograms were acquired for a pixel dwell time of 28 μ s, with varying incident beam current. Figure B-2(a) shows the image histograms for two values of the beam current. The histogram for $I = 7.8$ pA has a mean of 183, while that for $I = 0.5$ pA has a mean of 76. From these histogram mean values, we extracted the mean SE counts just as for the in-chamber detector. Figure B-2(b) is a plot of the extracted mean values (unfilled black circles) as a function of the incident beam current. The solid black line is a least-squares fit line and gives us the offset in mean values due to the contrast and image brightness values we used. This value is 72.6, close to the 0 SE-level of 64 we found from the histograms in Figure B-1. We used the offset-corrected mean pixel brightness values to find the in-lens DQE reported in chapter 4 Section 4.1.1.2.

Appendix C

Fitting SE probability distributions

In this appendix, we will show how the Neyman type-A distribution provides a much better fit to the SE emission probability distributions we extracted from the SE count images reported in chapter 5. The Neyman type-A distribution is a type of compound or generalized Poisson distribution consisting of a Poisson sum of independent, identically distributed Poisson random variables. Suppose X is a generalized Poisson distributed random variable, it is given by:

$$X = Y_1 + Y_2 + \dots + Y_S$$

Here $S \sim \text{Poisson}(N)$ and $Y_i \sim \text{Poisson}(\delta)$ are independent, identically distributed Poisson random variables. Physically, S represents the number of incident beam electrons with mean N and Y represents the number of SEs produced per incident beam electron with mean δ , equal to the SE yield. The mean and variance of X are given by:

$$E[X] = N\delta \tag{C.1}$$

$$\text{Var}[X] = N\delta(1 + \delta) \tag{C.2}$$

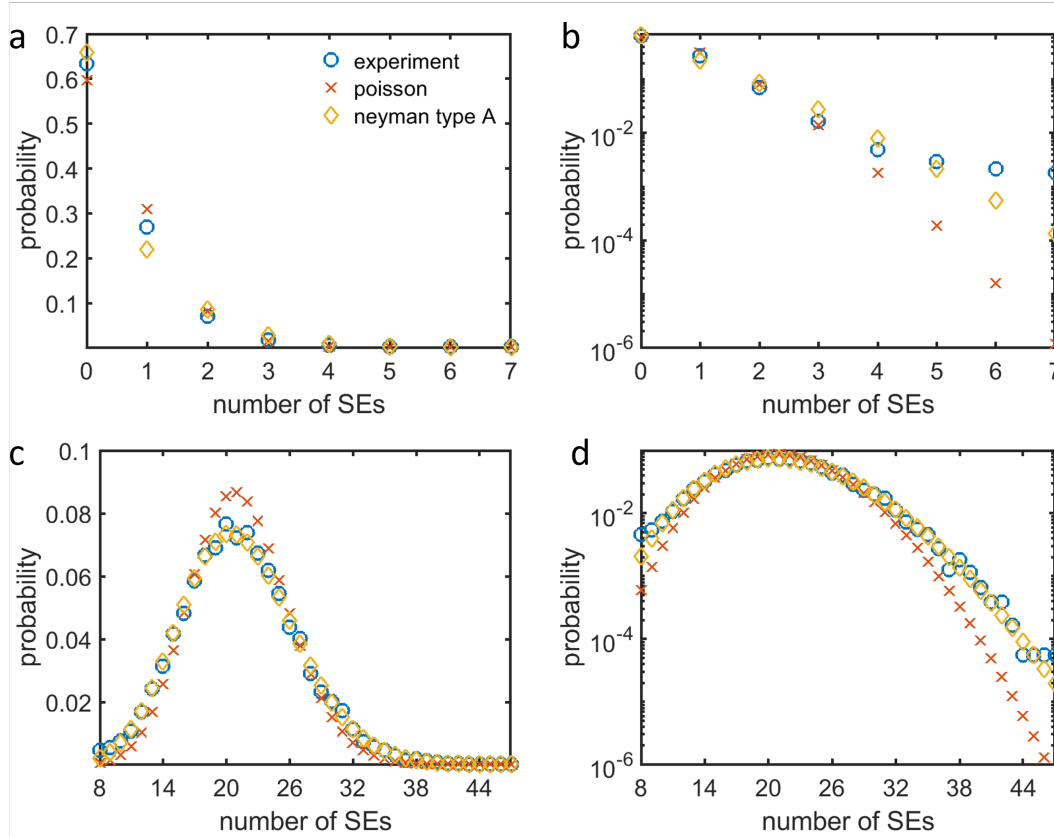


Figure C-1: Probability distribution of SE emission revisited. (a) Distribution of the number of SEs extracted from the background (vacuum) pixels in Figure 5-5(a) (unfilled blue circles). The mean SE count for this distribution is 0.52 and the variance was 0.74. The orange crosses indicate the probabilities of a Poisson process with the same mean SE count, and the yellow diamonds represent probabilities for a Neyman type-A process with parameters $N = 1.23$ and $\delta = 0.42$. (b) Same as (a) with the y-axis on a log scale. (c) Distribution of the number of SEs extracted from the sample (copper mesh) pixels in Figure 5-5(a) (unfilled blue circles). The mean SE count for this distribution is 21.29 and the variance was 29.8. The orange crosses indicate the probabilities of a Poisson process with the same mean SE count, and the yellow diamonds represent probabilities for a Neyman type-A process with parameters $N = 53.26$ and $\delta = 0.4$. (d) Same as (c) with the y-axis on a log scale. For both sample and background distributions, the Neyman type-A curve fits the experimental distribution much more closely than the Poisson distribution curve.

Figure C-1 shows the SE distribution extracted from the SE count images reported in Section 5.3.2 of chapter 5 and is identical to the distributions reported in Figure 5-6. In addition to the Poisson distribution with the same mean (red crosses), I have also plotted a Neyman type-A distribution with parameters extracted from the mean and variance of the experimental distribution (yellow diamonds). For the background distribution (Figure C-1(a) and (b)), the mean was equal to 0.52 and the variance was equal to 0.74. From these values, we can use equations C.2 and C.2 to extract N and δ . These extracted values are $N = 1.23$ and $\delta = 0.42$. Similarly, for the sample distribution (Figure C-1(c) and (d)), the mean was equal to 21.29 and the variance was 29.8. Therefore, $N = 53.26$ and $\delta = 0.4$. We can see that the Neyman type-A distribution fits the experimental distribution much more accurately than the Poisson distribution, validating the applicability of this model. The accuracy of the fit is particularly notable for the sample distribution, where it is almost exact. There are small deviations at the high-SE tail of the background distribution and the low-SE tail of the sample distribution, due to overlap between these distributions as discussed in Section 5.3.3 of chapter 5.

In our experiments, we used a beam current of 2 pA and a pixel dwell time of 440 ns, and we collected 32 acquisition frames. Using Equation (4.1), we get $N = 176$ over all frames. This value is about a factor of 3 larger than the N extracted from the Neyman type-A distribution parameters. This discrepancy can be accounted for by the non-ideal DQE of our detectors. As discussed in Section 4.1.3.3, the total DQE for the two detectors was about 0.5 at the working distance we used in our experiment. This DQE would reduce the expected number of SEs N_{SE} , thereby reducing the extracted N and δ too. More accurate accounting of the effects of non-ideal DQE would be required to extract accurate values of N and δ from this data.

Appendix D

MATLAB code

In this appendix, we will describe the MATLAB code that was used in the simulations and data analysis described in this thesis. Section D.1 has the MATLAB scripts corresponding to chapter 2, Section D.2 the code for chapter 3, Section D.3 the code for chapter 4, and Section D.2 the code for chapter 5.

D.1 MATLAB code for chapter 2

In chapter 2, Figures 2-1, 2-2(a), 2-3, and 2-5(a) are direct plots of expressions from the text; code for these plots is not included here. Script `classical_IFM_damage_errors.m` was used to generate figures 2-2(b) and 2-4. The function `monte_carlo_func.m` was used by the function `cond_reill.m` to perform Monte-Carlo simulations of conditional re-illumination. Scripts `cond_reill_run.m` and `cond_reill_plot.m` used these functions to generate figures 2-6 and 2-7.

```
%%-----classical_IFM_damage_errors.m-----%%  
  
% This code calculates and plots Perr as a function of ndamage and/or q,  
% using equations 2.5, 2.8, 2.11 and 2.14 for the four imaging schemes.  
  
clear;clc;  
%ndamarr=[0.5 2];  
%ndamarr=2;  
ndamarr=0.0011:0.01:10; % To calculate error probability for a range of ndamage  
[~,ndamsize]=size(ndamarr);  
%q=0.001:0.001:0.999; % To calculate error probability for a range of q  
q=0.5;
```

```

[~,n]=size(q);
%%
for nind=1:ndamsize
ndam=ndamarr(nind); %0 at 1.5309/2
lt_cl=ndam; % For classical imaging, lamda*t is equal to the ndamage
lt_ifm=2*ndam; % For IFM, lambda*t is twice ndamage
kstar=(ndam*log(q./(1-q)))/log(4);
kstar_d3=log(q./(1-q))/log(4);
factor_cl=1./(1+exp(lt_cl));
p_md_ifm=zeros(1,n);
p_fa_ifm=zeros(1,n);
p_md_ifm_d3=zeros(1,n);
p_fa_ifm_d3=zeros(1,n);
perr_cl=zeros(1,n);
qlim=zeros(1,n);
for i=1:size(q')
if(q(i)<factor_cl)
perr_cl(i)=q(i);
else
perr_cl(i)=(1-q(i))*exp(-lt_cl);
end
if(kstar(i)<0)
p_md_ifm(i)=exp(-lt_ifm/4);
p_fa_ifm(i)=0;
else
qlim(i)=ceil(kstar(i));
for mdi=1:qlim(i)
p_md_ifm(i)=p_md_ifm(i)+exp(-lt_ifm/4)*(lt_ifm/4)^(mdi-1)/factorial(mdi-1);
p_fa_ifm(i)=p_fa_ifm(i)+exp(-lt_ifm)*(lt_ifm)^(mdi-1)/factorial(mdi-1);
end
p_md_ifm(i)=exp(-lt_ifm/4)*(1-p_md_ifm(i));
end
if(kstar_d3(i)<0)
p_md_ifm_d3(i)=exp(-3*lt_ifm/4);
p_fa_ifm_d3(i)=0;
else
qlim_d3(i)=ceil(kstar_d3(i));
for mdi_d3=1:qlim_d3(i)
p_md_ifm_d3(i)=p_md_ifm_d3(i)+exp(-lt_ifm/4)*(lt_ifm/4)^(mdi_d3-1)/factorial(mdi_d3-1);
p_fa_ifm_d3(i)=p_fa_ifm_d3(i)+exp(-lt_ifm)*(lt_ifm)^(mdi_d3-1)/factorial(mdi_d3-1);
end
p_md_ifm_d3(i)=exp(-3*lt_ifm/4)*(1-p_md_ifm_d3(i));
end
if(q(i)<1/2)
perr_cl_d3(i)=q(i)*exp(-lt_cl);
else
perr_cl_d3(i)=(1-q(i))*exp(-lt_cl);
end
end
perr_ifm=(q).*p_md_ifm+(1-q).*(p_fa_ifm);
perr_ifm_d3=(q).*p_md_ifm_d3+(1-q).*(p_fa_ifm_d3);
perr_cl_mat(:,nind)=perr_cl;
perr_ifm_mat(:,nind)=perr_ifm;
perr_cl_d3_mat(:,nind)=perr_cl_d3;
perr_ifm_d3_mat(:,nind)=perr_ifm_d3;
%subplot(2,1,nind); %Figure 3 of paper
%q=plot(q,perr_cl,q,perr_cl_d3,q,perr_ifm,q,perr_ifm_d3, 'LineWidth',2);
plot(q,perr_cl,'--','LineWidth',2);
hold on;
plot(q,perr_cl_d3,'LineWidth',2,'Color',[0.4940 0.1840 0.5560]);
hold on;
%plot(q,perr_ifm,':','LineWidth',2,'Color',[0.8500, 0.3250, 0.0980]);
%plot(q,perr_ifm_d3,'-','LineWidth',2,'Color',[0.4660, 0.6740, 0.1880]);
set(gca,'XTick',0:0.2:1,'FontSize',18);
xlim([0 1]);
ylim([0 1.3*max(perr_cl)])
xlabel('$q$', 'FontSize',18,'Interpreter','Latex');
ylabel('$P_{\text{err}}$', 'FontSize',18,'Interpreter','Latex');
%xlabel('probability of opaque pixel','FontSize',18);
%ylabel('error probability','FontSize',18);
%set(y, 'Units', 'Normalized', 'Position', [-0.1, 0.5, 0]);
%if(nind==1)
%ylim([0 0.4]);
%set(gca,'YTick',0:0.1:0.4,'FontSize',18);
%end
%if(nind==2)
lgd=legend('Classical, no SD_3$', 'Classical, SD_3$');
%lgd=legend('Classical, no SD_3$', 'Classical, SD_3$', 'IFM, no SD_3$', 'IFM, SD_3$');
set(lgd, 'Interpreter', 'latex');
%lgd=legend('IFM, no D_3', 'Classical, D_3', 'IFM, no D_3', 'IFM, D_3');
lgd.FontSize=18;
lgd.Position=[0.65 0.83 0.2 0.05];
lgd.Color='White';
lgd.Box='off';
end
ax=gca;
ax.TickLength=[0.01, 0.01];
ax.LineWidth = 2;
%end
%saveas(gcf, 'Fig3.png');
%saveas(gcf, 'Figpres11.png');
%%

```

```

plot(ndamarr,perr_cl_mat,'-', 'LineWidth',2);
hold on;
plot(ndamarr,perr_cl_d3_mat, 'LineWidth',2, 'Color',[0.4940 0.1840 0.5560]);
%plot(ndamarr,perr_ifm_mat,':', 'LineWidth',2, 'Color',[0.8500, 0.3250, 0.0980]);
%plot(ndamarr,perr_ifm_d3_mat,'-', 'LineWidth',2, 'Color',[0.4660, 0.6740, 0.1880]);
set(gca, 'XTick',0:2:10, 'FontSize',18);
xlim([0 10]);
ylim([0 0.5])
xlabel('$\bar{n}_{\text{damage}}$', 'Interpreter', 'Latex', 'FontSize',18);
ylabel('$P_{\text{err}}$', 'FontSize',18, 'Interpreter', 'Latex');
%xlabel('dose (electrons/pixel)');
%ylabel('error probability');
ax=gca;
ax.TickLength=[0.01, 0.01];
ax.LineWidth = 2;
%pbaspect([1.5 1 1])
%saveas(gcf, 'chap2_classical_perr_ndam.png');
%%
%save('reill_data_0.05.mat', 'ndamarr', 'perr_ifm_mat', '-append');
% title(strcat('n_{damage}=', num2str(ndam)), 'FontSize',14);
% end
% saveas(gcf, 'perrvsq5.png');
%textbox5=uicontrol('Style','text','Units','norm','Position',[0.1 0.5 0.5 0.05], 'FontSize',14);
%set(textbox5, 'String','a', 'BackgroundColor',[1 1 1]);

%%
plot(q,perr_cl_d3,q,perr_ifm_d3,q_arr,perr_d3_single_q, 'd',q_arr,perr_d3_reill_q, 'bx',q_arr,perr_d3_single_cl_q, 's',
q_arr,perr_d3_reill_cl_q, 'go', 'LineWidth',2, 'MarkerSize',10);
xlabel('q', 'FontSize',14);
ylabel('P_{err}', 'FontSize',14);
ylim([0 0.06]);
set(gca, 'XTick',0:0.1:1, 'FontSize',14);
lgd=legend('Classical, D3, single ill., theory', 'IFM, D3, single ill., theory', 'IFM, D3, single ill., Monte-Carlo', 'IFM
, D3, cond. reill., Monte-Carlo', 'Classical, D3, single ill., Monte-Carlo', 'Classical, D3, cond. reill. Monte-
Carlo', 'Location', 'northwest');
lgd.Box='off';
%saveas(gcf, strcat('Classical_ifm_errors_q', '.png'));
%%
p=plot(ndamarr,perr_cl_mat,ndamarr,perr_ifm_mat,ndamarr,perr_ifm_d3_mat, 'LineWidth',2);
set(gca, 'XTick',0:0.5:5, 'FontSize',14);
xlim([0 5]);
ylim([0 0.5]);
xlabel('n_{damage}', 'FontSize',14);
ylabel('P_{err}', 'FontSize',14);
lgd=legend('D_1', 'D_1,D_2', 'D_1,D_2,D_3');
lgd.Box='off';
%plot(ndamarr,perr_cl_mat,ndamarr,perr_ifm_mat,ndamarr,0.5*(1-1.5*ndamarr),ndamarr,0.5*(1-ndamarr));

```

```

%%-----monte_carlo_func.m-----%%
% This function returns the counts at detectors D1, D2 and D3 for a
% Monte-Carlo simulation of imaging with N_pixels, given the probabilities
% at those detectors, the mean number of electrons in the beam, and the pixel
% transparency x.
function [counts]= monte_carlo_sim(mean,x,p_x1,N_pixels)
counts=zeros(3,1);
N_electrons=poissrnd(mean);
for j=1:N_electrons
    if(x==0)
        counts(1)=counts(1)+1;
    else
        ab=rand(1,1);
        if(ab<=p_x1(3))
            counts(3)=counts(3)+1;
        elseif(ab<=p_x1(3)+p_x1(2))
            counts(2)=counts(2)+1;
        else
            counts(1)=counts(1)+1;
        end
    end
end
end
end

```

```

%%-----cond_reill.m-----%%
% This function performs conditional re-illumination monte-carlo
% simulations and produces ndamage, perror and q given the type of imaging
% scheme, number of pixels, initial q, mean electron number per
% illumination and number of re-illuminations. It uses monte_carlo_func to
% perform the Monte-Carlo imaging simulation for each scheme.
function [n_damage,p_error, qtracker, retest_threshold_lower]= cond_reill(scheme,N_pixels,qin,mean_electron_no,N_reill)
%% Detector probabilities
%p_x0=[1 0 0];
if (scheme==0 || scheme==2)
    p_x1=[0.25 0.25 0.5];
else
    p_x1=[0 0 1];
end
%% Pixel assignment
%N_pixels=10000;
q0=qin*ones(1,N_pixels);
X=zeros(1,N_pixels);
for i=1:N_pixels
    aa=rand(1,1);
    if(aa<=q0)
        X(i)=1;
    end
end
N_black=sum(X);
%% Reillumination parameters
retest_threshold_lower=0.05;
retest_threshold_upper=1-retest_threshold_lower;
%N_reill=99;
N_ill=1+N_reill;
%pixel_test=1:N_pixels;
q=q0;
%[-,N_test]=size(pixel_test);
%mean_electron_no=1;
n_damage_per_pixel=zeros(1,N_pixels);
%% Illumination loop
for j=1:N_ill
    counts=zeros(3,N_pixels);
    for i=1:N_pixels
        if(q(i)>retest_threshold_lower && q(i)<retest_threshold_upper)
            counts(:,i)=monte_carlo_func(mean_electron_no,X(i),p_x1,N_pixels);
            if (counts(3,i)>0)
                n_damage_per_pixel(i)=n_damage_per_pixel(i)+counts(3,i);
            end
            % if(X(i)==1)
            %     N_black_pixels_rl=N_black_pixels_rl+1;
            %n_damage_rl=n_damage_rl/N_black_pixels_rl;
            %for i=1:N_test
            if (scheme==0)
                if (counts(2,i)==0)
                    q(i)=1-1./(1+exp(mean_electron_no/2)/4^(counts(1,i)).*(q(i)/(1-q(i))));
                else
                    q(i)=1;
                end
            elseif (scheme==1)
                if (counts(1,i)==0)
                    q(i)=1-1./(1+exp(mean_electron_no)*(q(i)/(1-q(i))));
                else
                    q(i)=0;
                end
            elseif (scheme==2)
                if (counts(2,i)==0 && counts(3,i)==0)
                    q(i)=1-1./(1+1/4^(counts(1,i)).*(q(i)/(1-q(i))));
                else
                    q(i)=1;
                end
            else
                if (counts(1,i)>0)
                    q(i)=0;
                elseif (counts(3,i)>0)
                    q(i)=1;
                end
            end
            end
            qtracker(j,i)=q(i);
            %if (counts(2,i)==0 && counts(3,i)==0)
            % eta_d3(i)=1./(1+1./4^(counts(1,i)).*(q/(1-q)));
            %else
            %eta_d3(i)=0;
        end
    end
    %q_nod3_rl=1-eta_nod3;
    %q_d3_rl=1-eta_d3;
    for i=1:N_pixels
        if (q(i)<0.5)
            Xhat(i)=0;
        else
            Xhat(i)=1;
        end
    end
end
end

```

```
n_damage=sum(n_damage_per_pixel)/N_black;  
p_error=sum(abs(X-Xhat))/N_pixels;
```

```

%%-----cond_reill_run.m-----%%
%This code uses the cond_reill.m function to produce and save values for
%damage and perror for different mean_electron_number and re-illumination
%threshold values.
clear;clc;
scheme=0;%0 for ifm without D3, 1 for classical without D3, 2 for ifm with D3, 3 for classical with D3
N_pixels=1e5;
%mean_electron_no=0.01:0.01:0.1;
mean_electron_no=0.2;
N_reill=[99 89 74 59 49 39 29 19 9 4 1 0]; %desired no. of illuminations -1
%N_reill=99;
[~,sz_reill]=size(N_reill);
%[~,sz_reill]=size(mean_electron_no);
qin=0.5;
for i=1:sz_reill
    i
    [n_damage(i), p_error(i), qtracker, eps]=cond_reill(scheme,N_pixels,qin,mean_electron_no,N_reill(i));
    %filename=strcat('ifm_d3_',num2str(N_reill+1),'_',num2str(mean_electron_no(i)),'_eps',num2str(eps),'.mat');
    %save(filename,'n_damage','p_error');
    beep on;beep;
end
filename='ifm_nod3_fig7_eps0.05.mat';
save(filename,'n_damage','p_error');
%qtracker=[qin*ones(N_pixels,1), qtracker'];
%load handel;
%player = audioplayer(y, Fs);
%play(player);
%%
%qtracker_plot=qtracker(13,:);
hAxis(1)=subplot(3,1,1);
plot(qtracker(9,:), 'Linewidth',2);
ax=gca;
ax.TickLength=[0.01, 0.01];
ax.LineWidth = 2;
%hold on;
%plot(qtracker(40,:), 'Linewidth',2);
%plot(qtracker(2,:), 'Linewidth',2);
set(gca, 'XTicklabel', []);
set(gca, 'YTick',0:1:1, 'FontSize',18);
xlim([1 20]);
ylim([0 1]);
%pos = get( hAxis(1), 'Position' );
%pos(2)=0.626;
%set( hAxis(1), 'Position', pos );
xlabel('Number of illuminations', 'FontSize',18);
ylabel('Probability of black (opaque) pixel', 'FontSize',18);
hAxis(2)=subplot(3,1,2);
plot(qtracker(10,:), 'Linewidth',2);
ax=gca;
ax.TickLength=[0.01, 0.01];
ax.LineWidth = 2;
set(gca, 'XTicklabel', []);
set(gca, 'YTick',0:1:1, 'FontSize',18);
xlim([1 20]);
ylim([0 1]);
xlabel('Number of illuminations', 'FontSize',18);
ylabel('Probability of black (opaque) pixel', 'FontSize',18);
hAxis(3)=subplot(3,1,3);
plot(qtracker(4,:), 'Linewidth',2);
ax=gca;
ax.TickLength=[0.01, 0.01];
ax.LineWidth = 2;
xlim([1 20]);
ylim([0 1]);
set(gca, 'XTick',0:5:20, 'FontSize',18);
set(gca, 'YTick',0:1:1, 'FontSize',18);
pos = get( hAxis(3), 'Position' );
%pos(2)=0.193;
%set( hAxis(3), 'Position', pos );
xlabel('Number of illuminations', 'FontSize',18);
ylabel('Probability of black (opaque) pixel', 'FontSize',18);
saveas(gcf, 'qtrajectoryifmmod3_2.png');
% plot(n_damage_cl_nod3_10,p_error_cl_nod3_10,'o--','Linewidth',2,'MarkerSize',10);
%save('reill_data_0.49.mat', 'n_damage_ifm_d3_5', 'p_error_ifm_d3_5','-append');
% figure();
% plot(N_reill+1,n_damage_ifm_nod3_10,'o--',N_reill+1,n_damage_ifm_nod3_10_5,'o--','Linewidth',2,'MarkerSize',10);
% xlim([0 100]);
% ylim([0 5.1]);
% set(gca, 'XTick',0:10:100, 'FontSize',18);
% ylabel('n_{damage}', 'FontSize',18);
% xlabel('Number of illuminations', 'FontSize',18);
% lgd=legend('\epsilon = 0.25', '\epsilon = 0.05');
% lgd.Box='off';
%saveas(gcf, strcat('Cond_reill_ndamvsN_ifm_0.05and0.25threshold_dose_10', '.png'));
%% figure();
%% plot(N_reill+1,n_damage_cl_nod3_10./mean_electron_no, 'o--','Linewidth',2, 'MarkerSize',10);
%% xlim([0 100]);
%% ylim([0 3]);
%% set(gca, 'XTick',0:10:100, 'FontSize',14);
%% ylabel('n_{damage} per incident electron', 'FontSize',14);
%% xlabel('Number of illuminations', 'FontSize',14);
%% saveas(gcf, strcat('Cond_reill_perrvsN_ifm_0.05threshold', '.png'));

```

```

% figure();
% plot(N_reill+1,p_error_ifm_nod3_10,'o--',N_reill+1,p_error_ifm_nod3_10_5,'o--','Linewidth',2,'MarkerSize',10);
% xlim([0 100]);
% ylim([0 0.2]);
% set(gca,'XTick',0:10:100,'FontSize',18);
% ylabel('P_{err}','FontSize',18);
% xlabel('Number of illuminations','FontSize',18);
%saveas(gcf,strcat('Cond_reill_perrvsN_ifm_0.05and0.25threshold_dose_10','.png'));
%%
perrormat=zeros(4,12);
ndammat=zeros(4,12);
load('cl_nod3_fig1');
perrormat(1,:)=p_error;
ndammat(1,:)=n_damage;
load('cl_d3_fig1');
perrormat(2,:)=p_error;
ndammat(2,:)=n_damage;
load('ifm_nod3_fig1');
perrormat(3,:)=p_error;
ndammat(3,:)=n_damage;
load('ifm_d3_fig1');
perrormat(4,:)=p_error;
ndammat(4,:)=n_damage;
semilogy(ndammat(1,:),perrormat(1,:),'-x','MarkerSize',10,'Linewidth',2,'Color',[0, 0.4470, 0.7410]);
hold on;
semilogy(ndammat(2,:),perrormat(2,:),'-o','MarkerSize',10,'Linewidth',2,'Color',[0.4940 0.1840 0.5560]);
semilogy(ndammat(3,:),perrormat(3,:),'-d','MarkerSize',10,'Linewidth',2,'Color',[0.8500, 0.3250, 0.0980]);
semilogy(ndammat(4,:),perrormat(4,:),'-s','MarkerSize',10,'Linewidth',2,'Color',[0.4660, 0.6740, 0.1880]);
xlim([0 12]);
ylim([1e-5 1]);
set(gca,'XTick',0:2:12,'FontSize',18);
xlabel('\bar{n}_{\text{damage}}','FontSize',18,'Interpreter','Latex');
ylabel('SP_{\text{err}}','FontSize',18,'Interpreter','Latex');
lgd=legend('Classical, no SD_3S','Classical, SD_3S','IFM, no SD_3S','IFM, SD_3S');
lgd.Box='off';
lgd.FontSize=18;
lgd.Interpreter='Latex';
ax=gca;
ax.TickLength=[0.01, 0.01];
ax.LineWidth = 2;
xlim([0 12]);
ylim([1e-5 1]);
set(gca,'XTick',0:2:12,'FontSize',18);
xlabel('\bar{n}_{\text{damage}}','FontSize',18,'Interpreter','Latex');
ylabel('SP_{\text{err}}','FontSize',18,'Interpreter','Latex');
lgd=legend('Classical, no SD_3S','Classical, SD_3S','IFM, no SD_3S','IFM, SD_3S');
lgd.Box='off';
lgd.FontSize=18;
lgd.Interpreter='Latex';
ax=gca;
ax.TickLength=[0.01, 0.01];
ax.LineWidth = 2;
pos = get(gcf, 'Position'); %// gives x left, y bottom, width, height
width = pos(3);
height = pos(4);
%saveas(gcf,strcat('Fig1','.png'));
%%
perrormat=zeros(2,12);
ndammat=zeros(2,12);
filename='ifm_nod3_fig7_eps0.05.mat';
load(filename);
perrormat(1,:)=p_error;
ndammat(1,:)=n_damage;
filename='ifm_nod3_fig7_eps0.25.mat';
load(filename);
perrormat(2,:)=p_error;
ndammat(2,:)=n_damage;
N_reill_fig1=[99 89 74 59 49 39 29 19 9 4 1 0];
plot(N_reill_fig1+1,perrormat(1,:),'-x','MarkerSize',10,'Linewidth',2,'Color',[0.8500, 0.3250, 0.0980]);
hold on;
plot(N_reill_fig1+1,perrormat(2,:),'-o','MarkerSize',10,'Linewidth',2,'Color',[0.8500, 0.3250, 0.0980]);
xlim([1 100]);
ylim([0 0.5]);
set(gca,'XTick',0:10:100,'FontSize',18);
xlabel('\text{Maximum number of illuminations } M','FontSize',18,'Interpreter','Latex');
ylabel('SP_{\text{err}}','FontSize',18,'Interpreter','Latex');
lgd=legend('$\epsilon=0.05$','$\epsilon=0.25$');
lgd.Box='off';
lgd.FontSize=18;
lgd.Interpreter='Latex';
ax=gca;
ax.TickLength=[0.01, 0.01];
ax.LineWidth = 2;
saveas(gcf,strcat('Fig7a','.png'));
figure();
plot(N_reill_fig1+1,ndammat(1,:),'-x','MarkerSize',10,'Linewidth',2,'Color',[0.8500, 0.3250, 0.0980]);
hold on;
plot(N_reill_fig1+1,ndammat(2,:),'-o','MarkerSize',10,'Linewidth',2,'Color',[0.8500, 0.3250, 0.0980]);
xlim([1 100]);
ylim([0 2]);
set(gca,'XTick',0:10:100,'FontSize',18);
xlabel('\text{Maximum number of illuminations } M','FontSize',18,'Interpreter','Latex');

```

```
ylabel('$\bar{n}_{\text{damage}}$', 'FontSize', 18, 'Interpreter', 'Latex');  
ax=gca;  
ax.TickLength=[0.01, 0.01];  
ax.LineWidth = 2;  
saveas(gcf, strcat('Fig7b', '.png'));
```

```

%%-----cond_reill_plot.m-----%%
% This code loads all the saved error and nadamage datasets for different
% re-illumination thresholds and uses them to plot figures 2-6 and 2-7
clear;clc;
eta=[0 0.05 0.1 0.15 0.2 0.25 0.3 0.49];
%%Read eta=0
load('reill_data_0.mat');
N_ill_50_perr_ifmnd3_0=[p_error_ifm_nod3_2(2) p_error_ifm_nod3_5(2) p_error_ifm_nod3_10(2) p_error_ifm_nod3_15(2)];
N_ill_5_perr_ifmnd3_0=[p_error_ifm_nod3_2(5) p_error_ifm_nod3_5(5) p_error_ifm_nod3_10(5) p_error_ifm_nod3_15(5)];
N_ill_2_perr_ifmnd3_0=[p_error_ifm_nod3_2(6) p_error_ifm_nod3_5(6) p_error_ifm_nod3_10(6) p_error_ifm_nod3_15(6)];
N_ill_1_perr_ifmnd3_0=[p_error_ifm_nod3_2(7) p_error_ifm_nod3_5(7) p_error_ifm_nod3_10(7) p_error_ifm_nod3_15(7)];

N_ill_50_ndam_ifmnd3_0=[n_damage_ifm_nod3_2(2) n_damage_ifm_nod3_5(2) n_damage_ifm_nod3_10(2) n_damage_ifm_nod3_15(2)];
N_ill_5_ndam_ifmnd3_0=[n_damage_ifm_nod3_2(5) n_damage_ifm_nod3_5(5) n_damage_ifm_nod3_10(5) n_damage_ifm_nod3_15(5)];
N_ill_2_ndam_ifmnd3_0=[n_damage_ifm_nod3_2(6) n_damage_ifm_nod3_5(6) n_damage_ifm_nod3_10(6) n_damage_ifm_nod3_15(6)];
N_ill_1_ndam_ifmnd3_0=[n_damage_ifm_nod3_2(7) n_damage_ifm_nod3_5(7) n_damage_ifm_nod3_10(7) n_damage_ifm_nod3_15(7)];

N_ill_50_perr_ifmd3_0=[p_error_ifm_d3_2(2) p_error_ifm_d3_5(2) p_error_ifm_d3_10(2) p_error_ifm_d3_15(2)];
N_ill_5_perr_ifmd3_0=[p_error_ifm_d3_2(5) p_error_ifm_d3_5(5) p_error_ifm_d3_10(5) p_error_ifm_d3_15(5)];
N_ill_2_perr_ifmd3_0=[p_error_ifm_d3_2(6) p_error_ifm_d3_5(6) p_error_ifm_d3_10(6) p_error_ifm_d3_15(6)];
N_ill_1_perr_ifmd3_0=[p_error_ifm_d3_2(7) p_error_ifm_d3_5(7) p_error_ifm_d3_10(7) p_error_ifm_d3_15(7)];

N_ill_50_ndam_ifmd3_0=[n_damage_ifm_d3_2(2) n_damage_ifm_d3_5(2) n_damage_ifm_d3_10(2) n_damage_ifm_d3_15(2)];
N_ill_5_ndam_ifmd3_0=[n_damage_ifm_d3_2(5) n_damage_ifm_d3_5(5) n_damage_ifm_d3_10(5) n_damage_ifm_d3_15(5)];
N_ill_2_ndam_ifmd3_0=[n_damage_ifm_d3_2(6) n_damage_ifm_d3_5(6) n_damage_ifm_d3_10(6) n_damage_ifm_d3_15(6)];
N_ill_1_ndam_ifmd3_0=[n_damage_ifm_d3_2(7) n_damage_ifm_d3_5(7) n_damage_ifm_d3_10(7) n_damage_ifm_d3_15(7)];

N_ill_50_perr_cld3_0=[p_error_cl_d3_2(2) p_error_cl_d3_5(2) p_error_cl_d3_10(2) p_error_cl_d3_15(2)];
N_ill_5_perr_cld3_0=[p_error_cl_d3_2(5) p_error_cl_d3_5(5) p_error_cl_d3_10(5) p_error_cl_d3_15(5)];
N_ill_2_perr_cld3_0=[p_error_cl_d3_2(6) p_error_cl_d3_5(6) p_error_cl_d3_10(6) p_error_cl_d3_15(6)];
N_ill_1_perr_cld3_0=[p_error_cl_d3_2(7) p_error_cl_d3_5(7) p_error_cl_d3_10(7) p_error_cl_d3_15(7)];

N_ill_50_ndam_cld3_0=[n_damage_cl_d3_2(2) n_damage_cl_d3_5(2) n_damage_cl_d3_10(2) n_damage_cl_d3_15(2)];
N_ill_5_ndam_cld3_0=[n_damage_cl_d3_2(5) n_damage_cl_d3_5(5) n_damage_cl_d3_10(5) n_damage_cl_d3_15(5)];
N_ill_2_ndam_cld3_0=[n_damage_cl_d3_2(6) n_damage_cl_d3_5(6) n_damage_cl_d3_10(6) n_damage_cl_d3_15(6)];
N_ill_1_ndam_cld3_0=[n_damage_cl_d3_2(7) n_damage_cl_d3_5(7) n_damage_cl_d3_10(7) n_damage_cl_d3_15(7)];

%%Read eta=0.05
load('reill_data_0.05.mat');
N_ill_100_perr_ifmnd3_005=[p_error_ifm_nod3_2(1) p_error_ifm_nod3_5(1) p_error_ifm_nod3_10(1) p_error_ifm_nod3_15(1)];
N_ill_50_perr_ifmnd3_005=[p_error_ifm_nod3_2(2) p_error_ifm_nod3_5(2) p_error_ifm_nod3_10(2) p_error_ifm_nod3_15(2)];
N_ill_25_perr_ifmnd3_005=[p_error_ifm_nod3_2(3) p_error_ifm_nod3_5(3) p_error_ifm_nod3_10(3) p_error_ifm_nod3_15(3)];
N_ill_10_perr_ifmnd3_005=[p_error_ifm_nod3_2(4) p_error_ifm_nod3_5(4) p_error_ifm_nod3_10(4) p_error_ifm_nod3_15(4)];
N_ill_5_perr_ifmnd3_005=[p_error_ifm_nod3_2(5) p_error_ifm_nod3_5(5) p_error_ifm_nod3_10(5) p_error_ifm_nod3_15(5)];
N_ill_2_perr_ifmnd3_005=[p_error_ifm_nod3_2(6) p_error_ifm_nod3_5(6) p_error_ifm_nod3_10(6) p_error_ifm_nod3_15(6)];
N_ill_1_perr_ifmnd3_005=[p_error_ifm_nod3_2(7) p_error_ifm_nod3_5(7) p_error_ifm_nod3_10(7) p_error_ifm_nod3_15(7)];

N_ill_100_ndam_ifmnd3_005=[n_damage_ifm_nod3_2(1) n_damage_ifm_nod3_5(1) n_damage_ifm_nod3_10(1) n_damage_ifm_nod3_15
(1)];
N_ill_50_ndam_ifmnd3_005=[n_damage_ifm_nod3_2(2) n_damage_ifm_nod3_5(2) n_damage_ifm_nod3_10(2) n_damage_ifm_nod3_15(2)
];
N_ill_25_ndam_ifmnd3_005=[n_damage_ifm_nod3_2(3) n_damage_ifm_nod3_5(3) n_damage_ifm_nod3_10(3) n_damage_ifm_nod3_15(3)
];
N_ill_10_ndam_ifmnd3_005=[n_damage_ifm_nod3_2(4) n_damage_ifm_nod3_5(4) n_damage_ifm_nod3_10(4) n_damage_ifm_nod3_15(4)
];
N_ill_5_ndam_ifmnd3_005=[n_damage_ifm_nod3_2(5) n_damage_ifm_nod3_5(5) n_damage_ifm_nod3_10(5) n_damage_ifm_nod3_15(5)
];
N_ill_2_ndam_ifmnd3_005=[n_damage_ifm_nod3_2(6) n_damage_ifm_nod3_5(6) n_damage_ifm_nod3_10(6) n_damage_ifm_nod3_15(6)
];
N_ill_1_ndam_ifmnd3_005=[n_damage_ifm_nod3_2(7) n_damage_ifm_nod3_5(7) n_damage_ifm_nod3_10(7) n_damage_ifm_nod3_15(7)
];

N_ill_50_perr_ifmd3_005=[p_error_ifm_d3_2(2) p_error_ifm_d3_5(2) p_error_ifm_d3_10(2) p_error_ifm_d3_15(2)];
N_ill_10_perr_ifmd3_005=[p_error_ifm_d3_2(4) p_error_ifm_d3_5(4) p_error_ifm_d3_10(4) p_error_ifm_d3_15(4)];
N_ill_5_perr_ifmd3_005=[p_error_ifm_d3_2(5) p_error_ifm_d3_5(5) p_error_ifm_d3_10(5) p_error_ifm_d3_15(5)];
N_ill_2_perr_ifmd3_005=[p_error_ifm_d3_2(6) p_error_ifm_d3_5(6) p_error_ifm_d3_10(6) p_error_ifm_d3_15(6)];
N_ill_1_perr_ifmd3_005=[p_error_ifm_d3_2(7) p_error_ifm_d3_5(7) p_error_ifm_d3_10(7) p_error_ifm_d3_15(7)];

N_ill_50_ndam_ifmd3_005=[n_damage_ifm_d3_2(2) n_damage_ifm_d3_5(2) n_damage_ifm_d3_10(2) n_damage_ifm_d3_15(2)];
N_ill_10_ndam_ifmd3_005=[n_damage_ifm_d3_2(4) n_damage_ifm_d3_5(4) n_damage_ifm_d3_10(4) n_damage_ifm_d3_15(4)];
N_ill_5_ndam_ifmd3_005=[n_damage_ifm_d3_2(5) n_damage_ifm_d3_5(5) n_damage_ifm_d3_10(5) n_damage_ifm_d3_15(5)];
N_ill_2_ndam_ifmd3_005=[n_damage_ifm_d3_2(6) n_damage_ifm_d3_5(6) n_damage_ifm_d3_10(6) n_damage_ifm_d3_15(6)];
N_ill_1_ndam_ifmd3_005=[n_damage_ifm_d3_2(7) n_damage_ifm_d3_5(7) n_damage_ifm_d3_10(7) n_damage_ifm_d3_15(7)];

N_ill_50_perr_cld3_005=[p_error_cl_d3_2(2) p_error_cl_d3_5(2) p_error_cl_d3_10(2) p_error_cl_d3_15(2)];
N_ill_10_perr_cld3_005=[p_error_cl_d3_2(4) p_error_cl_d3_5(4) p_error_cl_d3_10(4) p_error_cl_d3_15(4)];
N_ill_5_perr_cld3_005=[p_error_cl_d3_2(5) p_error_cl_d3_5(5) p_error_cl_d3_10(5) p_error_cl_d3_15(5)];
N_ill_2_perr_cld3_005=[p_error_cl_d3_2(6) p_error_cl_d3_5(6) p_error_cl_d3_10(6) p_error_cl_d3_15(6)];
N_ill_1_perr_cld3_005=[p_error_cl_d3_2(7) p_error_cl_d3_5(7) p_error_cl_d3_10(7) p_error_cl_d3_15(7)];

N_ill_50_ndam_cld3_005=[n_damage_cl_d3_2(2) n_damage_cl_d3_5(2) n_damage_cl_d3_10(2) n_damage_cl_d3_15(2)];
N_ill_10_ndam_cld3_005=[n_damage_cl_d3_2(4) n_damage_cl_d3_5(4) n_damage_cl_d3_10(4) n_damage_cl_d3_15(4)];
N_ill_5_ndam_cld3_005=[n_damage_cl_d3_2(5) n_damage_cl_d3_5(5) n_damage_cl_d3_10(5) n_damage_cl_d3_15(5)];
N_ill_2_ndam_cld3_005=[n_damage_cl_d3_2(6) n_damage_cl_d3_5(6) n_damage_cl_d3_10(6) n_damage_cl_d3_15(6)];
N_ill_1_ndam_cld3_005=[n_damage_cl_d3_2(7) n_damage_cl_d3_5(7) n_damage_cl_d3_10(7) n_damage_cl_d3_15(7)];
%%Read eta=0.1
load('reill_data_0.1.mat');
N_ill_50_perr_ifmnd3_01=[p_error_ifm_nod3_2(2) p_error_ifm_nod3_5(2) p_error_ifm_nod3_10(2) p_error_ifm_nod3_15(2)];
N_ill_5_perr_ifmnd3_01=[p_error_ifm_nod3_2(5) p_error_ifm_nod3_5(5) p_error_ifm_nod3_10(5) p_error_ifm_nod3_15(5)];
N_ill_2_perr_ifmnd3_01=[p_error_ifm_nod3_2(6) p_error_ifm_nod3_5(6) p_error_ifm_nod3_10(6) p_error_ifm_nod3_15(6)];
N_ill_1_perr_ifmnd3_01=[p_error_ifm_nod3_2(7) p_error_ifm_nod3_5(7) p_error_ifm_nod3_10(7) p_error_ifm_nod3_15(7)];

```



```

N_ill_2_ndam_cld3_02=[n_damage_cl_d3_2(6) n_damage_cl_d3_5(6) n_damage_cl_d3_10(6) n_damage_cl_d3_15(6)];
N_ill_1_ndam_cld3_02=[n_damage_cl_d3_2(7) n_damage_cl_d3_5(7) n_damage_cl_d3_10(7) n_damage_cl_d3_15(7)];

%%Read eta=0.25
load('reill_data_0.25.mat');
N_ill_100_perr_ifmnd3_025=[p_error_ifm_nod3_2(1) p_error_ifm_nod3_5(1) p_error_ifm_nod3_10(1) p_error_ifm_nod3_15(1)];
N_ill_50_perr_ifmnd3_025=[p_error_ifm_nod3_2(2) p_error_ifm_nod3_5(2) p_error_ifm_nod3_10(2) p_error_ifm_nod3_15(2)];
N_ill_25_perr_ifmnd3_025=[p_error_ifm_nod3_2(3) p_error_ifm_nod3_5(3) p_error_ifm_nod3_10(3) p_error_ifm_nod3_15(3)];
N_ill_10_perr_ifmnd3_025=[p_error_ifm_nod3_2(4) p_error_ifm_nod3_5(4) p_error_ifm_nod3_10(4) p_error_ifm_nod3_15(4)];
N_ill_5_perr_ifmnd3_025=[p_error_ifm_nod3_2(5) p_error_ifm_nod3_5(5) p_error_ifm_nod3_10(5) p_error_ifm_nod3_15(5)];
N_ill_2_perr_ifmnd3_025=[p_error_ifm_nod3_2(6) p_error_ifm_nod3_5(6) p_error_ifm_nod3_10(6) p_error_ifm_nod3_15(6)];
N_ill_1_perr_ifmnd3_025=[p_error_ifm_nod3_2(7) p_error_ifm_nod3_5(7) p_error_ifm_nod3_10(7) p_error_ifm_nod3_15(7)];

N_ill_100_ndam_ifmnd3_025=[n_damage_ifm_nod3_2(1) n_damage_ifm_nod3_5(1) n_damage_ifm_nod3_10(1) n_damage_ifm_nod3_15
(1)];
N_ill_50_ndam_ifmnd3_025=[n_damage_ifm_nod3_2(2) n_damage_ifm_nod3_5(2) n_damage_ifm_nod3_10(2) n_damage_ifm_nod3_15(2)
];
N_ill_25_ndam_ifmnd3_025=[n_damage_ifm_nod3_2(3) n_damage_ifm_nod3_5(3) n_damage_ifm_nod3_10(3) n_damage_ifm_nod3_15(3)
];
N_ill_10_ndam_ifmnd3_025=[n_damage_ifm_nod3_2(4) n_damage_ifm_nod3_5(4) n_damage_ifm_nod3_10(4) n_damage_ifm_nod3_15(4)
];
N_ill_5_ndam_ifmnd3_025=[n_damage_ifm_nod3_2(5) n_damage_ifm_nod3_5(5) n_damage_ifm_nod3_10(5) n_damage_ifm_nod3_15(5)
];
N_ill_2_ndam_ifmnd3_025=[n_damage_ifm_nod3_2(6) n_damage_ifm_nod3_5(6) n_damage_ifm_nod3_10(6) n_damage_ifm_nod3_15(6)
];
N_ill_1_ndam_ifmnd3_025=[n_damage_ifm_nod3_2(7) n_damage_ifm_nod3_5(7) n_damage_ifm_nod3_10(7) n_damage_ifm_nod3_15(7)
];

N_ill_50_perr_ifmd3_025=[p_error_ifm_d3_2(2) p_error_ifm_d3_5(2) p_error_ifm_d3_10(2) p_error_ifm_d3_15(2)];
N_ill_5_perr_ifmd3_025=[p_error_ifm_d3_2(5) p_error_ifm_d3_5(5) p_error_ifm_d3_10(5) p_error_ifm_d3_15(5)];
N_ill_2_perr_ifmd3_025=[p_error_ifm_d3_2(6) p_error_ifm_d3_5(6) p_error_ifm_d3_10(6) p_error_ifm_d3_15(6)];
N_ill_1_perr_ifmd3_025=[p_error_ifm_d3_2(7) p_error_ifm_d3_5(7) p_error_ifm_d3_10(7) p_error_ifm_d3_15(7)];

N_ill_50_ndam_ifmd3_025=[n_damage_ifm_d3_2(2) n_damage_ifm_d3_5(2) n_damage_ifm_d3_10(2) n_damage_ifm_d3_15(2)];
N_ill_5_ndam_ifmd3_025=[n_damage_ifm_d3_2(5) n_damage_ifm_d3_5(5) n_damage_ifm_d3_10(5) n_damage_ifm_d3_15(5)];
N_ill_2_ndam_ifmd3_025=[n_damage_ifm_d3_2(6) n_damage_ifm_d3_5(6) n_damage_ifm_d3_10(6) n_damage_ifm_d3_15(6)];
N_ill_1_ndam_ifmd3_025=[n_damage_ifm_d3_2(7) n_damage_ifm_d3_5(7) n_damage_ifm_d3_10(7) n_damage_ifm_d3_15(7)];

N_ill_50_perr_cld3_025=[p_error_cl_d3_2(2) p_error_cl_d3_5(2) p_error_cl_d3_10(2) p_error_cl_d3_15(2)];
N_ill_5_perr_cld3_025=[p_error_cl_d3_2(5) p_error_cl_d3_5(5) p_error_cl_d3_10(5) p_error_cl_d3_15(5)];
N_ill_2_perr_cld3_025=[p_error_cl_d3_2(6) p_error_cl_d3_5(6) p_error_cl_d3_10(6) p_error_cl_d3_15(6)];
N_ill_1_perr_cld3_025=[p_error_cl_d3_2(7) p_error_cl_d3_5(7) p_error_cl_d3_10(7) p_error_cl_d3_15(7)];

N_ill_50_ndam_cld3_025=[n_damage_cl_d3_2(2) n_damage_cl_d3_5(2) n_damage_cl_d3_10(2) n_damage_cl_d3_15(2)];
N_ill_5_ndam_cld3_025=[n_damage_cl_d3_2(5) n_damage_cl_d3_5(5) n_damage_cl_d3_10(5) n_damage_cl_d3_15(5)];
N_ill_2_ndam_cld3_025=[n_damage_cl_d3_2(6) n_damage_cl_d3_5(6) n_damage_cl_d3_10(6) n_damage_cl_d3_15(6)];
N_ill_1_ndam_cld3_025=[n_damage_cl_d3_2(7) n_damage_cl_d3_5(7) n_damage_cl_d3_10(7) n_damage_cl_d3_15(7)];

%%Read eta=0.3
load('reill_data_0.3.mat');
N_ill_50_perr_ifmnd3_03=[p_error_ifm_nod3_2(2) p_error_ifm_nod3_5(2) p_error_ifm_nod3_10(2) p_error_ifm_nod3_15(2)];
N_ill_5_perr_ifmnd3_03=[p_error_ifm_nod3_2(5) p_error_ifm_nod3_5(5) p_error_ifm_nod3_10(5) p_error_ifm_nod3_15(5)];
N_ill_2_perr_ifmnd3_03=[p_error_ifm_nod3_2(6) p_error_ifm_nod3_5(6) p_error_ifm_nod3_10(6) p_error_ifm_nod3_15(6)];
N_ill_1_perr_ifmnd3_03=[p_error_ifm_nod3_2(7) p_error_ifm_nod3_5(7) p_error_ifm_nod3_10(7) p_error_ifm_nod3_15(7)];

N_ill_50_ndam_ifmnd3_03=[n_damage_ifm_nod3_2(2) n_damage_ifm_nod3_5(2) n_damage_ifm_nod3_10(2) n_damage_ifm_nod3_15(2)
];
N_ill_5_ndam_ifmnd3_03=[n_damage_ifm_nod3_2(5) n_damage_ifm_nod3_5(5) n_damage_ifm_nod3_10(5) n_damage_ifm_nod3_15(5)];
N_ill_2_ndam_ifmnd3_03=[n_damage_ifm_nod3_2(6) n_damage_ifm_nod3_5(6) n_damage_ifm_nod3_10(6) n_damage_ifm_nod3_15(6)];
N_ill_1_ndam_ifmnd3_03=[n_damage_ifm_nod3_2(7) n_damage_ifm_nod3_5(7) n_damage_ifm_nod3_10(7) n_damage_ifm_nod3_15(7)];

N_ill_50_perr_ifmd3_03=[p_error_ifm_d3_2(2) p_error_ifm_d3_5(2) p_error_ifm_d3_10(2) p_error_ifm_d3_15(2)];
N_ill_5_perr_ifmd3_03=[p_error_ifm_d3_2(5) p_error_ifm_d3_5(5) p_error_ifm_d3_10(5) p_error_ifm_d3_15(5)];
N_ill_2_perr_ifmd3_03=[p_error_ifm_d3_2(6) p_error_ifm_d3_5(6) p_error_ifm_d3_10(6) p_error_ifm_d3_15(6)];
N_ill_1_perr_ifmd3_03=[p_error_ifm_d3_2(7) p_error_ifm_d3_5(7) p_error_ifm_d3_10(7) p_error_ifm_d3_15(7)];

N_ill_50_ndam_ifmd3_03=[n_damage_ifm_d3_2(2) n_damage_ifm_d3_5(2) n_damage_ifm_d3_10(2) n_damage_ifm_d3_15(2)];
N_ill_5_ndam_ifmd3_03=[n_damage_ifm_d3_2(5) n_damage_ifm_d3_5(5) n_damage_ifm_d3_10(5) n_damage_ifm_d3_15(5)];
N_ill_2_ndam_ifmd3_03=[n_damage_ifm_d3_2(6) n_damage_ifm_d3_5(6) n_damage_ifm_d3_10(6) n_damage_ifm_d3_15(6)];
N_ill_1_ndam_ifmd3_03=[n_damage_ifm_d3_2(7) n_damage_ifm_d3_5(7) n_damage_ifm_d3_10(7) n_damage_ifm_d3_15(7)];

N_ill_50_perr_cld3_03=[p_error_cl_d3_2(2) p_error_cl_d3_5(2) p_error_cl_d3_10(2) p_error_cl_d3_15(2)];
N_ill_5_perr_cld3_03=[p_error_cl_d3_2(5) p_error_cl_d3_5(5) p_error_cl_d3_10(5) p_error_cl_d3_15(5)];
N_ill_2_perr_cld3_03=[p_error_cl_d3_2(6) p_error_cl_d3_5(6) p_error_cl_d3_10(6) p_error_cl_d3_15(6)];
N_ill_1_perr_cld3_03=[p_error_cl_d3_2(7) p_error_cl_d3_5(7) p_error_cl_d3_10(7) p_error_cl_d3_15(7)];

N_ill_50_ndam_cld3_03=[n_damage_cl_d3_2(2) n_damage_cl_d3_5(2) n_damage_cl_d3_10(2) n_damage_cl_d3_15(2)];
N_ill_5_ndam_cld3_03=[n_damage_cl_d3_2(5) n_damage_cl_d3_5(5) n_damage_cl_d3_10(5) n_damage_cl_d3_15(5)];
N_ill_2_ndam_cld3_03=[n_damage_cl_d3_2(6) n_damage_cl_d3_5(6) n_damage_cl_d3_10(6) n_damage_cl_d3_15(6)];
N_ill_1_ndam_cld3_03=[n_damage_cl_d3_2(7) n_damage_cl_d3_5(7) n_damage_cl_d3_10(7) n_damage_cl_d3_15(7)];

%%Read eta=0.49
load('reill_data_0.49.mat');
N_ill_50_perr_ifmnd3_049=p_error_ifm_nod3_5(2);
N_ill_5_perr_ifmnd3_049=p_error_ifm_nod3_5(5);
N_ill_2_perr_ifmnd3_049=p_error_ifm_nod3_5(6);
N_ill_1_perr_ifmnd3_049=p_error_ifm_nod3_5(7);

N_ill_50_ndam_ifmnd3_049=n_damage_ifm_nod3_5(2);
N_ill_5_ndam_ifmnd3_049=n_damage_ifm_nod3_5(5);
N_ill_2_ndam_ifmnd3_049=n_damage_ifm_nod3_5(6);
N_ill_1_ndam_ifmnd3_049=n_damage_ifm_nod3_5(7);

```

```

N_ill_50_perr_ifmd3_049=p_error_ifm_d3_5(2);
N_ill_5_perr_ifmd3_049=p_error_ifm_d3_5(5);
N_ill_2_perr_ifmd3_049=p_error_ifm_d3_5(6);
N_ill_1_perr_ifmd3_049=p_error_ifm_d3_5(7);

N_ill_50_ndam_ifmd3_049=n_damage_ifm_d3_5(2);
N_ill_5_ndam_ifmd3_049=n_damage_ifm_d3_5(5);
N_ill_2_ndam_ifmd3_049=n_damage_ifm_d3_5(6);
N_ill_1_ndam_ifmd3_049=n_damage_ifm_d3_5(7);

N_ill_50_perr_cld3_049=p_error_cl_d3_5(2);
N_ill_5_perr_cld3_049=p_error_cl_d3_5(5);
N_ill_2_perr_cld3_049=p_error_cl_d3_5(6);
N_ill_1_perr_cld3_049=p_error_cl_d3_5(7);

N_ill_50_ndam_cld3_049=n_damage_cl_d3_5(2);
N_ill_5_ndam_cld3_049=n_damage_cl_d3_5(5);
N_ill_2_ndam_cld3_049=n_damage_cl_d3_5(6);
N_ill_1_ndam_cld3_049=n_damage_cl_d3_5(7);

%%
semilogy(N_ill_1_ndam_cld3_005,N_ill_1_perr_cld3_005, '-x', 'MarkerSize',10, 'LineWidth',2, 'Color', [0.4940 0.1840
0.5560]);
hold on;
semilogy(N_ill_1_ndam_ifmd3_005,N_ill_1_perr_ifmd3_005, '-x', 'MarkerSize',10, 'LineWidth',2, 'Color', [0.9290 0.6940
0.1250]);
semilogy(N_ill_10_ndam_cld3_005,N_ill_10_perr_cld3_005, '-o', 'MarkerSize',10, 'LineWidth',2, 'Color', [0.4940 0.1840
0.5560]);
semilogy(N_ill_10_ndam_ifmd3_005,N_ill_10_perr_ifmd3_005, '-o', 'MarkerSize',10, 'LineWidth',2, 'Color', [0.9290 0.6940
0.1250]);
%ylim([1e-5 1]);
xlim([0 10]);
%set(gca, 'YTick',0:0.05:0.2, 'FontSize',18);
set(gca, 'XTick',0:1:10, 'FontSize',18);
ylabel('P_{err}', 'FontSize',18);
xlabel('n_{damage}', 'FontSize',18);
lgd=legend('Classical, D3, single illumination', 'IFM, D3, single illumination', 'Classical, D3, conditional re-
illumination', 'IFM, D3, conditional re-illumination', 'Location', 'northeast');
lgd.Box='off';
%saveas(gcf, strcat('Cond_reill_fig8', '.png'));
%%
x1=[N_ill_1_ndam_cld3_0(1) N_ill_2_ndam_cld3_0(1) N_ill_5_ndam_cld3_0(1) N_ill_50_ndam_cld3_0(1)];
x2=[N_ill_1_ndam_ifmd3_0(1) N_ill_2_ndam_ifmd3_0(1) N_ill_5_ndam_ifmd3_0(1) N_ill_50_ndam_ifmd3_0(1)];
x3=[N_ill_1_ndam_ifmd3_0(1) N_ill_2_ndam_ifmd3_0(1) N_ill_5_ndam_ifmd3_0(1) N_ill_50_ndam_ifmd3_0(1)];
y1=[N_ill_1_perr_cld3_0(1) N_ill_2_perr_cld3_0(1) N_ill_5_perr_cld3_0(1) N_ill_50_perr_cld3_0(1)];
y2=[N_ill_1_perr_ifmd3_0(1) N_ill_2_perr_ifmd3_0(1) N_ill_5_perr_ifmd3_0(1) N_ill_50_perr_ifmd3_0(1)];
y3=[N_ill_1_perr_ifmd3_0(1) N_ill_2_perr_ifmd3_0(1) N_ill_5_perr_ifmd3_0(1) N_ill_50_perr_ifmd3_0(1)];
erry1=(y1.*(1-y1)/100000).^0.5;
erry2=(y2.*(1-y2)/100000).^0.5;
erry3=(y3.*(1-y3)/100000).^0.5;
errorbar(x1,y1,erry1, '-o', 'MarkerSize',10, 'CapSize',15, 'LineWidth',2, 'Color', [0.4940 0.1840 0.5560]);
hold on;
errorbar(x2,y2,erry2, '-o', 'MarkerSize',10, 'CapSize',15, 'LineWidth',2, 'Color', [0.8500, 0.3250, 0.0980]);
errorbar(x3,y3,erry3, '-o', 'MarkerSize',10, 'CapSize',15, 'LineWidth',2, 'Color', [0.4660, 0.6740, 0.1880]);
ax=gca;
ax.TickLength=[0.01, 0.01];
ax.LineWidth = 2;
xlim([0.5 2]);
ylim([0 0.2]);
set(ax, 'YTick',0:0.05:0.2, 'FontSize',18);
set(ax, 'XTick',0.5:0.25:2, 'FontSize',18);
ylabel('$P_{\text{err}}$', 'FontSize',18, 'Interpreter', 'Latex');
xlabel('$\bar{n}_{\text{damage}}$', 'FontSize',18, 'Interpreter', 'Latex');
lgd=legend('Classical, D3', 'IFM, no D3', 'IFM, D3', 'Location', 'northeast');
lgd.Box='off';
lgd.FontSize=18;
%gca.LineWidth = 100;
%saveas(gcf, strcat('Cond_reill_fig1_draft2', '.png'));
%%
%%semilogy(ndamarr,perr_ifm_mat,n_damage_ifm_nod3_2,p_error_ifm_nod3_2, 'x--',n_damage_ifm_nod3_5,p_error_ifm_nod3_5, 'x
--',n_damage_ifm_nod3_8,p_error_ifm_nod3_8, 'o--',n_damage_ifm_nod3_10,p_error_ifm_nod3_10, 'd--', 'Linewidth',2, '
MarkerSize',10);
%%semilogy(ndamarr,perr_ifm_mat,ndamarr,perr_ifm_d3_mat,ndamarr,perr_ifm_mat,n_damage_ifm_nod3_10,p_error_ifm_nod3_10, 'x
--',n_damage_ifm_nod3_15,p_error_ifm_nod3_15, 'd--',n_damage_ifm_nod3_20,p_error_ifm_nod3_20, 'o--',
n_damage_ifm_d3_10,p_error_ifm_d3_10, 'x--',n_damage_ifm_d3_15,p_error_ifm_d3_15, 'd--',n_damage_ifm_d3_20,
p_error_ifm_d3_20, 'o--', 'Linewidth',2, 'MarkerSize',10);
% plot(ndamarr,perr_cl_d3_mat, 'Linewidth',2);
% xlim([0 5]);
% hold on;
% plot(ndamarr,perr_ifm_d3_mat, 'Linewidth',2);
% plot(ndamarr,perr_ifm_mat, 'Linewidth',2, 'Color', [0.4660 0.6740 0.1880] );
% %plot(ndamarr,1000000000000./(ndamarr).^15, 'Linewidth',2);
% %xlim([0 10.1]);
% %ylim([4e-6 1]);
% ylim([0 0.5]);
% set(gca, 'XTick',0:1:5, 'FontSize',14);
% xlabel('n_{damage}', 'FontSize',14);
% ylabel('P_{err}', 'FontSize',14);
% %gd=legend('IFM, D3, single ill., theory', 'IFM, no D3, single ill., theory', 'IFM, no D3, cond. reill., MC dose
=2', 'IFM, no D3, cond. reill., MC dose=5', 'IFM, no D3, cond. reill., MC dose=10', 'IFM, no D3, cond. reill., MC
dose=50', 'IFM, no D3, cond. reill., MC dose=100', 'Location', 'southwest');

```

```

%lgd=legend('Classical, no D3, single ill., theory', 'Classical, no D3, cond. reill., MC, dose=2', 'Classical, no D3,
cond. reill., MC, dose=5','Classical, no D3, cond. reill., MC, dose=8','Classical, no D3, cond. reill., MC, dose
=10','Location','northeast');
%lgd=legend('Classical, D3, single ill., theory','IFM, D3, single ill., theory','IFM, no D3, single ill., theory','IFM
, no D3, cond. reill., MC, dose=10', 'IFM, D3, cond. reill., MC, dose=15','IFM, no D3, cond. reill., MC, dose=20','
IFM, D3, cond. reill., MC, dose=10','IFM, D3, cond. reill., MC, dose=15','IFM, D3, cond. reill., MC, dose=20','
Location','southwest');
%lgd=legend('Classical, D3, single ill., theory','IFM, D3, single ill., theory','IFM, no D3, single ill., theory');
%lgd.Box='off';
%saveas(gcf, strcat('Cond_reill_theory', '.png'));
%%
figure();plot(eta,[N_ill_50_ndam_cld3_0(end-1) N_ill_50_ndam_cld3_005(end-1) N_ill_50_ndam_cld3_01(end-1)
N_ill_50_ndam_cld3_015(end-1) N_ill_50_ndam_cld3_02(end-1) N_ill_50_ndam_cld3_025(end-1) N_ill_50_ndam_cld3_03(end
-1) N_ill_50_ndam_cld3_049], 'o--', 'Linewidth',2, 'MarkerSize',10);
hold on;
plot(eta,[N_ill_50_ndam_ifmmod3_0(end-1) N_ill_50_ndam_ifmmod3_005(end-1) N_ill_50_ndam_ifmmod3_01(end-1)
N_ill_50_ndam_ifmmod3_015(end-1) N_ill_50_ndam_ifmmod3_02(end-1) N_ill_50_ndam_ifmmod3_025(end-1)
N_ill_50_ndam_ifmmod3_03(end-1) N_ill_50_ndam_ifmmod3_049], 'x--', 'Linewidth',2, 'MarkerSize',10);
plot(eta,[N_ill_50_ndam_ifmd3_0(end-1) N_ill_50_ndam_ifmd3_005(end-1) N_ill_50_ndam_ifmd3_01(end-1)
N_ill_50_ndam_ifmd3_015(end-1) N_ill_50_ndam_ifmd3_02(end-1) N_ill_50_ndam_ifmd3_025(end-1) N_ill_50_ndam_ifmd3_03
(end-1) N_ill_50_ndam_ifmd3_049], 'd--', 'Linewidth',2, 'MarkerSize',10);
hold off;
xlim([0 0.5]);
ylim([0 2]);
set(gca, 'XTick',0:0.05:0.5, 'FontSize',14);
xlabel('\epsilon (error threshold)', 'FontSize',14);
ylabel('n_{damage}', 'FontSize',14);
lgd=legend('Classical, D3', 'IFM, no D3', 'IFM, D3', 'Location', 'northeast');
lgd.Box='off';
%saveas(gcf, strcat('Cond_reill_epsilon_damage', '.png'));

figure();plot(eta,[N_ill_50_perr_cld3_0(end-1) N_ill_50_perr_cld3_005(end-1) N_ill_50_perr_cld3_01(end-1)
N_ill_50_perr_cld3_015(end-1) N_ill_50_perr_cld3_02(end-1) N_ill_50_perr_cld3_025(end-1) N_ill_50_perr_cld3_03(end
-1) N_ill_50_perr_cld3_049], 'o--', 'Linewidth',2, 'MarkerSize',10);
hold on;
plot(eta,[N_ill_50_perr_ifmmod3_0(end-1) N_ill_50_perr_ifmmod3_005(end-1) N_ill_50_perr_ifmmod3_01(end-1)
N_ill_50_perr_ifmmod3_015(end-1) N_ill_50_perr_ifmmod3_02(end-1) N_ill_50_perr_ifmmod3_025(end-1)
N_ill_50_perr_ifmmod3_03(end-1) N_ill_50_perr_ifmmod3_049], 'x--', 'Linewidth',2, 'MarkerSize',10);
plot(eta,[N_ill_50_perr_ifmd3_0(end-1) N_ill_50_perr_ifmd3_005(end-1) N_ill_50_perr_ifmd3_01(end-1)
N_ill_50_perr_ifmd3_015(end-1) N_ill_50_perr_ifmd3_02(end-1) N_ill_50_perr_ifmd3_025(end-1) N_ill_50_perr_ifmd3_03
(end-1) N_ill_50_perr_ifmd3_049], 'd--', 'Linewidth',2, 'MarkerSize',10);
hold off;
xlim([0 0.5]);
ylim([0 0.5]);
set(gca, 'XTick',0:0.05:0.5, 'FontSize',14);
xlabel('\epsilon (error threshold)', 'FontSize',14);
ylabel('P_{err}', 'FontSize',14);
lgd=legend('Classical, D3', 'IFM, no D3', 'IFM, D3', 'Location', 'northeast');
lgd.Box='off';
%saveas(gcf, strcat('Cond_reill_epsilon_error', '.png'));
%%
figure();semilogx([N_ill_50_perr_cld3_0(end-1) N_ill_50_perr_cld3_005(end-1) N_ill_50_perr_cld3_01(end-1)
N_ill_50_perr_cld3_015(end-1) N_ill_50_perr_cld3_02(end-1) N_ill_50_perr_cld3_025(end-1) N_ill_50_perr_cld3_03(end
-1) N_ill_50_perr_cld3_049], [N_ill_50_ndam_cld3_0(end-1) N_ill_50_ndam_cld3_005(end-1) N_ill_50_ndam_cld3_01(end
-1) N_ill_50_ndam_cld3_015(end-1) N_ill_50_ndam_cld3_02(end-1) N_ill_50_ndam_cld3_025(end-1) N_ill_50_ndam_cld3_03
(end-1) N_ill_50_ndam_cld3_049], 'o--', 'Linewidth',2, 'MarkerSize',10);
hold on;
semilogx([N_ill_50_perr_ifmmod3_0(end-1) N_ill_50_perr_ifmmod3_005(end-1) N_ill_50_perr_ifmmod3_01(end-1)
N_ill_50_perr_ifmmod3_015(end-1) N_ill_50_perr_ifmmod3_02(end-1) N_ill_50_perr_ifmmod3_025(end-1)
N_ill_50_perr_ifmmod3_03(end-1) N_ill_50_perr_ifmmod3_049], [N_ill_50_ndam_ifmmod3_0(end-1)
N_ill_50_ndam_ifmmod3_005(end-1) N_ill_50_ndam_ifmmod3_01(end-1) N_ill_50_ndam_ifmmod3_015(end-1)
N_ill_50_ndam_ifmmod3_02(end-1) N_ill_50_ndam_ifmmod3_025(end-1) N_ill_50_ndam_ifmmod3_03(end-1)
N_ill_50_ndam_ifmmod3_049], 'x--', 'Linewidth',2, 'MarkerSize',10);
semilogx([N_ill_50_perr_ifmd3_0(end-1) N_ill_50_perr_ifmd3_005(end-1) N_ill_50_perr_ifmd3_01(end-1)
N_ill_50_perr_ifmd3_015(end-1) N_ill_50_perr_ifmd3_02(end-1) N_ill_50_perr_ifmd3_025(end-1) N_ill_50_perr_ifmd3_03
(end-1) N_ill_50_perr_ifmd3_049], [N_ill_50_ndam_ifmd3_0(end-1) N_ill_50_ndam_ifmd3_005(end-1)
N_ill_50_ndam_ifmd3_01(end-1) N_ill_50_ndam_ifmd3_015(end-1) N_ill_50_ndam_ifmd3_02(end-1) N_ill_50_ndam_ifmd3_025
(end-1) N_ill_50_ndam_ifmd3_03(end-1) N_ill_50_ndam_ifmd3_049], 'd--', 'Linewidth',2, 'MarkerSize',10);
xlim([1e-5 0.5]);
ylim([0 2]);
%set(gca, 'XTick',1e-5:0.01:0.5, 'FontSize',14);
ylabel('n_{damage}', 'FontSize',14);
xlabel('P_{err}', 'FontSize',14);
lgd=legend('Classical, D3', 'IFM, no D3', 'IFM, D3', 'Location', 'northeast');
lgd.Box='off';
%saveas(gcf, strcat('Cond_reill_epsilon_error_damage', '.png'));
%%
n_ill=[1 2 5 10 25 50 100];
plot(n_ill,[N_ill_1_ndam_ifmmod3_005(3),N_ill_2_ndam_ifmmod3_005(3),N_ill_5_ndam_ifmmod3_005(3),
N_ill_10_ndam_ifmmod3_005(3),N_ill_25_ndam_ifmmod3_005(3),N_ill_50_ndam_ifmmod3_005(3),N_ill_100_ndam_ifmmod3_005
(3)], 'o--', n_ill,[N_ill_1_ndam_ifmmod3_025(3),N_ill_2_ndam_ifmmod3_025(3),N_ill_5_ndam_ifmmod3_025(3),
N_ill_10_ndam_ifmmod3_025(3),N_ill_25_ndam_ifmmod3_025(3),N_ill_50_ndam_ifmmod3_025(3),N_ill_100_ndam_ifmmod3_025
(3)], 'o--', 'LineWidth',2, 'MarkerSize',10);
xlim([0 100]);
ylim([0 5]);
ylabel('$\bar{n}_{\{damage\}}$', 'FontSize',18, 'Interpreter', 'Latex');
xlabel('Maximum number of illuminations($N_{\{textrm{max}\}}$)', 'FontSize',18, 'Interpreter', 'Latex');
%lgd=legend('\epsilon=0.05', '\epsilon=0.25');
%lgd.Box='off';
%lgd.FontSize=18;
ax=gca;
ax.TickLength=[0.01, 0.01];

```

```

ax.LineWidth = 2;
set(ax, 'XTick', 0:10:100, 'FontSize', 18);
saveas(gcf, strcat('Cond_reill_nill_damage', '.png'));
figure(); plot(n_ill, [N_ill_1_perr_ifmmod3_005(3), N_ill_2_perr_ifmmod3_005(3), N_ill_5_perr_ifmmod3_005(3),
N_ill_10_perr_ifmmod3_005(3), N_ill_25_perr_ifmmod3_005(3), N_ill_50_perr_ifmmod3_005(3), N_ill_100_perr_ifmmod3_005
(3)], '—o', n_ill, [N_ill_1_perr_ifmmod3_025(3), N_ill_2_perr_ifmmod3_025(3), N_ill_5_perr_ifmmod3_025(3),
N_ill_10_perr_ifmmod3_025(3), N_ill_25_perr_ifmmod3_025(3), N_ill_50_perr_ifmmod3_025(3), N_ill_100_perr_ifmmod3_025
(3)], '—o', 'LineWidth', 2, 'MarkerSize', 10);
xlim([0 100]);
ylim([0 0.2]);
ylabel('$P_{\{\text{err}\}}$', 'FontSize', 18, 'Interpreter', 'Latex');
xlabel('Maximum number of illuminations ($N_{\{\text{max}\}}$)', 'FontSize', 18, 'Interpreter', 'Latex');
lgd=legend('\epsilon=0.05', '\epsilon=0.25');
lgd.Box='off';
lgd.FontSize=18;
ax=gca;
ax.TickLength=[0.01, 0.01];
ax.LineWidth = 2;
set(ax, 'XTick', 0:10:100, 'FontSize', 18);
%saveas(gcf, strcat('Cond_reill_nill_error', '.png'));
%%
semilogy(N_ill_1_ndam_cld3_005, N_ill_1_perr_cld3_005, '-x', 'LineWidth', 2, 'MarkerSize', 10, 'Color', [0.4940 0.1840
0.5560]);
hold on;
semilogy(N_ill_1_ndam_ifmd3_005, N_ill_1_perr_ifmd3_005, '-x', 'LineWidth', 2, 'MarkerSize', 10, 'Color', [0.4660 0.6740,
0.1880]);
semilogy(N_ill_10_ndam_cld3_005, [N_ill_10_perr_cld3_005(1:2) 1e-5 0], '—o', 'LineWidth', 2, 'MarkerSize', 10, 'Color', [0.4940
0.1840 0.5560]);
semilogy(N_ill_10_ndam_ifmd3_005, N_ill_10_perr_ifmd3_005, '—o', 'LineWidth', 2, 'MarkerSize', 10, 'Color', [0.4660 0.6740,
0.1880]);
ax=gca;
ax.TickLength=[0.01, 0.01];
ax.LineWidth = 2;
set(ax, 'XTick', 0:1:10, 'FontSize', 18);
xlabel('$\bar{n}_{\{\text{damage}\}}$', 'FontSize', 18, 'Interpreter', 'Latex');
ylabel('$P_{\{\text{err}\}}$', 'FontSize', 18, 'Interpreter', 'Latex');
lgd=legend('Classical, $D_3$, single ill.', 'IFM, $D_3$, single ill.', 'Classical, $D_3$, conditional re-ill.', 'IFM, $D_3$,
conditional re-ill. ');
lgd.Box='off';
lgd.FontSize=18;
lgd.Interpreter='Latex';
%saveas(gcf, strcat('Cond_reill_damage_error_comp', '.png'));

```

D.2 MATLAB code for chapter 3

The function `meanabsrelerr.m` was used by the script `image_contrast__mean-error.m` to generate the noisy images and calculate MARE in Figure 3-2. The same script was also used to calculate contrast in Figure 3-1. The script `Image_autocorr__noise.m` was used to calculate SNR from image autocorrelation in Figure 3-3.

```
%%-----meanabsrelerr.m-----%%
% This function generates a n_rep noisy images using the pixel values of a given
% image (im) as the ground truth. The final noisy image is the average of all
% n_rep images. The function outputs the mean absolute relative error (mae)
function [mae,im_poisson]=meanabserr(im,n_rep)
im=im/100;
im=im(1:600,:);
im_poisson=zeros(600,1024);
tic;
parfor i=1:600
    for j=1:1024
        prv=poissrnd(im(i,j),[n_rep 1]);
        im_poisson(i,j)=mean(prv);
    end
end
mae=mean(mean(abs((im_poisson-im)))/mean(mean(im)));
```

```

%%----- image_contrast_meanerror.m -----%%
%This code calculates the contrast and MARE. To calculate
%contrast this code scales a given image by a scale value. To
%calculate MARE this code calls the function meanabsreterr.m.
clear;clc;
%% Contrast
im=double(imread('img01.tif'));
scale_vals=1:0.1:2;
[~,sz]=size(scale_vals);
im=im(1:600,:);
cts=zeros(1,256);
[r,c,-]=find(im>=84);
[n_high,-]=size(r);
K=zeros(1,sz);
for k=1:sz
    im_mod=im;
    sum_high=0;
    for i=1:n_high
        im_mod(r(i),c(i))=im(r(i),c(i))/scale_vals(k);
        sum_high=sum_high+im_mod(r(i),c(i));
    end
    sum_low=sum(sum(im_mod))-sum_high;
    n_low=600*1024-n_high;
    mean_low=sum_low/n_low;
    mean_high=sum_high/n_high;
    K(k)=(mean_high-mean_low)/(mean_high+mean_low);
end
plot(scale_vals,K,'LineWidth',2,'Color','black');
xlim([1 4]);
ylim([0 0.7]);
ax=gca;
ax.TickLength=[0.01, 0.01];
ax.LineWidth = 2;
xlabel('scale factor','FontSize',18);
ylabel('contrast (K)','FontSize',18);
set(ax,'XTick',1:0.5:4,'FontSize',18);
set(ax,'YTick',0:0.1:0.7,'FontSize',18);
hold on
%% Plotting sample images for contrast figure in chapter 2
imagesc(im_mod);
colormap gray
caxis ([0 255]);
axis off
%% Absolute error
im=double(imread('img02.tif'));
n_max=5;
mae=zeros(1,n_max);
for i=1:n_max
    [mae(i),im_poisson]=meanabserr(im,i);
end
%% abserr plot for chapter 2
plot(1:100,mae,'LineWidth',2,'Color','black');
xlim([1 100]);
ylim([0 0.9]);
ax=gca;
ax.TickLength=[0.01, 0.01];
ax.LineWidth = 2;
xlabel('number of trials','FontSize',18);
ylabel('mean absolute error','FontSize',18);
set(ax,'XTick',0:20:100,'FontSize',18);
set(ax,'YTick',0:0.2:0.8,'FontSize',18);
hold on
%% images for abserr in chapter 2
imagesc(double(im(1:600,:))/100);
%imagesc(im_poisson)
colormap gray
caxis ([0 2.5]);
axis off

```

```

%%----- Image autocorr_noise_image.m -----%%
% This code calculates the autocorrelation of a given image and uses the
% sharp peak at zero offset to find the SNR as described in chapter 3. It
% also finds a least-squares fit line for the SNR values at different pixel
% dwell times
im_sz=768;
sz_files=7;
start_file_no=8;
SNR=zeros(1,sz_files);
a=zeros(1,sz_files);
lambda_autocorr=zeros(1,sz_files);
lambda_hist=zeros(1,sz_files);
lambda_diff=zeros(1,sz_files);
sz_fit=3;
tic;
ctr=1;
%scan_times=[28/3.6 15/3.6 7.5/3.6 1 1.8/3.6 1/3.6];
%scan_times=[1/3.6 1.8/3.6 1 7.5/3.6 15/3.6 28/3.6];
scan_times=1*ones(1,sz_files);
for i=start_file_no:start_file_no+sz_files-1
    i
    nf_im=double(imread(strcat('img',num2str(i,'%02d'),'tif')));
    test_im=nf_im(1:im_sz,1:im_sz);
    test_im_mean=mean(mean(test_im));
    test_im=test_im-test_im_mean;
    noise_corr=xcorr2(test_im,test_im)/im_sz/im_sz;
    %noise_corr=noise_corr+test_im_mean^2;
    [~,corr_sz]=size(noise_corr);
    %plot(noise_corr(im_sz-im_sz/2:im_sz+im_sz/2,im_sz));
    %hold on;
    fit_pts=noise_corr(im_sz-sz_fit:im_sz-1,im_sz);
    x_fit=im_sz-sz_fit:im_sz-1;
    fit_interp=polyfit(x_fit,fit_pts,1);
    x_interp=im_sz-sz_fit:im_sz;
    nf_fit=fit_interp(1)*x_interp+fit_interp(2);
    phi_nf=nf_fit(end);
    phi=noise_corr(im_sz,im_sz);
    phi_noise=phi-phi_nf;
    SNR(ctr)=phi_nf/phi_noise;
    v1=noise_corr(im_sz,im_sz)-noise_corr(im_sz,im_sz-1);
    v2=noise_corr(im_sz,im_sz-1);
    lambda_autocorr(ctr)=v2/v1;
    a(ctr)=(v1/lambda_autocorr(ctr))^0.5;
    lambda_hist(ctr)=hist_mean(nf_im);
    lambda_hist(ctr)=lambda_hist(ctr)*scan_times(ctr);
    lambda_diff(ctr)=(lambda_autocorr(ctr)-lambda_hist(ctr))/lambda_hist(ctr);
    ctr=ctr+1;
end
toc;

%% Error fitting
%[-,~,lambda_hist]=find(lambda_hist);
%[-,~,lambda_diff]=find(lambda_diff);
%SNR_p=SNR(1:4);
scan_t=[0.44 1 1.8 3.6 7.5 15 28]; %0.28 0.52
SNR_fitp=polyfit(scan_t,SNR,1);
SNR_fit=SNR_fitp(1)*scan_t+SNR_fitp(2);
%lambda_diff_fc=polyfit(lambda_hist,lambda_diff,1);
%lambda_diff_fit=lambda_diff_fc(1)*lambda_hist+lambda_diff_fc(2);
plt=plot(scan_t, SNR, 'o',scan_t,SNR_fit,'LineWidth',2,'Markersize',8,'Color','black');
%plt=plot(lambda_hist,lambda_diff,'o',lambda_hist,lambda_diff_fit,'LineWidth',2,'Markersize',8,'Color','black');
%xlim([0.8 3.3]);
%ylim([0 0.4]);
ax=gca;
ax.TickLength=[0.01, 0.01];
ax.LineWidth = 2;
xlabel('pixel dwell time (\mus)','FontSize',18);
ylabel('SNR','FontSize',18);
set(ax,'XTick',0:5:30,'FontSize',18);
set(ax,'YTick',0:0.5:1.5,'FontSize',18);
hold on;

```

D.3 MATLAB code for chapter 4

The script `SE_image_histograms.m` was used to generate the image histograms in Figure 4-1, 4-2, 4-3, 4-4, 4-5, and 4-7 and calculate the associated histogram mean brightnesses. The script `SEM_histogram_DQE.m` was used to calculate and plot mean SE counts and extract DQE in figures 4-4 and 4-5. The script `SEM_oscilloscope_imaging_peak_stats.m` was used for plotting the SE detector signal pulses, and pulse height and width histograms in Figure 4-6. The oscilloscope histograms in Figure 4-7 were generated on the oscilloscope directly.

```
%%-----SE_image_histograms.m-----%%
% This code calculates and plots the histogram of 8-bit SEM images and also
% calculates the mean SE count for the histogram.

clear;clc;
no_peaks=3;
%peak0=64; %in-lens
%peak_means=[75 87]; %in-lens
peak0=44; %SE2
peak_means=[58 73 88]; %SE2 % Positions of 1, 2 and 3 SE peaks
%pw1=5;
%peak_widths=[pw1 2*pw1 4*pw1];
peak_gap=peak_means(2)-peak_means(1);
img=(imread('img05.tif'));
%img=ct_image_avg;
grid=0:255;
cts=zeros(1,256);
for i=1:600
    for j=1:1024
        cts(img(i,j)+1)=cts(img(i,j))+1;
    end
end
cts=cts/sum(cts);
%cts=cts/cts(45);
grid2=grid/peak_gap;
mean_cts_pdf=(sum(grid2.*cts)-peak0/peak_gap);
%
plot(grid,cts,'-','LineWidth',2);
hold on;
xlim([0 150]);
ylim([0 0.085]);
ax=gca;
ax.TickLength=[0.01, 0.01];
ax.LineWidth = 2;
xlabel('brightness','FontSize',18);
ylabel('counts(normalized)','FontSize',18);
set(ax,'XTick',0:30:250,'FontSize',18);
set(ax,'YTick',0:0.02:0.08,'FontSize',18);
%%
```

```

%%-----SEM_histogram_DQE.m-----%%
% This code finds the mean SE counts for image histograms at different beam
% currents and extracts DQE from the slope of the mean SE number vs beam
% current plot. The fitting can be performed over a subset of all the
% available beam currents (in the chapter we fitted for beam currents below
% 5.5 pA)
clear;clc;
filenos=30:-2:2;
%filenos=[111 113 116 118 120 122 124 126 128];
%filenos=filenos+1;
%filenos=1;
[~,sz]=size(filenos);
mean_ct=zeros(sz,1);
%peaks=[44 58 73];
peaks=[64 75 87];
for i=1:sz
    filename=strcat('img',num2str(filenos(i),'%02d'),' .tif');
    img=imread(filename);
    mean_ct(i)=mean_hist_counts(peaks(1),peaks(2),peaks(3),img);
end
dqe=mean_ct/6.25/3.6/2.35/0.2;
%% fitting and plotting
beam_I=[0.5 1.05 2.25 3.3 3.88 4.25 4.55 4.88 5.2 5.55 5.95 6.35 6.8 7.25 7.75];
beam_I_fit=[0.5 1.05 2.25 3.3 3.88 4.25 4.55 4.88];
mean_ct_fit=mean_ct(1:8);
%WD=[34 32 28 24 20 18 16 14 13];
SE_fit=polyfit(beam_I_fit,mean_ct_fit,1);
SE_fit_line=SE_fit(1)*beam_I+SE_fit(2);
plot(beam_I,mean_ct,'o',beam_I,SE_fit_line,'Color','black','MarkerSize',8,'LineWidth',2);
%plot(WD,dqe,'o','Color','black','MarkerSize',8,'LineWidth',2);
xlim([0 8]);
ylim([0 6]);
ax=gca;
ax.TickLength=[0.01, 0.01];
ax.LineWidth = 2;
xlabel('beam current {\it I} (pA)','FontSize',18);
%xlabel('working distance (mm)','FontSize',18);
ylabel('mean SE number','FontSize',18);
%ylabel('DQE','FontSize',18);
set(ax,'XTick',0:1:8,'FontSize',18);
set(ax,'YTick',0:1:6,'FontSize',18);
hold on;
DQE=SE_fit(1)/6.25/3.6/0.2;

```

```

%%-----SEM_oscilloscope_imaging_peak_stats.m-----%%
% This code reads the SE detector and scan signals and calculates the
% width and height histograms of the detector pulses. It plots the SE
% detector waveform and the width and height histograms.
clear;clc;
scan=load('C3exp00011.dat');
pulses=load('C1exp00011.dat');
filenos=0:0;
[~,sz_fi]=size(filenos);
no_ppl=48;
no_lines=47;
start_first=-30.2761e-6;
end_first=-3.5361e-6;
gap=70.40e-6;
%img=imread('img12.tif');
ct_image_avg=zeros(no_ppl,no_lines);
int_image_avg=zeros(no_ppl,no_lines);
pulse_counting_threshold=2;

%h = fspecial('average', [1 5]);
%%
ctr=0;
for fi=1:sz_fi
    %scan_filename=strcat('C4pulses1_000',num2str(filenos(fi),'%02d'),' .dat');
    %pulses_filename=strcat('C1pulses1_000',num2str(filenos(fi),'%02d'),' .dat');
    %scan=load(scan_filename);
    %pulses=load(pulses_filename);
    sz_scan=size(scan,1);
    pklocs=zeros(1,sz_scan);
    % scan_dur=zeros(1,sz_scan);
    % true_pulses=zeros(1,sz_scan);
    % pulse_edges=zeros(1,sz_scan);
    % pixel_edges=zeros(1,sz_scan);
    % int_image=zeros(no_ppl,no_lines);
    % ct_image=zeros(no_ppl,no_lines);
    for i=1:no_lines
        % t_s=find(scan(:,1)>=start_first+(i-1)*gap,1);
        % t_e=find(scan(:,1)>=end_first+(i-1)*gap,1);
        % scan_dur_pixels(i)=t_e-t_s;
        % pixel_dwell_pixels(i)=floor(scan_dur_pixels(i)/no_ppl);
        % pixel_dwell_last_pixels(i)=scan_dur_pixels(i)-pixel_dwell_pixels(i)*(no_ppl-1);
        % scan_dur(t_s:t_e)=1;
        % true_pulses(t_s:t_e)=pulses(t_s:t_e,2);
        for k=t_s:t_e
            % if (pulses(k,2)>pulse_counting_threshold && pulses(k-1,2)<pulse_counting_threshold && pulses(k+1,2)>
            % pulse_counting_threshold)
            % pulse_edges(k)=1;
            % end
        end
        for j=1:no_ppl-1
            % start_index=t_s+(j-1)*(pixel_dwell_pixels(i));
            % end_index=t_s+j*pixel_dwell_pixels(i)-1;
            % pixel_edges(start_index:end_index)=mod(j,2);
            % int_image(j,i)=sum(pulses(start_index:end_index,2));
            % ct_image(j,i)=sum(pulse_edges(start_index:end_index));
            %for k=t_s+(j-1)*pixel_dwell_pixels+3:t_s+j*pixel_dwell_pixels-3
            %if (pulses(k,2)>3 && pulses(k-1,2)<3 && pulses(k+1,2)>3)
            %pulse_edges(k)=5;
            %ct_image(j,i)=ct_image(j,i)+1;
            %end
        end
        %end
        % int_image(no_ppl,i)=sum(pulses(end_index+1:t_e,2));
        % ct_image(no_ppl,i)=sum(pulse_edges(end_index+1:t_e));
    end
    % ct_image_avg=ct_image_avg+ct_image;
    % int_image_avg=int_image_avg+int_image;
    %figure();
    %fig=imagesc(ct_image_avg);
    %colormap gray;
    %saveas(fig, strcat('image', num2str(fi, '%01d'), '.png'));
    %pause(1);
    %int_image_gray=mat2gray(int_image);
    %int_image=mean(mean(ct_image))/mean(mean(int_image))*int_image;
    fi
    %filt_true_pulses=filter2(h,true_pulses);
    [pks,locs,widths]=findpeaks(pulses(:,2),'MinPeakHeight',1,'MinPeakProminence',1,'WidthReference','halfheight');
    [npeaks,-]=size(pks);
    widths=widths*10e-9;
    pks_all(ctr+1:ctr+npeaks)=pks;
    widths_all(ctr+1:ctr+npeaks)=widths;
    ctr=ctr+npeaks;
    pklocs(locs)=5;
    npeaks
end
%%
[width_hist,edges]=histcounts(widths_all,'BinWidth',10e-9);
width_pts=10e-9:10e-9:760e-9;
%f=fit(width_pts.',width_hist.','gauss1');
%width_fit=feval(f,width_pts);
plot(width_pts/1e-9,width_hist,'-', 'LineWidth',2);
%%

```

```

[height_hist,edges]=histcounts(pks, 'BinWidth',0.1);
height_pts=1.05:0.1:5.95;
%fit
f=fit(width_pts.',width_hist.', 'gauss1');
%width_fit=feval(f,width_pts);
plot(height_pts,height_hist/max(height_hist), '-','LineWidth',2,'Color','black');
ax=gca;
ax.TickLength=[0.01, 0.01];
ax.LineWidth = 2;
xlabel('pulse height (V)','FontSize',18);
ylabel('counts(normalized)','FontSize',18);
set(ax,'XTick',0:1:6,'FontSize',18);
set(ax,'YTick',0:0.2:1,'FontSize',18);
%%

%ct_image_avg=ct_image_avg;
%int_image_avg=mean(mean(ct_image_avg))/mean(mean(int_image_avg))*int_image_avg;
%%
%plot(scan(:,1)/1e-6,true_pulses(:,1),scan(:,1)/1e-6,pulse_edges(:,1),scan(:,1)/1e-6,pixel_edges(:,1));
%plot(scan(:,1)/1e-6,scan(:,2),scan(:,1)/1e-6,scan_dur);
plot(scan(:,1)/1e-6,pulses(:,2), 'LineWidth',1);
xlim([250 300]);
ylim([-1 6]);
ax=gca;
ax.TickLength=[0.01, 0.01];
ax.LineWidth = 2;
xlabel('time (\mus)','FontSize',18);
ylabel('voltage (V)','FontSize',18);
set(ax,'XTick',250:10:300,'FontSize',18);
set(ax,'YTick',-1:1:6,'FontSize',18);
%%
figure(); fig=imagesc(img);
% colormap gray
saveas(fig,'imageorg.png');
figure(); imagesc(int_image_avg');
% colormap gray
figure(); imagesc(ct_image_avg');
% colormap gray
hold on;

```

D.4 MATLAB code for chapter 5

The script `SEM_scan_plots.m` was used to generate plots of the SEM scan waveforms in Figure 5-1. The script `SEM_oscilloscope_imaging_averagingv2.m` was used to generate the SEM scan and SE detector waveform images in Figure 5-3 and the in-chamber SE count and conventional images in Figure 5-4. Script `SEM_oscilloscope_imaging_averaging_two_det.m` was used to generate the SE count images in Figure 5-5. This script used the functions `scanalign2.m`, `scan-gap.m`, and `scanpixels.m`. The scripts `mean_variance_total.m` and `mean_variance_partial.m` were used to generate the count and conventional image histograms, contrast and SNR plots in Figure 5-5 as well as the SE probability distribution plots in Figure 5-6. The script `cond_reill_SEM.m` was used to generate the conditional re-illumination SE count images in Figure 5-7 and the MARE and SNR plots comparing the two re-illumination schemes in Figure 5-8.

```
%%-----SE_scan_plots.m-----%%
% This code plots the SEM scan waveforms
clear;clc;
scan1=load('C3exp00012.dat');
pulses1=load('C1exp00012.dat');
%scan1=load('C1_red300005.dat');
%scan2=load('C1_red300007.dat');
%% Subplot of horizontal and vertical scan (300006 and 300007 from 10/3)
subplot(2,1,1);
plot(scan1(:,1)+0.33565,scan1(:,2),'Color','black'); %-0.33565 -0.15428
xlim([-0.1 0.65])
ax=gca;
ax.TickLength=[0.01, 0.01];
ax.LineWidth = 2;
set(ax,'XTick',-0.1:0.1:0.7,'FontSize',18);
set(ax,'YTick',0.5:0.5:1.5,'FontSize',18);
xlabel('time (ms)','FontSize',18);
ylabel('voltage (V)','FontSize',18);
subplot(2,1,2);
plot(scan2(:,1)+0.15428,scan2(:,2),'Color','black'); %-0.33565 -0.15428
xlim([-0.1 0.65])
ylim([0 0.5]);
ax=gca;
ax.TickLength=[0.01, 0.01];
ax.LineWidth = 2;
set(ax,'XTick',-0.1:0.1:0.7,'FontSize',18);
set(ax,'YTick',0:0.2:0.4,'FontSize',18);
xlabel('time (s)','FontSize',18);
ylabel('voltage (V)','FontSize',18);
%hold on;
%% For plotting first few lines from 30005
plot((scan1(:,1)+0.081)*1e3,scan1(:,2),'Color','black','LineWidth',1); %
xlim([0 20]);
ylim([0.4 1.8]);
ax=gca;
ax.TickLength=[0.01, 0.01];
ax.LineWidth = 2;
set(ax,'XTick',0:5:20,'FontSize',18);
set(ax,'YTick',0.5:0.5:1.5,'FontSize',18);
xlabel('time (ms)','FontSize',18);
ylabel('voltage (V)','FontSize',18);
%% For plotting one line showing pixels from 30004
plot((scan1(:,1)-0.0092767)*1e3,scan1(:,2),'Color','black','LineWidth',1); % 0.0092767
xlim([0 2.716]);
ylim([0.3 1.4]);
ax=gca;
ax.TickLength=[0.01, 0.01];
ax.LineWidth = 2;
set(ax,'XTick',0:0.5:3,'FontSize',18);
set(ax,'YTick',0.3:0.3:1.5,'FontSize',18);
xlabel('time (ms)','FontSize',18);
ylabel('voltage (V)','FontSize',18);
%% For plotting first few pixels from 30004
plot((scan1(:,1)-0.0094084)*1e6,scan1(:,2),'Color','black','LineWidth',1); %
xlim([0 300]);
ylim([0.81 0.9]);
ax=gca;
ax.TickLength=[0.01, 0.01];
ax.LineWidth = 2;
set(ax,'XTick',0:50:300,'FontSize',18);
```

```

set(ax, 'YTick', 0.81:0.02:0.9, 'FontSize', 18);
xlabel('time (\mus)', 'FontSize', 18);
ylabel('voltage (V)', 'FontSize', 18);
%% For plotting first part of scan 3 waveform from exp12, 10/16 data
plot((scan1(:,1)+7.8e-6)*1e6, scan1(:,2), 'Color', 'black', 'LineWidth', 1);
xlim([0 60]);
ylim([0.45 0.9]);
ax=gca;
ax.TickLength=[0.01, 0.01];
ax.LineWidth = 2;
set(ax, 'XTick', 0:10:60, 'FontSize', 18);
set(ax, 'YTick', 0.45:0.1:0.9, 'FontSize', 18);
xlabel('time (\mus)', 'FontSize', 18);
ylabel('voltage (V)', 'FontSize', 18);
%% For plotting a few scan 3 lines and signal for figure 2 of chapter 4 from exp12
subplot(2,1,1);
plot((scan1(:,1))*1e6, scan1(:,2), 'Color', 'black');
xlim([0 300]);
ylim([0.2 1.4]);
ax=gca;
ax.TickLength=[0.01, 0.01];
ax.LineWidth = 2;
set(ax, 'XTick', -100:1000:3000, 'FontSize', 18);
set(ax, 'YTick', 0:3:5, 'FontSize', 18);
%xlabel('time (\mus)', 'FontSize', 18);
%ylabel('voltage (V)', 'FontSize', 18);
subplot(2,1,2);
plot((scan1(:,1))*1e6, pulses1(:,2), 'Color', 'black');
xlim([0 300]);
ylim([0 6]);
ax=gca;
ax.TickLength=[0.01, 0.01];
ax.LineWidth = 2;
set(ax, 'XTick', -100:1000:3000, 'FontSize', 18);
set(ax, 'YTick', 10:30:60, 'FontSize', 18);
%xlabel('time (\mus)', 'FontSize', 18);
%ylabel('voltage (V)', 'FontSize', 18);

```

```

%%-----SEM_oscilloscope_imaging_averagingv2.m-----%%
% This code takes acquisition frames (consisting of signal from one detector
%and scan waveforms) and creates conventional and electron count images from
% these frames. It also plots the scan waveform lines and pulses with
% pixels in chapter 5 figure 3.
clear;clc;
scan1=load('C3exp100000.dat');
pulses1=load('C4exp100000.dat');
no_ppl=169;
%no_lines=122;
delt=10e-9;
start_first=-3866.4613e-6;
end_first=-3792.0913e-6;
[gap, no_lines]=scangap(scan1,delt);
%img=imread('img06.tif');
ct_image_avg=zeros(no_ppl,no_lines);
int_image_avg=zeros(no_ppl,no_lines);
pulse_counting_threshold=1; % tradeoff correct pixel and voltage level
ct_filename='ct_img.gif';
%%
filenos=0:1;
[~,sz_fi]=size(filenos);
for fi=1:sz_fi
    scan_filename=strcat('C3exp1000',num2str(filenos(fi),'%02d'),' .dat');
    pulses_filename=strcat('C4exp1000',num2str(filenos(fi),'%02d'),' .dat');
    scan=load(scan_filename);
    pulses=load(pulses_filename);
    sz_scan=size(scan,1);
    if (fi>1)
        %plot(pulses(:,1),pulses(:,2));
        %hold on;
        [misalign, pulses(:,2),scan(:,2)]=scanalign(scan1,scan,sz_scan,pulses);
        %plot(pulses(:,1),pulses(:,2));
    end
    scan_dur=zeros(1,sz_scan);
    true_pulses=zeros(1,sz_scan);
    pulse_edges=zeros(1,sz_scan);
    pixel_edges=zeros(1,sz_scan);
    int_image=zeros(no_ppl,no_lines);
    ct_image=zeros(no_ppl,no_lines);
    for i=1:no_lines
        t_s=find(scan(:,1)>=start_first+(i-1)*gap,1);
        t_e=find(scan(:,1)>=end_first+(i-1)*gap,1);
        scan_dur_pixels(i)=t_e-t_s;
        pixel_dwell_pixels(i)=floor(scan_dur_pixels(i)/no_ppl);
        pixel_dwell_last_pixels(i)=scan_dur_pixels(i)-pixel_dwell_pixels(i)*(no_ppl-1);
        scan_dur(t_s:t_e)=1;
        true_pulses(t_s:t_e)=pulses(t_s:t_e,2);
        for k=t_s:t_e
            if (pulses(k,2)>pulse_counting_threshold && pulses(k-1,2)<pulse_counting_threshold && pulses(k+1,2)>
                pulse_counting_threshold)
                pulse_edges(k)=1;
            end
        end
        for j=1:no_ppl-1
            start_index=t_s+(j-1)*(pixel_dwell_pixels(i));
            end_index=t_s+j*pixel_dwell_pixels(i)-1;
            pixel_edges(start_index:end_index)=mod(j,2);
            int_image(j,i)=sum(pulses(start_index:end_index,2));
            ct_image(j,i)=sum(pulse_edges(start_index:end_index));
        %for k=t_s+(j-1)*pixel_dwell_pixels+3:t_s+j*pixel_dwell_pixels-3
        %if (pulses(k,2)>3 && pulses(k-1,2)<3 && pulses(k+1,2)>3)
            %pulse_edges(k)=5;
            %ct_image(j,i)=ct_image(j,i)+1;
        %end
        %end
        end
        int_image(no_ppl,i)=sum(pulses(end_index+1:t_e,2));
        ct_image(no_ppl,i)=sum(pulse_edges(end_index+1:t_e));
    end
    ct_image_avg=ct_image_avg+ct_image;
    int_image_avg=int_image_avg+int_image;
    %figure();
    %fig=figure;
    %imagesc(ct_image_avg);
    %caxis([0 56]);
    %colormap gray;
    %saveas(fig, strcat('image', num2str(fi, '%01d'), '.png'));
    %pause(1);
    %int_image_gray=mat2gray(int_image);
    %int_image=mean(mean(ct_image))/mean(mean(int_image))*int_image;
    %plot(scan(:,1)/1e-6,scan(:,2));
    %hold on;
    %frame = getframe(fig);
    %im = frame2im(frame);
    %[A,map] = rgb2ind(im,256);
    if fi == 1
        % imwrite(A,map,ct_filename, 'gif', 'LoopCount', Inf, 'DelayTime', 0.5);
    else
        % imwrite(A,map,ct_filename, 'gif', 'WriteMode', 'append', 'DelayTime', 0.5);
    end
end
fi

```

```

end
%%

%ct_image_avg=ct_image_avg;
int_image_avg=mean(mean(ct_image_avg))/mean(mean(int_image_avg))*int_image_avg;
%%
%plot(scan(:,1)/1e-6,true_pulses(:,scan(:,1)/1e-6,pulse_edges(:,scan(:,1)/1e-6,pixel_edges(:)));
%plot(scan(:,1)/1e-6,scan(:,2),scan(:,1)/1e-6*scan_dur);
%hold on;
%plot(scan(:,1)/1e-6,pulses(:,2));
%%
%figure();fig=imagesc(img);
% colormap gray
%saveas(fig,'imageorg.png');
% figure();imagesc(int_image_avg');
% colormap gray
%ct_image_avg=ct_image_avg(1:191,:);
% figure();imagesc(ct_image_avg');
% colormap gray
% save('cto.mat','ct_image_avg');
% saveas(fig,'imagect.tif');
%hold on;
%%% Plotting two scan lines and signal for Chap 4 figure 3 from 1/16 data. Used exp0000 and exp0002
scanorg=load('C3exp100002.dat');
pulsesorg=load('C4exp100002.dat');
%%% Ctd..
plot((scan1(:,1)+4.1e-3)*1e3,scan1(:,2),(scanorg(:,1)+4.1e-3)*1e3,scanorg(:,2)+1.15);
xlim([0 1])
ylim([-0.16 2.15]);
ax=gca;
ax.TickLength=[0.01, 0.01];
ax.LineWidth = 2;
set(ax,'XTick',0:0.2:1,'FontSize',18);
set(ax,'YTick',0:1:2,'FontSize',18);
xlabel('time (ms)','FontSize',18);
ylabel('voltage (V)','FontSize',18);
%%% Plotting scan lines and signal for Chap 4 fig 3 (c) using 1/16 data exp0002
plot(scan(:,1)/1e-3+3.9,5*scan(:,2),scan(:,1)/1e-3+3.9,true_pulses,scan(:,1)/1e-3+3.9, pulses(:,2)+6);
xlim([0 0.47]);
ylim([-0.3 12]);
ax=gca;
ax.TickLength=[0.01, 0.01];
ax.LineWidth = 2;
set(ax,'XTick',0:0.1:0.5,'FontSize',18);
set(ax,'YTick',0:2:12,'FontSize',18);
xlabel('time (ms)','FontSize',18);
ylabel('voltage (V)','FontSize',18);
%%% Plotting pulses with pixels for Chap 4 fig 3 (c) using 1/16 data exp00002
plot(scan(:,1)/1e-6+3900,true_pulses,scan(:,1)/1e-6+3900,5*pixel_edges(:),'','LineWidth',2,'Color','black');
xlim([38.572 43.322]);
ylim([-0.3 6]);
ax=gca;
ax.TickLength=[0.01, 0.01];
ax.LineWidth = 2;
set(ax,'XTick',38:1:43,'FontSize',18);
set(ax,'YTick',0:2:6,'FontSize',18);
xlabel('time (\mus)','FontSize',18);
ylabel('voltage (V)','FontSize',18);

```

```

%%-----scanalign2.m-----%%
% This function finds the autocorrelation between two SEM scan waveforms
% and calculates the misalignment between them.
function [misalign, pulse2align, pulse3align, scan2align, scan2time]=scanalign2(scan1, scan2, sz_scan, pulse2, pulse3)
%plot(scan1(:,1)/1e-6, scan1(:,2), scan2(:,1)/1e-6, scan2(:,2));
scanwf1=scan1(:,2)-mean(mean(scan1(:,2)));
scanwf2=scan2(:,2)-mean(mean(scan2(:,2)));
scancorr=xcorr(scanwf1, scanwf2);
%plot(scancorr);
[~, maxind]=max(scancorr);
misalign=sz_scan-maxind;
scan2time=scan1(:,1);
%%
if misalign>0
    pulse2align=[pulse2(misalign+1:end,2)' zeros(misalign,1)']';
    pulse3align=[pulse3(misalign+1:end,2)' zeros(misalign,1)']';
    scan2align=[scan2(misalign+1:end,2)' zeros(misalign,1)']';
else
    pulse3align=[zeros(-misalign,1)' pulse3(1:end-(-misalign),2)']';
    pulse2align=[zeros(-misalign,1)' pulse2(1:end-(-misalign),2)']';
    scan2align=[zeros(-misalign,1)' scan2(1:end-(-misalign),2)']';
end

```

```

%%----- scangap.m -----%%
% This function finds the autocorrelation between two SEM scan waveforms
% and calculates the period of the waveform from the gap between the
% autocorrelation peaks
function [gap,no_lines]=scangap(scan1,delt)
scanwf1=scan1(:,2)-mean(mean(scan1(:,2)));
%scanwf2=scan2(:,2)-mean(mean(scan2(:,2)));
scancorr=xcorr(scanwf1,scanwf1);
[maxval,-]=max(scancorr);
[~,locs]=findpeaks(scancorr,'MinPeakHeight',0,'MinPeakProminence',maxval/1.5);
%findpeaks(scancorr,'MinPeakHeight',0,'MinPeakProminence',maxval/1.5,'Annotate','peaks');
locs_diff=diff(locs);
diff_mean=mean(locs_diff);
gap=diff_mean*delt;
maxscan=max(scan1(:,2));
[~,scanpklocs]=findpeaks(scan1(:,2),'MinPeakHeight',0.5,'MinPeakProminence',0.2,'MinPeakDistance',diff_mean-300,'
Annotate','peaks');
[no_lines,-]=size(scanpklocs);

```

```

%%-----scanpixels.m-----%%
% This code finds the number of pixels in each linescan.
clear;clc;
scanl=load('C3scan00000.dat');
img=imread('img01.tif');
%scanline=l-scanl(8711:121680,2);
scanline=scanl(:,2);
[-,scanreslocs]=findpeaks(scanl(:,2),'MinPeakProminence',0.2,'Annotate','peaks');
%%
plateau=70e-6; %for scan 9
delt=40e-9;
%scanline=l-scanl(8711:121680,2);
scanline=l-scanl(scanreslocs(1)+plateau/delt:scanreslocs(2),2);
%plot(scanline);
[-,scanpklocs]=findpeaks(scanline,'MinPeakProminence',0.005,'MinPeakDistance',500,'Annotate','peaks');
%findpeaks(scanline,'MinPeakProminence',0.005,'MinPeakDistance',500,'Annotate','peaks');
%figure();
%imagesc(img);
[no_pixels,-]=size(scanpklocs);
no_pixels=no_pixels-1;

```

```

%%-----SEM_oscilloscope_imaging_averaging_two_det.m-----%%
% This code takes acquisition frames (consisting of signal from both detectors
% and scan waveforms) and creates conventional and electron count images from
% these frames.
clear;clc;
scan1=load('C1scan0000.dat');
scan1=scan1(3:end-2,:);
pulses1il=load('C3scan00000.dat');
pulses1il=pulses1il(3:end-2,:);
pulses1ic=load('C4scan00000.dat');
%%
img=imread('img07.tif');
%%
no_ppl=262;
%no_lines=122;
delt=10e-9;
start_first=-50092.29e-6;
end_first=-49979.63e-6;
[gap, no_lines]=scangap(scan1,delt);
%img=imread('img06.tif');
ct_image_avgil=zeros(no_ppl,no_lines);
ct_image_avgic=zeros(no_ppl,no_lines);
int_image_avgil=zeros(no_ppl,no_lines);
int_image_avgic=zeros(no_ppl,no_lines);
pulse_counting_threshold=1; % tradeoff correct pixel and voltage level
ct_image_stack_il=zeros(no_ppl,no_lines,32);
ct_image_stack_ic=zeros(no_ppl,no_lines,32);
int_image_stack_il=zeros(no_ppl,no_lines,32);
int_image_stack_ic=zeros(no_ppl,no_lines,32);
ct_filename='ct_img.gif';
%%
filenos=0:31;
[~,sz_fi]=size(filenos);
for fi=1:sz_fi
    scan_filename=strcat('C1scan000',num2str(filenos(fi),'%02d'),' .dat');
    pulsesil_filename=strcat('C3scan000',num2str(filenos(fi),'%02d'),' .dat');
    pulsesic_filename=strcat('C4scan000',num2str(filenos(fi),'%02d'),' .dat');
    scan=load(scan_filename);
    scan=scan(3:end-2,:);
    pulsesil=load(pulsesil_filename);
    pulsesil=pulsesil(3:end-2,:);
    pulsesic=load(pulsesic_filename);
    sz_scan=size(scan,1);
    if (fi>1)
        %plot(pulses(:,1),pulses(:,2));
        %hold on;
        [misalign,pulsesil(:,2),pulsesic(:,2),scan(:,2),scan(:,1)]=scanalign2(scan1,scan,sz_scan,pulsesil,pulsesic);
        %plot(pulses(:,1),pulses(:,2));
    end
    scan_dur=zeros(1,sz_scan);
    true_pulsesil=zeros(1,sz_scan);
    true_pulsesic=zeros(1,sz_scan);
    pulseil_edges=zeros(1,sz_scan);
    pulseic_edges=zeros(1,sz_scan);
    pixel_edges=zeros(1,sz_scan);
    int_imageic=zeros(no_ppl,no_lines);
    int_imageil=zeros(no_ppl,no_lines);
    ct_imageic=zeros(no_ppl,no_lines);
    ct_imageil=zeros(no_ppl,no_lines);
    for i=1:no_lines
        t_s=find(scan(:,1)>=start_first+(i-1)*gap,1);
        t_e=find(scan(:,1)>=end_first+(i-1)*gap,1);
        scan_dur_pixels(i)=t_e-t_s;
        pixel_dwell_pixels(i)=floor(scan_dur_pixels(i)/no_ppl);
        pixel_dwell_last_pixels(i)=scan_dur_pixels(i)-pixel_dwell_pixels(i)*(no_ppl-1);
        scan_dur(t_s:t_e)=1;
        true_pulsesil(t_s:t_e)=pulsesil(t_s:t_e,2);
        true_pulsesic(t_s:t_e)=pulsesic(t_s:t_e,2);
        for k=t_s:t_e
            if (pulsesil(k,2)>pulse_counting_threshold && pulsesil(k-1,2)<pulse_counting_threshold && pulsesil(k+1,2)>
                pulse_counting_threshold)
                pulseil_edges(k)=1;
            end
            if (pulsesic(k,2)>pulse_counting_threshold && pulsesic(k-1,2)<pulse_counting_threshold && pulsesic(k+1,2)>
                pulse_counting_threshold)
                pulseic_edges(k)=1;
            end
        end
    end
    for j=1:no_ppl-1
        start_index=t_s+(j-1)*(pixel_dwell_pixels(i));
        end_index=t_s+j*pixel_dwell_pixels(i)-1;
        pixel_edges(start_index:end_index)=mod(j,2);
        int_imageic(j,i)=sum(pulsesic(start_index:end_index,2));
        int_imageil(j,i)=sum(pulsesil(start_index:end_index,2));
        ct_imageic(j,i)=sum(pulseic_edges(start_index:end_index));
        ct_imageil(j,i)=sum(pulseil_edges(start_index:end_index));
    %for k=t_s+(j-1)*pixel_dwell_pixels+3:t_s+j*pixel_dwell_pixels-3
        %if (pulses(k,2)>3 && pulses(k-1,2)<3 && pulses(k+1,2)>3)
            %pulse_edges(k)=5;
            %ct_image(j,i)=ct_image(j,i)+1;
        %end
    %end
end
end

```

```

end
int_imageic(no_ppl,i)=sum(pulsesic(end_index+1:t_e,2));
int_imageil(no_ppl,i)=sum(pulsesil(end_index+1:t_e,2));
ct_imageic(no_ppl,i)=sum(pulseic_edges(end_index+1:t_e));
ct_imageil(no_ppl,i)=sum(pulseil_edges(end_index+1:t_e));
end
ct_image_stack_il(:,:,fi)=ct_imageil;
ct_image_stack_ic(:,:,fi)=ct_imageic;
int_image_stack_ic(:,:,fi)=int_imageic;
int_image_stack_il(:,:,fi)=int_imageil;
ct_image_avgic=ct_image_avgic+ct_imageic;
ct_image_avgil=ct_image_avgil+ct_imageil;
int_image_avgic=int_image_avgic+int_imageic;
int_image_avgil=int_image_avgil+int_imageil;
%figure();
%fig=figure;
%imagesc(ct_image_avg');
%caxis([0 56]);
%colormap gray;
%saveas(fig, strcat('image', num2str(fi, '%01d'), '.png'));
%pause(1);
%int_image_gray=mat2gray(int_image);
%int_image=mean(mean(ct_image))/mean(mean(int_image))*int_image;
%plot(scan(:,1)/1e-6,scan(:,2));
%hold on;
%frame = getframe(fig);
%im = frame2im(frame);
%[A,map] = rgb2ind(im,256);
if fi == 1
% imwrite(A,map,ct_filename, 'gif', 'LoopCount', Inf, 'DelayTime', 0.5);
else
% imwrite(A,map,ct_filename, 'gif', 'WriteMode', 'append', 'DelayTime', 0.5);
end
fi
end
%%

%ct_image_avg=ct_image_avg;
%int_image_avg=mean(mean(ct_image_avg))/mean(mean(int_image_avg))*int_image_avg;
%%
%plot(scan(:,1)/1e-6,true_pulses(:,scan(:,1)/1e-6,pulse_edges(:,scan(:,1)/1e-6,pixel_edges(:)));
%plot(scan(:,1)/1e-6,scan(:,2),scan(:,1)/1e-6*scan_dur);
%hold on;
%plot(scan(:,1)/1e-6,pulses(:,2));
%%
%figure(); fig=imagesc(img);
% colormap gray
% saveas(fig, 'imageorg.png');
% figure(); imagesc(int_image_avg');
% colormap gray
%ct_image_avg=ct_image_avg(1:191,:);
% figure(); imagesc(ct_image_avg');
% colormap gray
% save('cto.mat', 'ct_image_avg');
% saveas(fig, 'imagect.tif');
%hold on;
%%
%save('ct_both.mat', 'ct_image_avgic', 'ct_image_avgil');
%save('int_both.mat', 'int_image_avgic', 'int_image_avgil');
%save('ct_stack.mat', 'ct_image_stack_il', 'ct_image_stack_ic');
%save('int_stack.mat', 'int_image_stack_il', 'int_image_stack_ic');

```

```

%%----- mean_variance_total.m -----%%
% This code calculates the histograms for the counting and conventional SEM
% images and finds the contrast between the sample and background pixels in the final images.
% It also fits the probability distribution of the sample and background
% pixels to Poisson and Neyman type A distributions
clear;clc;
ct_vars=load('ct_both.mat');
int_vars=load('int_both.mat');
im=double(imread('img06.tif'));
mean_im=mean(mean(im));
int_im_ic=sc=nt_vars.int_image_avgic*mean(mean(ct_vars.ct_image_avgic))/mean(mean(int_vars.int_image_avgic));
ct_im_mixed=ct_vars.ct_image_avgic+ct_vars.ct_image_avgil;
mean_ct_mixed=mean(mean(ct_im_mixed));
int_im_mixed=int_vars.int_image_avgic+int_vars.int_image_avgil;
mean_int_im=mean(mean(int_im_mixed));
%im_sc=im*mean_ct_mixed/mean_im;
int_im_sc=int_im_mixed*mean_ct_mixed/mean_int_im;
%% Plotting images – figures 4 and 5 in chapter 4
figure();
ctim=imagesc(ct_im_mixed');
colormap gray
axis off
pbaspect([1 188/262 1])
c = colorbar;
c.Ticks=[0 10 20 30 40];
figure();
intim=imagesc(int_im_sc');
pbaspect([1 188/262 1])
colormap gray
axis off
c = colorbar;
c.Ticks=[0 10 20 30 40];
%saveas(ctim,'ct_im_mixed.png');
%saveas(intim,'int_im_mixed.png');
%% Histogramming – figure 5 in chapter 4

histedges=-0.45:1:60.55;
ct_hist=histcounts(ct_im_mixed,histedges);
int_hist=histcounts(int_im_sc,histedges);
p=plot(0:60,ct_hist/sum(ct_hist),'-',0:60,int_hist/sum(int_hist),'-', 'Color','black','LineWidth',2);
xlim([0 40]);
ylim([0 0.5]);
ax=gca;
ax.TickLength=[0.01, 0.01];
ax.LineWidth = 2;
xlabel('intensity/number of SEs','FontSize',18);
ylabel('counts(normalized)','FontSize',18);
set(ax,'XTick',0:4:40,'FontSize',18);
set(ax,'YTick',0:0.1:0.5,'FontSize',18);
%saveas(p,'hist_osc_1.png');
%% Calculating contrast of sample to background and variance
[ctrows,ctcols,-]=find(ct_im_mixed>7);
[sz,-]=size(ctrows);
sample_ct_vals=zeros(1,sz);
sample_int_vals=zeros(1,sz);
dist_sample=zeros(1,40);
for i=1:sz
    sample_ct_vals(i)=ct_im_mixed(ctrows(i),ctcols(i));
    sample_int_vals(i)=int_im_sc(ctrows(i),ctcols(i));
    dist_sample(sample_ct_vals(i)-7)=dist_sample(sample_ct_vals(i)-7)+1;
end
sample_ct_vals_act=sample_ct_vals; %To find distribution of sample counts
mean_sample_acts=mean(sample_ct_vals_act);
var_sample_ct=var(sample_ct_vals_act);
sample_var_mean_rat=var_sample_ct/mean_sample_acts;
int_im_sc2=int_im_mixed*mean(sample_ct_vals)/mean(sample_int_vals);
[ctrows,ctcols,-]=find(ct_im_mixed<=7);
[sz,-]=size(ctrows);
vac_ct_vals=zeros(1,sz);
vac_int_vals=zeros(1,sz);
dist_vac=zeros(1,8);
for i=1:sz
    vac_ct_vals(i)=ct_im_mixed(ctrows(i),ctcols(i));
    vac_int_vals(i)=int_im_sc(ctrows(i),ctcols(i));
    dist_vac(vac_ct_vals(i)+1)=dist_vac(vac_ct_vals(i)+1)+1;
end
mean_vac_ct=mean(vac_ct_vals);
mean_vac_int=mean(vac_int_vals);
vac_ct_vals=vac_ct_vals; %To find distribution of vac counts
var_vac_ct=var(vac_ct_vals);
vac_var_mean_rat=var_vac_ct/(2*mean_vac_ct);
rat=dist_vac(2)/dist_vac(1);
%% Plotting vacuum distribution – figure 6 in chapter 4

poisson_dist=zeros(1,8);
for i=1:8
    poisson_dist(i)=exp(-mean_vac_ct)*(mean_vac_ct)^(i-1)/(factorial(i-1));
end
dist_vac=dist_vac/sum(dist_vac);
p=plot(0:7,dist_vac,'o',0:7,poisson_dist,'x','MarkerSize',10,'LineWidth',2);
xlim([0 7]);
ylim([1e-6 0.7]);

```

```

ax=gca;
ax.TickLength=[0.01, 0.01];
ax.LineWidth = 2;
xlabel('number of SEs','FontSize',18);
ylabel('probability','FontSize',18);
set(ax,'XTick',0:1:7,'FontSize',18);
set(ax,'YTick',0:0.1:0.7,'FontSize',18);
%saveas(p,'vac_dist.png');
%% Plotting sample distribution – figure 6 in chapter 4

poisson_dist_sample=zeros(1,40);
for i=1:40
    poisson_dist(i)=exp(-mean_sample_acts)*(mean_sample_acts)^(i+7)/(factorial(i+7));
end
dist_sample=dist_sample/sum(dist_sample);
p=semilogy(8:47,dist_sample,'o',8:47,poisson_dist,'x','MarkerSize',10,'LineWidth',2);
xlim([8 47]);
ylim([1e-6 0.1]);
ax=gca;
ax.TickLength=[0.01, 0.01];
ax.LineWidth = 2;
xlabel('number of SEs','FontSize',18);
ylabel('probability','FontSize',18);
set(ax,'XTick',8:6:47,'FontSize',18);
%set(ax,'YTick',0:0.02:0.1,'FontSize',18);
%saveas(p,'vac_dist.png');
%% Fitting vacuum to Neyman type A
v=(var_vac_ct-mean_vac_ct)/mean_vac_ct;
l=mean_vac_ct/v;
neyman_dist=zeros(1,8);
for i=0:7
    ps=0;
    for j=0:100
        ps=ps+(1*exp(-v))^j/factorial(j)*j^i;
    end
    neyman_dist(i+1)=v^i*exp(-1)/factorial(i)*ps;
end
p=plot(0:7,dist_vac,'o',0:7,poisson_dist,'x',0:7,neyman_dist,'d','MarkerSize',10,'LineWidth',2);
xlim([0 7]);
ylim([1e-6 0.7]);
ax=gca;
ax.TickLength=[0.01, 0.01];
ax.LineWidth = 2;
xlabel('number of SEs','FontSize',18);
ylabel('probability','FontSize',18);
set(ax,'XTick',0:1:7,'FontSize',18);
set(ax,'YTick',0:0.1:0.7,'FontSize',18);
%% Fitting sample to Neyman type A
v=(var_sample_ct-mean_sample_acts)/mean_sample_acts;
l=mean_sample_acts/v;
neyman_dist=zeros(1,40);
for i=1:40
    ps=0;
    for j=0:100
        ps=ps+(1*exp(-v))^j/factorial(j)*j^(i+7);
    end
    neyman_dist(i)=v^(i+7)*exp(-1)/factorial(i+7)*ps;
end
p=semilogy(8:47,dist_sample,'o',8:47,poisson_dist,'x',8:47,neyman_dist,'d','MarkerSize',10,'LineWidth',2);
xlim([8 47]);
ylim([1e-6 0.1]);
ax=gca;
ax.TickLength=[0.01, 0.01];
ax.LineWidth = 2;
xlabel('number of SEs','FontSize',18);
ylabel('probability','FontSize',18);
set(ax,'XTick',8:6:47,'FontSize',18);
%set(ax,'YTick',0:0.02:0.1,'FontSize',18);

```

```

%%----- mean_variance_partial.m -----%%
% This code finds the contrast between sample and background pixels and SNR
% for the SE counting and conventional SEM images as a function of the mean
% SE number (which varies linearly with the number of frames).
clear;clc;
ct_stack=load('ct_stack.mat');
int_stack=load('int_stack.mat'); %105,52
meanil=mean(ct_stack.ct_image_stack_ic,3);
meanil=meanil(:);
varil=var(ct_stack.ct_image_stack_ic,[],3);
varil=varil(:);
% plot(meanil,meanil,meanil,varil,'o','MarkerSize',8,'LineWidth',2,'Color','black');
% xlim([0 0.8]);
% ylim([0 0.8]);
% ax=gca;
% ax.TickLength=[0.01, 0.01];
% ax.LineWidth = 2;
% xlabel('mean','FontSize',18);
% ylabel('variance','FontSize',18);
% set(ax,'XTick',0:0.2:1,'FontSize',18);
% set(ax,'YTick',0:0.2:1,'FontSize',18);
%% Plot for chapter 4 figure 6
sum_im=sum(ct_stack.ct_image_stack_ic+ct_stack.ct_image_stack_il,3);
[rs,cs,-]=find(sum_im>7);
[szs,-]=size(rs);
par_cts=zeros(32,szs);
for i=1:32
    par_sum_im=sum(ct_stack.ct_image_stack_ic(:,:,1:i)+ct_stack.ct_image_stack_il(:,:,1:i),3);
    for j=1:szs
        par_cts(i,j)=par_sum_im(rs(j),cs(j));
    end
end
m1=mean(par_cts,2);
v1=var(par_cts,[],2);
B=v1./m1-1;
% figure();
% plot(m1,B,'o','MarkerSize',8,'LineWidth',2,'Color','black');
% xlim([0 22]);
% ylim([-0.5 0.5]);
% ax=gca;
% ax.TickLength=[0.01, 0.01];
% ax.LineWidth = 2;
% xlabel('mean','FontSize',18);
% ylabel('B-factor','FontSize',18);
% set(ax,'XTick',6:2:22,'FontSize',18);
% set(ax,'YTick',0:0.1:0.5,'FontSize',18);
% hold on;
%% Buildup of contrast with frames
sum_im=sum(ct_stack.ct_image_stack_ic+ct_stack.ct_image_stack_il,3);
[rs,cs,-]=find(sum_im>7);
[szs,-]=size(rs);
par_ct=zeros(32,szs);
par_int=zeros(32,szs);
for i=1:32
    par_sum_im_ct=sum(ct_stack.ct_image_stack_ic(:,:,1:i)+ct_stack.ct_image_stack_il(:,:,1:i),3);
    par_sum_im_int=sum(int_stack.int_image_stack_ic(:,:,1:i)+int_stack.int_image_stack_il(:,:,1:i),3);
    for j=1:szs
        par_ct(i,j)=par_sum_im_ct(rs(j),cs(j));
        par_int(i,j)=par_sum_im_int(rs(j),cs(j));
    end
end
mean_sample_ct=mean(par_ct,2);
mean_sample_int=mean(par_int,2);
[rv,cv,-]=find(sum_im<=7);
[szv,-]=size(rv);
par_ct=zeros(32,szv);
par_int=zeros(32,szv);
mean_ct=zeros(1,32);
for i=1:32
    par_sum_im_ct=sum(ct_stack.ct_image_stack_ic(:,:,1:i)+ct_stack.ct_image_stack_il(:,:,1:i),3);
    mean_ct(i)=mean(mean(par_sum_im_ct));
    par_sum_im_int=sum(int_stack.int_image_stack_ic(:,:,1:i)+int_stack.int_image_stack_il(:,:,1:i),3);
    for j=1:szv
        par_int(i,j)=par_sum_im_int(rv(j),cv(j));
        par_ct(i,j)=par_sum_im_ct(rv(j),cv(j));
    end
end
mean_vac_ct=mean(par_ct,2);
mean_vac_int=mean(par_int,2);
K_ct=(mean_sample_ct-mean_vac_ct)/(mean_sample_ct+mean_vac_ct);
K_int=(mean_sample_int-mean_vac_int)/(mean_sample_int+mean_vac_int);
plot(mean_ct,K_ct,'o',mean_ct,K_int,'x','MarkerSize',10,'LineWidth',2,'Color','black');
xlim([0 8.2]);
ylim([0 1]);
ax=gca;
ax.TickLength=[0.01, 0.01];
ax.LineWidth = 2;
xlabel('mean SE count','FontSize',18);
ylabel('contrast (K)','FontSize',18);
set(ax,'XTick',0:2:8,'FontSize',18);
set(ax,'YTick',0:0.2:1,'FontSize',18);
%% Image autocorr for full and partial images - figure 5 of chapter 4

```

```

% sum_im_ct=sum(ct_stack.ct_image_stack_ic+ct_stack.ct_image_stack_il,3);
% sum_im_int=sum(int_stack.int_image_stack_ic+int_stack.int_image_stack_il,3);
% sum_im_int=sum_im_int*mean(mean(sum_im_ct))/mean(mean(sum_im_int));
% sum_im_ct=sum_im_ct-mean(mean(sum_im_ct));
% sum_im_int=sum_im_int-mean(mean(sum_im_int));
% ct_corr=xcorr2(sum_im_ct,sum_im_ct);
% int_corr=xcorr2(sum_im_int,sum_im_int);
% [corr_sz,~]=size(ct_corr);
%plot(1:corr_sz,ct_corr(:,188),1:corr_sz,int_corr(:,188));
sz_fit=3;
% fit_pts=ct_corr(262,188-sz_fit:188-1);
x_fit=188-sz_fit:188-1;
% fit_interp=polyfit(x_fit,fit_pts,1);
x_interp=188-sz_fit:188;
% nf_fit=fit_interp(1)*x_interp+fit_interp(2);
% phi_nf=nf_fit(end);
% phi=ct_corr(262,188);
% phi_noise=phi-phi_nf;
% SNR=phi_nf/phi_noise;
SNR_ct=zeros(1,32);
SNR_int=zeros(1,32);
mean_ct=zeros(1,32);
for i=1:32
    par_im_ct=sum(ct_stack.ct_image_stack_ic(:, :, 1:i)+ct_stack.ct_image_stack_il(:, :, 1:i),3);
    mean_ct(i)=mean(mean(par_im_ct));
    par_im_int=sum(int_stack.int_image_stack_ic(:, :, 1:i)+int_stack.int_image_stack_il(:, :, 1:i),3);
    par_im_int=par_im_int*mean(mean(par_im_ct))/mean(mean(par_im_int));
    par_im_ct=par_im_ct-mean(mean(par_im_ct));
    par_im_int=par_im_int-mean(mean(par_im_int));
    ct_corr=xcorr2(par_im_ct,par_im_ct);
    int_corr=xcorr2(par_im_int,par_im_int);
    %SNR ct image
    fit_pts_ct=ct_corr(262,188-sz_fit:188-1);
    fit_interp=polyfit(x_fit,fit_pts_ct,1);
    nf_fit=fit_interp(1)*x_interp+fit_interp(2);
    phi_nf=nf_fit(end);
    phi=ct_corr(262,188);
    phi_noise=phi-phi_nf;
    SNR_ct(i)=phi_nf/phi_noise;
    %SNR int image
    fit_pts_int=int_corr(262,188-sz_fit:188-1);
    fit_interp=polyfit(x_fit,fit_pts_int,1);
    nf_fit=fit_interp(1)*x_interp+fit_interp(2);
    phi_nf=nf_fit(end);
    phi=int_corr(262,188);
    phi_noise=phi-phi_nf;
    SNR_int(i)=phi_nf/phi_noise;
end
figure();
plot(mean_ct/max(mean_ct),SNR_ct,'o',mean_ct/max(mean_ct),SNR_int,'x','MarkerSize',10,'LineWidth',2,'Color','black');
xlim([0 1]);
ylim([0 12]);
ax=gca;
ax.TickLength=[0.01, 0.01];
ax.LineWidth = 2;
xlabel('mean SE count','FontSize',18);
ylabel('SNR','FontSize',18);
set(ax,'XTick',0:2:8,'FontSize',18);
set(ax,'YTick',0:2:12,'FontSize',18);
hold on

```

```

%%-----cond_reill_SEM.m-----%%
% This code implements both conditional re-illumination schemes outlined in
% chapter 5 and generates count images, MARE and SNR plots
clear;clc;
ct_stack=load('ct_stack.mat');
int_stack=load('int_stack.mat');
im_ct_corr=zeros(262,188);
im_int_corr=zeros(262,188);
se_thresh=8;
[~,sz]=size(se_thresh);
abs_err=zeros(1,sz);
frac_dose=zeros(1,sz);
SNR_ctreill=zeros(1,sz);
sz_fit=3;
x_fit=188-sz_fit:188-1;
x_interp=188-sz_fit:188;
for i=1:32
    im_ct_corr=sum(ct_stack.ct_image_stack_ic(:,:,1:i)+ct_stack.ct_image_stack_il(:,:,1:i),3);
    im_int_corr=sum(int_stack.int_image_stack_ic(:,:,1:i)+int_stack.int_image_stack_il(:,:,1:i),3);
end
for k=1:sz
    k
    im_no=32*ones(262,188);
    par_im_ct=zeros(262,188);
    ct_pxs=zeros(262,188);
    for i=1:32
        for r=1:262
            for c=1:188
                if(par_im_ct(r,c)<se_thresh(k))
                    par_im_ct(r,c)=par_im_ct(r,c)+ct_stack.ct_image_stack_ic(r,c,i)+ct_stack.ct_image_stack_il(r,c,i);
                else
                    if(ct_pxs(r,c)==0)
                        im_no(r,c)=i;
                        ct_pxs(r,c)=1;
                    end
                end
            end
        end
    end
    par_im_ct=par_im_ct*32./im_no;
    par_im_ct_fin=par_im_ct;
    par_im_ct=par_im_ct-mean(mean(par_im_ct));
    ct_corr=xcorr2(par_im_ct,par_im_ct);
    fit_pts_ct=ct_corr(262,188-sz_fit:188-1);
    fit_interp=polyfit(x_fit,fit_pts_ct,1);
    nf_fit=fit_interp(1)*x_interp+fit_interp(2);
    phi_nf=nf_fit(end);
    phi=ct_corr(262,188);
    phi_noise=phi-phi_nf;
    SNR_ctreill(k)=phi_nf/phi_noise;
    % imagesc(im_ct_corr');
    % figure();
    % imagesc(par_im_ct');
    abs_err(k)=mean(mean(abs(im_ct_corr-par_im_ct_fin)))/mean(mean(im_ct_corr));
    frac_dose(k)=sum(sum(im_no))/(262*188*32);
    [rs,cs,-]=find(im_ct_corr>7);
    [szs,-]=size(rs);
    sum_ill_sample=0;
    for is=1:szs
        sum_ill_sample=sum_ill_sample+im_no(rs(is),cs(is));
    end
    frac_dose_sample(k)=sum_ill_sample/szs/32;
end
%% Plotting image at threshold of 8 SEs - SNR = 5.68, frac dose = 0.79
ctim=imagesc(im_int_corr'/mean(mean(im_int_corr))*mean(mean(im_ct_corr)));
colormap gray
caxis([0 50])
axis off
pbaspect([1 188/262 1])
c = colorbar;
c.Ticks=[0 10 20 30 40 50];

%%
SNR_ct=zeros(1,32);
SNR_int=zeros(1,32);
mean_ct=zeros(1,32);
abs_err_noreill=zeros(1,32);
for i=1:32
    par_im_ct=32/i*sum(ct_stack.ct_image_stack_ic(:,:,1:i)+ct_stack.ct_image_stack_il(:,:,1:i),3);
    mean_ct(i)=mean(mean(par_im_ct));
    par_im_ct_fin=par_im_ct;
    abs_err_noreill(i)=mean(mean(abs(im_ct_corr-par_im_ct)))/mean(mean(im_ct_corr));
    par_im_int=32/i*sum(int_stack.int_image_stack_ic(:,:,1:i)+int_stack.int_image_stack_il(:,:,1:i),3);
    par_im_int=par_im_int*mean(mean(par_im_ct))/mean(mean(par_im_int));
    par_im_ct=par_im_ct-mean(mean(par_im_ct));
    par_im_int=par_im_int-mean(mean(par_im_int));
    ct_corr=xcorr2(par_im_ct,par_im_ct);
    int_corr=xcorr2(par_im_int,par_im_int);
    %SNR ct image
    fit_pts_ct=ct_corr(262,188-sz_fit:188-1);
    fit_interp=polyfit(x_fit,fit_pts_ct,1);

```

```

    nf_fit=fit_interp(1)*x_interp+fit_interp(2);
    phi_nf=nf_fit(end);
    phi=ct_corr(262,188);
    phi_noise=phi-phi_nf;
    SNR_ct(i)=phi_nf/phi_noise;
    %%SNR int image
    fit_pts_int=int_corr(262,188-sz_fit:188-1);
    fit_interp=polyfit(x_fit,fit_pts_int,1);
    nf_fit=fit_interp(1)*x_interp+fit_interp(2);
    phi_nf=nf_fit(end);
    phi=int_corr(262,188);
    phi_noise=phi-phi_nf;
    SNR_int(i)=phi_nf/phi_noise;
end
%% Plotting image at 14 frames - SNR = 5.73, frac dose = 14/32 = 0.4375
ctim=imagesc(par_im_ct_fin');
colormap gray
caxis([0 50]);
axis off
pbaspect([1 188/262 1])
c = colorbar;
c.Ticks=[0 10 20 30 40 50];

%% Plotting absolute error - Chapter 4
figure();
plot((1:32)/32,abs_err_noreill, 'o',frac_dose_sample,abs_err, 'd', 'MarkerSize',10, 'LineWidth',2, 'Color', 'black');
xlim([0 1]);
ylim([0 1]);
ax=gca;
ax.TickLength=[0.01, 0.01];
ax.LineWidth = 2;
xlabel('fractional electron dose', 'FontSize',18);
ylabel('MARE', 'FontSize',18);
set(ax, 'XTick',0:0.2:1, 'FontSize',18);
set(ax, 'YTick',0:0.2:1, 'FontSize',18);
hold on
%% Plotting SNR - chapter 4
figure();
plot((1:32)/32,SNR_ct, 'o',frac_dose_sample,SNR_ctreill, 'd', 'MarkerSize',10, 'LineWidth',2, 'Color', 'black');
xlim([0 1]);
ylim([0 12]);
ax=gca;
ax.TickLength=[0.01, 0.01];
ax.LineWidth = 2;
xlabel('fractional electron dose', 'FontSize',18);
ylabel('SNR', 'FontSize',18);
set(ax, 'XTick',0:0.2:1, 'FontSize',18);
set(ax, 'YTick',0:2:12, 'FontSize',18);
hold on

%%
% [rs , cs, -]=find(im_ct_corr>7);
% [szs, -]=size(rs);
% for i=1:szs
%     sum_

```


Appendix E

The First (and Second) Question¹

I began T.440, “Teaching and Learning: The Having of Wonderful Ideas” at the Harvard Graduate School of Education in September 2019 on the recommendation of my favorite teacher at MIT. I was interested in eventually becoming a physics teacher after completing my PhD at MIT and thought the class would be a good way to expand my skillset. I was both amused and intrigued at the class title and felt ready to jump in. Looking back, as I reflect on my development through the class, several words come to mind: complexity, autonomy, dignity, noticing, moon. The words that perhaps encompass all of the rest are ‘the first and second question’.

The idea of the first and second question was first put forth to me by Reuben Henriques, a colleague from the class, during a conversation after a fieldwork we were doing together. An important component of the class, fieldworks were sessions where we worked with one or more learners to facilitate and follow their learning on a pre-defined subject matter. I recorded the conversation in my class journal from that day (Agarwal, Journal, November 24 2019):

Reuben summed this discussion up as follows: “The first question is always what the teacher gives you initially. The second question has to be yours.”... I think

¹The title of this essay is inspired by “The First Question” by Geerat Vermeij (Privileged Hands: A Scientific Life, 1996)

what Reuben meant was that the materials we present to our learners can be thought of as the first question. Alternatively, the question “What do you notice?” can be the first question. The second question, the one that the learner can use to anchor their learning, has to come from the learner.

This theme of the first and second questions captures a lot of my thoughts during the class, and I will use it to describe the development of my ideas about teaching and learning.

The first question

What is the first question? Before I took T.440, I would have answered that the first question was a simple, stripped-down demonstration or example of the main point the teacher was trying to make in the class. Pick an activity or a reading that removes all the complexity, all the distractions, that get in the way of your students quickly seeing the ‘point’ of your class, and you’ve got a good first question. It is the starting point for the teacher, in Paulo Freire’s words, “*to ‘fill’ the students with the contents of his narration*” (Freire 2005).

Over the course of this class, each of these ideas I had about the first question was challenged. I distinctly remember the disequilibrium in my mind when I read the following extract during the second week of class (Mulvihill 2014):

The students’ willingness to speculate without inhibition is remarkable. In my experience, this happens when teachers create an environment in which learners routinely engage multiple possibilities – may postulations at once – before settling on a best solution. In my classroom I see daily that our deepest thinking is nurtured by a culture of temporary or provisional solutions that can be modified, refined or expanded through further engagement and experience over time.

Multiple possibilities? Provisional solutions? Won’t that confuse my students? Isn’t it easier to direct them towards the right answer? In the same week I read

Duckworth question the very utility of ‘right answers’ (Duckworth 2006a):

It occurred to me, then, that of all the virtues related to intellectual functioning, the most passive is the virtue of knowing the right answer. Knowing the right answer requires no decisions, carries no risks, and makes no demands. It is automatic. It is thoughtless. Moreover, and most to the point in this context, knowing the right answer is overrated. It is a virtue—there is no debate about that—but in conventional views of intelligence it tends to be given far too much weight.

Knowing the right answer is overrated?! What are we aiming for in our classrooms, then? I was concurrently doing the first fieldwork for the class, “Going to the Movies”. In this activity, you give a learner four different objects, and ask them to come up with all the different arrangements of the objects they can think of. That seemed straightforward enough. I thought I would try out this idea of not settling for right answers, even though I did not really buy it – there were right answers in math, damn it! I did the fieldwork with S. Here’s the relevant section from my fieldwork report (Agarwal, Fieldwork 1, September 8 2019):

At this point, S said “the answer is 4 factorial, isn’t it?” I was not sure how to respond – should I tell her that this was the right answer, and risk ending the activity, or should I stay vague and risk losing her interest? I replied with “Why do you think that’s the answer? How would you convince yourself?”

Good job, I told myself. I didn’t just say “Yes” to S’s question, but asked S a follow up question instead! Look at me being reflective and open to multiple possibilities. You can imagine my consternation, then, when I received the following feedback from my Teaching Fellow:

In what ways is 4 factorial the “answer” or even “the right answer” and in what ways is it not?

Well, it is the right answer! There are exactly 24 ways to arrange 4 objects, and 4 factorial equals 24. I was pretty annoyed.

Luckily, in the next week’s reading, Duckworth provided a glimpse of a resolution (Duckworth 2006b):

I think a teacher’s job is to raise questions about even such a simple right answer, to push it to its limits, to see where it holds up and where it does not hold up. One right answer unconnected to other answers, unexplored, not pushed to its limits, necessarily means a less adequate grasp of our experience. Every time we push an idea to its limits, we find out how it relates to areas that might have seemed to have nothing to do with it.

By restricting my goal in “Going to the Movies” to getting S to ‘the answer’ of 24, I had not explored what was really interesting about the whole activity – how was S thinking about the arrangements? How was S laying them out? Could S show me all the different arrangements she could think of? How did S know when there was a repeat, and how did S know when she was done? By trying to follow S’s thinking about 4 factorial more closely, I could have seen “*where it holds up and where it does not hold up*”.

So, right answers in and of themselves were too simplistic and confining. So far so good. By following my learner’s thinking closely, I could see how they were constructing an approach to the Going to the Movies activity, and that’s what was really interesting. However, they were ultimately still building towards the right set of ideas for the activity, correct? What was the point of “multiple possibilities, provisional solutions”? Here too, Duckworth came to the rescue (Duckworth 2006b):

Teachers are often, and understandably, impatient for their students to develop clear and adequate ideas. But putting ideas in relation to each other is not a simple job. It is confusing, and that confusion does take time. All of us need time for our confusion if we are to build the breadth and depth that give significance to our knowledge.

I realized that I, too, was being impatient for S to get to the ‘right answer’. I

did not want to give S time with her confusion, because I understood this confusion as my failure to explain the activity properly to S. What Duckworth was saying here was that giving students space to hold on to her confusion, shape it, and really understand it was worthwhile. S was not just arranging 4 objects. S was using her previous knowledge and experiences with arrangements, with each of the four objects, and with counting to perform this activity. Putting all those ideas on relation to each other would take time, and that was good!

So, the aim of my first question to the learner should be to try to get at their thinking, the ideas that they had as they approached the question. Allowing them time to be confused about the question and formulate their ideas was good. As a teacher, my role was to accept my students' confusions and encourage them to keep thinking about them as they related ideas they previously had with the new ideas that would emerge from my first question. For this to happen authentically, I realized, my students must feel unafraid to voice their confusions, as noted in the following journal entry (Agarwal, Journal, September 15 2019):

I really feel that fear has no place in a place of learning. As a student, I was in constant fear of being physically or emotionally punished by my teachers for stepping out of line - not knowing an answer I was supposed to, not completing homework, or saying something that a teacher didn't like. This fear prevented me from being openly curious or genuinely interested in some of my classes - I was too focused on not messing up and avoiding a beating. I would never want students to be afraid in my classroom.

But surely that first question, that first example, had to be a simplified version of what you would find in the real world? Wouldn't the complexities of the real world introduce too many complications and distractions in the minds of my learners? Duckworth had anticipated this question too (Duckworth 2006c):

Notice the difference between what usually happens in formal education – presenting the simplest, neatest explanation of “the law of moments,” “the composition

of the atmosphere,” “density,” “buoyancy,” or whatever – and my experience of being enticed with the funny, frustrating, intriguing, unpredictable complexities of the world around me. Instead of disassociating myself from my own interests in my struggle to find out what whoever was supposed to “know” might have been understood by the word “buoyancy”, my learning was based on my own connections, within the idiosyncrasies of my own system of thoughts.

As had Lisa Schneier (Schneier 1990):

We organize subject matter into a neat series of steps which assumes a profound uniformity among students. We sand away at the interesting edge of subject matter until it is so free from its natural complexities, so neat, that there is not a crevice left as an opening. All that is left is to hand it to them, scrubbed and smooth, so that they can view it as outsiders.

I was exhilarated! The complexity of the real world was a gift because it allowed my learners to bring their backgrounds and experiences into the classroom. Approaching a new subject matter was challenging, and complexity allowed learners to find a familiar point to start off. A complex first question would allow my learners multiple interesting ways to access it, and together they could construct meaning from that question that would be much more powerful and lasting than a stripped-down question with a single ‘right’ answer. It was at this stage of my thinking that I read *Inventing Density* (Duckworth 2001). Here was an example of a group of adults constructing a complex scientific idea, starting off with some common objects and a genuinely curious and observant teacher. Reading through Duckworth’s joy, excitement, consternation, and reflection as her learners developed their ideas told me how grappling with complexity, confusion, and bewilderment was a key part of discovery, and if I took that process away from my students, I was denying their humanity. I now fully believed that, in Duckworth’s words (Duckworth 2006c),

There is a parallel here between a poet and a teacher: the universe is complex; science is complex; the poet’s thoughts and feelings are complex. “Forty-two” doesn’t

do the trick. Neither does “buoyancy.” Not, in this case, does “I love you.”

I believe that first question is the first interaction with an aspect of the world that a teacher gives to their learners. It could be a poem, a short story, a stroll through a garden, a visit to a museum. It could be a chemical reaction, an optical illusion, a political cartoon, a straw in water. The first question is the “*the real stuff of the world, primary sources*” (Schneier 2001)). It creates conflict and instability. It drives the class to action to resolve that instability, to “*stand up abruptly and move toward a resource, to turn to one another to compare notes, to forgo raising a hand and blurt out an idea, to stand and stare in disbelief*” (Mulvihill 2014) In short, it drives the class to learn.

The second question

I’m standing in a classroom. I’ve just presented a piece of the world in all its wonderful complexity to my students, for their consideration. What is my aim? To put it succinctly, my aim is to get to the second question. Or rather, the second questions. The second question is a genuine, authentic wondering that my students have. It is a student’s response to the teacher’s first question. It is *not* a question that I give to my learners. It is not a problem that I find fascinating or interesting. As Ramsey puts it (Ramsey 2007),

Teaching students to solve problems that students do not experience as problematic does not advance an understanding of the problems.

Unless my students see the problem as their problem, they won’t be motivated to address it. They must come up with a problem that is interesting to them. I cannot give them a problem and say “Wouldn’t it be neat if you solved it?” Maybe they’ll learn to solve it. Maybe they will even get very good at solving it. But that problem will exist in a vacuum, with no connections to their prior experiences. It will be locked away in an isolated room outside the teeming garden of their own ideas. My

goal as a teacher is to get them to “stand and stare in disbelief”, to “experience [the problem] as problematic”. As noted by Duckworth (Duckworth 2006d),

Nothing happens until the interest has been touched. The reality of the subject matter of the world, the reality of the learners’ minds.....If the integrity of each is preserved, they cannot but meet.

There are several aspects to this process of reaching the second question. One of the most important is dignity. Students must feel that their ideas are welcome and that they can use their ideas to approach “the real stuff of the world”. If the class environment implicitly or explicitly suggests a hierarchy of ideas, there is a barrier to students asking authentic questions about the subject matter. Such hierarchies can exist because of the language used in class, the people called upon to share ideas in class, and the sources, readings and assignments used in class. For example, the school I attended from the age of 4 to 12 enforced a strict “English only” policy in all classes (except classes on the Hindi language, which was the language I spoke at home). Consequently (Agarwal, Journal, November 30 2019),

I thought of Hindi as the language I spoke ‘at home’ and English as the language ‘of school, of academia.’ The scientific discourse was in English, and perhaps my teachers’ intention in encouraging us to speak in English was to make it easier for us to access it. However, in punishing the use of Hindi, the message I received was that my home discourse was to be kept out of school. I loved thinking about science, and my native language was not accorded a place of respect in that discourse. Consequently, my own respect for it diminished... Perhaps because of this negation of my home discourse I did not connect the scientific discourse with the things I saw around me at home. I was never curious about the trees that grew in my home, about the birds that nested there, about the flowers they produced, even though biology was my favorite subject.

Looking back, I wonder how many amazing ideas were kept out of the classroom because the students who had them could only express them in Hindi (a lan-

guage that most of our teachers also spoke). The class environment took away their dignity and prevented them from participating. Similarly, if the points-of-view of some students, some sources, or of the teacher, are valued more than other students, the deep, participatory learning that can occur in the classroom is stifled. Before we expect students to give us their authentic selves, we must provide them the dignity and legitimacy to do so. As Delpit writes (Delpit 1993),

First, teachers must acknowledge and validate students' home language without using it to limit students' potential. Students' home Discourses are vital to their perception of self and the sense of community connectedness.

Further, if students experience a classroom without hierarchies, they become more likely to notice and question hierarchies outside the classroom. Breaking down those hierarchies then becomes part of their problem.

Another aspect of the process of finding the second question is ownership. As Duckworth says (Duckworth 2006c),

It is, of course, exhilarating to find that your own ideas can lead you somewhere. Few feelings are likely to be more effective in getting you to keep on thinking about things on your own.

Too often, particularly in science classes, ideas are presented in their final, reduced form. Some person three hundred years ago took a piece of the world and reduced it to a set of neat ideas and equations that describe its behavior. We present the final product but not the process; the conclusion but not the story. Reflecting on discussions of this reductionism in the writings of Duckworth and Piaget, I wrote (Agarwal, Journal, October 28 2019):

It occurs to me that some of ED [Eleanor Duckworth] and Piaget's ideas are a call against reductionism. Physics is taught in the reductionist way - you learn about atoms, then molecules, then compounds, then solids. The physicist's argument would be to teach the basic components to the child which they will then put together.

However, this reductionism was made by someone who had studied and understood the larger system and convinced themselves through observation that the reduced components could be studied individually. The child has not convinced themselves of this yet - when they look at a rainbow, they don't see it as sunlight interacting with drops of water and teaching them individually about light and water and the interaction between them will not be sufficient for them to understand rainbows. I think that studying the reductionist way requires experience with physical objects and systems, which children have not developed yet.

ED and Piaget's alternative is to let kids see the whole system with all its complexity (hence the analogy to biological systems). They can then start noticing things in this complexity and may reduce it (or narrow it) to one question to think and experiment about.

As a teacher, I have to show my students that their own ideas are the focus of the classroom. My classes have to be driven by and be a response to their ideas. This does not mean that we re-invent the wheel every time, or that we ignore the vast history of similar ideas that others have come up with and document. I use these ideas and these writings when they will supplement my students' thinking. However, the focus remains my students' thinking, and I arrange external materials, experiments and writings to fit into the story that they are creating. One final aspect that I realized was equally important is trust. I summed up my thoughts on trust in the following journal entry (Agarwal, Journal, November 2 2019):

Trust has been a theme for me this week. During the first fieldwork, I was struck at how R was captured not by the 'fundamental' process I placed before him (the bending of light by water), but by the complexity of the shape of the bowl containing water and its effect on what I was seeing. I learnt that I should trust the complexity of my material to shine through and capture my learner's attention. When I was stating this in section on Friday, I said "I should trust the complexity of the material." Hilary added "and trust the learner". This was an aspect I had not considered

previously, but which I completely agree with. A passage from Chapter 2 of *Pedagogy of the Oppressed* (page 75) reveals the same idea:

His [The teacher's] efforts must be imbued with a profound trust in people and their creative power.

Trusting people and their creative power, and the complexity of the material to invite them to exercise their creative power. I saw this in action with R and his various experiments to understand the effect of the curvature of the bowl on the bending of the straw. Another aspect of this is trusting myself to be a valuable co-explorer with my student as they embark on their personal journeys. At times during the fieldwork I felt uncertain of where it was going, what I was going to do if we ended up in unfamiliar territory. Although I haven't shaken off this uncertainty and fear, I have to trust that I can be a valuable co-explorer, and together we can create a deeper understanding of light, glass and water for ourselves.

Trust your material, your learner, and yourself!

I want to present two examples of activities from class that let me observe these ideas in action: our semester-long observation of the moon and the process of designing and performing the final fieldwork of the class.

The moon

In the first meeting of the class, the instructors asked us to keep a diary with observations of the moon. Importantly, they did not specify what to look out for – where in the sky it was, how high up it was, how much of it was lit, or anything else. They gave us the primary source, the first question, and left it to us to notice something about it, to form our second questions. My first reaction to this is recorded in my class notes from that day (Agarwal, class notes September 3 2019):

Not sure what new things, if any, I'll be seeing. Maybe correlate with tides.

I did not know what the teaching staff expected me to see. However, over the next few weeks, I made observations of the moon and recorded them in my journal. I wasn't very regular but I wanted to give it a try. A journal entry from mid-September reads (Agarwal, Journal, September 14 2019):

When I started moon observations for the class, I was a little skeptical of what I would learn. The moon was always there, and I thought I was familiar with its basic properties (waxing and waning, moving across the sky). However, observing the moon has already brought up a host of surprises and questions. Here are some:

- 1. What does the exact shape of the moon (the size and orientation of the shadow on it) depend on? Why does this orientation seem to change over a few days?*
- 2. Why does the moon appear to shine so bright on some nights, and so dim on others?*
- 3. Why do I sometimes see a band of colors around the moon (a 'moonbow')?*

I look forward to making more observations and trying to resolve these questions!

I was interested but I wasn't yet hooked. I would report my observations in class, but I hadn't really bought into the whole exercise. There were questions forming in my mind, but I had not hit upon the question yet, the second question. The questions in my mind were questions that I thought the teaching staff wanted me to have. I found my question quite fortuitously. I was on a bus my way back to Boston from a conference in eastern Massachusetts on October 4. I saw the moon out the window and drew it in my journal. Later that same day, I went out to dinner and saw the moon again. It was different! Here's the relevant page from my moon diary (Agarwal, Moon Diary, October 4 2019):



The moon changed over the course of a couple hours! I was astonished. I had not expected this at all. I confirmed my observations over the course of the next few days, and each time the moon changed its orientation in a similar way. Why was it doing that? This was my question, and it drove me to make further and more detailed moon observations, sometimes several times a day. Looking back, I realize how crucial it was that this was my question. None of the teaching staff had suggested observing the moon many times every day. As we discussed our moon observations in class, I realized that others had the same question too. I was hungry for their observations and ideas. We would pick up Styrofoam balls provided by our teaching staff and re-enact the moon's journey around the earth and the sun, hoping for insights into changes in its appearance. The teaching staff, for their part, gave our ideas the chance to be expressed and considered seriously. They would ask people to come to the center of the class and explain an observation or hypothesis and then ask others for their thoughts. Each person, each idea was given respect and dignity. I realized that we were building an understanding of the habits of the moon as a group. Although I still have not figured out why the moon's orientation changes over the course of a few hours, I am going to continue making observations and hypotheses.

Final fieldwork

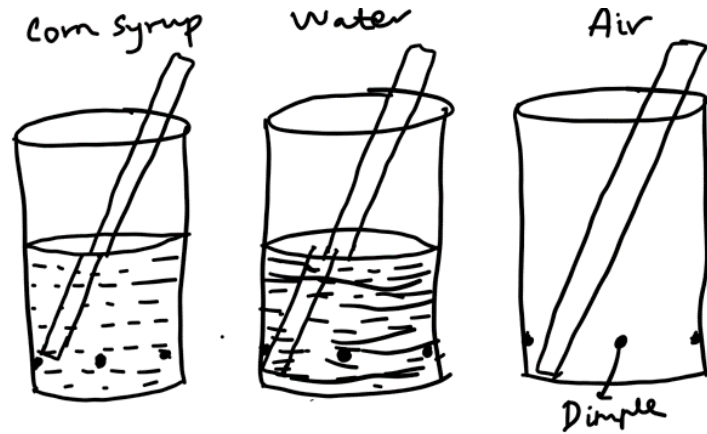
The denouement of the course was the final fieldwork. We were tasked with engaging a learner over the course of three sessions in an activity of our choice. Here was a chance to test the ideas of teaching that we had been discussing in class. I chose the bending of light as the focus of my fieldwork. This was a subject I had often encountered in the course of my academic and research work, but I had never had the chance to teach it before. Given its ubiquitous nature and the potential for surprise and awe, I thought it would be a good subject to engage my learners' attention for 3 sessions. Another aim I had through the sessions was for my learner to experience what it was like to be a physicist – to hypothesize, experiment and modify the hypothesis continually.

Beyond the subject, though, I was very unsure about the fieldwork. How should I present my first question? At what level of complexity should my learner encounter the bending of light? I considered using a very 'direct' demonstration of the effect by placing a glass slab on a piece of text, which would appear raised. In the same journal entry where I wrote about reductionism, I wrote about my dilemma in my journal (Agarwal, Journal, October 28 2019):

At what level of complexity should I introduce the idea of light bending? In my own education I was first introduced to the idea in theory, then shown some demos with glass slabs. Should I present a 'simple' (reductionist) demo that shows the basic idea, but strips away the context in which the learner would find it in the world (you don't usually see glass slabs lying about with pieces of text conveniently below them), or should I present it in a way that the learner may have already encountered before (straw in a glass), with the associated risk of them missing it?

I decided to present my learner (R) with a display of three glasses with straws in them. One glass was empty, one had water and one corn syrup. The straw at the surface of the liquids appeared broken, which was another manifestation of the bending of light. The following drawing from my fieldwork report illustrates the setup

(Agarwal, Final Fieldwork session 1, November 3 2019):



What happened over the course of the 3 fieldwork sessions was transformational for me. Not only did R notice the breaking of the straw, but he devised, tested and verified a hypothesis he had about the degree of bending in various containers. My learner's interest was initially sparked by something I had not even considered – the curvature of the glasses. It turned out that the curved glasses made the straw appear broken in very interesting ways, and it was this complexity that led my learner to their second question. I wrote about this in a journal entry (Agarwal, Journal, November 22 2019):

One of the most important lessons I will take away from my fieldwork with R is the importance of complexity in subject material. I had been agonizing over whether I should use square base containers or round glasses for my first session. I was leaning towards square base containers because I felt that the round one had too many effects intertwined. However, R's interest was initially captured by the curvature of the glass. At the end of the first session, he described how he had been going through the motions before the changing offset of the straw in the curved bowl surprised and intrigued him. If I had chosen a square base container, maybe his interest would not have been captured the same way, or maybe not at all! At the end of the second session, R had separated the effects he was seeing and decided that he wanted to use a square base container to investigate further. Him reaching this conclusion was much

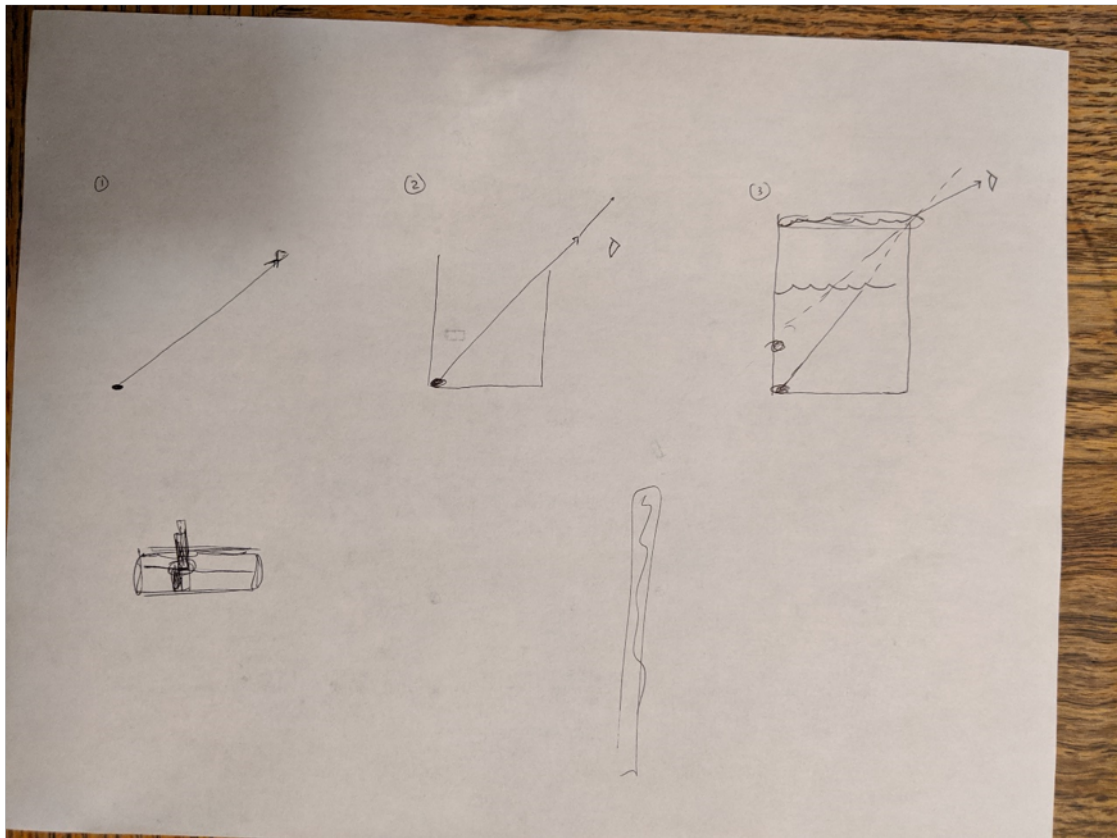
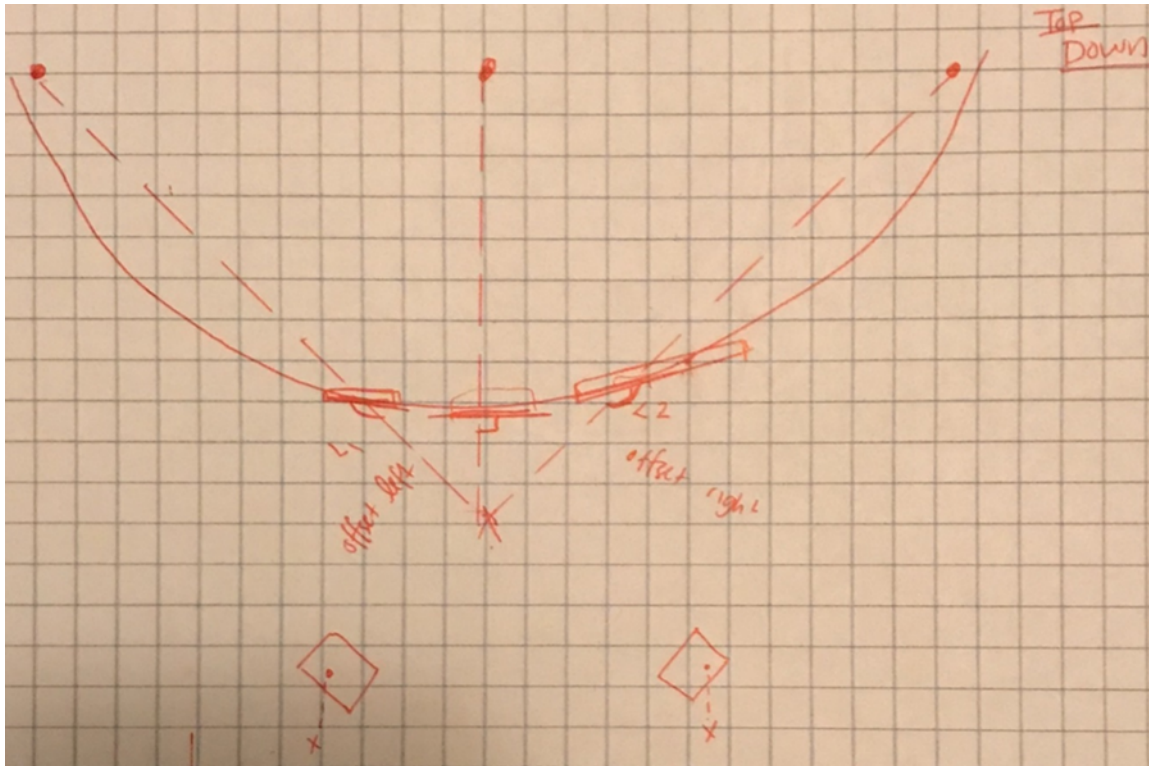
more powerful than me introducing it in the first session. The complexity of the curved glass gave him a point of entry into the phenomena I wanted to engage him in!

The complexities of the setup gave R a way of entering the activity. They gave him something unexpected, and that unexpectedness motivated him to formulate his question that he spent the rest of our time together answering. By the end, the understanding he had developed of the bending of light was his own. Some of his diagrams (attached at the end) were very similar to what one might find in a physics textbook in a chapter on the refraction of light, and he arrived at them all by himself! All because he owned the question and everything he did with it.

Conclusion

I have never experienced such anticipation and exhilaration as I did during T.440. Looking back at all my experiences in the class, all the discussions, readings and journaling seems like a giant first question. Here was an altogether different approach to teaching than what I had experienced in school and college. My second question in response to this was – could I do it? Could I teach this way? The final fieldwork was my first attempt, and I will continue to hypothesize, test and modify.

When I began T.440 in September 2019, I knew I wanted to be a teacher. I had known since I was in middle school and would picture myself standing in front of a classroom, explaining the concept I was studying to my imaginary students. In the course of doing the readings, fieldworks, and journals, I realized just how much I wanted to be a physics teacher. There is nothing else I would rather be.



References

(Freire 2005) Freire, P. Chapter 2, *Pedagogy of the Oppressed* (30th Anniversary Edition), The Continuum International Publishing Group Inc, 2005

(Mulvihill 2014) Mulvihill, N., “How Do You Say Twos in Spanish, If Two is Dos? Language as Means and Object in a Bilingual Classroom”, *Harvard Educational Review* 84, 3, ProQuest pg. 385, Fall 2014

(Duckworth 2006a) Duckworth, E. “The Virtues of Not Knowing”, *The Having of Wonderful Ideas and Other Essays on Teaching and Learning*, 3rd ed., Teachers College Press, 2006

(Duckworth 2006b) Duckworth, E., “Learning with Breadth and Depth”, *The Having of Wonderful Ideas and Other Essays on Teaching and Learning*, 3rd ed., Teachers College Press, 2006

(Duckworth 2006c) Duckworth, E., “Twenty-Four, Forty-Two, and I Love You: Keeping It Complex”, *The Having of Wonderful Ideas and Other Essays on Teaching and Learning*, 3rd ed., Teachers College Press, 2006

(Schneier 1990) Schneier, L. “Why not just say it?” Unpublished manuscript, Harvard Graduate School of Education, 1990

(Duckworth 2001) Duckworth, E., “Inventing Density”, *Tell Me More: Listening to Learners Explain* Teachers College Press, 2001

(Schneier 2001) Schneier, L. “A Schoolteacher’s View”, *Tell Me More: Listening to Learners Explain* Teachers College Press, 2001

(Ramsey 2007) Ramsey, L., *Understanding the Problem of Un-Prescribing the Curriculum*, *The New Educator*, 3:4, 283-302, 2007

(Duckworth 2006d) Duckworth, E., “A Reality to Which Each Belongs”, *Holding Values: What We Mean by Progressive Education*, Eds. Engel, B. S., and Martin,

A. C., Heinemann, 2006

(Delpit 1993) Delpit, L. D., "The Politics of Teaching Literate Discourse",
Freedom's Plow: Teaching in the Multicultural Classroom, Eds. Perry, T. and Fraser,
J. W., Routledge. 1993

Bibliography

- [1] David B. Williams and C. Barry Carter. *Transmission Electron Microscopy- A Textbook for Materials Science*. Springer US, 2016.
- [2] Pieter Kruit, R. G. Hobbs, C. S. Kim, Y. Yang, V. R. Manfrinato, J. Hammer, Sebastian Thomas, P. Weber, B. Klopfer, C. Kohstall, T. Juffmann, M. A. Kasevich, P. Hommelhoff, and K. K. Berggren. Designs for a quantum electron microscope. *Ultramicroscopy*, 164:31–45, 2016.
- [3] Thomas Juffmann, Stewart A. Koppell, Brannon B. Klopfer, Colin Ophus, Robert M. Glaeser, and Mark A. Kasevich. Multi-pass transmission electron microscopy. *Scientific Reports*, 7(1):1–7, 2017.
- [4] Fehmi S. Yasin, Tyler R. Harvey, Jordan J. Chess, Jordan S. Pierce, Colin Ophus, Peter Ercius, and Benjamin J. McMorran. Probing Light Atoms at Subnanometer Resolution: Realization of Scanning Transmission Electron Microscope Holography. *Nano Letters*, 18(11):7118–7123, 2018.
- [5] P. E. Batson, N. Dellby, and Ondrej L. Krivanek. Sub-angstrom resolution using aberration corrected electron optics. *Nature*, 418:617–620, 2002.
- [6] G. Y. Fan and M. H. Ellisman. Digital imaging in transmission electron microscopy. *Journal of Microscopy*, 200(1):1–13, 2000.
- [7] Xueming Li, Paul Mooney, Shawn Zheng, Christopher R. Booth, Michael B. Braunfeld, Sander Gubbens, David A. Agard, and Yifan Cheng. Electron counting and beam-induced motion correction enable near-atomic-resolution single-particle cryo-EM. *Nature Methods*, 10(6):584–590, 2013.
- [8] O. Scherzer. The theoretical resolution limit of the electron microscope. *Journal of Applied Physics*, 20(1):20–29, 1949.
- [9] Dirk van Dyck. High-resolution electron microscopy. *Advances in Imaging and Electron Physics*, 123(C):105–171, 2002.
- [10] Radostin Danev and Kuniaki Nagayama. Transmission electron microscopy with Zernike phase plate. *Ultramicroscopy*, 88(4):243–252, 2001.

- [11] Radostin Danev, Bart Buijsse, Maryam Khoshouei, Jürgen M. Plitzko, and Wolfgang Baumeister. Volta potential phase plate for in-focus phase contrast transmission electron microscopy. *Proceedings of the National Academy of Sciences of the United States of America*, 111(44):15635–15640, 2014.
- [12] Kazuyoshi Murata, Xiangang Liu, Radostin Danev, Joanita Jakana, Michael F. Schmid, Jonathan King, Kuniaki Nagayama, and Wah Chiu. Zernike phase contrast cryo-electron microscopy and tomography for structure determination at nanometer and subnanometer resolutions. *Structure*, 18(8):903–912, 2010.
- [13] Maryam Khoshouei, Mazdak Radjainia, Amy J. Phillips, Juliet A. Gerrard, Alok K. Mitra, Jürgen M. Plitzko, Wolfgang Baumeister, and Radostin Danev. Volta phase plate cryo-EM of the small protein complex Prx3. *Nature Communications*, 7:10534, 2016.
- [14] Maryam Khoshouei, Mazdak Radjainia, Wolfgang Baumeister, and Radostin Danev. Cryo-EM structure of haemoglobin at 3.2 Å determined with the Volta phase plate. *Nature Communications*, 8(1):1–6, 2017.
- [15] Yi Lynn Liang, Maryam Khoshouei, Mazdak Radjainia, Yan Zhang, Alisa Glukhova, Jeffrey Tarrasch, David M. Thal, Sebastian G.B. Furness, George Christopoulos, Thomas Coudrat, Radostin Danev, Wolfgang Baumeister, Laurence J. Miller, Arthur Christopoulos, Brian K. Kobilka, Denise Wootten, Georgios Skiniotis, and Patrick M. Sexton. Phase-plate cryo-EM structure of a class B GPCR-G-protein complex. *Nature*, 546(7656):118–123, 2017.
- [16] Yi Lynn Liang, Maryam Khoshouei, Alisa Glukhova, Sebastian G.B. Furness, Peishen Zhao, Lachlan Clydesdale, Cassandra Koole, Tin T. Truong, David M. Thal, Saifei Lei, Mazdak Radjainia, Radostin Danev, Wolfgang Baumeister, Ming Wei Wang, Laurence J. Miller, Arthur Christopoulos, Patrick M. Sexton, and Denise Wootten. Phase-plate cryo-EM structure of a biased agonistbound human GLP-1 receptor-Gs complex. *Nature*, 555(7694):121–125, 2018.
- [17] Yi Jiang, Zhen Chen, Yimo Han, Pratiti Deb, Hui Gao, Saien Xie, Prafull Purohit, Mark W. Tate, Jiwoong Park, Sol M. Gruner, Veit Elser, and David A. Muller. Electron ptychography of 2D materials to deep sub-ångström resolution. *Nature*, 559:343–349, 2018.
- [18] Ludwig Reimer. Emission of Backscattered and Secondary Electrons. In *Scanning Electron Microscopy*, pages 135–169. Springer-Verlag Berlin Heidelberg New York, 2nd edition, 1998.
- [19] Ludwig Reimer. Introduction. In *Scanning Electron Microscopy*, pages 1–12. Springer-Verlag Berlin Heidelberg New York, 2nd edition, 1998.
- [20] H. Seiler. Secondary electron emission in the scanning electron microscope. *Journal of Applied Physics*, 54(11):R1, 1983.

- [21] Luděk Frank. Noise in secondary electron emission : the low yield case. *Journal of Electron Microscopy*, 54(4):361–365, 2005.
- [22] Brendan J. Griffin. A comparison of conventional Everhart-Thornley style and in-lens secondary electron detectors-a further variable in scanning electron microscopy. *Scanning*, 33(3):162–173, 2011.
- [23] Gary H. Bernstein, Andrew D. Carter, and David C. Joy. Do SEII electrons really degrade SEM image quality? *Scanning*, 35:1–6, 2013.
- [24] Ludwig Reimer. Electron Detectors and Spectrometers. In *Scanning Electron Microscopy*, pages 171–205. Springer-Verlag Berlin Heidelberg New York, 2nd edition, 1998.
- [25] T. E. Everhart and R. F. M. Thornley. Wide-band detector for micro-microampere low-energy electron currents. *Journal of Scientific Instruments*, 37(7):246–248, 1960.
- [26] D C Joy, C S Joy, and R D Bunn. Measuring the performance of scanning electron microscope detectors. *Scanning*, 18(8):533–8, 1996.
- [27] David C. Joy. Noise and Its Effects on the Low-Voltage SEM. In *Biological Low-Voltage Scanning Electron Microscopy*, pages 129–144. Springer New York, New York, NY, 2007.
- [28] C. W. Oatley. The detective quantum efficiency of the scintillator/ photomultiplier in the scanning electron microscope. *Journal of Microscopy*, 139(2):153–166, 1985.
- [29] L. Novak and I. Müllerova. Single electron response of the scintillator-light guide-photomultiplier detector. *Journal of Microscopy*, 233(1):76–83, 2009.
- [30] Ray F. Egerton. Choice of operating voltage for a transmission electron microscope. *Ultramicroscopy*, 145:85–93, 2014.
- [31] R. F. Egerton. Radiation damage to organic and inorganic specimens in the TEM. *Micron*, 119:72–87, 2019.
- [32] Manoj Misra and Ray F. Egerton. Assessment of Electron Irradiation Damage To Biomolecules By. *Ultramicroscopy*, 15:337–343, 1984.
- [33] Robert M. Glaeser. Limitations to significant information in biological electron microscopy as a result of radiation damage. *Journal of Ultrastructure Research*, 36(3-4):466–482, 1971.
- [34] R. F. Egerton, P. Li, and M. Malac. Radiation damage in the TEM and SEM. *Micron*, 35(6):399–409, 2004.

- [35] Zino J.W.A. Leijten, Arthur D.A. Keizer, Gijsbertus De With, and Heiner Friedrich. Quantitative Analysis of Electron Beam Damage in Organic Thin Films. *Journal of Physical Chemistry C*, 121(19):10552–10561, 2017.
- [36] Stefan W Hell and Jan Wichmann. Breaking the diffraction resolution limit by stimulated emission : stimulated-emission-depletion fluorescence microscopy. *Optics Letters*, 19(11):780–782, 1994.
- [37] Samuel T Hess, Thanu P.K. Girirajan, and Michael D Mason. Ultra-High Resolution Imaging by Fluorescence Photoactivation Localization Microscopy. *Biophysical Journal*, 91(11):4258–4272, 2006.
- [38] Robert M Glaeser. How good can cryo-EM become? *Nat Methods*, 13(1):28–32, 2016.
- [39] Otilie von Loeffelholz, S. Kundhavai Natchiar, Nadia Djabeur, Alexander G. Myasnikov, Hanna Kratzat, Jean François Ménétret, Isabelle Hazemann, and Bruno P. Klaholz. Focused classification and refinement in high-resolution cryo-EM structural analysis of ribosome complexes. *Current Opinion in Structural Biology*, 46:140–148, 2017.
- [40] A. Stevens, L. Luzi, H. Yang, L. Kovarik, B. L. Mehdi, A. Liyu, M. E. Gehm, and N. D. Browning. A sub-sampled approach to extremely low-dose STEM. *Applied Physics Letters*, 112:043104, 2018.
- [41] Tim Dahmen, Michael Engstler, Christoph Pauly, Patrick Trampert, Niels de Jonge, Frank Mücklich, and Philipp Slusallek. Feature Adaptive Sampling for Scanning Electron Microscopy. *Scientific Reports*, 6(1):25350, 2016.
- [42] Avshalom C. Elitzur and Lev Vaidman. Quantum mechanical interaction-free measurements. *Foundations of Physics*, 23(7):987–997, 1993.
- [43] Andrew G. White, Jay R. Mitchell, Olaf Nairz, and Paul G. Kwiat. “Interaction-free” imaging. *Physical Review A*, 58(1):605–613, 1998.
- [44] Paul Kwiat, Harald Weinfurter, Thomas Herzog, Anton Zeilinger, and Mark A. Kasevich. Interaction-free measurement. *Physical Review Letters*, 74(24):4763–4766, 1995.
- [45] William P. Putnam and Mehmet Fatih Yanik. Noninvasive electron microscopy with interaction-free quantum measurements. *Physical Review A*, 80:040902(R), 2009.
- [46] Marco Turchetti, Chung Soo Kim, Richard Hobbs, Yujia Yang, Pieter Kruit, and Karl K. Berggren. Design and simulation of a linear electron cavity for quantum electron microscopy. *Ultramicroscopy*, 199:50–61, 2019.
- [47] Maurice Krielaart and Pieter Kruit. Potentially Programmable Virtual Phase Plate for Electron Beams. *Microscopy and Microanalysis*, 25(S2):92–93, 2019.

- [48] Navid Abedzadeh. Diffractive Electron Mirror for Use in Quantum Electron Microscopy. Master's thesis, Massachusetts Institute of Technology, 2018.
- [49] Yujia Yang, Chung Soo Kim, Richard G. Hobbs, Pieter Kruit, and Karl K. Berggren. Efficient two-port electron beam splitter via a quantum interaction-free measurement. *Physical Review A*, 98(4):043621, 2018.
- [50] Graeme Mitchison and Serge Massar. Absorption-free discrimination between semitransparent objects. *Physical Review A*, 63:032105, 2001.
- [51] Graeme Mitchison, Serge Massar, and Stefano Pironio. Minimum number of photons needed to distinguish two transparencies. *Physical Review A*, 65:022110, 2002.
- [52] Serge Massar, Graeme Mitchison, and Stefano Pironio. Minimal absorption measurements. *Physical Review A*, 64:062303, 2001.
- [53] Günther Krenn, Johann Summhammer, and Karl Svozil. Interferometric information gain versus interaction-free measurement. *Physical Review A*, 61:052102, 2000.
- [54] Sebastian Thomas, Christoph Kohstall, Pieter Kruit, and Peter Hommelhoff. Semitransparency in interaction-free measurements. *Physical Review A*, 90:053840, 2014.
- [55] P. Facchi, Z. Hradil, G. Krenn, S. Pascazio, and J. Rehacek. Quantum Zeno tomography. *Physical Review A*, 66:012110, 2002.
- [56] Adrian Kent and David Wallace. Quantum Interrogation and the Safer X-ray. *arXiv:quant-ph/0102118v1*, 2001.
- [57] Ju-Seog Jang. Optical interaction-free measurement of semitransparent objects. *Physical Review A*, 59(3):2322–2329, 1999.
- [58] T Rudolph. Better Schemes for Quantum Interrogation in Lossy Experiments. *Physical Review Letters*, 85(14):2925–2928, 2000.
- [59] Hiroshi Okamoto, Tatiana Latychevskaia, and Hans Werner Fink. A quantum mechanical scheme to reduce radiation damage in electron microscopy. *Applied Physics Letters*, 88:164103, 2006.
- [60] Hiroshi Okamoto. Noise suppression by active optics in low-dose electron microscopy. *Applied Physics Letters*, 92:063901, 2008.
- [61] Hiroshi Okamoto. Adaptive quantum measurement for low-dose electron microscopy. *Physical Review A*, 81:043807, 2010.
- [62] Akshay Agarwal, Chung Soo Kim, Richard Hobbs, Dirk Van Dyck, and Karl K. Berggren. A nanofabricated, monolithic, path-separated electron interferometer. *Scientific Reports*, 7:1677, 2017.

- [63] Akshay Agarwal. A Nanofabricated Amplitude-Division Electron Interferometer in a Transmission Electron Microscope. Master’s thesis, Massachusetts Institute of Technology, 2016.
- [64] Amir H. Tavabi, Martial Duchamp, Vincenzo Grillo, Rafal E. Dunin-Borkowski, and Giulio Pozzi. New experiments with a double crystal electron interferometer. *The European Physical Journal Applied Physics*, 78(1):10701, 2017.
- [65] Fehmi S Yasin, Tyler R Harvey, Jordan J Chess, Jordan S Pierce, and Benjamin J McMorran. Path-separated electron interferometry in a scanning transmission electron microscope. *Journal of Physics D*, 51:205104, 2018.
- [66] Fehmi S. Yasin, Ken Harada, Daisuke Shindo, Hiroyuki Shinada, Benjamin J. McMorran, and Toshiaki Tanigaki. A tunable path-separated electron interferometer with an amplitude-dividing grating beamsplitter. *Applied Physics Letters*, 113(23):233102, 2018.
- [67] Tyler R. Harvey, Fehmi S. Yasin, Jordan J. Chess, Jordan S. Pierce, Roberto M.S. Dos Reis, Vasfi Burak Özdöl, Peter Ercius, Jim Ciston, Wenchun Feng, Nicholas A. Kotov, Benjamin J. McMorran, and Colin Ophus. Interpretable and Efficient Interferometric Contrast in Scanning Transmission Electron Microscopy with a Diffraction-Grating Beam Splitter. *Physical Review Applied*, 10:061001, 2018.
- [68] G. Gronniger, B. Berwick, and H. Batelaan. A three-grating electron interferometer. *New Journal of Physics*, 8:224, 2006.
- [69] Amy Turner, Fehmi Yasin, Cameron Johnson, and Benjamin McMorran. Single Electron Interferometry: A Step Toward Quantum Electron Microscopy. *Microscopy and Microanalysis*, 25(S2):1712–1713, 2019.
- [70] Thomas Juffmann, Brannon B. Klopfer, Timmo L.I. Frankort, Philipp Haslinger, and Mark A. Kasevich. Multi-pass microscopy. *Nature Communications*, 7:1–5, 2016.
- [71] Stewart A. Koppell, Marian Mankos, Adam J. Bowman, Yonatan Israel, Thomas Juffmann, Brannon B. Klopfer, and Mark A. Kasevich. Design for a 10 keV multi-pass transmission electron microscope. *Ultramicroscopy*, 207:112834, 2019.
- [72] Colin Ophus, Thomas Juffmann, Stewart A Koppell, Brannon B Klopfer, Robert Glaeser, and Mark A Kasevich. Reducing Electron Beam Damage with Multipass Transmission Electron Microscopy. *Microscopy and Microanalysis*, 23(S1):1794–1795, 2017.
- [73] J. Verbeeck, H. Tian, and P. Schattschneider. Production and application of electron vortex beams. *Nature*, 467(7313):301–304, 2010.

- [74] Benjamin J. McMorran, Amit Agrawal, Ian M. Anderson, Andrew A. Herzing, Henri J. Lezec, Jabez J. McClelland, and John Unguris. Electron vortex beams with high quanta of orbital angular momentum. *Science*, 331(6014):192–195, 2011.
- [75] Giulio Guzzinati, Armand Béch e, Hugo Lourenço-Martins, J er ome Martin, Mathieu Kociak, and Jo Verbeeck. Probing the symmetry of the potential of localized surface plasmon resonances with phase-shaped electron beams. *Nature Communications*, 8:14999, 2017.
- [76] Jo Verbeeck, Armand B ech e, Knut M uller-Caspary, Giulio Guzzinati, Minh Anh Luong, and Martien Den Hertog. Demonstration of a 2x2 programmable phase plate for electrons. *Ultramicroscopy*, 190:58–65, 2018.
- [77] Colin Ophus, Jim Ciston, Jordan Pierce, Tyler R. Harvey, Jordan Chess, Benjamin J. McMorran, Cory Czarnik, Harald H. Rose, and Peter Ercius. Efficient linear phase contrast in scanning transmission electron microscopy with matched illumination and detector interferometry. *Nature Communications*, 7:10719, 2016.
- [78] James P. Buban, Quentin Ramasse, Bryant Gipson, Nigel D. Browning, and Henning Stahlberg. High-resolution low-dose scanning transmission electron microscopy. *Journal of Electron Microscopy*, 59(2):103–112, 2010.
- [79] L. Kovarik, A. Stevens, A. Liyu, and N. D. Browning. Implementing an accurate and rapid sparse sampling approach for low-dose atomic resolution STEM imaging. *Applied Physics Letters*, 109:164102, 2016.
- [80] Patrick Trampert, Faysal Bourghorbel, Pavel Potocek, Maurice Peemen, Christian Schlinkmann, Tim Dahmen, and Philipp Slusallek. How should a fixed budget of dwell time be spent in scanning electron microscopy to optimize image quality? *Ultramicroscopy*, 191:11–17, 2018.
- [81] Mark W. Tate, Prafull Purohit, Darol Chamberlain, Kayla X. Nguyen, Robert Hovden, Celesta S. Chang, Pratiti Deb, Emrah Turgut, John T. Heron, Darrell G. Schlom, Daniel C. Ralph, Gregory D. Fuchs, Katherine S. Shanks, Hugh T. Philipp, David A. Muller, and Sol M. Gruner. High Dynamic Range Pixel Array Detector for Scanning Transmission Electron Microscopy. *Microscopy and Microanalysis*, 22(1):237–249, 2016.
- [82] Ryo Ishikawa, Andrew R. Lupini, Scott D. Findlay, and Stephen J. Pennycook. Quantitative Annular Dark Field Electron Microscopy Using Single Electron Signals. *Microscopy and Microanalysis*, 20(01):99–110, 2014.
- [83] Xiahan Sang and James M Lebeau. Characterizing the response of a scintillator-based detector to single electrons. *Ultramicroscopy*, 161:3–9, 2016.

- [84] Andreas Mittelberger, Christian Kramberger, and Jannik C. Meyer. Software electron counting for low-dose scanning transmission electron microscopy. *Ultramicroscopy*, 188:1–7, 2018.
- [85] Bernhard Kurrelmeyer and Lucy J Hayner. Shot Effect of Secondary Electrons from Nickel and Beryllium. *Physical Review*, 52(1937):952–958, 1937.
- [86] T. E. Everhart, O. O. Wells, and C. W. Oatley. Factors affecting contrast and resolution in the scanning electron microscope. *Journal of Electronics and Control*, 7(2):97–111, 1959.
- [87] C. W. Oatley. Detectors for the scanning electron microscope. *Journal of Physics E: Scientific Instruments*, 14:971–976, 1981.
- [88] W. Baumann, A. Niemietz, L. Reimer, and B. Volbert. Noise Measurements of Different SEM Detectors. *Electron Microscopy 1980*, 3:174–175, 1980.
- [89] W. Baumann and L. Reimer. Comparison of the Noise of Different Electron Detection Systems Using a Scintillator-Photomultiplier Combination. *Scanning*, 4:141–151, 1981.
- [90] Makoto Sakakibara, Makoto Suzuki, Kenji Tanimoto, Yasunari Sohda, Daisuke Bizen, and Koji Nakamae. Impact of secondary electron emission noise in SEM. *Microscopy*, 68(4):279–288, 2019.
- [91] J. B. Pawley. Performance of SEM Scintillation Materials. In *Scanning Electron Microscopy 1974 (Part 1) - Proceedings of the Seventh Annual Scanning Electron Microscopy Symposium, IIT Research Institute, Chicago, Illinois 60616, USA*, pages 27–34, 1974.
- [92] N. R. Comins, M. M. E. Hengstberger, and J. T. Thirlwall. Preparation and evaluation of P-47 scintillators for a scanning electron microscope. *Journal of Physics E: Scientific Instruments*, 11(10):1041–1047, 1978.
- [93] S. Yamada, T. Ito, K. Gouhara, and Y. Uchikawa. Electron Counting for Secondary Electron Detection in SEM. *Scanning*, 12(5):I–28 – I–29, 1990.
- [94] S. Yamada, T. Ito, K. Gouhara, and Y. Uchikawa. Secondary Electron Counting Images in SEM. In *Proceedings of the XIIth International Congress for Electron Microscopy*, pages 402–403, 1990.
- [95] S. Yamada, T. Ito, K. Gouhara, and Y. Uchikawa. Electron-Count Imaging in SEM. *Scanning*, 13:165–171, 1991.
- [96] S. Yamada, T. Ito, K. Gouhara, and Y. Uchikawa. High-Speed Electron Counting System for TV-Scan Rate SE Images of SEM. In *Proceedings of the 49th Annual Meeting of the Electron Microscopy Society of America*, pages 512–513, 1991.

- [97] Yoshiki Uchikawa, Kazutoshi Gouhara, Satoru Yamada, Tsutomu Ito, Tetsuji Kodama, and Pooja Sardeshmukh. Comparative Study of Electron Counting and Conventional Analogue Detection of Secondary Electrons in SEM. *Journal of Electron Microscopy*, 41(4):253–260, 1992.
- [98] Ahmed Kirmani, Dheera Venkatraman, Dongeek Shin, Andrea Colaço, Franco N C Wong, Jeffrey H Shapiro, and Vivek K Goyal. First-Photon Imaging. *Science*, 343:58–62, 2014.
- [99] Christian Kramberger, Andreas Mittelberger, Christoph Hofer, and Jannik C Meyer. Analysis of Point Defects in Graphene Using Low Dose Scanning Transmission Electron Microscopy Imaging and Maximum Likelihood Reconstruction. *Physica Status Solidi B*, 254:1700176, 2017.
- [100] Andreas Mittelberger, Christian Kramberger, Christoph Hofer, Clemens Mangler, and Jannik C. Meyer. Automated Image Acquisition for Low-Dose STEM at Atomic Resolution. *Microscopy and Microanalysis*, 23(4):809–817, 2017.
- [101] Florian F Krause, Marco Schowalter, Tim Grieb, Knut Müller-caspar, Thorsten Mehrrens, and Andreas Rosenauer. Effects of instrument imperfections on quantitative scanning transmission electron microscopy. *Ultramicroscopy*, 161:146–160, 2016.
- [102] Sunghwan Hwang, Chang Wan Han, Singanallur V. Venkatakrisnan, Charles A. Bouman, and Volkan Ortolan. Towards the low-dose characterization of beam sensitive nanostructures via implementation of sparse image acquisition in scanning transmission electron microscopy. *Measurement Science and Technology*, 28:045402, 2017.
- [103] Daliang Zhang, Yihan Zhu, Lingmei Liu, Xiangrong Ying, Chia-En Hsiung, Rachid Sougrat, Kun Li, and Yu Han. Atomic-resolution transmission electron microscopy of electron beam-sensitive crystalline materials. *Science*, 359(6376):675–679, 2018.
- [104] Akshay Agarwal, Karl K. Berggren, Yuri J. van Staaden, and Vivek K. Goyal. Reduced damage in electron microscopy by using interaction-free measurement and conditional reillumination. *Physical Review A*, 99(6):063809, 2019.
- [105] Robert J. Moerland, I. Gerward C. Weppelman, Mathijs W. H. Garming, Pieter Kruit, and Jacob P. Hoogenboom. Time-resolved cathodoluminescence microscopy with sub-nanosecond beam blanking for direct evaluation of the local density of states. *Optics Express*, 24(21):24760, 2016.
- [106] Lixin Zhang, Mathijs W.H. Garming, Jacob P. Hoogenboom, and Pieter Kruit. Beam displacement and blur caused by fast electron beam deflection. *Ultramicroscopy*, 211:112925, 2020.

- [107] Safa C. Medin, John Murray-Bruce, and Vivek K. Goyal. Optimal stopping times for estimating bernoulli parameters with applications to active imaging. *ICASSP, IEEE International Conference on Acoustics, Speech and Signal Processing - Proceedings*, 2018-April(Section 2):4429–4433, 2018.
- [108] Safa C. Medin, John Murray-Bruce, David Castanon, and Vivek K Goyal. Beyond Binomial and Negative Binomial: Adaptation in Bernoulli Parameter Estimation. *IEEE Transactions on Computational Imaging*, 5(4):570–584, 2019.
- [109] Niccolò Banterle, Khanh Huy Bui, Edward A. Lemke, and Martin Beck. Fourier ring correlation as a resolution criterion for super-resolution microscopy. *Journal of Structural Biology*, 183(3):363–367, 2013.
- [110] David C. Joy, Joseph Michael, and Brendan Griffin. Evaluating SEM performance from the contrast transfer function. In Christopher J. Raymond, editor, *Metrology, Inspection, and Process Control for Microlithography XXIV*, volume 7638, page 76383J, 2010.
- [111] Denis G. Pelli and Peter Bex. Measuring contrast sensitivity. *Vision Research*, 90:10–14, 2013.
- [112] Glenn D. Boreman. Modulation Transfer Function. In *Modulation Transfer Function in Optical and Electro-Optical Systems*, pages 85–107. SPIE, 1000 20th Street, Bellingham, WA 98227-0010 USA, 2001.
- [113] Rajashree Dash and Pradipta K. Dash. MDHS-LPNN: A Hybrid FOREX Predictor Model Using a Legendre Polynomial Neural Network with a Modified Differential Harmony Search Technique. pages 459–486, jan 2017.
- [114] Mean Absolute Error. In Claude Sammut and Geoffrey I Webb, editors, *Encyclopedia of Machine Learning*, pages 652–652. Springer US, Boston, MA, 2011.
- [115] Arnaud de Myttenaere, Boris Golden, Bénédicte Le Grand, and Fabrice Rossi. Mean Absolute Percentage Error for regression models. *Neurocomputing*, 192:38–48, 2016.
- [116] J. T. L. Thong, K. S. Sim, and J. C. H. Phang. Single-image signal-to-noise ratio estimation. *Scanning*, 23(5):328–336, 2001.
- [117] F. Timischl. A dynamic scanning method based on signal-statistics for scanning electron microscopy. *Scanning*, 36(3):317–326, 2014.
- [118] F. Timischl, M. Date, and S. Nemoto. A statistical model of signal-noise in scanning electron microscopy. *Scanning*, 34(3):137–144, 2012.
- [119] Ray F. Egerton. Electron energy-loss spectroscopy in the TEM. *Reports on Progress in Physics*, 72(1):016502, 2009.

- [120] Pieter Kruit, Maurice Krielaart, and Yuri van Staaden. Phase Contrast in Quantum Electron Microscopy. *Microscopy and Microanalysis*, 25(S2):1664–1665, 2019.
- [121] Minxu Peng, John Murray-Bruce, Karl K. Berggren, and Vivek K Goyal. Source Shot Noise Mitigation in Focused Ion Beam Microscopy by Time-Resolved Measurement. *Ultramicroscopy*, 211:112948, 2020.